Dipartimento di Ingegneria Meccanica e Aerospaziale

Dottorato di Ricerca in Meccanica Teorica e Applicata
XXXI Ciclo

Fluctuating Hydrodynamics Model for Homogeneous and Heterogeneous Vapor Bubble Nucleation

PhD Candidate

Mirko Gallo

Supervisor

Prof. Carlo Massimo Casciola

Tutor

Dott. Francesco Magaletti

Fluctuating Hydrodynamics Model for Homogeneous and Heterogeneous Vapor Bubble Nucleation

Mirko Gallo

2 aprile 2019

Man is a mystery. It needs to be unravelled, and if you spend your whole life unravelling it, don't say that you've wasted time. I am studying that mystery because I want to be a human being.
Fyodor Dostoevsky.

Abstract

At the molecular scale, even in conditions of thermodynamic equilibrium, the fluids do not exhibit a deterministic behavior. Going down below the micrometer scale, the effects of thermal fluctuations play a dominant role in the dynamics of the system, calling for a suitable description of thermal fluctuations. These models not only play an important role in physics of fluids, but a deep understanding of these phenomena is necessary for the progress of some of the latest nanotechnology. For instance the modeling of thermal fluctuations is crucial in the design of flow micro-devices, in the study of biological systems, such as lipid membranes, in the theory of Brownian engines and in the development of artificial molecular motor prototypes. Another problem with a huge technological impact is the phenomenon of *nucleation* – the precursor of the phase transition in metastable systems – in this context related to bubble formation in liquid-vapor phase transition. Vapor bubbles form in liquids by two main mechanisms: boiling, by increasing the temperature over the boiling threshold, and cavitation, by reducing the pressure below the vapor pressure threshold. The liquid can be held in these metastable states (overheating and tensile conditions, respectively) for a long time without forming bubbles. Bubble nucleation is indeed an activated process, requiring a significant amount of energy to overcome the free energy barrier

and bring the liquid from the metastable conditions to the thermodynamically stable state where vapor is observed. Depending on the thermodynamic conditions, the nucleation time may be exceedingly long, the so-called "rare-event" issue. Nowadays molecular dynamics is the unique tool to investigate such thermally activated processes. However, its computational cost limits its application to small systems (less than few tenth of nanometers) and to very short times, preventing the study of hydrodynamic interactions. The latter effects are crucial to understand the cavitation phenomenon in its entirety, starting from the vapor embryos nucleation up to the macroscopic motion.

In this thesis a continuum diffuse interface model of the two-phase fluid has been embedded with thermal fluctuations in the context of the so-called Fluctuating Hydrodynamics (FH) and has been exploited to address cavitation. This model provides a set of partial stochastic differential equations, whose deterministic part is represented by the capillary Navier-Stokes equations and reproducing the Einstein-Boltzmann probability distribution for the macroscopic fields. This mesoscale approach enables the description of the liquid-vapor transition in extended systems and the evaluation of bubble nucleation rates in different metastable conditions by means of numerical simulations. Such model is expected to have a huge impact on the understanding of the nucleation dynamics since, by reducing the computational cost by orders of magnitude, it allows the unique possibility of investigating systems of realistic dimensions on macroscopic time scales. In addition, after the nucleating phase, the deterministic equations have been used to address the collapse of a cavitation nanobubble near a solid boundary, showing an unprecedented description of interfacial flows that naturally takes

into account topology modification and phase changes (both vapor/liquid and vapor/supercritical fluid transformations).

Overview

Nucleation is a complex and intrinsically multiscale problem representing the precursor of phase change in first order phase transitions. Among the huge variety of nucleation problems in nature, this thesis is devoted to the study of liquid-vapor phase change inception. The proposed model is based on a mesoscale approach exploiting a diffuse interface approach embedded with thermal fluctuations. The approach I follow in this PhD project is theoretical and numerical, and basically, can be structured as follows: I coupled a diffuse interface model with fluctuating hydrodynamics, exploiting the model to address homogeneous and heterogeneous nucleation. In order to perform *in silico experiments*, an *in-house* parallel code has been developed. Nucleation rates, have been calculated by numerically integrated the resulting equations (Landau-Lifshitz-Navier-Stokes equations with capillarity) showing very good agreement with MD simulations as well as more classical approach. The model is also able to capture long terms dynamics in nucleation –not easily detectable with conventional techniques– revealing some interesting effects. In fact, in closed system, the hydrodynamic effects have a great influence on the nucleation dynamics, where the *"bubble crowding"* strongly change the nucleation rate. Furthermore, I proposed a spherical version of the LLNS, particularly useful when dealing with homogeneous nucleation,

since it is reasonable to assume the spherical shape of nucleation embryos. In addition LLNS equations can be also used in a pure deterministic setting, showing a very accurate description of the hydrodynamics of a two phase system. In particular, the model is exploited to study the collapse of a cavitation nanobubble near a solid surface, showing an accurate reproduction of the main physical phenomena detected in the experiments, namely: strong peaks of pressure and temperature, shockwave emission and liquid jet formation.

In the first chapter, an introduction to vapor bubble nucleation will be given, with particular emphasis on cavitation. The main features of the phenomenon are exposed as well as the technological implications. Furthermore a brief overview on the state of art and about the importance of using mesoscale approaches in this context will be illustrated.

The second chapter retraces a detailed description of the Van der Walls diffuse interface approach. In the first sections the thermodynamics of a non-homogeneous system is recalled, deriving a thermodynamically consistent equations of motion for a multiphase system. In this context, I proposed a general expression to uniquely identify the solid-fluid contact angle, relating the solid-fluid free energy contributions with the bulk properties of the fluid. Furthermore a rare event technique (String Method) is coupled with the phase field description to address the bubble nucleation rate.

The third chapter recalls the Einstein theory of hydrodynamic fluctuations, focusing on capillary fluids. Starting from the probability density functional, under the hypothesis of small fluctuations, the field correlations of a Van der Walls fluid are obtained in a closed form. The celebrated fluctuation dissipation theorem is than derived in a phase field context, leading

to the Landau-Lifshitz-Navier-Stokes (LLNS) equations for a capillary fluid. These equations are used to address the vapor bubble nucleation in a metastable liquid. Furthermore, I derived a new set of stochastic equations for nucleation, arising from a spherical version of LLNS.

The fourth chapter is focused on the numerical analysis of the LLNS equations, highlighting the principal numerical issues in capillary and stochastic equations. The first sections concern the numerical analysis of the deterministic part of the equations, while the other ones are focused on the stochastic part.

Chapter 5 is devoted to draw the conclusions about this research activity, its implications and further possible developments.

The remaining chapters report the papers I published on high-impact peer-review journals. In particular in Chapter 6 the Van der Waals diffuse interface model is exploited to address the dynamics of a cavitation nanobubble near solid boundary, and in Chapter 7 the same diffuse interface model is coupled with a fluctuating hydrodynamic theory to study the vapor bubble homogeneous nucleation. Chapter 8 report the model extension to study heterogeneous nucleation (paper in preparation).

Finally, since the present PhD project is framed in an interdisciplinary context between engineering and physics, in the appendices are retraced the main features of mathematical techniques that are commonly known in the statistical physics community and not entirely taken for granted in the engineering one.

During my PhD work an international collaboration with Dr. X. Noblin from the "Institut de Physique de Nice"lead to the publication of paper concerning the acoustics of a micro-confined cavitation bubble [127]. In addition

I was Co-Advisor of three master thesis:

- Forward Flux Sampling technique in Fluctuating Hydrodynamics context to study vapor bubble nucleation. Vincenzo Andrea Montagna, master thesis in Nanotechnology Engineering Sapienza University of Rome.
- A numerical Model to address the dynamics of macroscopic bubbles near solid walls. Dario Abbondanza, master thesis in Mechanical Engineering Sapienza University of Rome.
- Stochastic Models for Bubble Nucleation, Davide Cocco master thesis in Nanotechnology Engineering Sapienza University of Rome.

Published Papers

- Magaletti, F., Gallo, M., Marino, L., & Casciola, C. M. (2015). Dynamics of a vapor nanobubble collapsing near a solid boundary. In Journal of Physics: Conference Series.
- Magaletti, F., Gallo, M., Marino, L., & Casciola, C. M. (2016). Shock-induced collapse of a vapor nanobubble near solid boundaries. International Journal of Multiphase Flow.
- Gallo, M., Magaletti, F ., & Casciola, C. M. Fluctuating hydrodynamics as a tool to investigate nucleation of cavitation bubbles.Multiphase Flow: Theory and Applications, 347. 2018.
- Gallo, M., Magaletti, F ., & Casciola, C. M. Thermally activated vapor bubble nucleation: the Landau–Lifshitz/Van der Waals approch. Physical Review Fluids, 2018.

- Scognamiglio, C., Magaletti, F., Izmaylov, Y., Gallo, M., Casciola, C. M., Noblin, X. (2018). The detailed acoustic signature of a micro-confined cavitation bubble. Soft matter.

Papers in preparation

- Gallo, M., Magaletti, F ., & Casciola, C. M. A mesoscale model for Heterogeneous Nucleation.
- Magaletti, F .,Gallo, M., & Casciola, C. M. Coupling a rare event technique with diffuse interface approach for vapor bubble heterogeneous nucleation.

Conferences and workshops

- Hydrodynamic Fluctuations in Soft-Matter Simulations, February 2016 - Prato, Italy (Poster).
- MolSimEng, September 2016 - Milan, Italy (Poster).
- Multiphase Flow, June 2017 - Tallin, Estonia (Talk).
- Numerical Simulations of Flow with Particles, Bubbles and Droplets, May 2018 - Venice, Italy (Talk).
- European Fluid Mechanics Conference, EFMC12, September 2018 - Vienna, Austria (Talk).

Indice

Capitolo 1

Introduction

The fundamental aspect underlying the phase change inception draws similarities in a very large number of applications such as vapor bubble cavitation on propeller blades and on turbines, ice formation on aircrafts, drying or de-foaming procedures in the food industry, solidification in material science and alloy production. The variety of technological applications combined with the complex nature of the phenomenon make nucleation a stimulant research area. The main challenging aspect concerning nucleation is its multiscale nature, ranging from the molecular scale up to the hydrodynamic one. From an experimental point of view, quantitative measurements during the phase change inception are not easy to perform, due to the wide spectrum of space-time scales to be investigated. This issue represents also a great challenge for theoreticians who need to develop consistent multiscale models to correctly capture the critical features of the nucleation phenomenon.

This Chapter is devoted to the presentation of the peculiar aspects of nucleation, with particular attention to the nucleation of vapor bubbles in liquids. The main features of the liquid vapor phase transition will be highlighted, as well as the possible technological implications.

1.1 The impact of nucleation phenomena in nature and technological applications

Nucleation is the "incipit" in the formation of a new thermodynamic phase, representing the precursor of phase transformation. In particular, the liquid-vapor phase transition can be achieved by two different mechanism: by increasing the temperature up to the boiling threshold, or by decreasing the pressure below the vapor pressure. We will refer to these two processes as *boiling* and *cavitation*, respectively. The qualitative mechanism during cavitation of water flowing at ambient conditions, for example, is simple: vapor nuclei locally appear where the liquid accelerates and its pressure decreases. Inside these bubbles the pressure is as low as the vapor pressure (that at ambient temperature is about $2.3kPa$) hence they can survive, and even grow, as long as they remain in the liquid low pressure regions. However, when the flow transports them in a region with higher pressure, they suddenly become unstable and collapse. Vapor bubble implosion is a very complicated physical phenomenon, which comprises large bubble deformation and topological changes, shockwave emission and propagation through the liquid, phase transition to and from supercritical conditions [60], and intense pressure and temperature peaks on the order of dozens GPa and 10^4K, respectively, [111]. The aforementioned effects are considered the main cause of damage that is observed on the ship propellers, hydraulic turbines, diesel engines [17, 14, 120].

Nowadays cavitation is also exploited as a positive source of damage in different areas of applied sciences, for instance in medicine SWL (shock wave lithotripsy) it is used to comminute kidney and gall stones with acoustic

waves and HIFU (high intensity focused ultrasound) for tumor treatment and other surgical applications [27, 29, 70]. In biochemistry applications the vorticity induced during the last stage of bubble collapse is being used to enhance mixing [89], furthermore manipulation of cavitation nuclei is employed in drugs and genetic material delivery, e.g., to enhance biological barrier layer permeability [38, 114] . Concerning nuclei manipulation, liposomes and microbubbles are designed with a variety of contents, structures and appendage in order to carry drugs to the target site. Drug can be incorporated by themselves, or if insoluble in water, within the lipid layer. After the bubbles/liposomes have reached the specific site, cavitation can be triggered by using ultrasound or laser-pulses. Hence by controlling liquid-jet formation or shockwave emission cell membrane poration (the so-called sonoporation) can be achieved. Recently gene-loaded structures have been used for DNA injection without destroying effects on the cell[19]. In a completely different context cavitation devices have been developed for the treatment of water pollution [1]. In wastewater treatment, the combined mechanical, thermal and chemical effects of bubble collapse are exploited. In particular the production of free radicals [134] is found to enhance enhances the oxidation of contaminants in water.

Another example of the cavitation occurrence is the phenomenon of cracking knuckles which have been recently theorized to derive from cavitation bubbles formed into synovial liquid within articulations. According to some authors osteoarthritis can be caused by repeated cavitation events occurring into joints when they are subjected to traction stress [140].

The crucial issue, and the important challenge, is to obtain quantitative information on all the different aspects involved in cavitation. An appropria-

te investigation down to the smallest length and time scale is needed in order to capture all the macroscopic effects. From an experimental point of view, quantitative measurements of relevant physical observables in cavitation are not easy to perform, due to the reduced space-time scales on which the phenomenon occurs ($ns/\mu s$ in terms of time and $nm/\mu m$ in terms of space), thus developing theoretical and numerical models is crucial in order to achieve a quantitative understanding of cavitation. On the other hand developing a fully consistent theory is still a great challenge for theoreticians. Concerning the bubble dynamics, the first mathematical model was developed by Lord Rayleigh in 1917 and subsequently improved by M. Plesset [118]. Rayleigh studied the dynamics of a bubble in an incompressible liquid under the assumption of spherical symmetry. He modeled the bubble interface as a mathematical, zero-thickness discontinuity, obtaining an evolution equation for the bubble radius. This model has proven to be very useful for predicting the time evolution of the gas pressure inside the bubble, the bubble oscillations, and an overview of the approximate dynamics of the collapse. However the model is not able to predict many other phenomena that characterise cavitation: starting from the nucleation phase up to the reabsorption. The main limitations of these *sharp interface models* emerge when the diffused nature of the vapour-liquid interface becomes important. This typically happens when the size of the bubble is comparable with the vapor-liquid interface thickness, like e.g. in the case of nanobubbles during nucleation inception, and during the last stages of bubble collapse. More complete models are required in these cases to correctly follow the dynamics down to the smallest relevant scales. One possible solution is relaxing the assumption of sharp interface, by adopting, e.g., a phase field approach, to be discussed in full

detail in Chapter 2.

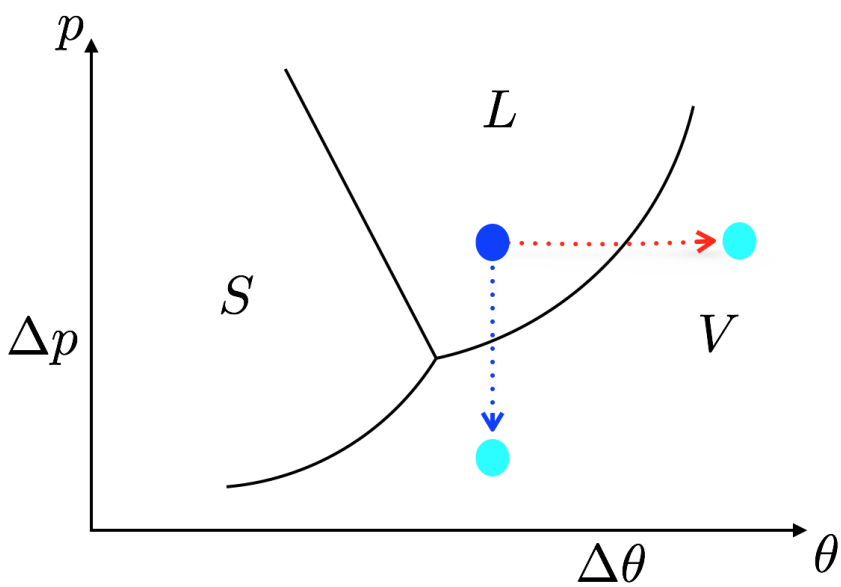

Figura 1.1: The sketch qualitatively describes the state of matter as a function of pressure and temperature. The *S-zone* represent the solid state, the *L-zone* the liquid one and the *V-zone* the vapor phase.

1.2 Metastability and Phase Transitions

Let us now focus on the thermodynamic aspects of the liquid-vapour phase transition analysing the phase diagram in Fig.1.1. Starting from the liquid state, evaporation and cavitation are represented by the red and the blue paths, respectively. This description is however oversimplified and a much more rigorous analysis of these processes is needed for a complete understanding of the phase transition in liquids [41]. In fact, after reaching the boiling temperature or the vapour pressure, the liquid can remain trapped near coexistence line for a long time (depending on the level of overheating

or stretching). The reason is that bubble nucleation is an activated process that needs to surmount the free energy barrier separating the liquid and the vapor states. As a consequence the system can remain trapped in a metastable state, unless the barrier vanishes altogether, i.e. the system is at the so-called spinodal conditions where the transition does not require an activation energy (spinodal decomposition).

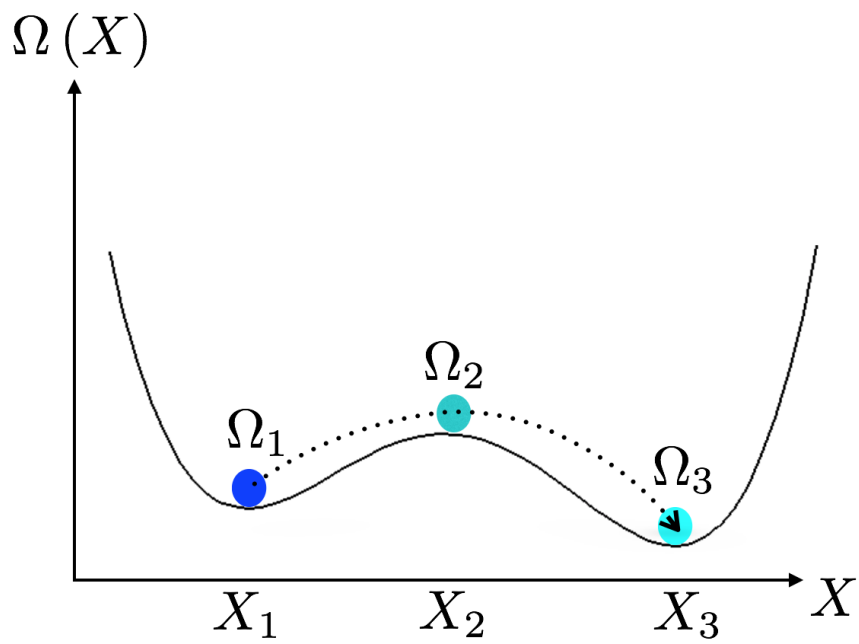

Figura 1.2: The sketch qualitatively describes the energetic configurations of a thermodynamic system as a function of a generic reaction coordinate X. The states $1, 2, 3$ represent the metastable, the critical and the stable configurations respectively.

In order to better explain this important point, it is worth focusing on a one dimensional system, whose free energy Ω is sketched in Fig. 1.2 as a function of a reaction coordinate X. The state X_1 is a metastable state, because it is living at the energetic level Ω_1, which corresponds to a relative

minimum of the free energy landscape. This "peculiar" state is not the thermodynamic equilibrium state that the system is expected to reach on the long time scale which corresponds to the absolute free energy minimum, X_3. Nevertheless, the system could remain trapped for a very long time around X_1. In fact, an amount of energy greater than $\Delta\Omega^* = \Omega_2 - \Omega_1$, with Ω_2 the energy value of the transition state X_2, is needed to bring the system to thermodynamic equilibrium. In *thermally activated process* the energy is provided by thermal fluctuations. In this case the life time τ of the metastable state is related to the energy barrier as $\tau \propto \exp(\Delta\Omega^*/k_B\theta)$, suggesting the definition of metastability as a stability limited over time.

There are many metastable systems in nature. One of the most popular is carbon in the diamond phase at ambient conditions that could undergo, in principle, the diamond-graphite phase transition. In standard conditions, the stable form of carbon is graphite. However the life time of diamond is so long that diamond can remain stable for million years [137, 7]. Metastability could be observed also in supercooled water [106, 103], (e.g freezing rain, icing aircraft) or in emulsions and colloids [85, 48], and in mechanical systems, for instance when dealing with avalanches [68], and more in general with *sandpile-like* systems [24].

Let us now focus on metastable liquids and liquid-vapor phase transition at constant temperature (cavitation). Figure 1.3 provides the phase diagram of a Lennard-Jones fluid [75] with *binodal* and the *spinodal* lines reported in the inset. In the $\rho - \theta$ plane, the binodal line is identified as the set of points having same temperature, chemical potential and pressure, blu and azure lines in the inset. The spinodal points are identified along isotherms where $\partial p/\partial\rho = 0$. They are represented by the red and orange lines. All the states

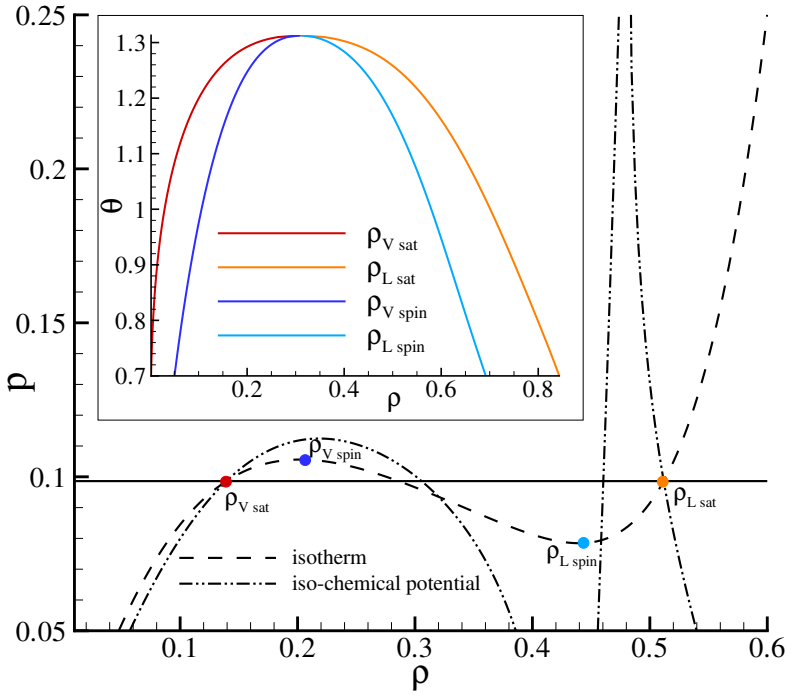

Figura 1.3: Phase diagram for the Lennard-Jones EoS[75]. In the main plot the isotherm $\theta = 1.25$ and the iso-chemical potential $\mu = \mu_{sat}$ with the saturation value are reported with dashed and dash-dotted lines, respectively. The saturation densities are identified as the two points with equal temperature, chemical potential and pressure; the red circle represent the vapor saturation point and the orange circle the liquid one. The other two circles, blue and light blue, represent the spinodal points, vapor and liquid respectively, identified on the isotherm where $\partial p/\partial \rho = 0$. In the inset the loci of all the saturation and spinodal points at different temperatures are reported in the $\rho - \theta$ plane.

in the regions comprised between binodals and spinodals are metastable (i.e. drops and bubbles can nucleate in the metastable regions on the left (vapour) and on the right (liquid) of the diagram, respectively).

Metastable liquid is represented by a point placed between the orange and azure line, and it is separated from its stable state (homogeneous vapor

phase), by an energy barrier that must be surmounted to bring the system in the new phase. This occurs due to thermal fluctuations, which, starting from an ideally homogeneous liquid phase, eventually induce the formation of vapour nuclei. After the nuclei reach a critical size, they start expanding surrounded by their mother phase, in a complex non-equilibrium process, leading the system to decompose in two different phases.

Depending on thermodynamic conditions, the time needed for the occurrence of a sufficiently intense fluctuation event able to produce a supercritical nucleus can be very long. For this reason, nucleation can be seen as a *rare event*. The relevance of thermal fluctuations underlines the microscopic nature of the phenomenon. However, despite its origin is to be definitely found at the atomistic level, nucleation takes place on temporal scales which, due to the rare event issue, is several order of magnitude greater than the molecular characteristic time. Moreover, in many cases the interest is centred on systems of macroscopic size.

The presence of impurities or dissolved gas strongly lowers the energy barrier and facilitates bubble formation. The presence of solid boundaries makes a similar effect. In fact the energy needed to form a vapour bubble on a solid surface depends on the contact angle and, as explained in the next section, it can be considerably lower than it is in a bulk phase. This is the reason why it is so common to observe cavitation in water at pressures considerably larger than the extreme cavitation limit of ultra-pure water which can sustain $1\,kbar$ tensions [10]. Moreover recent experimental works have highlighted how the wettability of ultra-smooth surfaces can strongly influence the onset temperature of pool boiling in superheated liquids [26, 25, 100].

Several theoretical models have been proposed in order to estimate the energy barrier and the nucleation rate, i.e. the number of nucleated bubble per unit time and volume, both in homogeneous and heterogeneous (near extraneous boundaries) conditions. The classical nucleation theory (CNT) [18], poses the basis for the understanding of the phenomena, and it may be easily extended to the non-homogeneous case [147], as recalled in Sec. 1.3. The major contribution to the work to create a vapour bubble into a metastable liquid is the positive work needed to create the bubble surface. Its value is related to the surface tension and to the surface extension. The counteracting contribution is the energy released to transform the liquid into the stable vapour phase. Its value is related to the difference between the vapour pressure and the ambient pressure and it is proportional to the bubble volume. The (algebraic) sum of these two contributions gives the total work needed to create a bubble of a given radius. At small radii the surface contribution prevails up to a critical bubble radius where the needed work is maximum and then the negative volume contribution becomes stronger and the work start decreasing. This maximum work corresponds to the energy barrier that must be overcome to create a vapor region.

1.3 Classical Nucleation theory

Classical nucleation theory (CNT) [80, 28, 147] provides the fundamental understanding of bubble nucleation in a metastable liquid, both for homogenous (bubble forming in the bulk liquid) and heterogenous conditions (bubble forming in contact with an extraneous phase, typically a solid with given geometry and chemical properties). The simplest example of heterogenous nucleation is a vapor bubble nucleating on a flat solid surface at fixed contact

angle ϕ. The free energy of a spherical cup laying on a flat solid wall,

$$\begin{aligned}\Omega\left(R,\phi\right) &= -\Delta p V_V\left(R,\phi\right)+\gamma_{LV}A_{LV}\left(R,\phi\right)+\\ &+ \gamma_{SV}A_{SV}\left(R,\phi\right)+\gamma_{LS}A_{LS}\left(R,\phi\right)\ ,\end{aligned} \tag{1.1}$$

depends on the vapor-liquid pressure jump $\Delta p = p_V - p_L$ (the Laplace pressure), the bubble volume V_V, the area of liquid-vapor A_{LV}, solid-vapor A_{SV} and liquid-solid A_{LS} interfaces and the respective surface energies $\gamma_{LV}, \gamma_{SV}, \gamma_{LS}$. Introducing the equilibrium (or Young) contact angle $\phi = \cos^{-1}(\gamma_{LS} - \gamma_{SV})/\gamma_{LV})$ (see the sketch in Fig. 1.4, where, at variance with the standard convention, the angle is measured from the vapor-solid interface, i.e. $\phi > \pi/2$ means hydrophilic) allows for re-expressing the relevant geometric quantities as $A_{SV} = \pi R^2 \sin^2\phi$, $A_{LV} = 2\pi R^2(1-\cos\phi)$, $A_{LS} = A_w - A_{SV}$, $V_V(R,\phi) = V_V(R,\pi)\Psi(\phi)$, where is A_w the total surface of the solid wall and $\Psi(\phi) = 1/4(1-\cos\phi)^2(2+\cos\phi)$. As $\phi \to \pi$ the free energy reduces to the homogeneous case. Thus, starting from a homogeneous metastable liquid and denoting by $\Delta\Omega_{hom} = -\Delta p V_V(R,\pi) + \gamma_{LV}A_{LV}(R,\pi)$ the free energy spent for a spherical bubble of radius R in the bulk liquid, the energy required to form a spherical cup at the wall reads

$$\Delta\Omega\left(R,\phi\right) = \Delta\Omega_{hom}\left(R\right)\Psi\left(\phi\right)\ . \tag{1.2}$$

The free energy consists of two contribution, one associated with volume terms and decreasing like R^3 with increasing bubble radius and the other depending on the surface area which increases with like the square of the bubble radius. The free-energy attains a maximum, the critical state, at the critical radius R^*.

$$R^* = \frac{2\gamma_{LV}}{\Delta p}\ , \tag{1.3}$$

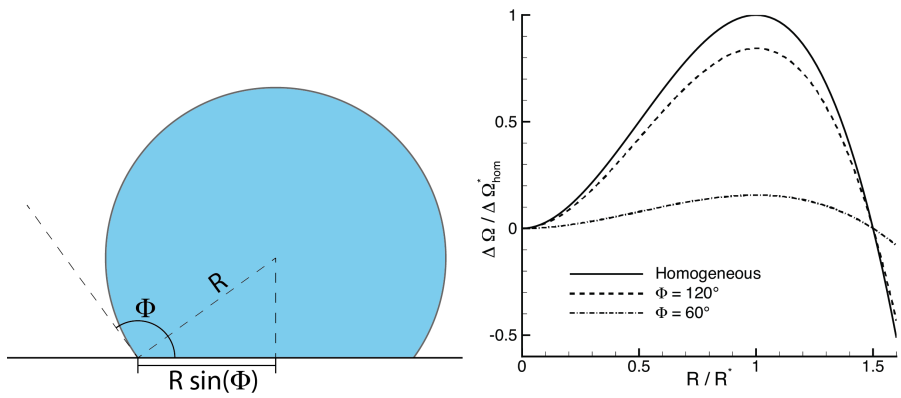

Figura 1.4: Left panel: bubble sketch illustrating the equilibrium contact angle ϕ and the bubble radius R. Right panel: CNT prediction of free-energy profiles for different contact angle ϕ, the continuous line corresponds to the homogeneous case ($\phi = \pi$), the dotted lines represent the heterogeneous case.

The corresponding free energy barrier is

$$\Delta\Omega^* = \Delta\Omega\left(R^*, \phi\right) = \Delta\Omega^*_{hom}\Psi\left(\phi\right) = \frac{16}{3}\pi\frac{\gamma^3_{LV}}{\Delta p^2}\Psi\left(\phi\right) \ . \tag{1.4}$$

The critical radius is the same both for heterogeneous and homogenous nucleation. On the opposite, the barrier $\Delta\Omega^*$ for heterogenous nucleation is lower than $\Delta\Omega_{hom}$ ($\Psi(\phi) \leq 1$). Clearly, for trivial geometrical reasons, also the critical volume $V^* = 4/3\pi R^{*3}\Psi(\phi)$ is smaller for the heterogeneous case.

As an example let us compare the work needed to form a vapour bubble in the bulk of the liquid phase $\Delta\Omega_{hom}$ (homogeneous nucleation) with the work needed to form a vapour bubble on a flat solid surface $\Delta\Omega_{het}$ (heterogeneous nucleation) by assuming, for the sake of simplicity, the contact angle $\phi = \pi/2$. It is straightforward to realize that $\Delta\Omega_{hom} = 2\Delta\Omega_{het}$, since the critical bubble is expected to be a perfect half of the one in homogeneous condition. It follows that the probability of observing a nucleated bubble on a solid surface

is significantly larger than the probability of observing a vapour bubble in the bulk.

1.3.1 The Blander and Katz Nucleation Rates

The crucial observable in the nucleation process is the nucleation rate, i.e. the normalized number of super-critical bubbles formed per unit time. In the heterogeneous context the normalization is per unit surface (as opposed to unit volume used in homogeneous conditions). The expression for the nucleation rates[18, 41] are

$$J_{BK} = n_L \sqrt{\frac{2\gamma_{LV}}{\pi m}} \exp\left(-\frac{\Delta\Omega^*}{k_B\theta}\right) \ , \tag{1.5}$$

concerning the homogeneous nucleation, and

$$J_{BK} = n_L^{2/3} \frac{(1-\cos\phi)}{2} \sqrt{\frac{2\gamma_{LV}}{\pi m}} \exp\left(-\frac{\Delta\Omega^*}{k_B\theta}\right) \ , \tag{1.6}$$

for the heterogeneous one, where n_L is the liquid number density and m the mass of the liquid molecule.

Equations (1.5–1.6) represent the famous Blander and Katz expressions for the nucleation rates in the CNT context. They are commonly used as a reference theory in nucleation.

1.3.2 The Kramers theory

Kramers theory [83] provides the mean time τ for the diffusion across a barrier (mean first passage time) of a random walker trapped in the metastable basin of a given potential. Let us denote $\mathcal{B} \subset \mathcal{S}$ the metastable basin where $\mathcal{S}$ is the space of the states for the physical system (each trajectory $\mathbf{X}(t) \in \mathcal{S}$).

In the present context the random walker is assumed to obey the Langevin equation

$$\frac{d\mathbf{X}}{dt} = \mu\left(\mathbf{X}\right) + \left(2\mathbf{D}\right)^{1/2}\xi(t)\,, \tag{1.7}$$

where ξ is delta-correlated process, $\langle \xi(t) \otimes \xi^T(t')\rangle = \delta(t-t')$ with $\mathbf{D}$ the diffusion tensor. Let us denote $P(\mathbf{X}, t|\mathbf{Y}, t_0)$ the transition probability from the state $\mathbf{Y}$ at the time t_0 to the state $\mathbf{X}$ at the time t. It obeys the Fokker Planck equation (see Appendix B for details)

$$\frac{\partial P\left(\mathbf{X}, t|\mathbf{Y}, t_0\right)}{\partial t} = -\mathcal{F}P\left(\mathbf{X}, t|\mathbf{Y}, t_0\right)\,, \tag{1.8}$$

where

$$\mathcal{F} = \frac{\partial}{\partial \mathbf{X}} \cdot \mu\left(\mathbf{X}\right) - \frac{\partial}{\partial \mathbf{X}} \otimes \frac{\partial}{\partial \mathbf{X}} : \mathbf{D}\,, \tag{1.9}$$

is the Fokker Planck operator.

Eq. 1.8 must be complemented with initial and boundary conditions, that in the context of *barrier crossing problems* can be assumed to be

$$P\left(\mathbf{X}, t_0|\mathbf{Y}, t_0\right) = \delta\left(\mathbf{X} - \mathbf{Y}\right) \qquad \mathbf{X} \in \mathcal{B}\,,$$

$$P\left(\mathbf{X}, t|\mathbf{Y}, t_0\right) = 0 \qquad \mathbf{X} \in \partial\mathcal{B}\,,$$

in other words $\partial\mathcal{B}$ is an absorbing boundary.

The probability that the trajectory $\mathbf{X}$ is still contained in the basin $\mathcal{B}$, or equivalently, the probability that the mean first passage time $\tau(\mathbf{Y})$ (time required to reach $\partial\mathcal{B}$ starting from $\mathbf{Y}$) is greater than the current time t, can be easily evaluated as

$$\Pi\left(t|\mathbf{Y}, t_0\right) = \int_{\mathcal{B}} P\left(\mathbf{X}, t|\mathbf{Y}, t_0\right) d\mathbf{X} \; = Pr\left(\tau(\mathbf{Y}) > t\right) = \int_t^{+\infty} \pi\left(\tau|\mathbf{Y}\right) d\tau\,, \tag{1.10}$$

with $\pi\left(\tau|\mathbf{Y}\right)$ the probability density distribution of the first passage times. Thus the mean value of τ is

$$\langle\tau\left(\mathbf{Y}\right)\rangle = \int_0^{+\infty} \tau\,\pi\left(\tau|\mathbf{Y}\right)d\tau = -\int_0^{+\infty} \tau\,\frac{\partial\Pi\left(\tau|\mathbf{Y},0\right)}{\partial\tau}d\tau\,, \tag{1.11}$$

that, after integrating by parts provides

$$\langle\tau\left(\mathbf{Y}\right)\rangle = \int_0^{+\infty} d\tau \int_{\mathcal{B}} P\left(\mathbf{X},\tau|\mathbf{Y},0\right)d\mathbf{X}\,. \tag{1.12}$$

Since $\mathbf{Y}$ is the starting state for the random walker $\mathbf{X}$, the governing equation for the mean first passage time, will be related to the Kolmogorov Backward equation, in fact by applying the adjoint of the operator $\mathcal{F}$ to the Eq. 1.12 one finds

$$\mathcal{F}^{\dagger}\langle\tau\left(\mathbf{Y}\right)\rangle = -\int_0^{+\infty} d\tau \int_{\mathcal{B}} \frac{\partial P\left(\mathbf{X},\tau|\mathbf{Y},0\right)}{\partial\tau}d\mathbf{X}\,, \tag{1.13}$$

where Eq. C.13 in Appendix B has been enforced, and the stationary conditions are invoked $P\left(\mathbf{X},t|\mathbf{Y},t_0\right) = P\left(\mathbf{X},t-t_0|\mathbf{Y},0\right)$. So, the Eq. 1.13 can be integrated, by using Eq. 1.10 leading to

$$\mathcal{F}^{\dagger}\langle\tau\left(\mathbf{X}\right)\rangle = 1\,, \tag{1.14}$$

representing a differential equation for the mean first passage time, with the boundary condition $\langle\tau\left(\mathbf{X}\right)\rangle = 0$ on $\partial\mathcal{B}$.

In the light of above general description, for a one dimensional physical system, moving in a bistable potential $\Omega(X)$, according to the equation

$$\frac{dX}{dt} = -\frac{d\Omega}{dX} + \sqrt{2D}\xi(t)\,, \tag{1.15}$$

a simple equation for $\langle\tau\rangle$ can be deduced by enforcing Eq. 1.14,

$$-\frac{d\Omega}{dX}\frac{d}{dX}\langle\tau\left(X\right)\rangle + D\frac{d^2}{dX^2}\langle\tau\left(X\right)\rangle + 1 = 0\,, \tag{1.16}$$

By multiplying both sides of Eq. 1.16 by the integrating factor $\exp(-\beta\Omega)/D$, the equation is rearranged as

$$\frac{d}{dX}\left(\exp\left(-\beta\Omega\right)\frac{d\langle\tau(X)\rangle}{dX}\right) = -\frac{1}{D}\exp\left(-\beta\Omega\right) , \tag{1.17}$$

with $\beta = 1/k_B\theta$.

Hence by initialising the system in the metastable basin $\cup$, the mean time required to reach the saddle point in the unstable basin $\cap$, is obtained by integrating Eq. 1.17, leading to

$$\langle\tau\rangle = \int_{\cup}\exp\left(-\frac{\Omega(X)}{k_B\theta}\right)dX\int_{\cap}\frac{1}{D}\exp\left(\frac{\Omega(X)}{k_B\theta}\right)dX . \tag{1.18}$$

The relationship between barrier crossing and nucleation, becomes evident when one considers the free energy of a vapor bubble in a surrounding liquid, as prescribed by CNT. In fact by imposing the potential $\Omega = \Delta\Omega$ in Eq. 1.2, the mean time required to form a critical bubble can be evaluated by solving Eq. 1.18.

Here for the sake of simplicity a simple approximation of Eq. 1.14 based on the Laplace's method is reported. This method provides accurate results for high barriers. Alternatively a numerical approach should be adopted. The approximation is

$$\tau = \frac{1}{D^*}\exp\left(\frac{\Delta\Omega^*}{k_B\theta}\right)\left[\int_{-\infty}^{+\infty}dr\exp\left(-\frac{1}{2}\frac{\chi}{k_B\theta}r^2\right)\right]^2 , \tag{1.19}$$

with $\chi = d^2\Delta\Omega/dR^2|_{R=0} = 8\pi\gamma_{LV}\Psi(\phi)$. The RHS of Eq. (1.19) is a Gaussian integral that is easily calculated providing

$$\tau\left(\phi\right) = \frac{1}{D^*}\frac{k_B\theta}{4\Psi(\phi)\gamma_{LV}}\exp\left(\frac{\Delta\Omega^*}{k_B\theta}\right) . \tag{1.20}$$

The diffusion coefficient $D^* = k_B\theta/16\mu\pi R^*$ as evaluated in [101], by enforcing the fluctuation dissipation balance for the overdamped Rayleigh-Plasset equation, where μ is the fluid viscosity.

Once τ is evaluated, the nucleation rate may be estimated as [12, 55]

$$J_{hom} = \frac{n_L}{\tau(\pi)} \ , \tag{1.21}$$

for the homogeneous case, and

$$J_{het} = \frac{n_L^{2/3}}{\tau(\phi)} \ , \tag{1.22}$$

for the heterogeneous one.

1.4 Modelling Thermal Fluctuations at the Continuum Level

As discussed in the previous sections, a suitable modelling of thermal fluctuations is crucial to address nucleation, and in general multiphase flow involving spontaneous phase transformations. For this reason a brief description of the theory of hydrodynamic fluctuations at the continuum level is included in the present Introduction.

At the molecular scale, even in conditions of thermodynamic equilibrium, the fluids exhibits a stochastic behaviour. In fact, going down below the micrometer scale, the effects of thermal fluctuations play a dominant role in the dynamics of the system. As a consequence, a suitable description of mesoscale fluid dynamics must include thermal fluctuations. Such fluctuations have been experimentally investigated by light and neutron scattering [15]. Since the pioneering work of Landau and Lifshitz (1958, 1959) [84] several models, describing the hydrodynamic fluctuations at the continuum level, have been developed [61, 152, 104, 124]. In the literature these approaches are grouped under the name of "Fluctuating Hydrodynamics". The main

idea of Lifshitz and Landau theory is to treat the thermodynamic fluxes as stochastic processes. As prescribed by the thermodynamics of irreversible processes, at macroscopic level, thermodynamic fluxes are the expression of microscopic molecular degrees of freedom of the thermodynamic system. Under this respect dissipation in fluids can be seen as macroscopic manifestation of the energy transfer arising from random molecular collisions [40]. Thus at mesoscopic scale, thermodynamic fluxes have to be modeled as stochastic tensor fields, whose statistical properties can be inferred by enforcing the fluctuation-dissipation-balance (FDB). Since the eminent work of Einstein on the theory of equilibrium thermal fluctuations [57], other investigators have analised the statistical fluctuation by considering the entropy as the probability functional of the fluctuations [61, 123, 124]. Each fluctuation results in an entropy deviation from the equilibrium value (the maximum value). Evidently, every large deviation from the equilibrium conditions (resulting for a great fluctuation) will have a very small probability of occurrence.

Once a suitable probability distribution functional of the fluctuations is available, a stochastic process reproducing such equilibrium statistical properties can be appropriately defined. In this context, the fluctuating hydrodynamics equations can be seen as a set of stochastic processes reproducing the Einstein-Boltzmann probability distribution for the fields, whose deterministic part is represented by the Navier-Stokes equations. In principle the theory of fluctuating hydrodynamics has been derived for the linearised Navier-Stokes equations, and as such, it can be considered valid only for small fluctuations. However some important works have advanced the theory to the non-linear regime [132, 133, 142], highlighting several differences with respect to the linear one. In particular the study of one dimensional

non-linear stochastic Burgers equations provides connections with the KPZ scaling behavior [78], and the Levy distribution. In addition, non-linear version of FDB are well know [136], as well as stochastic equations for non-linear hydrodynamics [59]. These theories, far away from equilibrium, provide critical changes in the field statistics, resulting in long-ranged correlations also in stationary non equilibrium conditions, like, e.g. in the Rayleigh-Bernard problem [39]. More commonly, the extension of the theory to the non-linear case, is based on the assumption on the *local-equilibrium* [21, 40]. This assumption implies that in a non-equilibrium condition, the expressions for the fluctuation statistics of a system in equilibrium continue to be valid, by substituting the equilibrium values with the local values of the hydrodynamic fields. Starting from the pioneering work of Garcia et al. [65], in recent years there has been an exponential increase of numerical methods for fluctuating hydrodynamics equations [54, 46, 11, 53, 13]. These models not only play an important role in the physics of fluids, but their predictive power can be useful to improve some of the latest nanotechnologies. For instance the modeling of thermal fluctuations is crucial in the design of flow micro-devices [47, 20], in the study of biological systems, such as lipid membranes [107], in the theory of Brownian engines and in the development of artificial molecular motors prototypes [115]. Inspired by organic devices able to convert chemical into mechanical energy by means of thermal noise, devices operating with the same principles have been theorised. For instance, the cell division is a mechanical process, driven by the chemical energy released during the ATP hydrolysis , with much higher efficiency than the common operating machines. Actually RNA and DNA polymerase can be seen as molecular motors. In addition, thermal fluctuations play also an important role in the breakup

of droplets in nano jets [105, 56, 77].

1.5 Beyond Classical Nucleation Theory

In the previous sections, the main features of nucleation have been described, highlighting the fundamental physical aspects. The CNT poses the foundations for basic understanding, however it still lacks some crucial features. More sophisticated theories like density functional theory (DFT) [113, 91], interesting extensions [95, 101], and molecular dynamics (MD) simulations can give more precise estimates of the barriers and can correct some mis–prediction of CNT. Such methods are extremely powerful in stationary conditions and need to be coupled to specialized techniques, like the string method [148], to study the nucleation events and the transition path [67].

Often, depending on the thermodynamic conditions, the time to be awaited to observe the nucleation event is so long and its probability is so small that the phenomenon is labeled as a "rare events". In particular this time grows exponentially as the energy barrier [83]. For this reason, in the last decades there have been several works addressing nucleation by the means of *rare-event techniques* [3, 4, 22, 42]. Forward Flux Sampling (FFS) explores a series of interfaces placed between an initial and final states to calculate rate constants and transition paths, both in equilibrium and nonequilibrium systems driven by stochastic dynamics. Transition Path Sampling (TPS) perturbs random paths in the space of configurations –as in Monte Carlo walks– by accepting or rejecting configurations to reconstruct the correct path probability. Alternatively the study of nucleation processes is almost uniquely addressed by direct molecular dynamics simulations [6, 49], which for a large part of the real systems are often computationally too expensive,

limiting its application to very small domains, often far from the technological applications. In addition molecular dynamics simulations are not able to capture the hydrodynamics effects, crucial for the next phases of the nucleation process. These aspects suggest the adoption of mesoscale models for the study of nucleation in its entirety, starting from the phase change inception up to the macroscopic motion.

Promising approaches are based on phase field models, having as order parameter the mass density itself. In stationary conditions they recover the DFT descriptions with a squared-gradient approximation of the excess energy [92]. The phase field models have the advantage of being easily extended to unsteady situations, enabling the full description of both the thermodynamic and the fluid dynamics fields [96, 99, 97]. The model, in its original form, is deterministic and cannot capture spontaneous nucleation originated by thermal fluctuations, in absence of external forcing. To this purpose, the theory of fluctuating hydrodynamic [40, 33] represents the natural framework to embed thermal fluctuations inside the phase field description, and also it has been recently stressed as the theory can be used to formulate dynamical theory of nucleation [93], providing stochastic equations for the evolution of order parameter and a formalism to evaluate the nucleation pathways.

During my PhD research, I developed a novel mesoscale approach, based on a diffuse interface description of the two-phase vapor-liquid system embedded with thermal fluctuations through a fluctuating hydrodynamics modeling. The model has been used to address vapor bubble nucleation in both homogeneous [63, 64] and heterogeneous case (see Chapter 7). This mesoscale approach offers a good level of accuracy (as exposed in the next sections) at a very cheap computational cost compared to other techniques, providing

the possibility of dealing with macroscopic system. The typical size of the simulated system on a small computational cluster ($200 \times 200 \times 200\,\mathrm{nm}^3$, corresponding to a system of order 10^8 atomistic particles) is comparable with one of the largest MD simulations [49] on a tier-0 machine. Moreover the simulated time is here $T_{\max} \sim \mu$s to be compared with the MD $T_{max} \sim$ ns. The enormous difference between the two time extensions allows us to address the simultaneous nucleation of several vapor bubbles, their expansion, coalescence and, at variance with most of the available methods dealing with quasi-static conditions, the resulting excitation of the macroscopic velocity field. These hydrodynamic effects –not easily detectable with conventional techniques– have a great influence on the nucleation dynamics, specially for closed systems [63], where *"bubble crowding"* strongly affects the nucleation rate. The above approach has been extended also to address heterogeneous vapor bubble nucleation, showing its applicability even when dealing with more complex physical systems, e.g., vapor bubble nucleation on solid surface having different wetting properties (see Chaper 8).

Capitolo 2

Diffuse interface models

Aim of this chapter is to introduce the diffuse interface approach that will be exploited in the present thesis. The chapter will start discussing the general thermodynamic description of the two-phase, liquid-vapour systems, and will analyse with great detail the particular case of the Van der Waals model, the so-called "square-gradient approximation". The resulting model provides a mesoscale description of the liquid-vapour system, enabling a robust characterisation of the interfacial properties, namely the interface thickness and the surface tension, down to the nanometer length scale.

The presence of a confining solid surface with different wetting properties can be also taken into account with this approach. In this context I propose a general expression to uniquely identify the solid-fluid contact angle, relating the solid-fluid free energy contributions with the bulk properties of the fluid. This model recovers the classical Young-Laplace equilibrium wetting condition and the prescribed expressions for the diffused contact line in the context of the famous Cahn-Hilliard phase field approach for binary flows. Successively, the governing equation of multiphase systems enodowed with capillarity will be derived in details, by choosing a thermodynamic consistent

constitutive relationship between thermodynamic forces and thermodynamic fluxes. During my research I exploited this model to address the collapse of a cavitation bubble near a solid boundary, showing an unprecedented description of interfacial flows, that naturally takes into account topology modification and phase changes (both vapour/liquid and vapour/supercritical fluid transformations).

In order to deal with the rare event issue described in the Introduction which, of course, is still present in the proposed mesoscale description, the diffuse interface model will be coupled with the string method, one of the specialised rare event techniques, in order to extract the free energy barriers and the transition paths during both homogeneous and heterogeneous vapour bubble nucleation.

2.1 Thermodynamic of non-homogeneous systems

Let us briefly describe the thermodynamic equilibrium of a two-phase system, focusing on a closed system with fixed temperature and volume. Van der Waals was the first to recognise that a description of the Helmholtz free energy based only on the local values of temperature and phase indicators was not sufficient to describe the internal structure of a transition zone separating two different phases. Indeed he showed how a local description of the free energy provides a separating interface having zero-thickness and zero surface tension. Thus, in order to describe to thermodynamics of a non-homogeneous system, in which the different phases are separated by a smooth transition zone, a non-local term (depending on the spatial gradients of the phase indicator) should be added to the free energy of the system. In modern terminology, the non-local terms in the free energy can be justified in

the context of Density Functional Theory, see Lutsko ([91, 92]) for a detailed derivation and related comments. Accounting for the presence of a solid wall in contact with the fluid, the general form of the (Helmholtz) free-energy functional F as a function of the temperature θ and a phase indicator Φ takes the form

$$F\left[\Phi,\theta\right]=\int_{V} f_{b}\left(\Phi,\theta\right)+f_{s}\left(\boldsymbol{\nabla}\Phi,...,\boldsymbol{\nabla}\Phi\otimes...\otimes\boldsymbol{\nabla}\Phi\right)\,dV+\int_{\partial V} f_{w}\left(\Phi,\theta\right)\,dS\,, \tag{2.1}$$

where f_b is the homogeneous bulk free-energy contribution, f_w is related to solid-fluid interactions and f_s is the gradient contribution, depending on the spatial gradients of the phase indicator Φ. At fixed temperature $\theta=\theta_0$ the equilibrium condition is reached when the first variation of the functional 2.1 with respect to the phase indicator Φ is zero, leading to the Euler-Lagrange equation

$$\frac{\delta F}{\delta\Phi}=\frac{\partial f_{b}}{\partial\Phi}+\sum_{k=1}^{N}\left(-1\right)^{k}\boldsymbol{\nabla}^{(k)}:\frac{\partial f_{s}}{\partial\left(\boldsymbol{\nabla}^{(k)}\Phi\right)}=0\,, \tag{2.2}$$

where the superscript $*^{(k)}$ on the differential operator $\boldsymbol{\nabla}$ denotes rank k tensor operator defined as the n-fold tensor product of $\boldsymbol{\nabla}$ with itself. Eq. 2.2 is a partial differential equation for the equilibrium profile of the phase indicator Φ with boundary conditions

$$\frac{\partial f_{w}}{\partial\Phi}+g\left(\boldsymbol{\nabla}\Phi,...,\boldsymbol{\nabla}\Phi\otimes...\otimes\boldsymbol{\nabla}\Phi,\mathbf{n}\right)=0\,, \tag{2.3}$$

with $\mathbf{n}$ as a unit normal on the domain V and g is a function arising from the boundary terms when integrating by parts. The boundary conditions arise, in fact, from the extremality condition on the free-energy functional, due the

presence of the solid-fluid interactions described by the free-energy boundary term.

It is worth stressing that the existence of a smooth equilibrium configuration Φ_{eq} of two distinct phases, i.e. a diffuse interface separating them, originates from the presence of the gradient contribution to the free energy.

2.2 The Van der Waals approach

In the last part of XIX century scientists were starting to recognise that the separation surface between two thermodynamic phases could have a finite thickness. Van der Waals, based on phenomenological assumptions, proposed a gradient theory that led him to predict the interface thickness of a fluid near the critical point. In the framework of a general phase field theory, Van der Waals assumes the density field as the relevant phase indicator, and the density gradient square norm as a surface contribution basically localised at the liquid-vapour interface where the density gradient is large (see. Eq. 2.4 below). The model is extremely powerful both for steady and unsteady conditions, providing a robust description of interfacial flows that naturally accounts for topology modification of the regions occupied by the two phases and the phase change between them [96, 98]. Since in this initial illustration of the model the focus is on the properties of the fluid irrespective of the solid walls it may be in contact with, like e.g. surface tension, interface thickness and the constitutive relationship for thermodynamic fluxes, for the time being the solid-liquid free energy contribution is neglected. It will be taken up again in some detail in the forthcoming sections.

For a closed system, with a given mass M_0, the constrained Helmholtz free-energy of a two phase flow in the Van der Waals gradient approximation

[45, 72, 5] is:

$$
\begin{aligned}
F_c[\rho,\theta] &= F[\rho,\theta] + l\left(M_0 - \int_V \rho dV\right) = \int_V f dV + l\left(M_0 - \int_V \rho dV\right) = \\
&= \int_V \left(f_b\left(\rho,\theta\right) + \frac{\lambda}{2}\boldsymbol{\nabla}\rho\cdot\boldsymbol{\nabla}\rho\right) dV + l\left(M_0 - \int_V \rho dV\right), \qquad (2.4)
\end{aligned}
$$

where l is a Lagrange multiplier, $f = f_b + \lambda/2|\nabla\rho|^2$ with $f_b\left(\rho,\theta\right)$ the classical Helmholtz free energy density per unit volume of the homogeneous fluid at temperature θ and mass density ρ. The coefficient $\lambda(\rho,\theta)$, in general a function of the thermodynamic state, embodies all the information on the interfacial properties of the liquid-vapour system (i.e. surface tension and interface thickness). At given temperature, equilibrium is characterized by the minimum of the free energy functional (2.4), where variations are performed with respect to the density distribution ρ assumed to be the proper phase descriptor for the liquid-vapour phase transition. The relevant Euler-Lagrange equation is

$$
\mu_c^b - \boldsymbol{\nabla}\cdot\left(\lambda\boldsymbol{\nabla}\rho\right) - l = 0\,, \qquad (2.5)
$$

where the temperature is constrained to be constant, $\theta = const$, $\mu_c^b = \partial f_b/\partial\rho|_\theta$ is the classical chemical potential, and the Lagrange multiplier is identified as $l = \mu_c^b - \boldsymbol{\nabla}\cdot\left(\lambda\boldsymbol{\nabla}\rho\right) = \mu_c(\rho_{eq}) = \mu_{eq}$ evaluated at the equilibrium density field. The equation defines a generalised chemical potential $\mu_c = \mu_c^b - \boldsymbol{\nabla}\cdot\left(\lambda\boldsymbol{\nabla}\rho\right)$ that must be constant at equilibrium.

The consequence of the above equilibrium conditions is better illustrated in the simple case of a single planar liquid-vapour interface separating the two bulk, homogenous phase (liquid and vapour, respectively). The only direction of inhomogeneity is s and a constant λ is assumed. The constant temperature appears in the problem as a parameter and will not be further mentioned

throughout the present section. Hence, determining the equilibrium density distribution amounts to finding a solution of

$$\mu_c = \mu_c^b(\rho) - \lambda \frac{d^2\rho}{ds^2} = \mu_{eq} \ . \tag{2.6}$$

The boundary conditions for this second order ordinary differential equation are obtained by evaluating the generalised chemical potential far away on the two sides of the interface, namely in the bulk liquid and bulk vapour where $d\rho/ds = 0$. It follows $\mu_{eq} = \mu_c^b(\rho_V) = \mu_c^b(\rho_L)$.

The solution of Eq. (2.6) is readily obtained by multiplying through by $d\rho/ds$ and integrating between $\rho_\infty = \rho_V$ and ρ,

$$w_b(\rho) - w_b(\rho_V) = \frac{\lambda}{2}\left(\frac{d\rho}{ds}\right)^2 , \tag{2.7}$$

where $w_b(\rho) = f_b(\rho) - \mu_{eq}\rho$. Equation (2.7) shows that w_b has the same value in both the bulk phases, where the spatial derivative of mass density vanishes: $w_b(\rho_L) = w_b(\rho_V)$.

The grand potential, defined as the Legendre transform of the free energy,

$$\Omega = F - \int_V \rho \frac{\delta F}{\delta \rho} dV = \int_V w dV \, , \tag{2.8}$$

has the density (*actual* grand potential density)

$$w[\rho] = f - \mu_c \rho = f_b + \frac{\lambda}{2}\left(\frac{d\rho}{ds}\right)^2 - \left(\mu_c^b - \lambda \frac{d^2\rho}{ds^2}\right)\rho \, , \tag{2.9}$$

implying that, in the bulk, $w = w_b$, i.e. w_b is the *bulk* grand potential density.

Given the form of $w_b(\rho)$, the solution of Eq. (2.7) provides the (implicit expression for the) equilibrium density profile $\rho(s)$:

$$s = \sqrt{\frac{\lambda}{2}} \int_{\rho_v}^{\rho} \frac{d\rho}{\sqrt{w_b(\rho) - w_b(\rho_V)}} + const \, . \tag{2.10}$$

Eq. (2.10) provides the equilibrium density profile characterized by two bulk regions separated by a thin layer. The layer thickness can be estimated as

$$\epsilon = \frac{\rho_L - \rho_V}{d\rho/ds|_{max}} \,. \tag{2.11}$$

The equilibrium condition, Eq. (2.7), provides the interface thickness in terms of the *bulk* grand potential density $w_b(\rho)$ and of the parameter λ,

$$\epsilon = (\rho_L - \rho_V) \sqrt{\frac{\lambda}{2\left[w_b(\bar{\rho}) - w_b(\rho_V)\right]}} \,, \tag{2.12}$$

without explicitly addressing the density profile. $\bar{\rho}$ is the density corresponding to the maximum of $d\rho/ds$, achieved where $dw_b/d\rho = 0$, in Eq. (2.7).

The surface tension can be defined as the excess (*actual*) grand potential density,

$$\begin{aligned} \gamma &= \int_{-\infty}^{S_i} \left(w[\rho] - w[\rho_V]\right) ds + \int_{S_i}^{\infty} \left(w[\rho] - w[\rho_L]\right) ds = \\ &= \int_{-\infty}^{\infty} \left(w[\rho] - w[\rho_V]\right) ds, \end{aligned} \tag{2.13}$$

where S_i is the position of the Gibbs dividing surface, whose precise value is ininfluential since $w[\rho_V] = w[\rho_L]$ (we stress that, e.g., $w[\rho_V]$ should be interpreted as the functional (2.9) evaluated at the constant density field ρ_V). Given the definition of $w[\rho]$, Eq. (2.9), and exploiting the equilibrium condition for the chemical potential, Eq. (2.6), it follows that

$$\begin{aligned} \gamma &= \int_{-\infty}^{\infty} \left[f_b + \frac{1}{2}\lambda \left(\frac{d\rho}{ds}\right)^2 - \mu_{eq}\rho - w_b(\rho_V) \right] ds = \\ &= \int_{-\infty}^{\infty} \left[w_b + \frac{1}{2}\lambda \left(\frac{d\rho}{ds}\right)^2 - w_b(\rho_V) \right] ds \,. \end{aligned} \tag{2.14}$$

Using Eq. (2.7) one finds

$$\begin{aligned}\gamma &= \int_{-\infty}^{+\infty} \lambda \left(\frac{d\rho}{ds}\right)^2 ds = \int_{\rho_V}^{\rho_L} \lambda \frac{d\rho}{ds} d\rho = \\ &= \int_{\rho_V}^{\rho_L} \sqrt{2\lambda \left(w_b(\rho) - w_b(\rho_V)\right)}\, d\rho\,,\end{aligned} \tag{2.15}$$

where the second expression can be evaluated with no *a priori* knowledge of the equilibrium density profile. It worths stressing that, as for the interface thickness, the surface tension only depends on the form of the *bulk* grand potential density $w_b(\rho)$ in the density range between the two equilibrium values, $[\rho_V; \rho_L]$, and on the parameter λ. Figure 2.1 reports the comparison between the diffuse interface prediction of surface tension and molecular dynamics simulations, for a Lennard-Jones fluid. A constant value of λ was assumed to reproduce the simulation data. It is evident how the Van der Waals model is able to capture the temperature dependence of surface tension. Of course, equation (2.7) applied to the two adjoining bulk regions where $d\rho/ds = 0$ implies the mechanical equilibrium condition $p(\rho_L) = p(\rho_V)$, where

$$p = -\frac{\partial \hat{f}_b}{\partial v} = -\frac{\partial f_b/\rho}{\partial v} = \rho\mu_c^b - f_b \tag{2.16}$$

is the classical thermodynamic pressure, $\hat{f}_b = f_b/\rho$ the specific bulk free energy, and $v = 1/\rho$ the specific volume. Indeed Eq. (2.7) implies $w_b(\rho_V) = w_b(\rho_L)$, which corresponds to the equality of the pressures given that $p = -w_b$.

2.3 Solid-Fluid Free Energy

In order to describe a non-homogeneous liquid-vapour system interacting with a solid surface, I again start from the Van der Waals square gradient approximation of the (Helmoholtz) free energy functional,

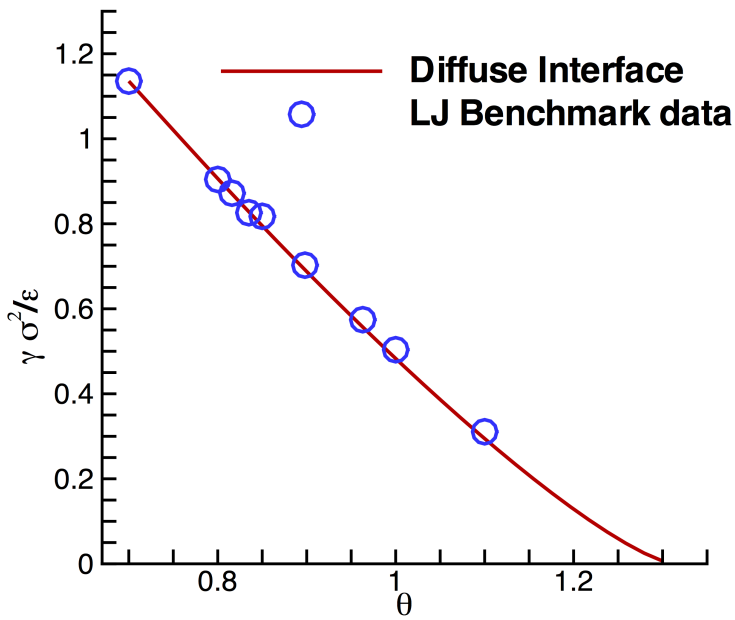

Figura 2.1: Comparison between the temperature dependence of the surface tension obtained through Eq. (2.15), when using the Lennard-Jones EoS [75], and the benchmark data provided at the url *https://www.nist.gov/mml/csd/chemical-informatics-research-group/lennard-jones-fluid-properties*. The value of the capillary coefficient is fixed to $\lambda m^2/(\sigma^5\epsilon) = 5.224$. The results are presented in a non-dimensional form, taking as reference values the Lennard-Jones parameters.

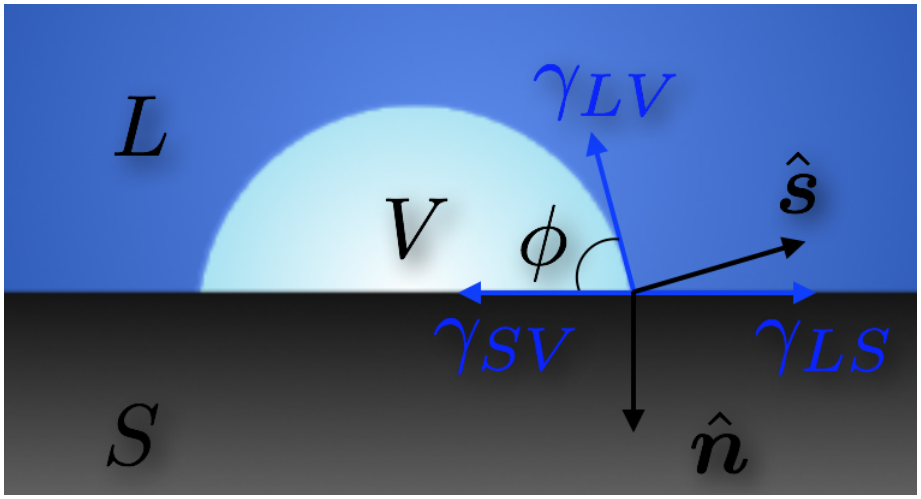

Figura 2.2: Bubble sketch illustrating both geometrical and wetting properties.

$$F_c\left[\rho,\theta\right]=\int_V dV\left(f_b\left(\rho,\theta\right)+\frac{1}{2}\lambda\boldsymbol{\nabla}\rho\cdot\boldsymbol{\nabla}\rho\right)+l\left(M_0-\int_V\rho dV\right)+\int_{\partial V}dSf_w\left(\rho,\theta\right)\ . \tag{2.17}$$

For the sake of uniformity with the previous section, I address the equilibrium problem in the canonical ensemble, i.e. at constant mass, volume and temperature, but the generalization to the microcanonical ensemble (constant mass, volume, energy) is straightforward and is addressed in Chapter 8. By minimising the free-energy, it follows that, in equilibrium, temperature and (generalized) chemical potential μ_c must be constant, as expected,

$$\theta=const=\theta_{eq} \tag{2.18}$$

$$\mu_c=\mu_c^b-\lambda\nabla^2\rho=const=\mu_c^{eq}\ . \tag{2.19}$$

Furthermore the boundary term gives rise to the additional requirement

$$\left(\lambda \boldsymbol{\nabla}\rho \cdot \hat{\mathbf{n}} + \frac{\partial f_w}{\partial \rho}\right)\Big|_{\partial V} = 0\,, \tag{2.20}$$

where $\hat{\mathbf{n}}$ is the outward normal, to be read as a (non-linear) boundary condition for the density. The free energy contribution f_w arises from the fluid-wall interactions and accounts for the wetting properties of the surface. In order to come up with a model f_w, I deduced an analytic form that generalises an approach that has been already used to describe two immiscible fluids, see e.g [126, 71].

The analytic form of f_w is constructed by observing that the equilibrium contact angle ϕ is related to the inhomogeneity direction $\hat{\mathbf{s}}$ as $\hat{\mathbf{s}}\cdot\hat{\mathbf{n}} = -\cos\phi$, (see Fig. 2.2), and the density gradient is $\boldsymbol{\nabla}\rho = d\rho/ds\,\hat{\mathbf{s}}$, so that Eq. 2.20 reads

$$\frac{df_w}{d\rho} - \lambda\frac{d\rho}{ds}\cos\phi = 0\,, \tag{2.21}$$

the above equation can be integrated by using Eq. 2.7 providing

$$f_w(\rho) = \cos\phi \int_{\rho_V}^{\rho} \sqrt{2\lambda\left(w_b\left(\tilde{\rho}\right) - w_b\left(\rho_V\right)\right)}\, d\tilde{\rho} + f_w\left(\rho_V\right)\,. \tag{2.22}$$

The analytic form of f_w recovers the physical evidence that for a pure vapor of density ρ_V in contact with the wall, the free-energy should be given by the solid-vapor surface tension, $f_w(\rho_V) = \gamma_{SV}$. Similarly, for a pure liquid of density ρ_L, $f_w(\rho_L) = \gamma_{LS}$. These aspects become even more evident by enforcing Eq. 2.15, leading to

$$f_w(\rho_L) = \gamma_{LS} = \gamma_{LV}\cos\phi + \gamma_{SV}\,, \tag{2.23}$$

the famous Young equilibrium wetting condition.

Using the expression (2.22), $\partial f_w/\partial\rho \equiv 0$ in both stable liquid and stable vapor. In this case Eq. (2.20) is tantamount to enforcing zero normal

derivative for the density outside coexistence and metastable regions and assigning the contact angle ϕ otherwise, i.e. in the small region where the finite thickness liquid-vapour interface meets the wall. In fact Eq. (2.21) provides a uniquely defined relationship between contact angle and the normal derivative of the density, confirming that the surface energy f_w encodes the wetting properties of the wall. In addition, when a pure liquid in metastable state is in contact with the wall, the model provides a wall normal stratified density profile, in which the density is higher toward the solid surface, for a hydrophilic wall, and is lower for a hydrophobic one. In Fig. 2.3 the equilibrium density profiles are reported as a function of the wall normal z, showing the depletion or absorption layering of the liquid in proximity of the solid surfaces, as commonly detected [34, 74] in MD simulations. As evident, the density profiles are not monotonic, foretelling the existence of an extended region near walls where $\rho(z) < \rho_b$ for hydrophilic interactions ($\phi > \pi/2$) and $\rho(z) > \rho_b$ for hydrophobic ones. Such behaviour is consistent with the constant mass constraint which characterises closed systems. These aspects play an important role in heterogeneous nucleation, inasmuch bubble formation is favoured on hydrophobic walls and discouraged on hydrophilic ones. Such qualitative statement is corroborated both by energetic considerations and by fluctuating hydrodynamics simulations of spontaneous heterogeneous bubble nucleation to be discussed in forthcoming sections (see Chapter 8).

2.4 The String method: energy barriers and the critical bubble

During my PhD research, I coupled the diffuse interface description together with a rare-event technique (the string method), in order to obtain the cri-

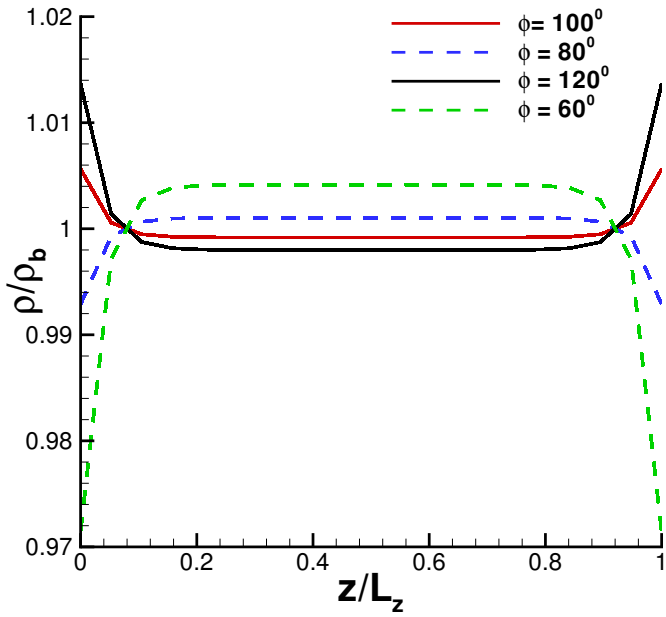

Figura 2.3: Spatial density distribution in wall normal direction z. The density values are normalized with mean bulk density ρ_b, the normal coordinate z is normalized with the total domain lenght L_z. Two walls with the same wetting properties are located at $z = 0$ and $z = L_z$. The different profiles refer to different contact angle ϕ.

tical configurations of the bubbles both in homogeneous and heterogeneous nucleation. The procedure was successfully exploited by Ren [122] to study the wetting transition on structured hydrophobic walls for a Cahn-Hillard binary fluid. In this work, it is extended to study vapour bubble nucleation, for a Van der Waals diffuse interface model.

The minimisation of the free energy functional (2.4), stating that the generalised chemical potential $\mu_c = \mu_c^b(\rho) - \lambda\nabla^2\rho$ must be constant and equal to the external chemical potential μ_{ext}, allows the evaluation of the equilibrium density profiles at the different thermodynamic conditions. Clearly, in

thermodynamic conditions where either the liquid or the vapour are stable, constant chemical potential corresponds to a homogeneous phase. When the liquid or the vapour are metastable instead three solutions at constant chemical potential are found: i) the homogeneous vapour; ii) the homogeneous liquid; iii) a two-phase solution with a spherical (critical) nucleus of a given radius (vapour/liquid in the case of bubble/droplet, respectively), the critical nucleus being surrounded by the metastable phase.

Dealing with nucleation, the non-trivial solution of case (iii), $\rho(r) = \rho_{crit}(r)$ where the critical bubble is surrounded by the metastable liquid at $\rho = \rho_L^{met}, \theta = \bar{\theta}$ and $\mu_c(\rho_L^{met}, \bar{\theta}) = \mu^{met}$ is particularly significant. The solution $\rho(r) = \rho_{crit}(r)$ is found by solving the non linear Euler-Lagrange equation of the functional 2.4 which, in spherical coordinates and at fixed temperature, reads

$$\mu_c^b(\rho, \bar{\theta}) - \frac{\lambda}{r^2}\frac{\partial}{\partial r}\left(r^2 \frac{\partial \rho}{\partial r}\right) = \mu^{met}\,. \tag{2.24}$$

The critical bubble, $\rho_c(r)$, is an unstable solution of Eq. (2.24) which requires specialised numerical techniques. In this work the powerful string method is applied [149] which, as additional information, identifies the minimum energy path (MEP) joining the metastable fluid (e.g. the liquid) to the fluid (e.g. the vapour ensuing form cavitation). Since our interest here in mainly on cavitation, the problem is specified as a liquid in metastable conditions inside a domain of fixed volume. The stable state will correspond to the presence of an equilibrium bubble enclosed by the liquid contained in the domain. Please note that at fixed volume, mass and temperature the stable state is in fact a vapor bubble surrounded by the liquid phase. The MEP can be visualised as the continuous sequence of density configurations, $\rho(r, \alpha)$, the system assumes when transitioning from the metastable to the stable state,

where α is a suitably defined parameter along the path. The distance between two configurations is expressed as

$$\Delta\ell = \sqrt{\frac{1}{V}\int \Delta\rho^2(r)dV} \tag{2.25}$$

and defines the arclength along the path. The discrete form of the path, consisting of a finite number of configurations, is called the *string*. The string method numerically approximates this path starting from an initial set of N_s configurations $\{\rho^k(r)\}$. The head of the string ($k = 1$) is initialised as a uniform density field corresponding to the uniform metastable liquid $\rho(r) = \rho_L^{met}$; the tail ($k = N_s$) is initialised as a guessed tanh-density profile adjoining the liquid and the vapour density to approximate a vapour bubble. All the intermediate images on the string are obtained by interpolation of these two density fields with respect to the above defined arclength. The algorithm used for relaxing the string to its final configuration, follows two steps:

1) All the images $\rho^k(r)$ are evolved over one pseudo-time-step $\Delta\tau$ following the steepest-descent algorithm (over-damped regime)

$$\frac{\partial\rho}{\partial\tau} = \mu^{met} - \left[\mu_c^b(\rho) - \frac{\lambda}{r^2}\frac{\partial}{\partial r}\left(r^2\frac{\partial\rho}{\partial r}\right)\right] . \tag{2.26}$$

2) The images are redistributed along the string following a reparametrization procedure by equal arclength. The algorithm is arrested when the string converges within a prescribed error.

It is worthwhile noting that the transition path geometry depends in general on the relaxation dynamics used to evolve the string. In an over-damped regime, steepest descent relaxation (Eq. 2.26), could still be used as a reference

theory, as often done in the current literature. In this context the string converges to the MEP connecting the local minimum to the saddle point, that under the above assumption is also the most probable transition path [122] . However critical cluster as well as the energy barriers do not depend on the relaxation dynamics. The density profile of the critical nucleus, plotted in panel of Fig. (2.4) at different metastable conditions, allows the evaluation of the critical radius, by following the relation [44]

$$R^* = \frac{\int_0^\infty r(\partial\rho_c/\partial r)^2 r^2 \,\mathrm{d}r}{\int_0^\infty (\partial\rho_c/\partial r)^2 r^2 \,\mathrm{d}r}\,, \tag{2.27}$$

and the evaluation of the energy barrier

$$\Delta\Omega^* = \int_0^\infty \left\{ f(\rho_c(r)) - f(\rho_L^{met}) - \mu^{met}\left[\rho_c(r) - \rho_L^{met}\right]\right\} 4\pi r^2 \mathrm{d}r\,, \tag{2.28}$$

defined as the difference in grand potential Ω between the critical nucleus and the metastable liquid.

The results of the string method are compared in Tab. 2.1 with those obtained by classical nucleation theory (CNT) which yields the estimate $\Delta\Omega^{*CNT} = 4/3\pi\gamma R_c^2$. The data show that CNT underestimates the energy barrier at high temperature while overestimates it near the spinodal [31].

In Fig. 2.4 the critical density profiles as evaluated from the string method are reported for different temperatures. In The thermodynamic conditions considered here a significant zone of transitions is detected, confirming the importance of considering a phase field approach when dealing with phase transitions, specially for high temperatures and near spinodal conditions. In addition, the energy landscape for a specific thermodynamic condition $\rho_L = 0.47$ and $\theta = 1.25$ is reported in Fig. 2.5 as a function of the bubble radius.

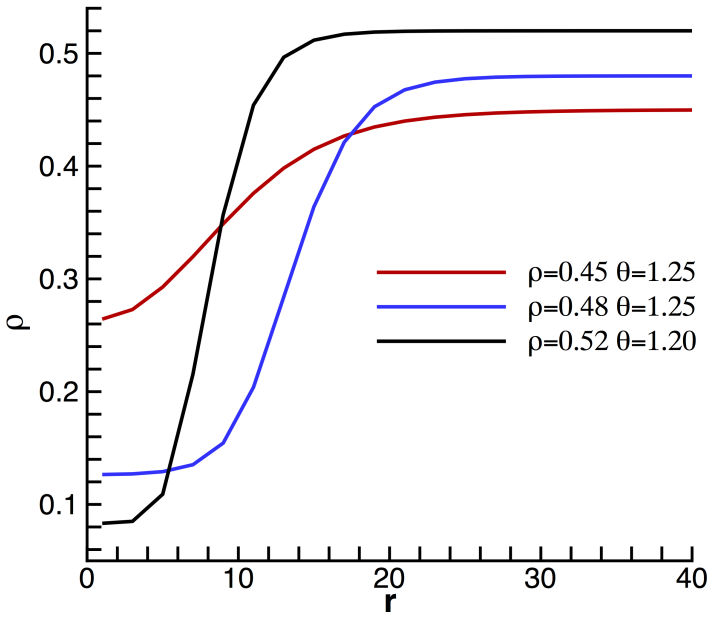

Figura 2.4: Density profiles of the critical nuclei, evaluated with the string method, at different thermodynamic conditions of the metastable liquid. The results are presented in a non-dimensional form, taking as reference values the Lennard-Jones parameters.

θ_0	ρ_L^{met}	R^*	R^{*CNT}	$\Delta\Omega^*/\theta_0$	$\Delta\Omega^{*CNT}/\theta_0$
1.25	0.45	12.04	8.07	2.99	12.89
1.25	0.46	11.16	8.42	11.21	14.05
1.25	0.47	11.85	9.17	22.81	16.67
1.25	0.48	14.18	10.64	43.5	22.41
1.20	0.51	8.28	6.35	19.20	18.13
1.20	0.52	8.79	6.93	33.58	21.60

Tabella 2.1: Comparison between CNT and the string method applied to the Diffuse Interface model. Critical radii and (Landau) free energy barriers $\Delta\Omega^*$ for bubble nucleation from the liquid. The discrepancy close to the spinodal and at higher temperature are well known from the literature.

The free energy profile shown in Fig. 2.5, differs by the CNT prediction not only for the energy barrier value (see Table 2.1), but also for the curvatures in both metastable and transition basins.

2.5 Navier-Stokes equation with capillarity

Since my PhD project combined statistical thermodynamics of nucleation and dynamics of nucleated bubbles, an appropriate description of the macroscopic motion is needed. The present section is devoted to the latter issue and describes the hydrodynamics of two phase systems.

Hydrodynamics is governed by the conservation equations for mass ρ, momentum $\rho\mathbf{u}$, and total energy E

$$\frac{\partial \rho}{\partial t} + \boldsymbol{\nabla} \cdot (\rho \mathbf{u}) = 0\,, \tag{2.29}$$

$$\frac{\partial \rho \mathbf{u}}{\partial t} + \boldsymbol{\nabla} \cdot (\rho \mathbf{u} \otimes \mathbf{u}) = \boldsymbol{\nabla} \cdot \boldsymbol{\Sigma}\,, \tag{2.30}$$

$$\frac{\partial E}{\partial t} + \boldsymbol{\nabla} \cdot (\mathbf{u} E) = \boldsymbol{\nabla} \cdot [\boldsymbol{\Sigma} \cdot \mathbf{u} - \mathbf{q}]\,. \tag{2.31}$$

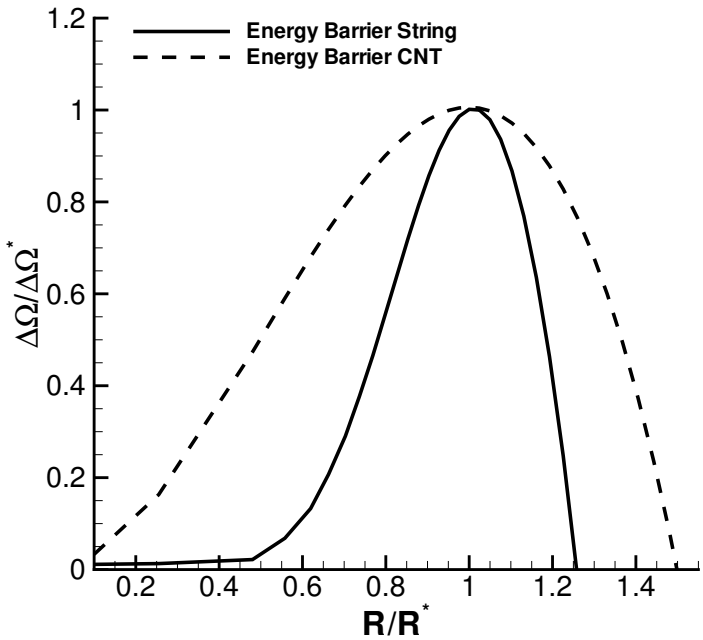

Figura 2.5: Free energy profile as a function of the bubble radius as evaluated by string method (solid line) and CNT (dotted line). All quantities are normalized with their critical values, i.e. energy barrier $\Delta\Omega^*$ and R^*.

System (2.29 – 2.31) needs to be complemented with thermodynamically consistent constitutive relations for the stress tensor $\mathbf{\Sigma}$ and the energy flux $\mathbf{q}$. Their derivation is outlined below for the simplest case of constant λ, following the general approach for non-equilibrium processes described in [37].

It is instrumental to rewrite the energy equation in terms of specific internal energy $\mathcal{U}$, obtained by subtracting the equation for the kinetic energy from Eq. (2.31)

$$\rho \frac{D\mathcal{U}}{Dt} = \mathbf{\Sigma} : \boldsymbol{\nabla}\mathbf{u} - \boldsymbol{\nabla} \cdot \mathbf{q}\,, \tag{2.32}$$

where $D/Dt = \partial/\partial t + \mathbf{u} \cdot \boldsymbol{\nabla}$ is the material derivative. By definition $\mathcal{U} = \hat{f} + \theta\,\eta$, with $\hat{f} = f/\rho$ the specific Helmholtz free energy and η the specific entropy. The total derivative of $\mathcal{U}$ reads

$$\mathrm{d}\mathcal{U} = \frac{\partial \hat{f}}{\partial \rho}\mathrm{d}\rho + \frac{\partial \hat{f}}{\partial \boldsymbol{\nabla}\rho} \cdot \mathrm{d}\boldsymbol{\nabla}\rho + \theta \mathrm{d}\eta\,. \tag{2.33}$$

The partial derivatives of the specific free energy can be derived from its definition, Eq. (2.4), and from the definition of the thermodynamic pressure, Eq. (2.16). Explicitly, one finds

$$\frac{D\mathcal{U}}{Dt} = \frac{1}{\rho^2}\left(p - \frac{\lambda}{2}|\boldsymbol{\nabla}\rho|^2\right)\frac{D\rho}{Dt} + \theta\frac{D\eta}{Dt} + \frac{\lambda}{\rho}\boldsymbol{\nabla}\rho \cdot \frac{D\boldsymbol{\nabla}\rho}{Dt}\,. \tag{2.34}$$

The material derivative of the density gradient (last term in the RHS of Eq. (2.34)) can be evaluated by applying the gradient operator to the equation of mass conservation, Eq. (2.29):

$$\frac{\lambda}{\rho}\boldsymbol{\nabla}\rho \cdot \frac{D\boldsymbol{\nabla}\rho}{Dt} = -\frac{\lambda}{\rho}\boldsymbol{\nabla}\rho \cdot \boldsymbol{\nabla}\left(\rho\boldsymbol{\nabla} \cdot \mathbf{u}\right) - \frac{\lambda}{\rho}\boldsymbol{\nabla}\rho \otimes \boldsymbol{\nabla}\rho : \boldsymbol{\nabla}\mathbf{u}\,. \tag{2.35}$$

After substitution of Eqs. (2.29, 2.34, 2.35) into Eq. (2.32), a few more elementary manipulations allow to write the evolution equation for the entropy

as

$$\rho\frac{D\eta}{Dt} = \boldsymbol{\nabla}\cdot\left(\frac{\lambda\rho\boldsymbol{\nabla}\rho\boldsymbol{\nabla}\cdot\mathbf{u}-\mathbf{q}}{\theta}\right)+\frac{1}{\theta^2}\left[\lambda\rho\boldsymbol{\nabla}\rho\boldsymbol{\nabla}\cdot\mathbf{u}-\mathbf{q}\right]\cdot\boldsymbol{\nabla}\theta+ \tag{2.36}$$
$$+\frac{1}{\theta}\left[\boldsymbol{\Sigma}+\left(p-\frac{\lambda}{2}|\boldsymbol{\nabla}\rho|^2-\rho\boldsymbol{\nabla}\cdot(\lambda\boldsymbol{\nabla}\rho)\right)\mathbf{I}+\lambda\boldsymbol{\nabla}\rho\otimes\boldsymbol{\nabla}\rho\right]:\boldsymbol{\nabla}\mathbf{u}\,.$$

The term under divergence defines the entropy flux. The remaining terms define the entropy production. Since the entropy production must be positive definite in terms of the thermodynamic forces (Clausius-Duhem inequality), the sum of the other two contributions on the right hand side is required to be positive. In fact by using the so-called Curie principle [37], one can show that each single term should be positive. Assuming linear dependence of thermodynamic fluxes – terms in square brackets in (2.36) – on thermodynamic forces [37], namely $\boldsymbol{\nabla}\theta$ and $\boldsymbol{\nabla}\mathbf{u}$, leads to identify the stress tensor with the following expression,

$$\boldsymbol{\Sigma} = \left(-p+\frac{\lambda}{2}|\boldsymbol{\nabla}\rho|^2+\rho\boldsymbol{\nabla}\cdot(\lambda\boldsymbol{\nabla}\rho)\right)\mathbf{I}+$$
$$-\lambda\boldsymbol{\nabla}\rho\otimes\boldsymbol{\nabla}\rho+\mu\left[\left(\boldsymbol{\nabla}\mathbf{u}+\boldsymbol{\nabla}\mathbf{u}^T\right)-\frac{2}{3}\boldsymbol{\nabla}\cdot u\mathbf{I}\right], \tag{2.37}$$

where the usual viscous terms with $\mu > 0$ in the last line are the source of mechanical irreversibility (for the sake of simplicity we have assumed the second viscosity coefficient equal to $-2\mu/3$). Concerning the energy flux, positive entropy production, second line in Eq. (2.36), calls for

$$\mathbf{q}=\lambda\rho\boldsymbol{\nabla}\rho\boldsymbol{\nabla}\cdot\mathbf{u}-k\boldsymbol{\nabla}\theta\,, \tag{2.38}$$

where $k > 0$ is the thermal conductivity.

It is worth noting that the spatial inhomogeneities of the density field (related to the surface tension), strongly influence the dynamics of the two

phase system. In particular the density gradients modify the structure of thermodynamic fluxes, providing for instance shear stresses, even when the fluid is at rest ($\mathbf{u} = 0$). From a mechanical point of view these features are not detected in simple continua, e.g. Cauchy continua, and are framed in the general context of *second gradient continua* [44, 9].

Capitolo 3

Fluctuating Hydrodynamics

This chapter will introduce the theory of fluctuating hydrodynamics, focusing on capillary fluids. It will be shown how capillarity induces different correlations for the density field, with respect to simple Newtonian fluids. Under the assumption of small fluctuations, the probability functional of the field fluctuations turns out to be Gaussian and the correlation tensor can be evaluated in a closed form by solving Gaussian path integrals. Once the probability functional of equilibrium thermal fluctuations has been determined, a set of stochastic processes (Langevin equations) is designed to reproduce the same statistical properties. The stochastic partial differential equations we are arriving at have the Navier-Stokes equations with capillarity described in Chapter 2 as deterministic part. The random part accounts for the fluctuating components of the thermodynamic fluxes which are expressed by a Gaussian white noise acted upon by suitable operators in order to enforce the fluctuation dissipation balance.

3.1 Thermal fluctuations for a capillary fluid at equilibrium

As anticipated in the previous sections, in order to achieve a suitable description of fluids at mesoscopic scale the effects of thermal fluctuations have to be included in the classical hydrodynamic equations. The aim of this chapter is to retrace the theory of fluctuating hydrodynamics, extending the Landau-Lifshitz approach to the phase field context.

The static correlation functions of a thermodynamic system in equilibrium can be evaluated from the entropy deviation ΔS from its equilibrium value S_0. For single component systems ΔS can be expressed as a functional of fluctuating fields of mass density, $\delta\rho(\mathbf{x}, t)$, velocity, $\delta\mathbf{v}(\mathbf{x}, t)$, and temperature, $\delta\theta(\mathbf{x}, t)$

$$\Delta S = S - S_0 = \Delta S\left[\delta\rho, \delta\mathbf{v}, \delta\theta\right] = \int_V \left[s\left(\mathbf{x}, t\right) - s_0\right]\, dV\,, \tag{3.1}$$

where the integration is over the system volume V, $s\left(\mathbf{x}, t\right)$ is the entropy density per unit volume, and s_0 is its equilibrium value, (*i.e.* S_0 *is the entropy maximum).* The actual entropy maximum must respect the constraint of given total mass (M_0) and given total energy (E_0), if we are interested in the study of closed and isolated systems. Hence the correct functional to be maximized at equilibrium is the constrained entropy ΔS_c expressed as

$$\Delta S_c = \Delta S + k_1\left(M_0 - \int_V \rho\, dV\right) + k_2\left(E_0 - \int_V e\, dV\right)\,, \tag{3.2}$$

where k_1 and k_2 are two Lagrange multipliers. In order to describe the two phase liquid-vapour system the famous Van der Waals square gradient approximation of the free energy functional is adopted

$$F\left[\rho, \theta\right] = \int_V dV\left(f_b\left(\rho, \theta\right) + \frac{1}{2}\lambda\boldsymbol{\nabla}\rho\cdot\boldsymbol{\nabla}\rho\right)\,, \tag{3.3}$$

where, again, f_b is the classical bulk free energy density and λ is the capillary coefficient, controlling both the surface tension and the interface thickness. The entropy S as a functional of the density and temperature fields is the functional derivative of the free energy with respect to temperature

$$S\left[\rho,\theta\right]=\int_V -\frac{\delta F}{\delta\theta}\,dV=\int_V -\frac{\partial f_b}{\partial\theta}\,dV=\int_V s_b(\rho,\theta)\,dV\ , \tag{3.4}$$

where the second equality holds if λ does not depend on temperature, and the last identity follows by the classical definition of the bulk entropy density s_b, i.e. the entropy density of the homogeneous pahse. Thus the constrained functional in Eq. (3.2) reads

$$\Delta S_c=\Delta S_b+k_1\left(M_0-\int_V\rho\,dV\right)+k_2\left(E_0-U-\int_V\frac{1}{2}\rho\mathbf{v}\cdot\mathbf{v}\,dV\right)\ , \tag{3.5}$$

where the internal energy functional U is defined in terms of free energy as

$$U=F-\int dV\frac{\delta F}{\delta\theta}\theta=\int_V dV\left(u_b\left(\rho,\theta\right)+\frac{1}{2}\lambda\boldsymbol{\nabla}\rho\cdot\boldsymbol{\nabla}\rho\right)\ , \tag{3.6}$$

with $u_b=f_b-\theta\partial f_b/\partial\theta$ where the bulk internal energy density. The two Lagrange multipliers k_1 and k_2 are found by imposing that the first variation of the functional in Eq. (3.5) evaluated in the equilibrium state, must be zero:

$$\delta\Delta S_c\left[\rho_0,0,\theta_0\right]=0, \tag{3.7}$$

The above equation leads to $k_1=-\mu_{c0}/\theta_0$, $k_2=1/\theta_0$, where μ_{c0} is the equilibrium chemical potential, $\mu_b=\partial f_b/\partial\rho$ is the *bulk* chemical potential. For small fluctuations, the entropy functional can be expanded in a Taylor series around the equilibrium value with respect to the variables

$\mathbf{U} = (\rho, \boldsymbol{\nabla}\rho, \ldots, \nabla^n\rho, \theta, \mathbf{v})^T$ as follows

$$\begin{aligned}\Delta S_c &= \int_V \Delta s_c(\rho, \boldsymbol{\nabla}\rho, \ldots, \nabla^n\rho, \theta, \mathbf{v})\, dV = \\ &= \int_V dV \left[\sum_i \frac{\partial \Delta s_c}{\partial U_i}\bigg|_0 \delta U_i + \frac{1}{2}\sum_{i,j} \frac{\partial^2 \Delta s_c}{\partial U_i \partial U_j}\bigg|_0 \delta U_i \delta U_j + \ldots\right]\end{aligned} \tag{3.8}$$

All terms appearing in the right hand side of Eq. (3.8) can be rearranged in terms of suitable thermodynamic coefficients and of the fluctuations of density, temperature and velocity, e.g.

$$\begin{aligned}\mathrm{d}s_b &= \frac{1}{\theta}\mathrm{d}u_b - \frac{\mu_b}{\theta}\mathrm{d}\rho\,, \\ \mathrm{d}u_b &= \rho c_v \mathrm{d}\theta + \left(\mu_b + \theta \frac{\partial s_b}{\partial \rho}\bigg|_\theta\right)\mathrm{d}\rho\,, \\ \mathrm{d}\mu_b &= \frac{c_T^2}{\rho}\mathrm{d}\rho + \left(\frac{1}{\rho}\frac{\partial p}{\partial \theta}\bigg|_\rho - \frac{s_b}{\rho}\right)\mathrm{d}\theta\,,\end{aligned} \tag{3.9}$$

where c_v is the specific heat at constant specific volume, c_T the isothermal speed of sound, p the pressure.

Assuming that the fluid is very close to equilibrium and the fluctuations are small with respect to the mean value, the entropy functional can be approximated by a quadratic form in the fluctuating fields,

$$\Delta S_c \simeq -\frac{1}{2}\int_V dV \left[\frac{c_{T0}^2}{\theta_0\rho_0}\delta\rho^2 - \frac{\lambda}{\theta_0}\delta\rho\left(\nabla^2\delta\rho\right) + \frac{\rho_0}{\theta_0}\delta\mathbf{v}\cdot\delta\mathbf{v} + \frac{\rho_0 c_{v0}}{\theta_0^2}\delta\theta^2\right]. \tag{3.10}$$

For future reference, it is worth expressing the above integral as

$$\begin{aligned}\Delta S_c \simeq -\frac{1}{2} & \int_V\int_V dV_{\mathbf{x}} dV_{\tilde{\mathbf{x}}} \Bigg\{\delta\mathbf{v}(\mathbf{x})\frac{\rho_0}{\theta_0}\delta\left(\mathbf{x}-\tilde{\mathbf{x}}\right)\cdot\delta\mathbf{v}(\tilde{\mathbf{x}}) + \\ & +\delta\rho(\mathbf{x})\left[\frac{c_{T0}^2}{\theta_0\rho_0}\delta\left(\mathbf{x}-\tilde{\mathbf{x}}\right) - \frac{\lambda}{\theta_0}\nabla_{\mathbf{x}}^2\delta\left(\mathbf{x}-\tilde{\mathbf{x}}\right)\right]\delta\rho(\tilde{\mathbf{x}}) + \\ & +\delta\theta(\mathbf{x})\frac{\rho_0 c_{v0}}{\theta_0^2}\delta\left(\mathbf{x}-\tilde{\mathbf{x}}\right)\delta\theta(\tilde{\mathbf{x}})\Bigg\}\,,\end{aligned} \tag{3.11}$$

where integration by parts is used twice to move the Laplacian ∇^2 from the density to the Dirac delta function. Eq. (3.11) can be rewritten in operator form as

$$\Delta S_c = -\frac{1}{2}\int_V \mathbf{\Delta}^\dagger \mathcal{H}\, \mathbf{\Delta}\, dV\,, \tag{3.12}$$

where $\mathbf{\Delta} = (\delta\rho, \delta\mathbf{v}, \delta\theta)$ is the vector of the the fluctuating fields and $\mathcal{H}$ is a diagonal, positive definite matrix operator

$$\Gamma(\mathbf{x}) = (\mathcal{H}\mathbf{\Delta})(\mathbf{x}) = \int_V \mathbf{H}(\mathbf{x},\tilde{\mathbf{x}})\mathbf{\Delta}(\tilde{\mathbf{x}})dV_{\tilde{\mathbf{x}}} = \int_V \hat{\mathbf{H}}(\mathbf{x})\delta(\mathbf{x}-\tilde{\mathbf{x}})\mathbf{\Delta}(\tilde{\mathbf{x}})dV_{\tilde{\mathbf{x}}}\,, \tag{3.13}$$

where

$$\hat{\mathbf{H}}(\mathbf{x}) = \begin{pmatrix} \hat{H}_{\delta\rho\delta\rho} & 0 & 0 \\ 0 & \mathbf{I}\hat{H}_{\delta\mathbf{v}\delta\mathbf{v}} & 0 \\ 0 & 0 & \hat{H}_{\delta\theta\delta\theta} \end{pmatrix} = \begin{pmatrix} \frac{c_{T0}^2}{\theta_0\rho_0} - \frac{\lambda}{\theta_0}\nabla^2_{\mathbf{x}} & 0 & 0 \\ 0 & \frac{\rho_0}{\theta_0}\mathbf{I} & 0 \\ 0 & 0 & \frac{\rho_0 c_{v0}}{\theta_0^2} \end{pmatrix}$$

involves differential operators and $\mathbf{I}$ is the 3×3 identity matrix. Note that, indeed the Laplace operator $-\nabla^2$ appearing in the first line, which is in general non-negative, is strictly positive under the constraint of mass conservation since the mean spatial density fluctuation is identically zero.

Under these assumptions the more general probability distribution functional for the fluctuating fields $\mathbf{\Delta}$ [58]

$$P_{eq}[\mathbf{\Delta}] = \frac{1}{Z}\exp\left(\frac{\Delta S_c}{k_B}\right)\,, \tag{3.14}$$

can be rewritten by using the second order approximation, Eq. (3.12),

$$P_{eq}[\Delta] = \frac{1}{Z}\exp\left(-\frac{1}{2k_B}\int_V \Delta^\dagger \mathcal{H}\,\Delta\, dV\right)\,, \tag{3.15}$$

which can be factorized since $\hat{\mathbf{H}}$ is diagonal

$$P_{eq}[\mathbf{\Delta}] = P_{\delta\rho}[\delta\rho]P_{\delta\mathbf{v}}[\delta\mathbf{v}]P_{\delta\theta}[\delta\theta]\,, \tag{3.16}$$

with

$$P_{\delta\rho} = \frac{1}{Z_{\delta\rho}} \exp\left[-\frac{1}{2\mathrm{k}_B}\int\int d\mathbf{x}d\mathbf{x}'\delta\rho(\mathbf{x})H_{\delta\rho\delta\rho}\delta(\mathbf{x}-\mathbf{x}')\delta\rho(\mathbf{x}')\right] , \quad (3.17)$$

$$P_{\delta\mathbf{v}} = \frac{1}{Z_{\delta\mathbf{v}}} \exp\left[-\frac{1}{2\mathrm{k}_B}\int\int d\mathbf{x}d\mathbf{x}'\delta\mathbf{v}^T(\mathbf{x})H_{\delta\mathbf{v}\delta\mathbf{v}}\delta(\mathbf{x}-\mathbf{x}')\delta\mathbf{v}(\mathbf{x}')\right] , \quad (3.18)$$

$$P_{\delta\theta} = \frac{1}{Z_{\delta\theta}} \exp\left[-\frac{1}{2\mathrm{k}_B}\int\int d\mathbf{x}d\mathbf{x}'\delta\theta(\mathbf{x})H_{\delta\theta\delta\theta}\delta(\mathbf{x}-\mathbf{x}')\delta\theta(\mathbf{x}')\right] , \quad (3.19)$$

and is normalized by the constant Z

$$Z = \int D\delta\rho D\delta\mathbf{v}D\delta\theta \, \exp\left(-\frac{1}{2k_B}\int_V \mathbf{\Delta}^\dagger \mathcal{H}\, \mathbf{\Delta}\, dV\right) = Z_{\delta\rho}Z_{\delta\mathbf{v}}Z_{\delta\theta} \, . \quad (3.20)$$

The generic correlation function

$$\begin{aligned} \mathbf{C}_{\mathbf{\Delta}}(\mathbf{x}) &= \langle \mathbf{\Delta} \otimes \mathbf{\Delta}^\dagger \rangle = \quad (3.21) \\ &= \frac{1}{Z}\int D\delta\rho D\delta\mathbf{v}D\delta\theta \, \mathbf{\Delta} \otimes \mathbf{\Delta}^\dagger \, \exp\left(\frac{1}{k_B}\int_V \Delta s_c(\delta\rho, \delta\mathbf{v}, \delta\theta)\, dV\right) \end{aligned}$$

can now be evaluated in closed form by integrating Gaussian path integrals. To this end it is helpful to resort to the characteristic functional [136] of the pdf which, for a generic process $X(\mathbf{x})$, is

$$\Phi[\chi] = \int DX \; P\,[X] \exp\left(\int \chi\,(\mathbf{x})\, X\,(\mathbf{x})\, dV_{\mathbf{x}}\right) \, . \quad (3.22)$$

For a Gaussian process governed by the pdf

$$P\,[X] = \frac{1}{Z}\exp\left(\int -\frac{1}{2}X(\mathbf{x})A(\mathbf{x},\tilde{\mathbf{x}})X(\tilde{\mathbf{x}})dV_{\mathbf{x}}dV_{\tilde{\mathbf{x}}}\right)$$

the characteristic functional reduces to

$$\Phi[\chi] = \int DX \exp\left[-\frac{1}{2}\int\int d\hat{\mathbf{x}}d\tilde{\mathbf{x}}X\,(\hat{\mathbf{x}})\,A\,(\hat{\mathbf{x}},\tilde{\mathbf{x}})\,X\,(\tilde{\mathbf{x}}) + \int \chi\,(\hat{\mathbf{x}})\,X\,(\hat{\mathbf{x}})\,d\hat{\mathbf{x}}\right] , \quad (3.23)$$

and is easily evaluated by completing the square (see Appendix A) as

$$\Phi[\chi] = \Phi[0] \exp\left(\frac{1}{2}\int\int d\hat{\mathbf{x}}d\tilde{\mathbf{x}}\,\chi\left(\hat{\mathbf{x}}\right)\,G\left(\hat{\mathbf{x}},\tilde{\mathbf{x}}\right)\,\chi\left(\tilde{\mathbf{x}}\right)\right)\,, \tag{3.24}$$

where

$$G\left(\hat{\mathbf{x}},\tilde{\mathbf{x}}\right) = A^{-1}\left(\hat{\mathbf{x}},\tilde{\mathbf{x}}\right) \tag{3.25}$$

(we stress that A is the kernel of an operator $\mathcal{A}$, such that A^{-1} should be understood as the kernel of the inverse $\mathcal{A}^{-1}$). The two-point correlation can be written in terms of the characteristic functional as

$$\begin{aligned} C_{XX}\left(\hat{\mathbf{x}},\tilde{\mathbf{x}}\right) &= \langle X\left(\hat{\mathbf{x}}\right)X\left(\tilde{\mathbf{x}}\right)\rangle = \\ &= \left(\frac{1}{\Phi[0]}\frac{\delta}{\delta\chi\left(\hat{\mathbf{x}}\right)}\frac{\delta}{\delta\chi\left(\tilde{\mathbf{x}}\right)}\Phi[\chi]\right)_{\chi=0} = G\left(\hat{\mathbf{x}},\tilde{\mathbf{x}}\right)\ . \end{aligned} \tag{3.26}$$

In the present case, Eq. (3.15), the kernel of the operator A is given by

$$A\left(\hat{\mathbf{x}},\tilde{\mathbf{x}}\right) = \frac{1}{\mathrm{k}_B}\hat{\mathbf{H}}\delta\left(\hat{\mathbf{x}}-\tilde{\mathbf{x}}\right)\,, \tag{3.27}$$

implying the equation

$$\begin{aligned} \int \mathbf{A}(\mathbf{x},\mathbf{x}'')\mathbf{G}\left(\mathbf{x}'',\mathbf{x}'\right)dV_{\mathbf{x}''} &= \\ \frac{1}{\mathrm{k}_B}\int \hat{\mathbf{H}}\delta(\mathbf{x}-\mathbf{x}'')\mathbf{G}\left(\mathbf{x}'',\mathbf{x}'\right)dV_{\mathbf{x}''} &= \hat{\mathbf{U}}\delta(\mathbf{x}-\mathbf{x}')\,, \end{aligned} \tag{3.28}$$

which, written in terms of operators, corresponds to the equation $\mathcal{A}\mathcal{A}^{-1} = \mathcal{U}$, with $\mathcal{U}$ the identity operator on the space of fluctuations. $\hat{\mathbf{U}}$ is the identity matrix acting on the five-dimensional tangent space at a given position $\mathbf{x}$, $\mathbf{\Delta}(\mathbf{x}) = (\delta\rho(\mathbf{x}), \delta\mathbf{v}(\mathbf{x}), \delta\theta(\mathbf{x}))$.

In particular, since the matrix $\hat{\mathbf{H}}$ is diagonal, the $\delta\rho\,\delta\rho$ component of the above equation is

$$\begin{aligned} \int A_{\delta\rho\delta\rho}(\mathbf{x},\mathbf{x}'')G_{\delta\rho\delta\rho}\left(\mathbf{x}'',\mathbf{x}'\right)dV_{\mathbf{x}''} &= \\ \mathrm{k}_B^{-1}\int\left[\left(\frac{c_T^2}{\theta_0\rho_0}-\frac{\lambda}{\theta_0}\nabla_{\mathbf{x}}^2\right)\delta(\mathbf{x}-\mathbf{x}'')\right]G_{\delta\rho\delta\rho}\left(\mathbf{x}'',\mathbf{x}'\right)dV_{\mathbf{x}''} &= \delta(\mathbf{x}-\mathbf{x}'). \end{aligned} \tag{3.29}$$

After integration by parts, Eq. (3.29) reads

$$\frac{c_T^2}{\theta_0 \rho_0 \mathrm{k}_B} G_{\delta\rho\delta\rho}\left(\hat{\mathbf{x}}, \tilde{\mathbf{x}}\right) - \frac{\lambda}{\theta_0 \mathrm{k}_B} \nabla_{\hat{\mathbf{x}}}^2 G_{\delta\rho\delta\rho}\left(\hat{\mathbf{x}}, \tilde{\mathbf{x}}\right) = \delta\left(\hat{\mathbf{x}} - \tilde{\mathbf{x}}\right) \tag{3.30}$$

After Fourier transformation the equation becomes

$$\hat{G}\left(\mathbf{k}\right) + \frac{\lambda \rho_0}{c_T^2} \mathbf{k} \cdot \mathbf{k} \, \hat{G}\left(\mathbf{k}\right) = \frac{\rho_0 \mathrm{k}_B \theta_0}{c_T^2} \,, \tag{3.31}$$

allowing to express the solution (the Green's function for the Helmholtz equation) as

$$G_{\delta\rho\delta\rho}\left(\hat{\mathbf{x}}, \tilde{\mathbf{x}}\right) = \int d\mathbf{k} \frac{\mathrm{k}_B \rho_0 \theta_0}{c_T^2 + \rho_0 \lambda \, \mathbf{k} \cdot \mathbf{k}} e^{i\mathbf{k} \cdot \left(\hat{\mathbf{x}} - \tilde{\mathbf{x}}\right)} \,. \tag{3.32}$$

Explicitly performing the inverse Fourier transform yields

$$G_{\delta\rho\delta\rho}\left(\hat{\mathbf{x}}, \tilde{\mathbf{x}}\right) = C_{\delta\rho\delta\rho}\left(\hat{\mathbf{x}}, \tilde{\mathbf{x}}\right) = \frac{\mathrm{k}_B \theta_0}{4\pi\lambda \left|\hat{\mathbf{x}} - \tilde{\mathbf{x}}\right|} \exp\left(- \left|\hat{\mathbf{x}} - \tilde{\mathbf{x}}\right| \sqrt{\frac{c_T^2}{\rho_0 \lambda}} \right) \,, \tag{3.33}$$

where we have recognised that $\mathbf{G} = \mathbf{C}_{\mathbf{\Delta}}$, Eq. (3.26). The same procedure can be used to reconstruct the entire correlation tensor $\mathbf{C}_{\mathbf{\Delta}} = \langle \mathbf{\Delta} \otimes \mathbf{\Delta}^\dagger \rangle$, Eqs. (3.34-3.37):

$$\mathbf{C}_{\mathbf{\Delta}} = \begin{pmatrix} C_{\delta\rho\delta\rho} & 0 & 0 \\ 0 & \mathbf{C}_{\delta\mathbf{v}\delta\mathbf{v}} & 0 \\ 0 & 0 & C_{\delta\theta\delta\theta} \end{pmatrix} \,, \tag{3.34}$$

with

$$C_{\delta\rho\delta\rho} = \frac{\mathrm{k}_B \theta_0}{4\pi\lambda \left|\hat{\mathbf{x}} - \tilde{\mathbf{x}}\right|} \exp\left(- \left|\hat{\mathbf{x}} - \tilde{\mathbf{x}}\right| \sqrt{\frac{c_T^2}{\rho_0 \lambda}} \right) \,, \tag{3.35}$$

$$\mathbf{C}_{\delta\mathbf{v}\delta\mathbf{v}} = \frac{k_B \theta_0}{\rho_0} \mathbf{I} \delta\left(\hat{\mathbf{x}} - \tilde{\mathbf{x}}\right) \,, \tag{3.36}$$

$$C_{\delta\theta\delta\theta} = \frac{k_B \theta_0^2}{\rho_0 c_v} \delta\left(\hat{\mathbf{x}} - \tilde{\mathbf{x}}\right) \,. \tag{3.37}$$

It can be deduced that, in the Gaussian approximation, the equilibrium correlations for velocity and temperature are short-ranged (delta-correlated in space, actually) and the cross-correlation of the fluctuating fields are zero.

3.1.1 Static structure factor

An important quantity in the theory of liquids is the Fourier transform of the correlation tensor, the so called *static structure factor*. In particular the density structure factor, defined as

$$S(\mathbf{k}) = \langle \delta\rho(\mathbf{k})\delta\rho^*(\mathbf{k})\rangle \tag{3.38}$$

assumes a key role, both from an experimental [15] and a numerical [54] point of view. In Eq. (3.38) $\delta\rho(\mathbf{k})$ is the Fourier transform of the density fluctuation

$$\delta\rho(\mathbf{k}) = \int d\mathbf{x} e^{-i\mathbf{k}\cdot\mathbf{x}}(\rho(\mathbf{x}) - \langle\rho\rangle) \tag{3.39}$$

with $\langle\rho\rangle$ being the bulk mean density and the symbol * denoting the complex conjugate. For a single component fluid with capillarity, the Fourier transform of the density correlation can be deduced from the spatial density correlation Eq. (3.35), by enforcing the Wiener-Khinchin theorem as:

$$S(\mathbf{k}) = \int d\mathbf{x} e^{-i\mathbf{k}\cdot\mathbf{x}} \langle\delta\rho(\hat{\mathbf{x}})\delta\rho(\tilde{\mathbf{x}})\rangle = \frac{\langle\rho\rangle\, k_B\theta}{c^2{}_T + \langle\rho\rangle\, \lambda\mathbf{k}\cdot\mathbf{k}} \ . \tag{3.40}$$

3.2 Fluctuation dissipation balance

To correctly model the stochastic fluxes (stress tensor and heat flux) one needs to use the fluctuation-dissipation theorem which is worthwhile recalling here in the context of the Navier-Stokes system for a capillary fluid. For the sake of clarity, the full calculation is illustrated first for the one-dimensional case. Apart from some attention needed to deal with the vector counterpart, generalisation to the three dimensional case is straightforward, and it will be postponed to the next section.

The system of equations presented in Chapter 2 (eqs.(2.29 – 2.31)) can be rewritten in the 1D case as

$$
\begin{aligned}
\partial_t \rho + \partial_x (\rho v) &= 0 \,, \qquad (3.41)\\
\partial_t (\rho v) + \partial_x (\rho v) &= -\partial_x p + \mu \partial_{xx} v + \partial_x \left(-\frac{\lambda}{2} \partial_x \rho \partial_x \rho + \rho \lambda \partial_{xx} \rho \right) + \sigma_v W_v \,, \\
\rho c_v (\partial_t \theta + v \partial_x \theta) &= -\theta \frac{\partial p}{\partial \theta} \partial_x v + k \partial_{xx} \theta + \mu (\partial_x v)^2 + \sigma_\theta W_\theta + \sigma_v W_v \partial_x v \,,
\end{aligned}
$$

where, for the ease of calculation the energy equation is here expressed in terms of temperature. In the equations μ is the dynamic viscosity, k is the thermal conductivity and the terms $\sigma_v W_v$ and $\sigma_\theta W_\theta$ represent the stochastic forcing. W is a standard Wiener process and $\sigma_{v/\theta}$ two suitable operators that will be later identified by means of fluctuation-dissipation balance.

The above system of equations can be linearized around the mean solution $\{\rho_0, 0, \theta_0\}$. Such linearization provides a set of stochastic partial differential equations, whose equilibrium (statistically stationary) solution is a Gaussian field. The linearized system can be formally expressed in the form

$$
\partial_t \mathbf{\Delta} = \mathbf{L}\, \mathbf{\Delta} + \mathbf{f} \,, \qquad (3.42)
$$

where $\mathbf{L}$ is the linearized Navier-Stokes operator with capillarity which reads

$$
\mathbf{L} = \begin{pmatrix} 0 & -\rho_0 \partial_x & 0 \\ -\frac{c_T^2}{\rho_0} \partial_x + \lambda \partial_{xxx} & \frac{\mu}{\rho_0} \partial_{xx} & -\frac{1}{\rho_0} \partial_\theta p \partial_x \\ 0 & -\frac{\theta_0}{\rho_0 c_v} \partial_\theta p \partial_x & \frac{k}{\rho_0 c_v} \partial_{xx} \end{pmatrix} . \qquad (3.43)
$$

$\mathbf{f}(x,t)$ is a Gaussian vector process (with three components, in the case of Eq. (3.42)) whose correlation is

$$
\langle \mathbf{f}(\tilde{x}, s) \otimes \mathbf{f}^\dagger(\hat{x}, q) \rangle = \mathbf{Q}(\tilde{x}, \hat{x}) \delta(s - q) \,, \qquad (3.44)
$$

with $\mathbf{Q}(\tilde{x}, \hat{x})$ a matrix depending on $\tilde{x}$ and $\hat{x}$. Note that delta-correlation in time is explicitly assumed. The stochastic forcing $\mathbf{f}$ is related to the standard Wiener process $\mathbf{W}dt = d\mathbf{B}$ by the linear relationship

$$\mathbf{f} = \mathbf{K}\mathbf{W}\,, \tag{3.45}$$

where $\mathbf{W} = \{W_\rho, W_v, W_\theta\}^T$ is a Gaussian delta correlated process characterized by the correlation

$$\langle \mathbf{W}(\tilde{y}, s) \otimes \mathbf{W}(\hat{y}, q) \rangle = \mathbf{I}\delta(\tilde{y} - \hat{y})\delta(s - q)\,, \tag{3.46}$$

and

$$\mathbf{K} = \begin{pmatrix} 0 & 0 & 0 \\ 0 & \dfrac{\sigma_v}{\rho_0} & 0 \\ 0 & 0 & -\dfrac{\sigma_\theta}{\rho_0 c_v} \end{pmatrix} \tag{3.47}$$

is a linear operator acting on the noise.

The solution of Eq. (3.42) is formally expressed as [36]

$$\mathbf{\Delta}\,(x, t) = \int_0^t e^{\mathbf{L}(t-s)}\mathbf{f}(s)\,ds + e^{\mathbf{L}t}\mathbf{\Delta_0}\,, \tag{3.48}$$

where the last term which keeps memory of the initial conditions vanishes for large times. Consequently the equilibrium correlation is

$$\langle \mathbf{\Delta}(\tilde{x}, t) \otimes \mathbf{\Delta}^\dagger(\hat{x}, t) \rangle = \int_0^t e^{\mathbf{L}(t-s)}\mathbf{Q}\, e^{\mathbf{L}^\dagger(t-s)} ds\,, \tag{3.49}$$

where $\mathbf{Q}$ was introduced in Eq. (3.44) above. The integral can be performed in closed form assuming the existence of a Hermitian non singular operator $\mathbf{E}^{-1}$ such that the operator $\mathbf{Q}$ can be decomposed as

$$\mathbf{Q} = -\mathbf{L}\mathbf{E}^{-1} - \mathbf{E}^{-1}\mathbf{L}^\dagger\ . \tag{3.50}$$

With this position the integrand appearing in Eq. (3.49) is the exact derivative with respect to the delay time s of $e^{\mathbf{L}(t-s)}\mathbf{E}^{-1}\, e^{\mathbf{L}^\dagger(t-s)}$. Hence Eq. (3.49) leads to

$$\lim_{t\to\infty}\langle \mathbf{\Delta}\otimes\mathbf{\Delta}^\dagger\rangle = \mathbf{E}^{-1} = \mathbf{C}_{\mathbf{\Delta}}\,, \tag{3.51}$$

hence the operator $\mathbf{E}^{-1}$ exists indeed and coincides with the correlation matrix $\mathbf{C}_{\mathbf{\Delta}}$, see Eq. (3.34).

Given the expression for $\mathbf{Q}$, Eq. (3.50), and the identity $\mathbf{E}^{-1} = \mathbf{C}_{\mathbf{\Delta}}$ it follows

$$\mathbf{Q} = -\left(\mathbf{L}\mathbf{C}_{\mathbf{\Delta}} + \mathbf{C}_{\mathbf{\Delta}}\mathbf{L}^\dagger\right) = \left(\mathbf{M}+\mathbf{M}^\dagger\right) = 2\mathrm{k}_B\mathbf{O}\,, \tag{3.52}$$

where $\mathbf{M} = -\mathbf{L}\mathbf{C}_\Delta$ and $\mathbf{O}$ is called the Onsager matrix. Relationship (3.52) is the form the celebrated fluctuation-dissipation balance takes for the present system. Highlighting the connection between the intensity of the fluctuations and dissipation mechanisms. The physical interpretation is that, in thermodynamic equilibrium, the response of a system to a perturbation is equivalent to the one provided by spontaneous fluctuation. So that one can infer non-equilibrium properties for a physical system looking at equilibrium properties.

The unknown operators $\sigma_{v/\theta}$ can be finally identified by enforcing the fluctuation-dissipation balance Eq. (3.52), by introducing Eqs. (3.44) and (3.45),

$$\mathbf{Q}(\tilde{x},\hat{x})\delta(s-q) = \mathbf{K}\langle\mathbf{W}\mathbf{W}^\dagger\rangle\mathbf{K}^\dagger = 2\mathrm{k}_B\mathbf{O}\delta(s-q)\,, \tag{3.53}$$

$$\mathbf{K}\mathbf{K}^\dagger = 2\mathrm{k}_B\mathbf{O} = -\left(\mathbf{L}\mathbf{C}_{\mathbf{\Delta}} + \mathbf{C}_{\mathbf{\Delta}}\mathbf{L}^\dagger\right) = \mathbf{M}+\mathbf{M}^\dagger\ . \tag{3.54}$$

The explicit calculation of the right hand side of this equation, where $\mathbf{L}$ and $\mathbf{C}_\Delta$ are known from Eq. (3.43) and (3.34), respectively, provides

$$\mathbf{M} = \begin{pmatrix} 0 & \mathrm{k}_B\theta_0\partial_x\left[\delta(x-\hat{x})\right] & 0 \\ \mathrm{k}_B\theta_0\partial_x\left[\delta(x-\hat{x})\right] & -\dfrac{\mu_0\mathrm{k}_B\theta_0}{\rho_0^2}\partial_{xx}\left[\delta(x-\hat{x})\right] & \dfrac{\mathrm{k}_B\theta_0^2}{\rho_0^2 c_v}\partial_\theta p\partial_x\left[\delta(x-\hat{x})\right] \\ 0 & \dfrac{\mathrm{k}_B\theta_0^2}{\rho_0^2 c_v}\partial_\theta p\partial_x\left[\delta(x-\hat{x})\right] & -\dfrac{k\mathrm{k}_B\theta_0^2}{\rho_0^2 c_v^2}\partial_{xx}\left[\delta(x-\hat{x})\right] \end{pmatrix},$$

The expression for the Hermitian conjugate matrix is immediately obtained by taking the transpose of the real matrix $\mathbf{M}$ after considering that even differential operators are self-adjoint ($\partial_{xx}^\dagger = \partial_{xx}$) while odd one are skew-adjoint ($\partial_x^\dagger = -\partial_x$). Summing together $\mathbf{M}$ and its hermitian conjugate Eq. (3.54) becomes

$$\mathbf{M} + \mathbf{M}^\dagger = \mathbf{K}\mathbf{K}^\dagger = \begin{pmatrix} 0 & 0 & 0 \\ 0 & -\dfrac{2\mu_0\mathrm{k}_B\theta_0}{\rho_0^2}\partial_{xx}\left[\delta\left(x-\hat{x}\right)\right] & 0 \\ 0 & 0 & -\dfrac{2k\mathrm{k}_B\theta_0^2}{\rho_0^2 c_v^2}\partial_{xx}\left[\delta\left(x-\hat{x}\right)\right] \end{pmatrix} \tag{3.55}$$

So, that

$$\sigma_v {\sigma_v}^\dagger = -2\mu\mathrm{k}_B\theta_0\partial_{\hat{x}\hat{x}}\delta\left(\hat{x}-\tilde{x}\right) \tag{3.56}$$

$$\sigma_\theta {\sigma_\theta}^\dagger = -2k\mathrm{k}_B{\theta_0}^2\partial_{\hat{x}\hat{x}}\delta\left(\hat{x}-\tilde{x}\right), \tag{3.57}$$

providing the explicit expressions

$$\sigma_v W_v = \sqrt{2\mu\mathrm{k}_B\theta_0}\,\partial_x W_v \tag{3.58}$$

$$\sigma_\theta W_\theta = \sqrt{2k\mathrm{k}_B{\theta_0}^2}\,\partial_x W_\theta\,. \tag{3.59}$$

The above results can be directly proved by choosing the form of the operator $\sigma_v = -\sqrt{2\mu k_B\theta}\partial_{\hat{x}}\delta\left(\hat{x}-\tilde{x}\right)$, in fact

$$\sigma_v {\sigma_v}^\dagger\left(\hat{x}-\tilde{x}\right) = 2\mu k_B\theta\int \partial_{\hat{x}}\delta\left(\hat{x}-y\right)\,\partial_y\delta\left(\tilde{x}-y\right)\,dy \tag{3.60}$$

and the action of the operator σ_v on the Wiener process W_v reads

$$\boldsymbol{\sigma_v} W_v\left(x,t\right) = -\sqrt{2\mu k_B \theta} \int \partial_{\hat{x}} \delta\left(\hat{x}-x\right) W_v\left(\hat{x},t\right) d\hat{x} = \sqrt{2\mu \mathrm{k}_B \theta_0}\, \partial_x W_v\left(x,t\right) \ . \tag{3.61}$$

3.2.1 Restating the LLNS equations with capillarity in terms of entropy functional

In the present section is reported a particularly impressive form of Langevin equation, having as a drift term a linear functional acting on the entropy deviation. This formulation provides a link between the fluctuation probability distributions (the entropy functional) and the dynamics of the physical system. In fact, as common in the linear non-equilibrium thermodynamics, the thermodynamic forces are defined as the functional derivatives of the entropy (see Eq. (3.12), with respect to the conjugate field $\boldsymbol{\Delta}$, that under the hypothesis of Gaussian fluctuations read

$$\mathbf{Y} = \frac{\delta \Delta S_c}{\delta \boldsymbol{\Delta}} = -\mathbf{H}\,\boldsymbol{\Delta}\,, \tag{3.62}$$

suggesting (see [12] for details) the analogy with Hookean springs, in which $\mathbf{Y}$ acts as returning force enforcing to restore che thermodynamic equilibrium at maximum entropy.

As exposed in the previous sections, the thermodynamic force $\mathbf{Y}$ is related with the fluctuation through the correlation tensor as $\mathbf{Y} = -\mathbf{C}^{-1}\,\boldsymbol{\Delta}$, providing the equality $\mathbf{M}\,\mathbf{Y} = \mathbf{L}\,\boldsymbol{\Delta}$.

Thus, after enforcing the FDB Eq. (3.52), the equation of motion (3.42) can be rewritten in the form

$$\partial_t \boldsymbol{\Delta} = \mathbf{M}\,\frac{\delta \Delta S_c}{\delta \boldsymbol{\Delta}} \ + \sqrt{2}\,\mathbf{M}_{\mathrm{H}}^{1/2}\mathbf{W}\,, \tag{3.63}$$

where $\mathbf{M}_{\mathrm{H}} = 1/2(\mathbf{M} + \mathbf{M}^{\dagger}) = k_B\,\mathbf{O}$ is the Hermitian part of $\mathbf{M}$ and the operation $(\cdot)^{1/2}$ has to be intended in the functional sense, i.e., $\mathbf{M}_{\mathrm{H}}^{1/2}\mathbf{M}_{\mathrm{H}}^{\dagger 1/2} = \mathbf{M}_{\mathrm{H}}$. The Eq. (3.63) admits as static probability distribution $P[\mathbf{\Delta}] = Z^{-1}\,\exp(\Delta S_c/k_B)$, as evident as stationary solution of Fokker-Planck equation, see Eq. (C.8) in Appendix B.

In fact the stationary probability distribution $P\,[\mathbf{\Delta}]$ obeys to

$$\left(\frac{\delta}{\delta\mathbf{\Delta}}\cdot\mathbf{M}\,\frac{\delta\Delta S_c}{\delta\mathbf{\Delta}}\;-\frac{\delta}{\delta\mathbf{\Delta}}\otimes\frac{\delta}{\delta\mathbf{\Delta}}:\mathbf{M}_{\mathrm{H}}\right)\,P\,[\mathbf{\Delta}]\;=0\,, \tag{3.64}$$

that after imposing as $P[\mathbf{\Delta}] = Z^{-1}\,\exp(\Delta S_c/k_B)$, yields

$$\left[(\mathbf{M}_{\mathrm{H}}-\mathbf{M}):\frac{\delta}{\delta\mathbf{\Delta}}\otimes\frac{\delta}{\delta\mathbf{\Delta}}\right]\frac{P\,[\mathbf{\Delta}]}{k_B}+\left[(\mathbf{M}_{\mathrm{H}}-\mathbf{M}):\frac{\delta}{\delta\mathbf{\Delta}}\otimes\frac{\delta\Delta S_c}{\delta\mathbf{\Delta}}\right]\,P\,[\mathbf{\Delta}]=0\,, \tag{3.65}$$

so that

$$\left[\mathbf{M}_{\mathrm{SH}}:\frac{\delta}{\delta\mathbf{\Delta}}\otimes\frac{\delta}{\delta\mathbf{\Delta}}\right]\frac{P\,[\mathbf{\Delta}]}{k_B}+\left[\mathbf{M}_{\mathrm{SH}}:\frac{\delta}{\delta\mathbf{\Delta}}\otimes\frac{\delta\Delta S_c}{\delta\mathbf{\Delta}}\right]\,P\,[\mathbf{\Delta}]=0\,, \tag{3.66}$$

the latter identity is satisfied since $\mathbf{M}_{\mathrm{SH}} = 1/2\,(\mathbf{M}-\mathbf{M}_{\mathrm{H}})$ is a skew-Hermitian operator double contracted with two Hermitian ones.

3.2.2 FDB for the 3D system

In this section, the derivation of the FDB is retraced for a 3D system. As shown in the previous subsection, the Liftshitz -Landau-Navier-Stokes equations can be formally written as

$$\partial_t\mathbf{\Delta} = \mathbf{L}\,\mathbf{\Delta} + \mathbf{f}\,. \tag{3.67}$$

For a 3D system, the linearised differential operator $\mathbf{L}$ is now rewritten as

$$\mathbf{L} = \begin{pmatrix} 0 & -\rho_0\mathbf{\nabla}\cdot & 0 \\ -\dfrac{c_T^2}{\rho_0}\mathbf{\nabla}+\lambda\mathbf{\nabla}\nabla^2 & \dfrac{\mu}{\rho_0}\left(\nabla^2+\dfrac{1}{3}\mathbf{\nabla}\mathbf{\nabla}\cdot\right) & -\dfrac{1}{\rho_0}\partial_\theta p\mathbf{\nabla} \\ 0 & -\dfrac{\theta_0}{\rho_0 c_v}\partial_\theta p\mathbf{\nabla}\cdot & \dfrac{k}{\rho_0 c_v}\nabla^2 \end{pmatrix}\,. \tag{3.68}$$

The stochastic force $\mathbf{f} = \mathbf{K}\mathbf{W}$ is obtained through the linear operator $\mathbf{K}$

$$\mathbf{K} = \begin{pmatrix} 0 & 0 & 0 \\ 0 & \dfrac{\sigma_{\mathbf{v}}}{\rho_0} & 0 \\ 0 & 0 & -\dfrac{\sigma_\theta}{\rho_0 c_v} \end{pmatrix} \tag{3.69}$$

as exposed for 1D case (see Eq. 3.41), acting on the Gaussian delta correlated process $\mathbf{W}$. In three dmensions $\sigma_{\mathbf{v}}$ is a 3×3 matrix whose components are scalar linear operators to be determined.

For the present system $\mathbf{W} = \{W_\rho, \mathbf{W}_v, W_\theta\}^T$, where $\mathbf{W}_v = \left(W_{v_x}, W_{v_y}, W_{v_z}\right)^T$. It is worth remembering that the process $\mathbf{W}$ is characterized by the correlation

$$\langle \mathbf{W}(\tilde{y}, s) \otimes \mathbf{W}(\hat{y}, q) \rangle = \mathbf{I}\delta(\tilde{y} - \hat{y})\delta(s - q)\,, \tag{3.70}$$

in which $\mathbf{I}$ is now, a (5×5) identity matrix in the space of $\mathbf{W}$.

After discussing the specific structure of the operators appearing in Eq. (3.67) and following the procedure illustrated in the previous part of the present section for the one dimensional problem, it is straightforward to show that the FDB for the 3D system takes the form

$$\mathbf{Q} = -\left(\mathbf{L}\mathbf{C}_{\boldsymbol{\Delta}} + \mathbf{C}_{\boldsymbol{\Delta}}\mathbf{L}^\dagger\right) = \left(\mathbf{M} + \mathbf{M}^\dagger\right) = 2\mathrm{k}_B\mathbf{O}\,. \tag{3.71}$$

By using the new expression for $\mathbf{L}$ given in Eq. (3.68) and correlation matrix $\mathbf{C}_\Delta$ for the 3D system, Eq. (3.34), respectively, one finds

$$\mathbf{M} = \begin{pmatrix} 0 & m_{12} & 0 \\ m_{21} & \mathbf{m}_{22} & m_{23} \\ 0 & m_{32} & m_{33} \end{pmatrix}\,.$$

The entries of the matrix $\mathbf{M}$ are

$$m_{12} = m_{12} = \mathrm{k}_B\theta_0\boldsymbol{\nabla}\delta\left(\mathbf{x} - \hat{\mathbf{x}}\right), \tag{3.72}$$

$$m_{23} = m_{32} = \frac{\mathrm{k}_B \theta_0^2}{\rho_0^2 c_v} \partial_\theta p \boldsymbol{\nabla} \delta\left(\mathbf{x} - \hat{\mathbf{x}}\right), \tag{3.73}$$

$$\mathbf{m}_{22} = -\frac{\mu_0 \mathrm{k}_B \theta_0}{\rho_0^2} \left(\mathbf{I} \nabla^2 + \frac{1}{3} \boldsymbol{\nabla} \otimes \boldsymbol{\nabla} \right) \delta\left(\mathbf{x} - \hat{\mathbf{x}}\right), \tag{3.74}$$

$$m_{33} = -\frac{\mathrm{k}_B \theta_0^2 k}{\rho_0^2 c_v^2} \nabla^2 \delta\left(\mathbf{x} - \hat{\mathbf{x}}\right). \tag{3.75}$$

Thus, the sum of $\mathbf{M}$ and its hermitian conjugate $\mathbf{M}^\dagger$ provides the explicit expression for the *square* of the unknown matrix operator $\mathbf{K}$, Eq. (3.69), i.e. the explicit form of the FDB,

$$\mathbf{K}\mathbf{K}^\dagger = \mathbf{M} + \mathbf{M}^\dagger = \begin{pmatrix} 0 & 0 & 0 \\ 0 & 2\,\mathbf{m}_{22} & 0 \\ 0 & 0 & 2\,m_{33} \end{pmatrix}. \tag{3.76}$$

Determining $\mathbf{K}$ amounts to solve the system of equations (3.76) satisfied component-wise,

$$\sigma_\theta \sigma_\theta^\dagger = -2\mathrm{k}_B \theta_0^2 k \nabla^2 \delta\left(\hat{\mathbf{x}} - \tilde{\mathbf{x}}\right), \tag{3.77}$$

$$\sigma_{\mathbf{v}} \otimes \sigma_{\mathbf{v}}^\dagger = -2\mu_0 \mathrm{k}_B \theta_0 \left(\mathbf{I}\, \nabla^2 + \frac{1}{3} \boldsymbol{\nabla} \otimes \boldsymbol{\nabla} \right) \delta\left(\hat{\mathbf{x}} - \tilde{\mathbf{x}}\right). \tag{3.78}$$

Providing an explicit expression for the stochastic fluxes (denoted by the prefix δ before the deterministic counterpart)

$$\delta \boldsymbol{\Sigma} = \sqrt{2\mu_0 \mathrm{k}_B \theta_0} \tilde{\mathbf{W}}_v - \frac{1}{3} \sqrt{2\mu \mathrm{k}_B \theta}\, \mathrm{Tr}\left(\tilde{\mathbf{W}}_v \right) \mathbf{I}, \tag{3.79}$$

$$\delta \mathbf{q} = \sqrt{2k \mathrm{k}_B \theta_0^2} \mathbf{W}_\theta. \tag{3.80}$$

Where $\tilde{\mathbf{W}}_{\mathbf{v}} = \left(\mathbf{W}_v + (\mathbf{W}_v)^T \right) / \sqrt{2}$ is a stochastic symmetric tensor field, and $\mathbf{W}_\theta$ is a stochastic vector, with the following statistical properties

$$\left\langle W^v{}_{\alpha\beta}(\hat{x}, \hat{t}) W^v{}_{\gamma\delta}(\tilde{x}, \tilde{t}) \right\rangle = \delta_{\alpha\gamma} \delta_{\beta\delta} \delta(\hat{x} - \tilde{x}) \delta(\hat{t} - \tilde{t}), \tag{3.81}$$

$$\left\langle W^\theta{}_{\alpha}(\hat{x}, \hat{t}) W^\theta{}_{\beta}(\tilde{x}, \tilde{t}) \right\rangle = \delta_{\alpha\beta} \delta(\hat{x} - \tilde{x}) \delta(\hat{t} - \tilde{t}). \tag{3.82}$$

It can be easily shown that expressions (3.79), (3.80) are consistent with the equations (3.77),(3.78), in fact

$$\langle \sigma_\theta W_\theta W_\theta^\dagger \sigma_\theta^\dagger \rangle = \langle \boldsymbol{\nabla}_{\hat{\mathbf{x}}} \cdot \delta \mathbf{q}\left(\hat{\mathbf{x}}, t\right) \boldsymbol{\nabla}_{\tilde{\mathbf{x}}} \cdot \delta \mathbf{q}\left(\tilde{\mathbf{x}}, t\right) \rangle = -2\mathrm{k}_B \theta_0^2 k \nabla^2 \delta\left(\hat{\mathbf{x}} - \tilde{\mathbf{x}}\right), \tag{3.83}$$

and

$$\begin{aligned} \langle \sigma_{\mathbf{v}} \mathbf{W}_v \otimes \mathbf{W}_v^\dagger \sigma_{\mathbf{v}}^\dagger \rangle &= \langle \boldsymbol{\nabla}_{\hat{\mathbf{x}}} \cdot \delta \boldsymbol{\Sigma}\left(\hat{\mathbf{x}}, t\right) \otimes \boldsymbol{\nabla}_{\tilde{\mathbf{x}}} \cdot \delta \boldsymbol{\Sigma}\left(\tilde{\mathbf{x}}, t\right) \rangle = \\ &= -2\mu_0 \mathrm{k}_B \theta_0 \left(\mathbf{I}\, \nabla^2 + \frac{1}{3} \boldsymbol{\nabla} \otimes \boldsymbol{\nabla} \right) \delta\left(\hat{\mathbf{x}} - \tilde{\mathbf{x}}\right) \end{aligned} \tag{3.84}$$

The covariance of the stochastic process corresponding to the stress is

$$\left\langle \delta \boldsymbol{\Sigma}(\hat{x}, \hat{t}) \otimes \delta \boldsymbol{\Sigma}^\dagger(\tilde{x}, \tilde{t}) \right\rangle = \mathbf{Q}^{\boldsymbol{\Sigma}} \delta(\hat{x} - \tilde{x}) \delta(\hat{t} - \tilde{t}), \tag{3.85}$$

with

$$\mathbf{Q}^{\boldsymbol{\Sigma}}{}_{\alpha\beta\nu\eta} = 2\mathrm{k}_B \theta \mu \left(\delta_{\alpha\nu}\delta_{\beta\eta} + \delta_{\alpha\eta}\delta_{\beta\nu} - \frac{2}{3}\delta_{\alpha\beta}\delta_{\nu\eta} \right) . \tag{3.86}$$

Analogously, the covariance of the fluctuating heat-flux is

$$\left\langle \delta \mathbf{q}(\hat{x}, \hat{t}) \otimes \delta \mathbf{q}^\dagger(\tilde{x}, \tilde{t}) \right\rangle = \mathbf{Q}^{\mathbf{q}} \delta(\hat{x} - \tilde{x}) \delta(\hat{t} - \tilde{t}), \tag{3.87}$$

with

$$\mathbf{Q}^{\mathbf{q}}{}_{\alpha\beta} = 2\mathrm{k}_B \theta^2 k \delta_{\alpha\beta} . \tag{3.88}$$

It is worth noting that the correlation between thermodynamic force of different tensor rank is zero, consistently with the Curie-Prigogine principle *i.e.* ($\left\langle \delta \mathbf{q}^\dagger(\tilde{x}, \tilde{t}) \otimes \delta \boldsymbol{\Sigma}(\hat{x}, \hat{t}) \right\rangle = 0$).

Finally, combining these results all together yields the Landau-Lifshitz-Navier-Stokes. The evolution of the system is driven by stochastic tensor fields, with statistical properties defined by the *fluctuation-dissipation balance* (FDB), which force the deterministic part of the operator. The ensuing

balance equations for mass, momentum and energy read

$$
\begin{aligned}
\frac{\partial \rho}{\partial t} + \boldsymbol{\nabla} \cdot (\rho \mathbf{u}) &= 0\,, \\
\frac{\partial \rho \mathbf{u}}{\partial t} + \boldsymbol{\nabla} \cdot (\rho \mathbf{u} \otimes \mathbf{u}) &= \boldsymbol{\nabla} \cdot \boldsymbol{\Sigma} + \boldsymbol{\nabla} \cdot \delta \boldsymbol{\Sigma}\,, \\
\frac{\partial E}{\partial t} + \boldsymbol{\nabla} \cdot (\mathbf{u} E) &= \boldsymbol{\nabla} \cdot (\boldsymbol{\Sigma} \cdot \mathbf{u} - \mathbf{q}) + \boldsymbol{\nabla} \cdot (\delta \boldsymbol{\Sigma} \cdot \mathbf{u} - \delta \mathbf{q})\,,
\end{aligned}
\tag{3.89}
$$

where $\mathbf{u}$ is the fluid velocity, E is the total energy density, $E = \mathcal{U} + 1/2\rho|\mathbf{u}|^2$ with $\mathcal{U}$ the internal energy density. In the momentum and energy equations, $\boldsymbol{\Sigma}$ and $\mathbf{q}$ are the classical deterministic stress tensor and energy flux, respectively, defined as

$$
\begin{aligned}
\boldsymbol{\Sigma} = \left[-p + \frac{\lambda}{2} |\boldsymbol{\nabla} \rho|^2 + \lambda \rho \boldsymbol{\nabla} \cdot (\lambda \boldsymbol{\nabla} \rho) \right] \mathbf{I} - \lambda \boldsymbol{\nabla} \rho \otimes \boldsymbol{\nabla} \rho + \\
\mu \left[(\boldsymbol{\nabla} \mathbf{u} + \boldsymbol{\nabla} \mathbf{u}^T) - \frac{2}{3} \boldsymbol{\nabla} \cdot \mathbf{u}\, \mathbf{I} \right]\,,
\end{aligned}
\tag{3.90}
$$

$$
\mathbf{q} = \lambda \rho \boldsymbol{\nabla} \rho \boldsymbol{\nabla} \cdot \mathbf{u} - k \boldsymbol{\nabla} \theta\,. \tag{3.91}
$$

3.3 FDB for wall bounded systems

Wall bounded systems differ from unbounded systems under several respects. This makes a short clarification concerning fluctuation dissipation balance for wall-bounded systems worthwhile. For the sake of simplicity the focus will be an a simple one dimensional problem –the stochastic linear diffusion problem– with generic boundary conditions. Let $c(x,t)$ be a scalar field, $\boldsymbol{L}$ a self-adjoint differential operator and $\boldsymbol{K}$ a skew-adjoint one

The dynamics of c is represented by the following stochastic equation

$$
\frac{\partial c}{\partial t} = \boldsymbol{L} c + \sqrt{2}\, \boldsymbol{K} \boldsymbol{W}\,, \tag{3.92}
$$

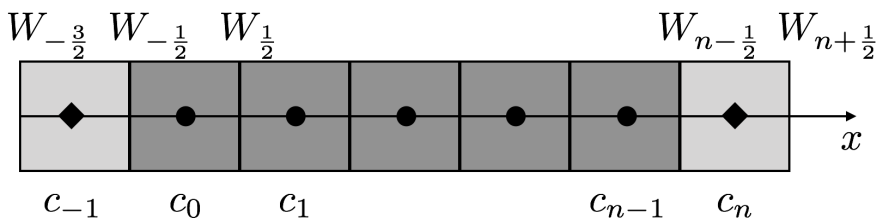

Figura 3.1: Staggered grid: scalar fields like c are defined at cell center, and vector fields like $\boldsymbol{W}$ are defined on the cell faces. The field cells are colored in dark gray, and the ghost cells in light gray. Black circles and rhombus represent the spatial collocation of the field c.

where $\boldsymbol{W}$ is a Weiner process with statistical properties to be determined by enforcing the fluctuation dissipation balance. Assuming c as a Gaussian, delta-correlated process ($\langle c(\hat{x},\hat{t})c(\tilde{x},\tilde{t})\rangle = \delta(\hat{x}-\tilde{x})\delta(\hat{t}-\tilde{t})$), the procedure previously discussed leads to (see Eq. 3.54)

$$\boldsymbol{L} = -\boldsymbol{K}\langle \boldsymbol{W}\boldsymbol{W}^{\dagger}\rangle \boldsymbol{K}^{\dagger}. \tag{3.93}$$

The model problem Eq. (3.94) is now specified assuming $\mathbf{L}$ to be the Laplacian ∇^2 operator and $\boldsymbol{K}$ the divergence operator $\boldsymbol{\nabla}\cdot$. For periodic boundary conditions Eq. 3.93 is automatically satisfied if $\langle \boldsymbol{W}\boldsymbol{W}^{\dagger}\rangle = \boldsymbol{\mathcal{U}}$, where $\boldsymbol{\mathcal{U}}$ is the identity operator on the space of fluctuations.

In presence of different boundary conditions, however, the structure of the noise $\boldsymbol{W}$ needs to be changed to preserve the balance prescribed in Eq. 3.93.

This problem has been successfully addressed by Donev et al in [52], where a simple recipe has been provided to modify the noise structure in the discretized equations preserving the fluctuation dissipation balance. Here the procedure is retraced for a staggered grid. The discrete form of Eq. 3.94 on a staggered grid reads

$$\frac{d\boldsymbol{c}}{dt} = \boldsymbol{\mathcal{L}}\boldsymbol{c} + \sqrt{2}\,\boldsymbol{\mathcal{K}}\boldsymbol{W}\,, \tag{3.94}$$

where $\boldsymbol{c} = (c_0, c_1, \ldots, c_{n-1})$ is a n-dimensional vector, collecting the n values of the scalar field $c(x,t)$, $\boldsymbol{W} = (W_{-1/2}, W_{1/2}, \ldots, W_{n-1/2})$ is the $(n+1)$-dimensional vector of the the stochastic process $\boldsymbol{W}(x,t)$. $\boldsymbol{\mathcal{L}}$ and $\boldsymbol{\mathcal{K}}$ are the discrete versions of Laplacian and divergence operators. In particular, for a staggered grid $\boldsymbol{\mathcal{K}}$ is represented by a rectangular $(n \times n+1)$ matrix defined as

$$\boldsymbol{\mathcal{K}} = \Delta x^{-1} \begin{pmatrix} -1 & 1 & 0 & \ldots \\ 0 & -1 & 1 & \ldots \\ 0 & 0 & -1 & \ldots \\ \vdots & \vdots & \vdots & \ddots \\ \ldots & \ldots & -1 & 1 \end{pmatrix}, \tag{3.95}$$

and the discrete laplacian $\boldsymbol{\mathcal{L}}$ is represented by a square $(n \times n)$ matrix defined as

$$\boldsymbol{\mathcal{L}} = \Delta x^{-2} \begin{pmatrix} \alpha - 2 & 1 & 0 & \ldots \\ 1 & -2 & 1 & \ldots \\ 0 & 1 & -2 & \ldots \\ \vdots & \vdots & \vdots & \ddots \\ \ldots & \ldots & 1 & \alpha - 2 \end{pmatrix}, \tag{3.96}$$

where Δx is the constant grid space, and α is an integer number depending of the boundary conditions, i.e. $\alpha = 1$ for Neumann BC and $\alpha = -1$ for Dirichlet ones. It is important to stress here that the adjoint of the discrete divergence operator is the discrete gradient. By taking the product of discrete divergence and discrete gradient it is clear that the discrete Laplacian is recovered, at least at all internal grid nodes.

Let us come to the discrete version of the fluctuation dissipation balance in Eq. (3.93) which reads

$$\boldsymbol{\mathcal{L}} = -\boldsymbol{\mathcal{K}} \langle \boldsymbol{W} \boldsymbol{W}^T \rangle \boldsymbol{\mathcal{K}}^T . \tag{3.97}$$

Evidently, assuming $\langle \boldsymbol{W}\boldsymbol{W}^T \rangle$ to coincide with the identity matrix, as expected from a delta correlated process, shows that the discrete FDB is satisfied at internal boundary points. The correlations at boundary points need however to be modified. An additional degree of freedom, β in the following equation, can be added to accomodate the discrete FDB, introducing a generalised form of noise correlation

$$\langle \boldsymbol{W}\boldsymbol{W}^T \rangle = \begin{pmatrix} \beta & 0 & 0 & \dots \\ 0 & 1 & 0 & \dots \\ 0 & 0 & 1 & \dots \\ \vdots & \vdots & \vdots & \ddots \\ \dots & \dots & 0 & \beta \end{pmatrix} . \tag{3.98}$$

By multiplying the matrix in Eq. (3.97) one obtains $\beta = 1-\alpha$. This procedure shows that, by modifying the nature of the noise one can have the discrete FDB satisfied also in presence of non trivial boundary conditions. As a comment, it could be stressed that this procedure is significantly less elegant that the more clean approach available for bulk systems, since it lacks full generality, being based on a specific discrete form of the equations. However we are working on a general approach to address the fluctuation dissipation balance for LLNS equations with capillarity for wall bounded systems.

3.4 Spherical Formulation of Fluctuating Hydrodynamics Equations and its application to nucleation process

This section is devoted to the spherical formulation of the LLNS equations, in particular is presented a procedure developed in collaboration with Davide Cocco during his master thesis, I was Co-Advisor, and it is adapted from a paper in preparation. This approach provides an equivalent noise term

forcing the momentum balance equation. Such simplified model could be particular useful when dealing with thermally activated processes since it provides a set stochastic equations for the fields as a function of the reaction coordinate (the radius of the cluster of the new phase).

Spherical symmetry is a reasonable assumption when searching for simplified models. For instance it is always assumed in CNT, see Introduction and recent work by Lutsko where a systematic hierarchy of increasingly simplified nucleation models is derived from a general theory based on DFT [94]. Quite naturally the reaction coordinate representing the progress of the phase transition in a spherically symmetric model can be selected to be the radius of the nucleus (see Lutsko [93] for discussion on the topic and the alternative solution of assuming the mass of the nucleus as the most appropriate reaction coordinate). A reduced model that takes into account only "averaged" information as a function of the bubble radius, is expected to be able able to capture the main features of the nucleation process and the subsequent bubble evolution, at a substantially cheaper computational cost, (see however the paper by Valeriani at al. [146], showing from molecular dynamics supplemented with suitable rare event techniques that the shape of actual cavitation nuclei can hardly be classified as spherical.)

Concerning stochastic systems, the assumption of spherical symmetry, seems to be quite strong, since the random flux breaks this symmetry of the system. However stochastic spherical models, like e.g. stochastic Rayleigh-Plesset equation, have been already considered to address nucleation [90, 101].

As anticipated, a more systematic approach, was developed by Lutsko in [93], where the dynamical equations have been averaged on a spherical

shell, to directly obtain an evolution equation for the order parameter of the system. Here as a preliminary study, the spherical symmetry is taken as an assumption.

Let us start from the capillary Navier-Stokes equations in spherical symmetry, reported here for the isothermal case, for the sake of simplicity

$$\frac{\partial \rho}{\partial t} + \frac{1}{r^2}\frac{\partial}{\partial r}\left(r^2 \mathrm{p}\right) = 0, \tag{3.99}$$

$$\frac{\partial \mathrm{p}}{\partial t} + \frac{1}{r^2}\frac{\partial}{\partial r}\left(r^2 \mathrm{p} u\right) = \boldsymbol{\nabla}^S \cdot \boldsymbol{\Sigma}^S \cdot \hat{\mathbf{r}} + \boldsymbol{\nabla}^S \cdot \delta\boldsymbol{\Sigma}^S \cdot \hat{\mathbf{r}}\,, \tag{3.100}$$

where $u(r,t)$ is the radial velocity, $\mathrm{p}(r,t) = \rho(r,t)u(r,t)$ the fluid momentum density, $\boldsymbol{\Sigma}^S = -p_0\mathbf{I} + \tau^S$ is the stress tensor and $\hat{\mathbf{r}}$ the radial unit vector. The superscript S denotes that spherical polar base coordinates are used. In order to express the tensor appearing in RHS of Eq. (3.100) (known in the Cartesian representation in the basis $\mathcal{B} = \{\mathbf{e}_x, \mathbf{e}_y, \mathbf{e}_z\}$, so far) into the new base spanned by the spherical-polar basis $\mathcal{B}^S = \{\mathbf{e}_r, \mathbf{e}_\theta, \mathbf{e}_\varphi\}$, we used the orthogonal transformations

$$\Sigma^S_{pq} = B^{\mathcal{B}^S\to\mathcal{B}}_{pk} B^{\mathcal{B}^S\to\mathcal{B}}_{ql} \Sigma_{kl} \qquad \delta\Sigma^S_{pq} = B^{\mathcal{B}^S\to\mathcal{B}}_{pk} B^{\mathcal{B}^S\to\mathcal{B}}_{ql}\, \delta\Sigma_{kl} \qquad , \tag{3.101}$$

where the transformation matrix $\mathbf{B}^{\mathcal{B}^S\to\mathcal{B}}$ is an orthogonal (3×3) matrix, whose entries are

$$\mathbf{B}_{\mathcal{B}^S\to\mathcal{B}} = \begin{pmatrix} \sin\theta\cos\varphi & \sin\theta\sin\varphi & \cos\theta \\ \cos\theta\cos\varphi & \cos\theta\sin\varphi & -\sin\theta \\ -\sin\phi & \cos\phi & 0 \end{pmatrix}. \tag{3.102}$$

so that the coordinate transformation is accomplished by rotating the Cartesian basis, i.e. $B^{\mathcal{B}^S\to\mathcal{B}}_{ik} B^{\mathcal{B}^S\to\mathcal{B}}_{jk} = \delta_{ij}$. The above transformation lead to the following expressions for the non vanishing components of the deterministic stress tensor

$$\tau^S_{rr} = \lambda\left[-\frac{1}{2}\left(\frac{\partial\rho}{\partial r}\right)^2 + \frac{\rho}{r^2}\frac{\partial}{\partial r}\left(r^2\frac{\partial\rho}{\partial r}\right)\right] + 2\mu\left[\frac{\partial u}{\partial r} - \frac{1}{3r^2}\left(r^2 u\right)\right], \tag{3.103}$$

$$\tau^S_{\theta\theta} = \lambda \left[\frac{1}{2} \left(\frac{\partial \rho}{\partial r} \right)^2 + \frac{\rho}{r^2} \frac{\partial}{\partial r} \left(r^2 \frac{\partial \rho}{\partial r} \right) \right] + 2\mu \left[\frac{u}{r} - \frac{1}{3r^2} \left(r^2 u \right) \right] , \tag{3.104}$$

and, the radial component (the only non-vanishing one under spherical symmetry) of its divergence of the fluxes reads

$$\boldsymbol{\nabla}^S \cdot \boldsymbol{\Sigma}^S \cdot \hat{\mathbf{r}} = -\frac{\partial p_0}{\partial r} + \frac{1}{r^2} \frac{\partial}{\partial r} \left(r^2 \tau_{rr} \right) - \frac{2\tau_{\theta\theta}}{r} . \tag{3.105}$$

Analogously, the stochastic contributions reduce to the three diagonal terms $\delta\Sigma_{rr}$, $\delta\Sigma_{\theta\theta}$, $\delta\Sigma_{\phi\phi}$, such that the divergence on the stochastic stress is

$$\boldsymbol{\nabla}^S \cdot \delta\boldsymbol{\Sigma}^S \cdot \hat{\mathbf{r}} = \frac{1}{r^2} \frac{\partial}{\partial r} \left(r^2 \delta\Sigma_{rr} \right) - \frac{\delta\Sigma_{\theta\theta}}{r} - \frac{\delta\Sigma_{\varphi\varphi}}{r} . \tag{3.106}$$

The correlations in the spherical representation are deduced from those known in Cartesian coordinates, see Eq. (3.86), by enforcing transformation rules (3.101),

$$\langle \delta\Sigma^S_{mn}(\hat{x}, \hat{t}) \delta\Sigma^S_{pq}(\tilde{x}, \tilde{t}) \rangle = \mathcal{I} \left(\delta_{mp}\delta_{nq} + \delta_{mq}\delta_{np} - \frac{2}{3}\delta_{mn}\delta_{pq} \right) , \tag{3.107}$$

with $\mathcal{I} = 2\mu k_B \theta \delta(\hat{x} - \tilde{x}) \delta(\hat{t} - \tilde{t})$, and $m, n, p, q = r, \theta, \varphi$. Explicitly, the relevant correlations are

$$\langle \delta\Sigma^S_{rr}(\hat{x}, \hat{t}) \delta\Sigma^S_{rr}(\tilde{x}, \tilde{t}) \rangle = \langle \delta\Sigma^S_{\theta\theta}(\hat{x}, \hat{t}) \delta\Sigma^S_{\theta\theta}(\tilde{x}, \tilde{t}) \rangle = \langle \delta\Sigma^S_{\varphi\varphi}(\hat{x}, \hat{t}) \delta\Sigma^S_{\varphi\varphi}(\tilde{x}, \tilde{t}) \rangle = \frac{4}{3}\mathcal{I} , \tag{3.108}$$

$$\langle \delta\Sigma^S_{rr}(\hat{x}, \hat{t}) \delta\Sigma^S_{\theta\theta}(\tilde{x}, \tilde{t}) \rangle = \langle \delta\Sigma^S_{rr}(\hat{x}, \hat{t}) \delta\Sigma^S_{\varphi\varphi}(\tilde{x}, \tilde{t}) \rangle = \langle \delta\Sigma^S_{\theta\theta}(\hat{x}, \hat{t}) \delta\Sigma^S_{\varphi\varphi}(\tilde{x}, \tilde{t}) \rangle = -\frac{2}{3}\mathcal{I} . \tag{3.109}$$

The procedure to be followed to obtain the stochastic equation for the spherically symmetric system consists in the integration of the Eqs. (3.99, 3.100) on a sphere of radius R to obtain a new set of stochastic processes, whose stochastic contribution will be modified by defining an equivalent noise term.

In the light of the above procedure mass conservation equation Eq. (3.99) reads

$$\frac{\partial}{\partial t}\int_{r<R}\rho(r,t)dV+\int_{r<R}\frac{1}{r^2}\frac{\partial}{\partial r}\left(r^2\mathrm{p}(r,t)\right)dV=0\,, \tag{3.110}$$

leading to

$$\frac{\partial\mathcal{M}}{\partial t}\left(R,t\right)+4\pi R^2\mathrm{p}\left(R,t\right)=0\,, \tag{3.111}$$

where $\mathcal{M}(R,t)$ is the fluid mass inside the sphere of radius R.

Concerning the momentum equation, the same procedure applied to Eq. (3.100) leads to

$$\frac{\partial\mathcal{P}}{\partial t}\left(R,t\right)+4\pi R^2\mathrm{p}\left(R,t\right)u\left(R,t\right)=\Gamma\left(R,t\right)+\delta\Gamma\left(R,t\right)\,, \tag{3.112}$$

where $\mathcal{P}(R,t)$ is the total fluid momentum inside the sphere of radius R. The two terms on the RHS of are

$$\Gamma\left(R,t\right)=\int_{r<R}\boldsymbol{\nabla}^S\cdot\boldsymbol{\Sigma}^S\cdot\hat{\mathbf{r}}dV\,,\qquad \delta\Gamma\left(R,t\right)=\int_{r<R}\boldsymbol{\nabla}^S\cdot\delta\boldsymbol{\Sigma}^S\cdot\hat{\mathbf{r}}dV\,, \tag{3.113}$$

respectively.

Let us focus on the stochastic term $\delta\Gamma$. Since the angular terms $\delta\Sigma_{\theta\theta}$ and $\delta\Sigma_{\varphi\varphi}$ are two Gaussian processes with the correlations given by Eq.s (3.108, 3.109), it is useful to define the new Gaussian process $\delta\Sigma_{\phi\phi}=\delta\Sigma_{\theta\theta}+\delta\Sigma_{\varphi\varphi}$, so that $\langle\delta\Sigma_{\phi\phi}(\hat{x},\hat{t})\delta\Sigma_{\phi\phi}(\tilde{x},\tilde{t})\rangle=4/3\mathcal{I}$, thus the stochastic force is decomposed as

$$\delta\Gamma\left(R,t\right)=\int_{r<R}\frac{1}{r^2}\frac{\partial}{\partial r}\left(r^2\delta\Sigma_{rr}\right)dV-\int_{r<R}\frac{\delta\Sigma_{\phi\phi}}{r}dV=\delta\Gamma_r\left(R,t\right)+\delta\Gamma_\phi\left(R,t\right)\,. \tag{3.114}$$

The simplest way to proceed is by introducing a stochastic process equivalent to process Eq. (3.114). To this purpose we need the correlations of

$\delta\Gamma$,

$$\begin{aligned}\langle\delta\Gamma(\hat{R},\hat{t})\delta\Gamma(\tilde{R},\tilde{t})\rangle &= \int_{\hat{r}<\hat{R}}\int_{\tilde{r}<\tilde{R}} d\hat{V}d\tilde{V}\frac{1}{\hat{r}^2}\frac{\partial}{\partial\hat{r}}\left(\hat{r}^2\delta\Sigma_{rr}(\hat{r},\hat{t})\right)\frac{1}{\tilde{r}^2}\frac{\partial}{\partial\tilde{r}}\left(\tilde{r}^2\delta\Sigma_{rr}(\tilde{r},\tilde{t})\right)+\\ &- 2\int_{\hat{r}<\hat{R}}\int_{\tilde{r}<\tilde{R}} d\hat{V}d\tilde{V}\frac{1}{\hat{r}^2}\frac{\partial}{\partial\hat{r}}\left(\hat{r}^2\delta\Sigma_{rr}(\hat{r},\hat{t})\right)\frac{1}{\tilde{r}}\delta\Sigma_{\phi\phi}(\tilde{r},\tilde{t})+\\ &+ \int_{\hat{r}<\hat{R}}\int_{\tilde{r}<\tilde{R}} d\hat{V}d\tilde{V}\frac{1}{\hat{r}}\delta\Sigma_{\phi\phi}(\hat{r},\hat{t})\frac{1}{\tilde{r}}\delta\Sigma_{\phi\phi}(\tilde{r},\tilde{t})\ . \end{aligned} \tag{3.115}$$

After some algebra one finds

$$\begin{aligned}\langle\delta\Gamma(\hat{R},\hat{t})\delta\Gamma(\tilde{R},\tilde{t})\rangle &= \\ &= \frac{16\pi}{3}\mathcal{Z}\left(\hat{R}^2\delta(\hat{R}-\tilde{R})+\int_0^{\hat{R}}\int_0^{\tilde{R}}\delta(\hat{r}-\tilde{r})d\hat{r}d\tilde{r}+2\int_0^{\tilde{R}}\hat{R}\delta(\hat{R}-\tilde{r})d\tilde{r}\right),\end{aligned} \tag{3.116}$$

with $\mathcal{Z}=2\mu k_B\theta\delta(\hat{t}-\tilde{t})$. It is now easy to show that the process

$$\delta\Gamma^*(R,t)=\int_0^R\frac{\partial}{\partial r}\left(\alpha(r)\xi(r,t)\right)dr+\int_0^R\beta\xi(r,t)dr\,, \tag{3.117}$$

expressed in terms of the Weiner process ξ, $\langle\xi(\hat{r},\hat{t})\xi(\tilde{r},\tilde{t})\rangle=\delta(\hat{r}-\tilde{r})\delta(\hat{t}-\tilde{t})$, is statistically equivalent to $\delta\Gamma$ in Eq. (3.112), provided $\beta=(32/3\pi k_B\mu\theta)$, $\alpha=R\beta$.

To summarise, the evolution equations for the mass and momentum contained in a sphere of generic radius R can be written as

$$\frac{\partial\mathcal{M}(R,t)}{\partial t}+4\pi R^2\mathrm{p}(R,t)=0\,, \tag{3.118}$$

$$\frac{\partial\mathcal{P}(R,t)}{\partial t}+4\pi R^2\mathrm{p}(R,t)\,u(R,t)=\Gamma(R,t)+\delta\Gamma^*(R,t)\ . \tag{3.119}$$

Equivalently, by taking the R-derivative of both equations, a corresponding local form is obtained as

$$\frac{\partial\rho}{\partial t}+\frac{1}{R^2}\frac{\partial}{\partial R}\left(R^2\mathrm{p}\right)=0\,, \tag{3.120}$$

$$\frac{\partial \mathrm{p}}{\partial t}+\frac{1}{R^2}\frac{\partial}{\partial R}\left(R^2\mathrm{p}u\right)=\frac{1}{R^2}\frac{\partial}{\partial R}\left(R^2\Sigma_{rr}\right)-2\frac{\tau_{\theta\theta}}{R}+\frac{1}{4\pi R^2}\left[\frac{\partial}{\partial R}\left(\alpha(R)\xi(R,t)\right)+\beta\xi(R,t)\right]. \tag{3.121}$$

Eqs. (3.120, 3.122) are the spherically symmetric form of the LLNS equations in spherical symmetry. Their main advantage is that only one stochastic process $\xi(r,t)$ is involved (clearly the FDB is already satisfied). The model allows for the numerical modelling of spherical cluster nucleation – starting from the very appearance of the phase formation up to the consequent hydrodynamic motion – at very cheap computational cost, in comparison with the three dimensional case.

The model is validated by numerically evaluating the correlations of the radial velocity field and comparing them with their theoretical predictions. The general procedure needed to obtain the correlations will be explained in detail in Chapter 4, where the effect of numerical discretisation is fully taken into account. The procedure is based on expressing the probability density function in terms of the entropy functional, Section 3, and Eq. (4.20) for further detail. This leads to

$$\langle\delta u(R)\delta u(R)\rangle=\frac{k_B\theta_0}{4\pi\rho_0\Delta r}R^{-2}\,, \tag{3.122}$$

with ρ_0 the mean density, Δr the step of the numerical grid, and θ_0 the temperature. Figure 3.2 compares the theoretical prediction for the discrete model with the numerical simulation focusing on the velocity variance. The agreement between theory and numerics is rather good, confirming that the FDB is preserved.

After validation, the model can be exploited to deal with vapour bubble nucleation. Starting from the metastable state (uniform liquid) the evolution of the system is followed by numerically integrating Eqs. (3.120, 3.122) up

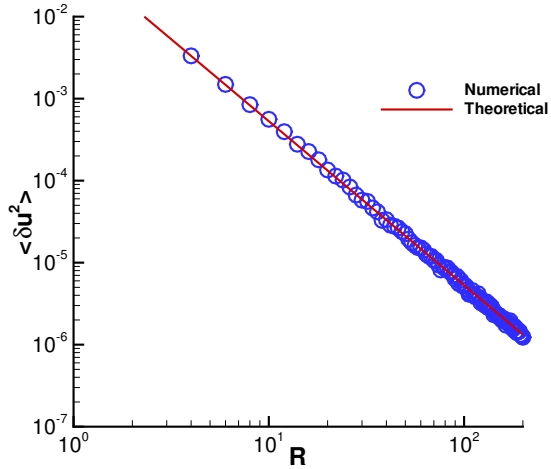

Figura 3.2: Velocity variance as a function of the radius R, the red line represent the theoretical prediction and the blue circles the numerical calculation.

to the eventual stable state (specifically, a vapour bubble surrounded by liquid in a confined system). The density profiles (broken lines) are plotted in Fig.3.3 for different time instants along the transition up to the final equilibrium state (black solid line). As explained in Chapter 2, the most probable transition path, (under the assumption of over-damped regime), and the critical state in particular, can be evaluated in parallel using the string method. This provides access to the critical density profile and the energy barrier (see Fig. 2.4 and Fig. 2.5 in Chapter 2). The red line in the figure is the critical density profile from the string. In the stochastic system, starting from the homogeneous liquid phase (the dotted dark green line), thermal fluctuations lead to the formation of a vapour nucleus. In proximity of the nucleation time –roughly $t = 30000$ for the specific case reported in Fig. 3.3 – the density profile obtained by time integration of the stochastic

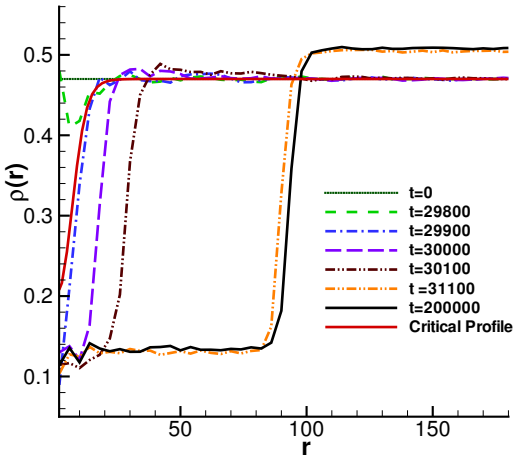

Figura 3.3: Density profiles as a function of radial distance r, the critical profiles (red line) is evaluated with the string method. The other ones represent the numerical results.

system matches quite well the critical profile provided by the string. In these thermodynamic condition the process conform precisely to the notion of a thermally activated transition. Indeed, reaching the activated (transition) state requires quite some time. After the critical state has been reached the successive dynamics is comparatively much faster, requiring a dimensionless time of 10^3 to be completed as compared to the tenfold time, 10^4, required to form the critical nucleus.

The simulations allow to evaluate the mean first passage time $\langle\tau\rangle$, from the metastable(uniform liquid) to the critical state (when the critical density profile is reached). Numerical results are compared with the theoretical prediction of Kramers theory, showing an agreement, in particular far from the spinodal limit, that can be considered quite reasonable, if the simplifying assumption of theory are considered. In order to be as fair as possible in

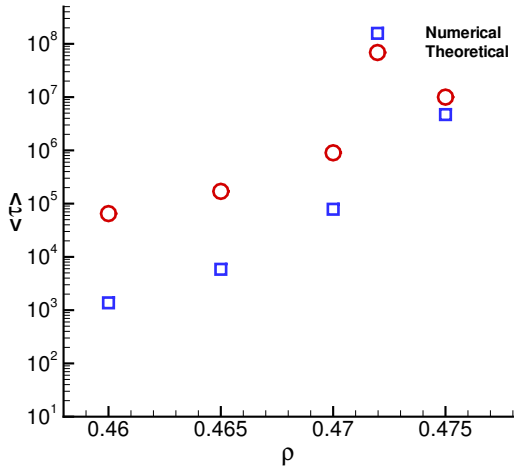

Figura 3.4: Mean first passage time for different thermodynamic conditions, the blue squares represent numerical calculation and the red circles theoretical prediction.

the comparison, Kramers theory (summarised in Chapter 1) has been used in the context of the diffuse interface approach. This boils down to using the potential (free-energy) obtained from the string method, $\Delta\Omega(R) = \Delta\Omega_s(R)$ (see Fig. 2.5), as energy landscape in the theory. The integral providing Kramers first passage time,

$$\langle\tau\rangle = \int_{\cup} \exp\left(-\frac{\Delta\Omega(R)}{k_B\theta}\right) dR \int_{\cap} \frac{1}{D} \exp\left(\frac{\Delta\Omega(R)}{k_B\theta}\right) dR\,, \tag{3.123}$$

is numerically evaluated. In order to do so, a further modelling assumption is needed to estimate the diffusion coefficient. In the present case, the diffusion coefficient, $D^* = k_B\theta/16\mu\pi R^*$, has been estimated in correspondence with the critical state following Menzl, et al in [101], i.e. by enforcing the fluctuation dissipation balance on the stochastic over-damped Rayleigh-Plesset equation.

Capitolo 4

Numerical Analysis of the LLNS Equations with capillarity

This Chapter is devoted to the numerical analysis of stochastic partial differential equations arising from the diffuse interface model endowed with thermal fluctuations. In particular a general overview on the deterministic part of the equations is given, stressing the numerical challenges characterising the proposed approach to multiphase flows. Subsequently the stochastic contribution will be addressed in detail, focusing on the preservation of the statistical properties of the system in the discretised form of the equations. The validation of the numerical algorithm is performed by comparing theoretical and numerical equilibrium properties, e.g the static structure factor and the static probability distribution, of the macroscopic field.

4.1 The deterministic equations

The system of equations to be solved (2.29 – 2.31) must to be coupled with a suitable equation of state. The van der Waals EoS has been exploited to study the collapse of cavitation nanobubbles, since it qualitatively well

represents the behavior of the most common fluids. Conversely, an EoS recovering the physical properties of a Lennard Jones fluid has been used in the bubble nucleation simulations, in order to directly compare the results with Molecular Dynamics simulations available from literature.

The numerical solution of the system of equations (2.29 – 2.31) is challenging due to a combination of different physical phenomena, which all require a different specialized numerical techniques. Apart from the extremely thin liquid-vapor interface that requires a high numerical resolution, the system supports i) the emission and the propagation of shock waves; ii) viscous diffusion and capillary dispersion; iii) phase change and transition to and from supercritical conditions.

4.1.1 The different mathematical features of the equations

In the system of the equations (2.29 – 2.31) both hyperbolic features (Euler equations) and diffusive and dispersive behavior induced by viscosity and capillarity (Navier-Stokes-Kortweeg equations) are present. Moreover, at least for the van der Waals equation of state, a region of the thermodynamic phase space exists where $\partial p_0/\partial\rho|_\eta < 0$. As well known, in ordinary conditions, this derivative defines the square of the sound speed, implying that where $c^2 < 0$ hyperbolic behavior changes into parabolic, see Fig. 4.1 for an explanatory diagram. From a numerical point of view, compressibility and shock wave propagation would suggest the adoption of specialized shock-capturing methods, like the Essentially Non Oscillatory schemes, or their Weighted WENO extension [130]. Unfortunately these schemes fail when the system explores a thermodynamic unstable state (certainly it happens in a two pha-

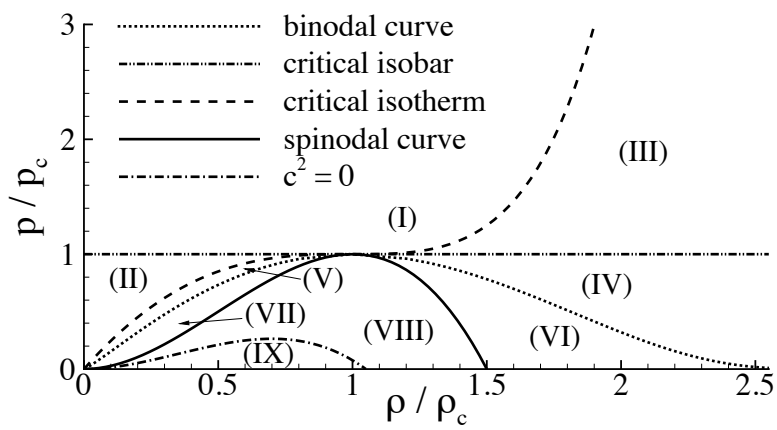

Figura 4.1: Phase diagram in the $p - \rho$ plane. In the zone (I) where $p > p_c$ and $\theta > \theta_c$ the fluid is in supercritical state. Zone (II), characterized by $p < p_c$ but $\theta > \theta_c$, is the gas region. Conversely, zone (III) where $p > p_c$ but $\theta < \theta_c$ is the compressible-liquid region. In zone (IV) and (V) the fluid is in liquid or vapor state, respectively. Under the binodal curve, which represent the saturation conditions, we find zones (VI) and (VII) of metastable liquid and metastable vapor state, respectively. The spinodal curve, defined as $\partial p/\partial\rho|_\theta = 0$, separates the metastable regions from the unstable region (VIII). Finally, in subset of the unstable region, zone (IX), $c^2 = \partial p/\partial\rho|_\eta < 0$, i.e. the sound speed becomes imaginary.

se system due to the diffuse interface). The strategy conceived to deal with this complex mathematical structure, is based on two basic ingredients: 1) Identification of the hyperbolic part of the operator and its extension to the parabolic region where $c^2 < 0$; 2) Operator splitting into hyperbolic and non-hyperbolic part. For convenience, these two ingredients will be discussed in revers order.

4.1.2 Operator splitting strategy

As discussed in Chapter 2, the state of the system is identified by three basic, conserved fields, namely mass, momentum and total energy density, to be collectively addressed here as the state vector $\mathbf{U}(\mathbf{x}, t) = (\rho, \rho\mathbf{u}, E)^T$. Formally system (2.29 – 2.31) can be written as

$$\frac{\partial \mathbf{U}}{\partial t} = \mathcal{N}\left[\mathbf{U}\right] = \mathcal{H}_e\left[\mathbf{U}\right] + \mathcal{P}\left[\mathbf{U}\right],$$

where $\mathcal{H}_e$ is the extension to the whole phase space of the hyperbolic part of the operator and $\mathcal{P} = \mathcal{N} - \mathcal{H}_e$ is defined accordingly. The explicit expressions of the two operators $\mathcal{H}_e$ and $\mathcal{P}$ will be provided below. After the operator is split as explained, the state vector can be evolved in time exploiting a solution strategy in terms of Strang splitting [135]. Denoting $F_{\mathcal{N}}(t)$ the full propagator such that

$$\mathbf{U}(t + \tau) = F_{\mathcal{N}}(\tau)\mathbf{U}(t),$$

for small τ we can approximate

$$F_{\mathcal{N}}(\tau) = F_{\mathcal{P}}(\tau/4)F_{\mathcal{H}_e}(\tau/2)F_{\mathcal{P}}(\tau/4)$$

where $F_{\mathcal{P}}(\tau)$ is the propagator of system

$$\frac{\partial \mathbf{U}}{\partial t} = \mathcal{P}\left[\mathbf{U}\right],$$

while $F_{\mathcal{H}_e}(\tau)$ is defined by

$$\frac{\partial \mathbf{U}}{\partial t} = \mathcal{H}_e\left[\mathbf{U}\right] \ .$$

Strang splitting allows for using different algorithms, specialized for each component of the system. The algorithms we selected are a third order WENO [130] scheme for the hyperbolic part and a second order accurate, centered finite difference scheme for the parabolic part. We performed the time integration of the hyperbolic part with a full explicit, third-order TVD Runge-Kutta scheme. The parabolic operator is advanced in time with a mixed, implicit-explicit scheme, where the linear terms (viscous stress and heat flux) are treated implicitly in order to increase the stability limit. In the region of phase space where the sound speed is well defined, the hyperbolic step is

$$\frac{\partial \rho}{\partial t} = -\boldsymbol{\nabla} \cdot (\rho \mathbf{u}) \ , \tag{4.1}$$

$$\frac{\partial \rho \mathbf{u}}{\partial t} = -\boldsymbol{\nabla} \cdot (\rho \mathbf{u} \otimes \mathbf{u} + p\mathbf{I}) \ , \tag{4.2}$$

$$\frac{\partial E_0}{\partial t} = -\boldsymbol{\nabla} \cdot \left[\mathbf{u}\left(E_0 + p\right)\right] - \frac{\partial \left(\rho \mathcal{U}_c\right)}{\partial t} \ . \tag{4.3}$$

where $E_0 = \rho\left(\mathcal{U}_0 + 1/2|\mathbf{u}|^2\right)$ is the total energy density deprived of the capillary contribution, which reproduces the classical Euler equation. The capillary contribution to the energy $(\rho \mathcal{U}_c)$ is treated as an explicit forcing term depending on the density gradient. Here, as already stated, a van der Waals fluid is assumed in the equations of state. The parabolic part of the operator

corresponds to

$$\frac{\partial \rho}{\partial t} = 0\,, \tag{4.4}$$

$$\frac{\partial \rho \mathbf{u}}{\partial t} = \boldsymbol{\nabla} \cdot \tau\,, \tag{4.5}$$

$$\frac{\partial E}{\partial t} = \boldsymbol{\nabla} \cdot \left(-\frac{1}{2}\lambda |\boldsymbol{\nabla}\rho|^2 \mathbf{u} + \tau \cdot \mathbf{u} - \mathbf{q} \right)\,, \tag{4.6}$$

where the capillary contribution (first term in the right hand side of the equation for E) has been included in the energy flux. In the coexistence region below the binodal (or coexistence curve, Fig. 4.1), which contains the region where $c^2 < 0$, a Maxwell-like rule is used. Using the additivity of specific volume and entropy, mass density and specific entropy can be written as

$$\frac{1}{\rho} = (1-\alpha)\frac{1}{\rho_V(\theta)} + \alpha\frac{1}{\rho_L(\theta)}$$
$$\eta_{sat} = (1-\alpha)\eta_V(\theta) + \alpha\eta_L(\theta)$$

where subscript L and V denote pure liquid and vapor at the given temperature. The above relations can be inverted to yield

$$\alpha = \alpha(\rho, \eta_{sat})$$
$$\theta = \theta(\rho, \eta_{sat})\ .$$

For the mixture of vapor and liquid, the saturation pressure depends only on temperature, such that

$$p_{sat} = p_{sat}(\theta) = p_{sat}(\rho, \eta_{sat})\ .$$

This expression allows to extract the sound speed as

$$c_{sat}^2 = \left.\frac{\partial p_{sat}}{\partial \rho}\right|_{\eta_{sat}} > 0$$

whose final expression is

$$c_{sat}^2 = \frac{\left(\frac{\mathrm{d}p_{sat}}{\mathrm{d}\theta}\right)^2}{\rho^2\left(\frac{d\eta_L}{d\theta} + \frac{1}{\rho_L^2}\frac{dp_{sat}}{d\theta}\frac{d\rho_L}{d\theta} - \frac{\rho-\rho_L}{\rho\rho_L}\frac{d^2p_{sat}}{d\theta^2}\right)} \,. \tag{4.7}$$

The interested reader is referred to [102] for details on the thermodynamic derivation of the sound speed for the mixture.

In fact, the actual pressure differs from the saturation pressure,

$$p = p(\theta,\rho) = p_{sat}(\theta) + \delta p(\theta,\rho)\,,$$

to the extent that $c^2 = \partial p/\partial\rho|_\eta$ may become negative. We stress however that $c_{sat}^2 > 0$, thereby allowing to identify the hyperbolic part of the evolution operator in the region below the binodal (which includes the region where $c^2 < 0$).

Concerning the energy density, we consistently address the energy of the liquid-vapor mixture,

$$E_{sat} = 1/2\rho|\mathbf{u}|^2 + \rho\left[(1-\alpha)\mathcal{U}_V + \alpha\mathcal{U}_L\right] \,.$$

Again, the actual energy is

$$E = E_{sat} + \delta E \,.$$

With the above position, the split system in the region below the binodal reads

$$\frac{\partial\rho}{\partial t} = -\boldsymbol{\nabla}\cdot(\rho\mathbf{u})\,, \tag{4.8}$$

$$\frac{\partial\rho\mathbf{u}}{\partial t} = -\boldsymbol{\nabla}\cdot(\rho\mathbf{u}\otimes\mathbf{u} + p_{sat}\mathbf{I})\,, \tag{4.9}$$

$$\frac{\partial E_{sat}}{\partial t} = -\boldsymbol{\nabla}\cdot\left[\boldsymbol{\nabla}u\left(E_{sat}+p_{sat}\right)\right] - \frac{\partial\delta E}{\partial t}\,, \tag{4.10}$$

for the hyperbolic part and

$$\frac{\partial \rho}{\partial t} = 0\,, \tag{4.11}$$

$$\frac{\partial \rho \mathbf{u}}{\partial t} = -\boldsymbol{\nabla}\delta p + \boldsymbol{\nabla}\cdot\tau\,, \tag{4.12}$$

$$\frac{\partial E}{\partial t} = \boldsymbol{\nabla}\cdot\left[-\mathbf{u}\left(\delta E + \delta p\right) + \tau\cdot\mathbf{u} - \mathbf{q}\right]\,, \tag{4.13}$$

for the parabolic part, respectively.

We stress that the definitions of the operators given separately for the two regions of phase space join continuously at the binodal curve.

4.2 The stochastic equations

The system of equations (3.89) has been discretized in the spirit of the method of lines, consisting in two stages: the first stage concerns the spatial discretization, the second one is focused on the temporal integrator. Concerning the spatial discretization it is worth stressing that the different physical phenomena described by the LLNS system ask for specialized numerical techniques. A crucial point to be addressed is the correct reproduction of the system statistical properties, in particular the adopted numerical scheme need to be consistent with the fluctuation-dissipation balance. A necessary condition for this restriction is that the mathematical properties of the relevant continuum differential operators are conserved in the discrete formulation [8]. Eqs. (3.89) have been discretized on a equi-spaced staggered grid, following [54]. Due to staggering, scalar fields, like density, e.g., are located at the cell center while components of vector fields in a given direction are located at the center of the perpendicular face (see Fig.3.1 in Chapter 3 for details).

4.2.1 Thermal fluctuations for a capillary fluid at equilibrium in a discrete system

Before discussing the numerical results, it is worth remembering the statistical properties of fluctuations in equilibrium state, that will be used as benchmark for the numerical validation. In Chapter 3 the Einstein theory of fluctuations has been recalled. Here the main results are shortly reported for the reader convenience. By assuming that the fluid is very close to equilibrium and the fluctuations are small with respect to the mean value, the entropy functional can be approximated by a quadratic form in the fluctuating fields,

$$\Delta S_c \simeq -\frac{1}{2}\int_V dV \frac{c_{T0}^2}{\theta_0\rho_0}\delta\rho^2 - \frac{\lambda}{\theta_0}\delta\rho\left(\nabla^2\delta\rho\right) + \frac{\rho_0}{\theta_0}\delta\mathbf{u}\cdot\delta\mathbf{u} + \frac{\rho_0 c_{v0}}{\theta_0^2}\delta\theta^2 \ . \quad (4.14)$$

The probability distribution functional for the fluctuating fields $\mathbf{\Delta} = (\delta\rho, \delta\mathbf{u}, \delta\theta)$ is

$$P_{eq}\left[\mathbf{\Delta}\right] = \frac{1}{Z}\exp\left(\frac{\Delta S_c}{k_B}\right) \ , \quad (4.15)$$

hence the correlation tensor takes the fosllowing quadratic form

$$\mathbf{C}_{\mathbf{\Delta}}(\mathbf{x}) = \langle \mathbf{\Delta}\otimes\mathbf{\Delta}^\dagger\rangle = \int D\delta\rho D\delta\mathbf{u} D\delta\theta\, \mathbf{\Delta}\otimes\mathbf{\Delta}^\dagger\, P_{eq}\, dV \ , \quad (4.16)$$

and can be evaluated in closed form by elementary techniques for Gaussian path integrals.

The discrete correlations are evaluated by dividing the system in cubic cells V_n of volume $\Delta V = \Delta x^3$, such that the set V is written as $V = \bigcup_{n=1}^N V_n$ and $V_n \cap V_m = \emptyset$ if $m \neq n$, i.e. the subsets V_n form a partition of V. The discrete fields are defined at each cell as the space-average of the continuum fields over that volume, i.e. letting $\mathbf{U}_n = (\rho_n, \mathbf{u}_n, \theta_n)$ be the discrete field at

a generic grid cell n, one has

$$\mathbf{U}_n(t) = \frac{1}{\Delta V}\int_{V_n} dV\ \mathbf{U}_n(\mathbf{x},t)\ . \tag{4.17}$$

It is worth stressing that the system of equations Eq. (3.89), can be linearized around the mean value of the hydrodynamic fields, providing in a discretized form, a set of Ito's stochastic ordinary differential equations for the fluctuations $\mathbf{\Delta}_n = \mathbf{U}_n - \langle \mathbf{U}_n \rangle$ as

$$d\,\mathbf{\Delta}_n(t) = \mathcal{L}_{nm}\mathbf{\Delta}_m\,dt + \mathcal{K}_{nm}d\,\mathbf{B}_m\ , \tag{4.18}$$

where the first term of RHS of Eq. (4.18) is the discrete form of the deterministic terms in the linearised Eq. (3.89), and the second one corresponds to the stochastic contributions. The operators $\mathcal{L}_{nm}, \mathcal{K}_{nm}$ are block matrices acting on all the N five dimensional vectors $\mathbf{\Delta}_n\,, d\,\mathbf{B}_n$. The stochastic contributions are constructed to reproduce the probability distribution of the fluctuating fields that, in the discrete limit, reads (see Eq. (4.14))

$$P_{eq}(\mathbf{\Delta}_n) \;=\; \frac{1}{Z}\exp\left(\frac{\Delta S_c}{k_B}\right) = \frac{1}{Z}\exp\left[-\frac{\Delta V}{2k_B}\sum_{l,m}^{N}\mathbf{\Delta}_l\,\mathcal{H}_{lm}\,\mathbf{\Delta}_m\right]\ . \tag{4.19}$$

The corresponding covariance matrix is

$$\langle \mathbf{\Delta}_l \otimes \mathbf{\Delta}_m \rangle = \frac{1}{Z}\int\prod_{n=1}^{N} d^5\mathbf{\Delta}_n\,\mathbf{\Delta}_l\mathbf{\Delta}_m\,P_{eq}(\mathbf{\Delta}_n) \;=\; \frac{k_B}{\Delta V}\mathcal{H}^{-1}_{lm}\,.$$

To be more explicit, the set of fluctuating fields $\mathbf{\Delta}_n$ have been collected in a $5N$-dimensional vector, and $\mathbf{H}$ is a $5N \times 5N$ block matrix defined as

$$\mathbf{H} = \begin{pmatrix} \mathbf{h} & \Theta_{13} & \Theta_{11} \\ \Theta_{31} & \frac{\rho_0}{\theta_0}\mathbf{I}_{33} & \Theta_{31} \\ \Theta_{11} & \Theta_{13} & \frac{\rho_0 c_v}{\theta_0^2}\mathbf{I}_{11} \end{pmatrix} \tag{4.20}$$

with $\mathbf{I}_{11}$ and $\mathbf{I}_{33}$ are $N \times N$ and $3N \times 3N$ identity matrices, respectively, and $\mathbf{\Theta}_{pq}$ are $pN \times qN$ zero-matrices, with all zero entries. Particular attention must be paid to the term $\mathbf{h} = c_{T0}^2 \Delta V \mathbf{I}_{11}/\theta_0\rho_0 - \lambda\Delta V/\theta_0 \mathbf{L}$, that for a capillary fluids induces long-ranged correlations due to the presence of the discrete Laplacian operator $\mathbf{L}$ (instead of the classical delta-correlation for simple fluids).

After rearranging the fluctuating fields as above, the covariance matrix (discrete Green's function) is easily evaluated by solving the multidimensional Gaussian integral. The procedure yields the statistical properties of the discretised equations,

$$\begin{aligned} \langle \delta\rho_l \delta\rho_m \rangle &= Z_{\delta\rho}^{-1} \int \prod_{n=1}^{N} d\Delta_n \, \Delta_l \Delta_m \, \exp\left[-\frac{\Delta V}{2k_B} \sum_{l,m=1}^{N} \Delta_l \, \mathbf{h}_{lm} \, \Delta_m \right] = \\ &= \frac{k_B}{\Delta V} \mathbf{h}_{lm}^{-1} \, , \end{aligned} \tag{4.21}$$

$$\begin{aligned} \langle \delta u_l \delta u_m \rangle &= Z_{\delta v}^{-1} \int \prod_{n=1}^{3N} d\Delta_n \, \Delta_l \Delta_m \, \exp\left[-\frac{\Delta V \rho_0}{2k_B\theta_0} \sum_{l,m=1}^{3N} \Delta_l \, \delta_{lm} \, \Delta_m \right] = \\ &= \frac{k_B\theta_0}{\rho_0 \Delta V} \delta_{lm} \, , \end{aligned} \tag{4.22}$$

$$\begin{aligned} \langle \delta\theta_l \delta\theta_m \rangle &= Z_{\delta\theta}^{-1} \int \prod_{n=1}^{N} d\Delta_n \, \Delta_l \Delta_m \, \exp\left[-\frac{\Delta V \rho_0 c_v}{2k_B\theta_0^2} \sum_{l,m=1}^{N} \Delta_l \, \delta_{lm} \, \Delta_m \right] \\ &= \frac{k_B\theta_0^2}{\rho_0 c_v \Delta V} \delta_{lm} \, . \end{aligned} \tag{4.23}$$

In other words, in the theory of (discrete) fluctuating hydrodynamics the fluctuating fields are a set of Gaussian stochastic processes, with zero mean and the variance given by Eq. (4.21,4.22,4.23). It is worthwhile noting as all the fields are mutually statistically independent ($\langle \delta\mathbf{u}\delta\rho \rangle = 0$, for example). Also, the density field is not delta-correlated due to the presence of capillarity.

4.2.2 Discrete static structure factor and weak convergence analysis

As already discussed in Sec.3.1.1 a relevant quantity both from the experimental and the numerical point of view is the static structure factor (see.Eq. 3.40). Here we report the comparison of the density static structure factor, which is the Fourier transform of the static correlation function $C_{\delta\rho\delta\rho}$ in Eq. (3.35). In the discrete limit, the theoretical static structure factor reads

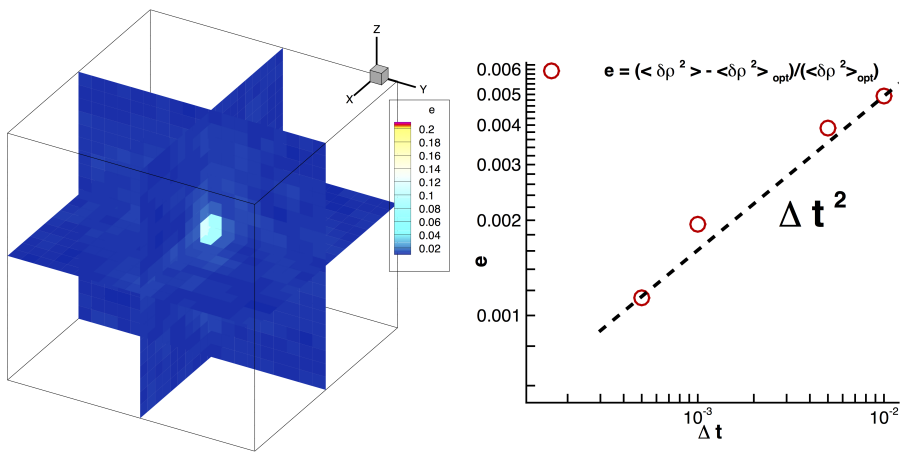

Figura 4.2: Left panel: Static structure factor comparison for a capillary fluid in a 3D system. We report the relative error $e = |S_f - S_t|/S_t$ between the theoretical prediction and numerical calculation for each wavenumbers k_x, k_y, k_z in the Fourier space. Right panel: Error of the density variance at different simulation time steps. As expected, the error follows a square power law $e \propto \Delta t^2$.

$$S_t(\mathbf{k_d}) = \frac{\rho_0 k_B \theta_0}{c_T^2 + \rho_0 \lambda \mathbf{k_d} \cdot \mathbf{k_d}} \ , \tag{4.24}$$

where

$$\mathbf{k_d} \cdot \mathbf{k_d} = \left(\frac{\sin\left(k_x \Delta x/2\right)}{\Delta x/2}\right)^2 + \left(\frac{\sin\left(k_y \Delta y/2\right)}{\Delta y/2}\right)^2 + \left(\frac{\sin\left(k_z \Delta z/2\right)}{\Delta z/2}\right)^2 \tag{4.25}$$

is the discrete version of the square norm of $\mathbf{k}$, arising from the discrete laplacian operator in Fourier space [33]. The numerical value of the density structure factor is calculated, following its definition, as

$$S_f(\mathbf{k_d}) = \langle \delta\rho(\mathbf{k_d})\delta\rho^*(\mathbf{k_d})\rangle \ . \tag{4.26}$$

As shown in the left panel of Fig. 4.2, the numerical results are in very good agreement with the theoretical prediction. In particular the relative error e is almost everywhere less than $2-3\%$ in the field, except for the small wavenumbers, due to the slow convergence of low wavelength modes [33]. Nevertheless, even in the latter case, the relative error is lower then 10%.
As a second test, we compared the variance of velocity and temperature fluctuations. In particular, the velocity fluctuations must reproduce the celebrated equipartition theorem, here reported in the discretized version:

$$\langle \delta\mathbf{u}\cdot\delta\mathbf{u}\rangle = 3\frac{k_B\theta_0}{\rho_0\Delta V}\,, \tag{4.27}$$

$$\left\langle \delta\theta^2\right\rangle = \frac{k_B\theta_0^2}{\rho_0 c_v\Delta V}\,. \tag{4.28}$$

The values reported in Tab. 4.1 clearly show a perfect matching between numerical results and theoretical expectation.

Variances	Theoretical prediction	Numerical value	Error %
$\langle\delta u_x^2\rangle$	$1.3333\cdot 10^{-4}$	$1.3332\cdot 10^{-4}$	0.01
$\langle\delta u_y^2\rangle$	$1.3333\cdot 10^{-4}$	$1.3331\cdot 10^{-4}$	0.02
$\langle\delta u_z^2\rangle$	$1.3333\cdot 10^{-4}$	$1.3335\cdot 10^{-4}$	0.02
$\langle\delta\theta^2\rangle$	$5.8361\cdot 10^{-5}$	$5.8443\cdot 10^{-5}$	0.15

Tabella 4.1: Numerical temperature and velocity variances in comparison with theoretical values.

As a last test, we validated the accuracy of our time integration method. We performed the time evolution by means of a second order Runge Kutta

scheme [46]. We compared the numerical error, e, on the variance of density fluctuations $\langle \delta\rho(\mathbf{x})^2 \rangle$ at different time steps Δt with respect to $\langle \delta\rho(\mathbf{x})^2 \rangle_{opt}$ obtained with our finest integration step $\Delta t = 10^{-4}$

$$e = \frac{\left| \langle \delta\rho(\mathbf{x})^2 \rangle - \langle \delta\rho(\mathbf{x})^2 \rangle_{opt} \right|}{\langle \delta\rho(\mathbf{x})^2 \rangle_{opt}} \,, \tag{4.29}$$

where the average is evaluated as $1/(T\,V) \int_0^T \int_V \delta\rho(\mathbf{x})^2 \, dV dt$ with the time window T fixed as $T = 100$ LJ units. The right panel of Fig. 4.2 clearly show the expected power law, $e \propto \Delta t^2$ as expected for the weak convergence of such stochastic pde [46]. All these tests ensure that the numerical scheme correctly reproduce the statistical properties of the system, i.e. the numerics preserves the fluctuation-dissipation balance in the discretised equations.

4.2.3 Static Probability Distributions

In Fig. 4.3 we report the comparison between the theoretical probability distribution functions of density and temperature, and the numerical calculation. Figure 4.4 provides the comparison between the numerical and theoretical normalised mean kinetic energy. Since the fields $u_n(\rho_0 \Delta V / k_B \theta_0)^{1/2}$ are normally distributed Gaussian stochastic processes, the mean kinetic energy normalised with $1/2 k_B \theta$ must be a Chi-squared stochastic process with mean value 3. For the generic fluctuating field Δ the numerical variance is computed as $1/TV \int_0^T \int_V \Delta(\mathbf{x}, t)^2 \, dV dt$, where the time window is set to $T = 100t$. As shown in Figs. (4.3,4.4) numerical results are in very good agreement with the theoretical prediction. This ensures that the numerical scheme is able to reproduce the statistical properties of the system.

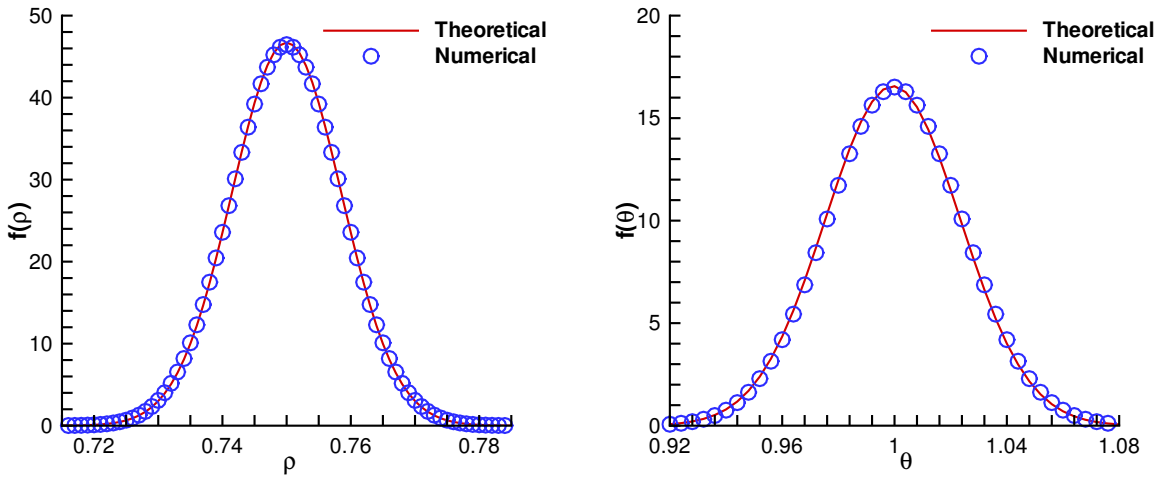

Figura 4.3: Probability distribution functions for density and temperature fields, the red lines represent the theoretical predictions (Gaussian distributions) and the blue circles the numerical calculations. The results are presented in an non dimensional form, according to Lennard-Jones units.

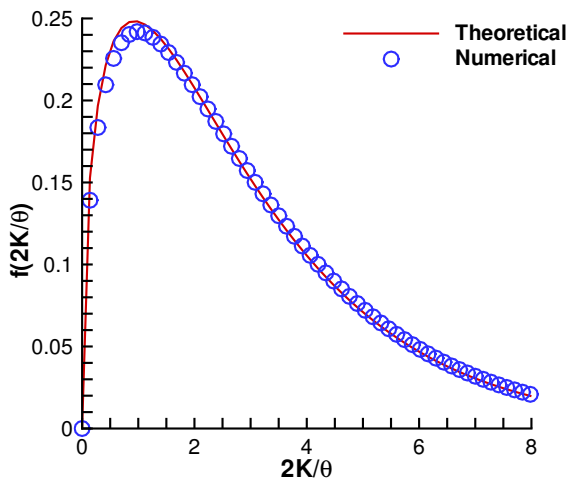

Figura 4.4: Probability distribution functions of the kinetic energy $K = 1/2\rho_0\Delta V\left(\langle \mathbf{u}\cdot\mathbf{u}\rangle\right)$ normalized with $k_B\theta/2$, the red line represent the theoretical prediction (Chi-squared distribution) and the blue circle the numerical calculation. The results are presented in an non dimensional form, according to Lennard-Jones units.

Capitolo 5

Conclusion and Perspectives

In these PhD thesis a mesoscale model based on the Van der Waals diffuse interface approach endowed with thermal fluctuations has been developed to address cavitation in its entirety, starting from the nuclei formation (nucleation) up to the macroscopic motion (bubble dynamics). In order to describe spontaneous nucleation, two crucial aspects have been addressed. The first aspect concerns the thermodynamics of two-phase system. For this purpose a diffuse interface (DI) description has been adopted. The results show a correct modeling of phase change, latent heat release, compressibility as well as surface tension effects. The second one consists in modeling thermal fluctuation, addressed by fluctuating hydrodynamics (FH). The FH theory was developed for simple fluids in the eminent work of Landau and Lifshitz. That approach has been extended in this thesis to the diffuse interface context for capillary fluids. The model has been used to numerically address vapor bubble nucleation both in homogeneous and heterogeneous conditions. The calculated nucleation rates are favorably compared with state of the art simulations. Concerning the comparison with classical approaches (CNT, string method, Kramers theory) it is found that the simultaneous nucleation

of several bubbles strongly affects the nucleation rate, providing different view point with respect to the single-bubble models.

However the nucleation rate in the initial phase is only mildly affected by the simultaneous presence of newly nucleated bubbles and compared favourably with the available results of large scale MD simulations. From a computational point of view, the present technique has revealed extremely more cheap than traditional MD simulations, allowing the analysis of the very long bubble expansion stage where bubble-bubble interaction (coalescence and collapse) events turn out to determine the eventual bubble size distribution. In order to complete the analysis, a spherical version of the model is proposed, particularly useful when dealing with homogeneous nucleation, where is is reasonable (and common) to assume a spherical shape for nucleation embryos. The reduced model is able to reproduce the Einstein-Boltzmann probability distribution for fluctuations and well agrees with Kramers theory in predicting the mean first passage time.

The model has great potential also for use in a pure deterministic setting, showing a very accurate description of the hydrodynamics of multiphase systems. In particular, it has been exploited to study the collapse of a cavitation nanobubble near a solid boundary, showing an accurate reproduction of physical phenomena observed in the experiments, namely: strong peaks of pressure and temperature, shockwave emission and liquid jet formation.

In addition the Van der Walls model coupled with the a rare event technique (the string method) was used to evaluate critical cluster and energy barriers. This method has been used under the hypothesis of over-damped regime, where the MEP is also the most probable path for the gradient dynamics (Allen Cahn equation). Notwithstanding the path geometry the

system follows when transitioning from the metastable basin to the saddle point, could be considerably different with respect to an over-damped regime. Since inertial effects could be crucial. Thus, determining most probable path from FH simulations, where inertial effects are considered , is a very interesting perspective, and I am presently presenting this as an interesting perspective objective for future work. Finally the most probable path could be also determined for the simplified spherical model we developed.

The encouraging results obtained with the present mesoscale model, stimulate its exploitation in more complex conditions. For instance, developing a multi-species systems is crucial in liquid-vapour nucleation, since the presence of dissolved gases and impurities is unavoidable and always detected in common liquids, e.g. water. The extension of the present model to multi-species system consists in more or less straightforward generalisation of the Helmholtz free energy both in its bulk part (depending on the density of all the species involved) and in the capillary term (depending on a capillary tensor and on the spatial gradients of all species). The model can be immediately and directly coupled to macroscopic flows address nucleation in dynamic environments –like the engineering contexts where cavitation process usually occurs– focusing on nucleation rates and bubble interactions. A little further ahead fluctuating hydrodynamics can be extended to the phase field crystal framework, to address solidification dynamics at mesoscale level.

As final remark, I would like to point out an apparent conceptual inconsistency of Van der Waals theory when dealing with multiphase systems. In fact, the diffuse interface model is derived from gradient expansion of exact DFT expressions, under the assumption small density gradients on molecular length scales. This hypothesis is reasonable when studying fluids at high

temperatures (the cases in force in this thesis), where the transition zone between the two different phases is characterized by a smooth interface. However, its validity in more general contexts is not so evident, since the widths of the derived interfaces are often only a few molecular diameters in extent. These problems are also detected in phase field theory for crystallization, where it is supposed to describe localization of the density onto molecular-scale. Onto these length scales, molecular correlation effects can be crucial in modeling fluids, showing the need of more sophisticated theories, namely microscopic DFT models. Unfortunately, such microscopic theories are often unaffordable in many cases in terms of computational resources. For this reasons, at the expense of generality, the efficiency of the Van der Waals model in the description of both the phase change inception and macroscopic motion, seems to be a fair compromise. Nevertheless, the theoretical advance in phase field approaches will be crucial in continuum models of multiphase systems.

In conclusion, we believe that the work done with this thesis could be useful in the development of innovative continuum formulation for thermally activated processes.

Acknowledgments

I would like to acknowledge my supervisor, Prof. Carlo Massimo Casciola, for being an exceptional mentor. Without his guidance, this work would have never been possible. In addition, I'd like to express my gratitude to Dr. Francesco Magaletti, who contributed significantly to the work done in this thesis. I personally want to extend my thanks to European Research Council for supporting this research and CINECA award under the Iscra project, for the availability of high performance computing resources and support. Last, but not least, I would like to thank to my *great Family*, for being part of my journey.

Capitolo 6

Shock-induced collapse of a vapor nanobubble near solid boundaries

The deterministic diffuse interface approach described in Chapter 2 has been used to address the collapse of a cavitation nano bubble in proximity of a solid wall. The method was found to be suitable in the description of the complex mechanisms behind the cavitation collapse, namely: topology modification, phase changes also in supercritical regime, shockwave emission, liquid jet formation. Qualitatively reproducing the existing experimental observations.

The simulated system –consisting of a pure van der Waals fluid– is initialized with a vapor bubble of radius R_{eq} in equilibrium with a surrounding liquid, and placed at a distance z_0 from the wall. The collapse is triggered by an impinging shockwave, that as soon as it touches the bubble causes its collapse. Several initial condition have been investigated, by changing both the bubble initial wall distance and the intensity of the triggering shockwave. Overall the bubble dynamics is characterized by a sequence of rebounds during which many complex physical phenomena are detected. In particular when the bubble reaches its minimum volume extreme values of temperature and pressure are detected, these peaks are considered the forerunners of

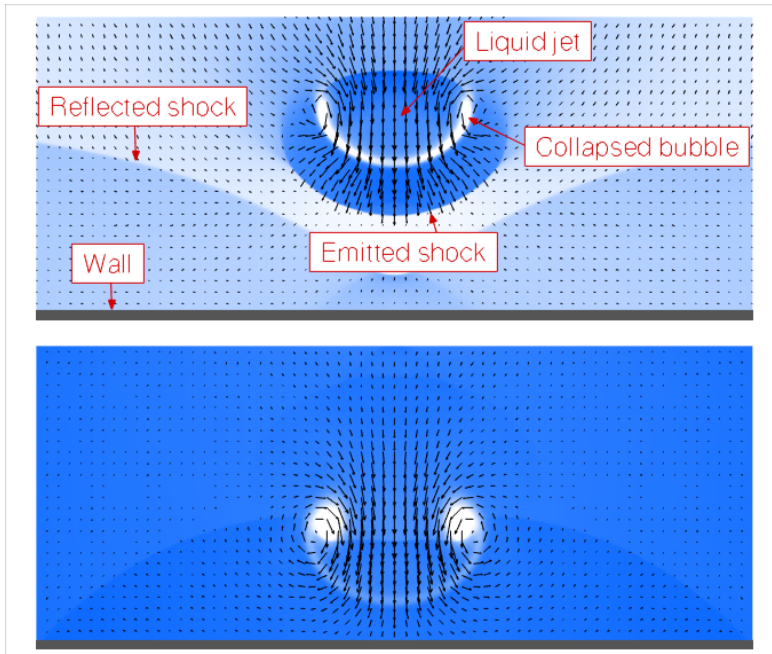

Figura 6.1: Simulation snapshot during bubble collapse.

the shockwave emission. The emitted shockwave strong interacts with the dynamics following the collapse stage, especially when the collapsing bubbles are very close to the solid boundaries. In addition the presence of the wall and the triggering collapse mechanism, determine the breaking of the spherical symmetry in the system, leading, for sufficiently strong intensity of the incoming shock wave, to the poration of the bubble and the formation of a toroidal structure surrounding a liquid nano jet, as it is highlighted in Fig.6.1 representing the latter phase.

Intense peaks of pressure and temperatures are found also at the wall, confirming that the strong localized loading combined with the jet impinging the wall is a potential source of substrate damage induced by the cavitation.

The complete results have been published on IJMF (Volume 84, September 2016, Pages 34-45), and are reported here with the permission of the authors.

abstract

The collapse of a nano-bubble near a solid wall is addressed here exploiting a phase field model recently used to describe the process in free space. Bubble collapse is triggered by a normal shock wave in the liquid. The dynamics is explored for different bubble wall normal distances and triggering shock intensities. Overall the dynamics is characterized by a sequence of collapses and rebounds of the pure vapor bubble accompanied by the emission of shock waves in the liquid. The shocks are reflected by the wall to impinge back on the re-expanding bubble. The presence of the wall and the impinging shock wave break the symmetry of the system, leading, for sufficiently strong intensity of the incoming shock wave, to the poration of the bubble and the formation of an annular structure and a liquid jet. Intense peaks of pressure and temperatures are found also at the wall, confirming that the strong localized loading combined with the jet impinging the wall is a potential source of substrate damage induced by the cavitation.

Introduction

The collapse of vapor bubbles near solid boundaries has been deeply investigated in the last century. The triggering episode goes back to the finding of the destructive effects of cavitation phenomena on the propellers of the great ocean liners at the beginning of the XXth century. Similar effects ha-

ve been observed successively on the blade of big hydraulic machines like turbines and pumps [131, 88]. Only recently, due to the increasing impact of the micro and nano technologies, the attention from millimeter-size bubbles has shifted downwards, toward micro or sub-micro bubbles. Indeed in microfluidic devices, the so called *lab on a chip*, cavitation phenomena can be employed for microfluidic pumping [50], to enhance mixing by means of vorticity generation during the final stage of bubble collapse and for surface cleaning purposes [112]. Cavitation bubbles are also used in advanced medical procedures like high intensity focused ultrasound (HIFU) and extracorporeal shock wave lithotripsy (ESWL) [35] to enhance drug delivery or increase local heat deposition deep within the body, to control localized cell membrane poration [125], and to comminute kidney stones [151]. Moreover, the use of femtosecond lasers, generating nanometric bubbles, has recently found important applications in nanosurgery of cells and tissues [144, 145].

The experimental investigation has played the most important part in the understanding of bubble-wall interactions, so far. The improvements in the bubble generation techniques led to cleaner and better reproducible data, starting from the kinetic impulse technique [14]. This approach suffers from the disadvantage that the bubble must be located before the application of the impulse. Successively the problem of localization has been overcome by means of the generation of the bubble by using an electric spark [108, 139]. As a drawback, the electrodes perturb the bubble motion in the last stage of the collapse. At the moment, the best bubble generation technique is, probably, the non-intrusive pulsed-laser discharge [143] that can focus an intense local heating and vaporization of the liquid through application of a thermal impulse. The visualization of the bubble dynamics can be performed by

illuminating the scene with diffuse backlighting [16] and by means of high-speed cameras, up to 20 million frames per second [111]. More recently, the μ-PIV technique has been used to measure the flow field during the bubble collapse [125]. The experiments allowed the visualization of the jet formation during the bubble collapse near solid surfaces and the assessment of the role of shock-wave emission, jet-wall interaction and chemical effects on cavitation damage [14, 120]. Notwithstanding the extreme frame-rate of modern cameras, the complete and detailed description of thermo-acoustic and flow fields, is still lacking. The temperature and pressure inside the bubble at the collapse instant is not easily accessible with non-intrusive measurements. The pressure indeed can be only extrapolated by measuring it with an hydrophone at some distance from the bubble and by assuming a classical $1/r$ decay [87]. The temperature instead can be estimated by matching a blackbody radiation with the measured spectrum of the emitted light upon collapse [60].

On the other hand, the mathematical modeling of cavitation is still a great challenge. The cornerstone in the theory of bubble dynamics was the pioneering work of Lord Rayleigh [121] who described the collapse of a bubble immersed in a unbounded incompressible liquid. Despite the significant simplifying assumptions, the correspondence with experimental results is still impressive. The model has been successively refined by taking into account compressibility effects in the liquid [81, 69] and the presence of a dilute gas in the bubble. These refined models provided an estimate of the pressure peaks reached inside the bubble on the order of hundred times the pressure of the liquid environment. Numerical simulations and more complex analysis followed [117, 119, 129] in order to describe the effect of a nearby bounda-

ry. Different numerical techniques have been used in order to capture the interfacial dynamics, ranging from the Boundary Element Method (BEM) for irrotational conditions [16] to the Arbitrary Lagrangian Eulerian (ALE) schemes [138, 51]. Recently more sophisticated models have been proposed to gain new insights on the effects of dissolved gas and phase change [2] and to obtain a deeper knowledge in fascinating phenomena like sonoluminescence [30]. Of particular interest is the diffuse interface approach which enables a natural description of interfacial flows, changes of topology, vapor/liquid and vapor/supercritical fluid phase changes which have been shown to be crucial for the correct description of the final stages of the bubble collapse [96].

In this work we will exploit the diffuse interface model to numerically investigate the collapse of a sub-micron vapor bubble near solid boundaries. The effect of the initial bubble-wall distance will be analyzed and the visualization of the entire flow and thermo-acoustic fields will be provided. Particular attention will be paid to the stress distribution on the solid wall and we will address the role of the different pressure waves on cavitation damage.

The paper is organized as follows: in § 1 the diffuse interface model and the relevant conservation equations is derived; § 2 provides details on the numerical scheme and describes the numerical setting of the simulations; finally, the results of the numerical experiments will be discussed in § 3 to finally draw conclusions and provide final comments in the last § 4.

Mathematical model

Thermodynamics of non-homogeneous systems We exploit an unsteady diffuse interface description [5] of the multiphase flow in a domain

$\mathcal{D}$ based on the van der Waals gradient approximation of the free energy functional $F[\rho, \theta]$ [45, 72]:

$$F[\rho, \theta] = \int_{\mathcal{D}} \hat{f} dV = \int_{\mathcal{D}} \left(\hat{f}_0 (\rho, \theta) + \frac{\lambda}{2} |\boldsymbol{\nabla} \rho|^2 \right) dV \,, \tag{6.1}$$

where $\hat{f} = \hat{f}_0 + \lambda/2|\nabla\rho|^2$ with $\hat{f}_0 (\rho, \theta)$ the classical Helmholtz free energy density per unit volume of the homogeneous fluid at temperature θ and mass density ρ. The coefficient $\lambda(\rho, \theta)$, in general function of the thermodynamic state, embodies all the information on the interfacial properties of the liquid-vapor system (i.e. surface tension and interface thickness). In particular, for a van der Waals fluid, the free energy reads

$$\hat{f}_0 (\rho, \theta) = \bar{R} \rho \theta \left[-1 + \log \left(\frac{\rho \, K \, \theta^{1/\delta}}{1 - b\rho} \right) \right] - a\rho^2 \,, \tag{6.2}$$

with $\delta = \bar{R}/c_v$, $\bar{R}$ the gas constant, c_v the constant volume specific heat, a and b the van der Waals coefficients and K a constant related to the de Broglie length [150].

Equilibrium conditions The present paragraph summarizes, for the reader convenience, results concerning thermodynamic equilibrium for systems described by the free energy functional (6.1). Although well known to specialists, we deemed useful to present a short summary to rationalize this classical material which is hardly described comprehensively in literature, [73].

At given temperature, equilibrium is characterized by the minimum of the free energy functional in Eq. (6.1), where variations are performed with respect to the density distribution ρ. The evaluation of the functional derivative leads to the following equilibrium condition:

$$\mu_c^0 - \boldsymbol{\nabla} \cdot (\lambda \boldsymbol{\nabla} \rho) = const \,, \tag{6.3}$$

where the temperature is constrained to be constant, $\theta = const$, and $\mu_c^0 = \partial \hat{f}_0/\partial\rho|_\theta$ is the classical chemical potential. The equation defines a generalized chemical potential $\mu_c = \mu_c^0 - \boldsymbol{\nabla} \cdot (\lambda \boldsymbol{\nabla} \rho)$ that must be constant at equilibrium.

The consequence of the above equilibrium conditions is better illustrated in the simple case of a planar interface, where the only direction of inhomogeneity is x, under the assumption of constant λ. The constant temperature appears in the equilibrium problem as a parameter and will not be further mentioned throughout the present section. Hence, determining the equilibrium density distribution amounts to finding a solution of

$$\mu_c = \mu_c^0(\rho) - \lambda d^2\rho/dx^2 = \mu_{eq}\,, \tag{6.4}$$

where the chemical potential in the bulk fluid (the vapor phase, say), far from the interface where $d\rho/dx = 0$, determines the constant $\mu_{eq} = \mu_c^0(\rho_V) = \mu_c^0(\rho_L)$. By multiplying Eq. (8.16) by $d\rho/dx$ and integrating between $\rho_\infty = \rho_V$ and ρ, leads to

$$\hat{w}_0(\rho) - \hat{w}_0(\rho_V) = \frac{\lambda}{2}\left(\frac{d\rho}{dx}\right)^2\,, \tag{6.5}$$

where $\hat{w}_0(\rho) = \hat{f}_0(\rho) - \mu_{eq}\rho$. Equation (6.5) shows that $\hat{w}_0$ has the same value in both the bulk phases, where the spatial derivative of mass density vanishes: $\hat{w}_0(\rho_L) = \hat{w}_0(\rho_V)$.

The grand potential, defined as the Legendre transform of the free energy,

$$\Omega = F - \int_{\mathcal{D}} \rho \frac{\delta F}{\delta \rho} dV = \int_{\mathcal{D}} \hat{w} dV\,, \tag{6.6}$$

has the density (*actual* grand potential density)

$$\hat{w}[\rho] = \hat{f} - \mu_c\rho = \hat{f}_0 + \frac{\lambda}{2}\left(\frac{d\rho}{dx}\right)^2 - \left(\mu_c^0 - \lambda\frac{d^2\rho}{dx^2}\right)\rho\,, \tag{6.7}$$

implying that, in the bulk, $\hat{w} = \hat{w}_0$, i.e. $\hat{w}_0$ is the *bulk* grand potential density.

Given the form of $\hat{w}_0(\rho)$, the solution of Eq. (6.5) provides the equilibrium density profile $\rho(x)$:

$$x = \sqrt{\frac{\lambda}{2}} \int_{\rho_v}^{\rho} \frac{d\rho}{\sqrt{w_0(\rho) - w_0(\rho_V)}} + const\,. \tag{6.8}$$

Eq. (6.8) provides the equilibrium density profile characterized by two bulk regions separated by a thin layer. The layer thickness can be estimated as

$$\epsilon = \frac{\rho_L - \rho_V}{d\rho/dx|_{max}}\,. \tag{6.9}$$

The equilibrium condition, Eq. (6.5), provides the interface thickness in terms of the *bulk* grand potential density $\hat{w}_0(\rho)$ and of the parameter λ,

$$\epsilon = (\rho_L - \rho_V) \sqrt{\frac{\lambda}{2\left[\hat{w}_0(\bar{\rho}) - \hat{w}_0(\rho_V)\right]}}\,, \tag{6.10}$$

without explicitly addressing the density profile. $\bar{\rho}$ is the density corresponding to the maximum of $d\rho/dx$, achieved where $d\hat{w}_0/d\rho = 0$, Eq. (6.5).

The surface tension can be defined as the excess (*actual*) grand potential density,

$$\sigma = \int_{-\infty}^{x_i} \left(\hat{w}[\rho] - \hat{w}[\rho_V]\right) dx \; + \int_{x_i}^{\infty} \left(\hat{w}[\rho] - \hat{w}[\rho_L]\right) dx = \\ \int_{-\infty}^{\infty} \left(\hat{w}[\rho] - \hat{w}[\rho_V]\right) dx\,, \tag{6.11}$$

where x_i is the position of the Gibbs dividing surface, whose precise value is not influential since $\hat{w}[\rho_V] = \hat{w}[\rho_L]$ (we stress that, e.g., $\hat{w}[\rho_V]$ should be interpreted as the functional (6.7) evaluated on the constant density ρ_V). Given the definition of $\hat{w}[\rho]$, Eq. (6.7), and exploiting the equilibrium condition

for the chemical potential, Eq. (6.4), it follows that

$$\sigma = \int_{-\infty}^{\infty} \left[\hat{f}_0 + \frac{1}{2}\lambda \left(\frac{d\rho}{dx} \right)^2 - \mu_{eq}\rho - \hat{w}_0(\rho_V) \right] dx = \int_{-\infty}^{\infty} \left[\hat{w}_0 + \frac{1}{2}\lambda \left(\frac{d\rho}{dx} \right)^2 - \hat{w}_0(\rho_V) \right] dx \ . \tag{6.12}$$

Using Eq. (6.5) one finds

$$\sigma = \int_{-\infty}^{+\infty} \lambda \left(\frac{d\rho}{dx} \right)^2 dx = \int_{\rho_V}^{\rho_L} \lambda \frac{d\rho}{dx} d\rho \ = \int_{\rho_V}^{\rho_L} \sqrt{2\lambda \left(\hat{w}_0(\rho) - \hat{w}_0(\rho_V) \right)} \, d\rho \, , \tag{6.13}$$

where the second expression can be evaluated with no *a priori* knowledge of the equilibrium density profile. We observe that, as for the interface thickness, the surface tension only depends on the form of the *bulk* grand potential density $\hat{w}_0(\rho)$ in the density range between the two equilibrium values, $[\rho_V; \rho_L]$, and on the parameter λ.

Equation (6.5) applied to the two bulk regions where $d\rho/dx = 0$ implies the mechanical equilibrium condition $p_0(\rho_L) = p_0(\rho_V)$, where

$$p_0 = -\frac{\partial f_0}{\partial v} = -\frac{\partial \hat{f}_0/\rho}{\partial v} = \rho\mu_c^0 - \hat{f}_0 \tag{6.14}$$

is the classical thermodynamic pressure, $f_0 = \hat{f}_0/\rho$ the specific bulk free energy, and $v = 1/\rho$ the specific volume. Indeed Eq. (6.5) implies $\hat{w}_0(\rho_V) = \hat{w}_0(\rho_L)$, which corresponds to the equality of the pressures given that $p_0 = -\hat{w}_0$.

Equations of motion The dynamics of the inhomogeneous system is described by the conservation equations for mass ρ, momentum $\rho\mathbf{u}$, and total

energy E densities of

$$\frac{\partial \rho}{\partial t} + \boldsymbol{\nabla} \cdot (\rho \mathbf{u}) = 0\,, \tag{6.15}$$

$$\frac{\partial \rho \mathbf{u}}{\partial t} + \boldsymbol{\nabla} \cdot (\rho \mathbf{u} \otimes \mathbf{u}) = \boldsymbol{\nabla} \cdot \boldsymbol{\tau}\,, \tag{6.16}$$

$$\frac{\partial E}{\partial t} + \boldsymbol{\nabla} \cdot (\mathbf{u} E) = \boldsymbol{\nabla} \cdot [\boldsymbol{\tau} \cdot \mathbf{u} - \mathbf{q_e}]\,. \tag{6.17}$$

The system (6.15 – 6.17) needs to be complemented with thermodynamically consistent constitutive relations for the stress tensor $\boldsymbol{\tau}$ and the energy flux $\mathbf{q_e}$. Their derivation is outlined below for the simplest case of constant λ, following the general approach for non-equilibrium processes described in [37].

It is instrumental to rewrite the energy equation in terms of specific internal energy $\mathcal{U}$, obtained by subtracting the equation for the kinetic energy from Eq. (6.17)

$$\rho \frac{D\mathcal{U}}{Dt} = \boldsymbol{\tau} : \boldsymbol{\nabla} \mathbf{u} - \boldsymbol{\nabla} \cdot \mathbf{q_e}\,, \tag{6.18}$$

where $D/Dt = \partial/\partial t + \mathbf{u} \cdot \boldsymbol{\nabla}$ is the material derivative. By definition $\mathcal{U} = f + \theta\,\eta$, with $f = \hat{f}/\rho$ the specific Helmholtz free energy and η the specific entropy. The total derivative of $\mathcal{U}$ reads

$$\mathrm{d}\mathcal{U} = \frac{\partial f}{\partial \rho}\mathrm{d}\rho + \frac{\partial f}{\partial \boldsymbol{\nabla}\rho} \cdot \mathrm{d}\boldsymbol{\nabla}\rho + \theta \mathrm{d}\eta\,. \tag{6.19}$$

The partial derivatives of the specific free energy can be derived from its definition, Eq. (6.1), and from the definition of the thermodynamic pressure, Eq. (6.14). Explicitly, one finds

$$\frac{D\mathcal{U}}{Dt} = \frac{1}{\rho^2}\left(p_0 - \frac{\lambda}{2}|\boldsymbol{\nabla}\rho|^2\right)\frac{D\rho}{Dt} + \theta\frac{D\eta}{Dt} + \frac{\lambda}{\rho}\boldsymbol{\nabla}\rho \cdot \frac{D\boldsymbol{\nabla}\rho}{Dt}\,.$$

The material derivative of the density gradient (last term in the RHS of Eq. (6.20)) can be evaluated by applying the gradient operator to the equation of mass conservation, Eq. (6.15):

$$\frac{\lambda}{\rho}\boldsymbol{\nabla}\rho\cdot\frac{D\boldsymbol{\nabla}\rho}{Dt}=-\frac{\lambda}{\rho}\boldsymbol{\nabla}\rho\cdot\boldsymbol{\nabla}\left(\rho\boldsymbol{\nabla}\cdot\mathbf{u}\right)-\frac{\lambda}{\rho}\boldsymbol{\nabla}\rho\otimes\boldsymbol{\nabla}\rho:\boldsymbol{\nabla}\mathbf{u}\,. \tag{6.20}$$

After substitution of Eqs. (6.15, 6.20, 6.20) into Eq. (6.18), a few more elementary manipulations allow to write the evolution equation for the entropy as

$$\begin{aligned}\rho\frac{D\eta}{Dt} &= \boldsymbol{\nabla}\cdot\left(\frac{\lambda\rho\boldsymbol{\nabla}\rho\boldsymbol{\nabla}\cdot\mathbf{u}-\mathbf{q_e}}{\theta}\right)+\\ &\quad+\frac{1}{\theta^2}\left[\lambda\rho\boldsymbol{\nabla}\rho\boldsymbol{\nabla}\cdot\mathbf{u}-\mathbf{q_e}\right]\cdot\boldsymbol{\nabla}\theta+\\ &\quad+\frac{1}{\theta}\left[\boldsymbol{\tau}+\left(p_0-\frac{\lambda}{2}|\boldsymbol{\nabla}\rho|^2-\rho\boldsymbol{\nabla}\cdot(\lambda\boldsymbol{\nabla}\rho)\right)\boldsymbol{I}+\right.\\ &\quad\left.\lambda\boldsymbol{\nabla}\rho\otimes\boldsymbol{\nabla}\rho\right]:\boldsymbol{\nabla}\mathbf{u}\,.\end{aligned} \tag{6.21}$$

The term under divergence defines the entropy flux. Since the entropy production must be positive definite in terms of the thermodynamic forces (Clausius-Duhem inequality), the other two contributions on the right hand side are required to be positive. Assuming linear dependence of thermodynamic fluxes – terms in square brackets in (6.21) – on thermodynamic forces – $\boldsymbol{\nabla}\theta$ and $\boldsymbol{\nabla}\mathbf{u}$ – leads to identify the stress tensor with the following expression,

$$\begin{aligned}\boldsymbol{\tau} &= -p_0\boldsymbol{I}+\boldsymbol{\Sigma}\\ &= \left(-p_0+\frac{\lambda}{2}|\boldsymbol{\nabla}\rho|^2+\rho\boldsymbol{\nabla}\cdot(\lambda\boldsymbol{\nabla}\rho)\right)\boldsymbol{I}\\ &\quad-\lambda\boldsymbol{\nabla}\rho\otimes\boldsymbol{\nabla}\rho+\\ &\quad+\mu\left[\left(\boldsymbol{\nabla}\mathbf{u}+\boldsymbol{\nabla}\mathbf{u}^T\right)-\frac{2}{3}\boldsymbol{\nabla}\cdot u\boldsymbol{I}\right]\,,\end{aligned} \tag{6.22}$$

where the usual viscous terms with $\mu > 0$ in the last line are the source of mechanical irreversibility (for the sake of simplicity we have assumed the second viscosity coefficient equal to $-2\mu/3$). Concerning the energy flux, positive entropy production, second line in Eq. (6.21), calls for

$$\mathbf{q_e} = \lambda\rho\boldsymbol{\nabla}\rho\boldsymbol{\nabla}\cdot\mathbf{u} - k\boldsymbol{\nabla}\theta\,, \tag{6.23}$$

where $k > 0$ is the thermal conductivity.

Hereafter we assume constant values for μ and k and we adopt the van der Waals free energy density $\hat{f}_0$, Eq. (6.2), to obtain

$$p_0 = \bar{R}\frac{\rho\theta}{1-b\rho} - a\rho^2\,, \tag{6.24}$$

$$\mathcal{U} = \frac{\bar{R}}{\delta}\theta - a\rho + \frac{\lambda}{2\rho}|\boldsymbol{\nabla}\rho|^2\,, \tag{6.25}$$

where the last term corresponds to the capillary contribution to the internal energy, $\mathcal{U}_c = \dfrac{\lambda}{2\rho}|\boldsymbol{\nabla}\rho|^2$.

Dimensionless parameters By introducing the dimensionless (or reduced) variables

$$\rho^* = \rho/\rho_c\,, \qquad p^* = p/p_c\,, \qquad \theta^* = \theta/\theta_c\,,$$

where

$$\rho_c = \frac{1}{3b}\,, \qquad p_c = \frac{a}{27b^2}\,, \qquad \theta_c = \frac{8a}{27\bar{R}b}$$

are the critical values of density, pressure and temperature, respectively, the caloric and thermal equations of state take the form

$$\begin{aligned} E^* &= \frac{8}{3\delta}\rho^*\theta^* - 3\rho^{*2} + \frac{1}{2}\rho^*|\mathbf{u}^*|^2 + \\ &\quad + \frac{1}{2}\mathcal{C}\,|\boldsymbol{\nabla}^*\rho^*|^2\,, \end{aligned} \tag{6.26}$$

$$p_0^* = \frac{8\theta^*\rho^*}{3-\rho^*} - 3\rho^{*2}\,, \tag{6.27}$$

where $u_R = \sqrt{p_c/\rho_c}$ is a reference velocity and L_R is a reference length. Time is made dimensionless with respect to the reference time $t_R = L_R/u_R$. $\mathcal{C} = \lambda\rho_c^2/(p_c L_R^2)$ is a dimensionless parameter quantifying the relevance of capillary stress to the dynamics.

For the reader's convenience, the constitutive laws are rewritten in dimensionless variables to highlight the relevant control parameters. The asterisk (*) is hereafter suppressed for the ease of notation:

$$\begin{aligned}\boldsymbol{\tau} &= \left(-p_0 + \frac{\mathcal{C}}{2}|\boldsymbol{\nabla}\rho|^2 + \mathcal{C}\rho\nabla^2\rho\right)\boldsymbol{I} - \mathcal{C}\,\boldsymbol{\nabla}\rho\otimes\boldsymbol{\nabla}\rho + \\ &\quad + \frac{1}{Re}\left[\left(\boldsymbol{\nabla}\mathbf{u} + \boldsymbol{\nabla}\mathbf{u}^T\right) - \frac{2}{3}\boldsymbol{\nabla}\cdot u\boldsymbol{I}\right], \end{aligned} \tag{6.28}$$

$$\mathbf{q_e} = \mathcal{C}\,\rho\boldsymbol{\nabla}\rho\boldsymbol{\nabla}\cdot\mathbf{u} - \frac{1}{Re\,Pr}\boldsymbol{\nabla}\theta\ . \tag{6.29}$$

$Re = L_R\sqrt{p_c\rho_c}/\mu$ is a Reynolds number based on critical quantities and $Pr = 3\mu\bar{R}/(8k)$ is the analogous for a van der Waals fluid of the familiar Prandtl number.

Algorithms & solution techniques

The numerical solution of the system of equations (6.15 – 6.17) is challenging due to a combination of different physical phenomena, which all require a specialized numerical technique.

Apart from the extremely thin liquid-vapor interface that requires a high numerical resolution, the system supports i) the propagation of shock waves; ii) viscous diffusion and capillary dispersion; iii) phase change and transition to and from supercritical conditions.

From a numerical point of view, compressibility and shock wave propagation would suggest the adoption of specialized shock-capturing methods, like

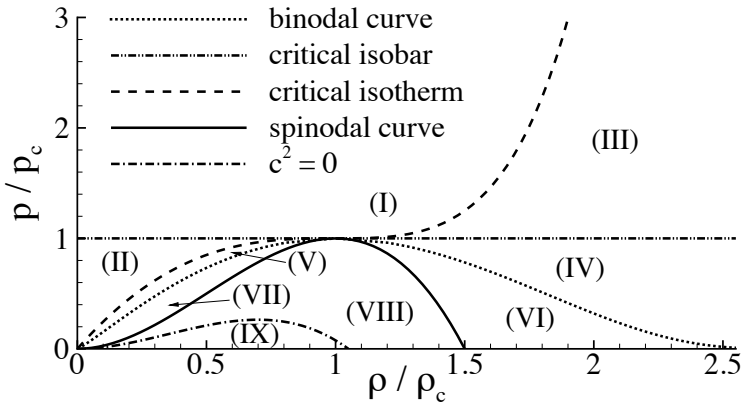

Figura 6.2: Phase diagram in the $p - \rho$ plane. In the zone (I) where $p > p_c$ and $\theta > \theta_c$ the fluid is in supercritical state. Zone (II), characterized by $p < p_c$ but $\theta > \theta_c$, is the gas region. Conversely, zone (III) where $p > p_c$ but $\theta < \theta_c$ is the compressible-liquid region. In zone (IV) and (V) the fluid is in liquid or vapor state, respectively. Under the binodal curve, which represent the saturation conditions, we find zones (VI) and (VII) of metastable liquid and metastable vapor state, respectively. The spinodal curve, defined as $\partial p/\partial\rho|_\theta = 0$, separates the metastable regions from the unstable region (VIII). Finally, in subset of the unstable region, zone (IX), $c^2 = \partial p/\partial\rho|_\eta < 0$, i.e. the sound speed becomes imaginary.

the Essentially Non Oscillatory schemes, or their Weighted WENO extension [130]. However hyperbolic features conflict with the diffusive and dispersive behavior induced by viscosity and capillarity. Moreover, at least for the van der Waals equation of state, (6.27), a region of the thermodynamic phase space exists where $\partial p_0/\partial\rho|_\eta < 0$. As well known, in ordinary conditions, this derivative defines the square of the sound speed, implying that where $c^2 < 0$ hyperbolic behavior changes into parabolic, see Fig. 6.2 for an explanatory diagram. The strategy conceived to deal with this complex mathematical structure, is based on two basic ingredients: 1) Identification of the hyperbolic part of the operator and its extension to the parabolic region where

$c^2 < 0$; 2) Operator splitting into hyperbolic and non-hyperbolic part. For convenience, these two ingredients will be discussed in revers order.

Operator splitting As discussed in § 1, the state of the system is identified by three basic, conserved fields, namely mass, momentum and total energy density, to be collectively addressed here as the state vector $\mathbf{U}(\mathbf{x}, t) = (\rho, \rho\mathbf{u}, E)^T$. Formally system (6.15 – 6.17) can be written as

$$\frac{\partial \mathbf{U}}{\partial t} = \mathcal{N}[\mathbf{U}] = \mathcal{H}_e[\mathbf{U}] + \mathcal{P}[\mathbf{U}],$$

where $\mathcal{H}_e$ is the extension to the whole phase space of the hyperbolic part of the operator and $\mathcal{P} = \mathcal{N} - \mathcal{H}_e$ is defined accordingly. The explicit expressions of the two operators $\mathcal{H}_e$ and $\mathcal{P}$ will be provided below. After the operator is split as explained, the state vector can be evolved in time exploiting a solution strategy in terms of Strang splitting [135]. Denoting $F_{\mathcal{N}}(t)$ the full propagator such that

$$\mathbf{U}(t + \tau) = F_{\mathcal{N}}(\tau)\mathbf{U}(t),$$

for small τ we can approximate

$$F_{\mathcal{N}}(\tau) = F_{\mathcal{P}}(\tau/4)F_{\mathcal{H}_e}(\tau/2)F_{\mathcal{P}}(\tau/4)$$

where $F_{\mathcal{P}}(\tau)$ is the propagator of system

$$\frac{\partial \mathbf{U}}{\partial t} = \mathcal{P}[\mathbf{U}],$$

while $F_{\mathcal{H}_e}(\tau)$ is defined by

$$\frac{\partial \mathbf{U}}{\partial t} = \mathcal{H}_e[\mathbf{U}] \ .$$

Strang splitting allows for using different algorithms, specialized for each component of the system. The algorithms we selected are a third order

WENO [130] scheme for the hyperbolic part and a second order accurate, centered finite difference scheme for the parabolic part. We performed the time integration of the hyperbolic part with a full explicit, third-order TVD Runge-Kutta scheme. The parabolic operator is advanced in time with a mixed, implicit-explicit scheme, where the linear terms (viscous stress and heat flux) are treated implicitly in order to increase the stability limit.

Definition of the operators above the binodal In the region of phase space where the sound speed is well defined, the hyperbolic step is

$$\frac{\partial \rho}{\partial t} = -\boldsymbol{\nabla} \cdot (\rho \mathbf{u}) \ , \tag{6.30}$$

$$\frac{\partial \rho \mathbf{u}}{\partial t} = -\boldsymbol{\nabla} \cdot (\rho \mathbf{u} \otimes \mathbf{u} + p_0 \boldsymbol{I}) \ , \tag{6.31}$$

$$\frac{\partial E_0}{\partial t} = -\boldsymbol{\nabla} \cdot [\mathbf{u} (E_0 + p_0)] - \frac{\partial (\rho \mathcal{U}_c)}{\partial t} \ . \tag{6.32}$$

where $E_0 = \rho (\mathcal{U}_0 + 1/2|\mathbf{u}|^2)$ is the total energy density deprived of the capillary contribution, which reproduces the classical Euler equation. The capillary contribution to the energy $(\rho \mathcal{U}_c)$ is treated as an explicit forcing term depending on the density gradient. Here, as already stated, a van der Waals fluid is assumed in the equations of state. The parabolic part of the operator corresponds to

$$\frac{\partial \rho}{\partial t} = 0 \, , \tag{6.33}$$

$$\frac{\partial \rho \mathbf{u}}{\partial t} = \boldsymbol{\nabla} \cdot \boldsymbol{\Sigma} \, , \tag{6.34}$$

$$\frac{\partial E}{\partial t} = \boldsymbol{\nabla} \cdot \left(-\frac{1}{2} \lambda |\boldsymbol{\nabla} \rho|^2 \mathbf{u} + \boldsymbol{\Sigma} \cdot \mathbf{u} - \mathbf{q}_e \right) \ , \tag{6.35}$$

where the capillary contribution (first term in the right hand side of the equation for E) has been included in the energy flux.

Definition of the operators below the binodal In the coexistence region below the binodal (or coexistence curve, Fig. 6.2), which contains the region where $c^2 < 0$, a Maxwell-like rule is used. Using the additivity of specific volume and entropy, mass density and specific entropy can be written as

$$\frac{1}{\rho} = (1-\alpha)\frac{1}{\rho_V(\theta)} + \alpha\frac{1}{\rho_L(\theta)}$$
$$\eta_{sat} = (1-\alpha)\eta_V(\theta) + \alpha\eta_L(\theta)$$

where subscript L and V denote pure liquid and vapor at the given temperature. The above relations can be inverted to yield

$$\alpha = \alpha(\rho, \eta_{sat})$$
$$\theta = \theta(\rho, \eta_{sat}) \ .$$

For the mixture of vapor and liquid, the saturation pressure depends only on temperature, such that

$$p_{sat} = p_{sat}(\theta) = p_{sat}(\rho, \eta_{sat}) \ .$$

This expression allows to extract the sound speed as

$$c_{sat}^2 = \left.\frac{\partial p_{sat}}{\partial \rho}\right|_{\eta_{sat}} > 0$$

whose final expression is

$$c_{sat}^2 = \frac{\left(\frac{\mathrm{d}p_{sat}}{\mathrm{d}\theta}\right)^2}{\rho^2\left(\frac{\mathrm{d}\eta_L}{\mathrm{d}\theta} + \frac{1}{\rho_L^2}\frac{\mathrm{d}p_{sat}}{\mathrm{d}\theta}\frac{\mathrm{d}\rho_L}{\mathrm{d}\theta} - \frac{\rho-\rho_L}{\rho\rho_L}\frac{\mathrm{d}^2p_{sat}}{\mathrm{d}\theta^2}\right)} \ . \tag{6.36}$$

The interested reader is referred to [102] for details on the thermodynamic derivation of the sound speed for the mixture.

In fact, the actual pressure differs from the saturation pressure,

$$p_0 = p_0(\theta, \rho) = p_{sat}(\theta) + \delta p(\theta, \rho)\,,$$

to the extent that $c^2 = \partial p/\partial\rho|_\eta$ may become negative. We stress however that $c^2_{sat} > 0$, thereby allowing to identify the hyperbolic part of the evolution operator in the region below the binodal (which includes the region where $c^2 < 0$).

Concerning the energy density, we consistently address the energy of the liquid-vapor mixture,

$$E_{sat} = 1/2\rho|\mathbf{u}|^2 + \rho\left[(1-\alpha)\mathcal{U}_V + \alpha\mathcal{U}_L\right]\ .$$

Again, the actual energy is

$$E = E_{sat} + \delta E\ .$$

With the above position, the split system in the region below the binodal reads

$$\frac{\partial\rho}{\partial t} = -\boldsymbol{\nabla}\cdot(\rho\mathbf{u})\ , \tag{6.37}$$

$$\frac{\partial\rho\mathbf{u}}{\partial t} = -\boldsymbol{\nabla}\cdot(\rho\mathbf{u}\otimes\mathbf{u} + p_{sat}\boldsymbol{I})\ , \tag{6.38}$$

$$\frac{\partial E_{sat}}{\partial t} = -\boldsymbol{\nabla}\cdot\left[\mathbf{u}\left(E_{sat} + p_{sat}\right)\right] - \frac{\partial\delta E}{\partial t}\,, \tag{6.39}$$

for the hyperbolic part and

$$\frac{\partial\rho}{\partial t} = 0\,, \tag{6.40}$$

$$\frac{\partial\rho\mathbf{u}}{\partial t} = -\boldsymbol{\nabla}\delta p + \boldsymbol{\nabla}\cdot\boldsymbol{\Sigma}\,, \tag{6.41}$$

$$\frac{\partial E}{\partial t} = \boldsymbol{\nabla}\cdot\left[-\mathbf{u}\left(\delta E + \delta p\right) + \boldsymbol{\Sigma}\cdot\mathbf{u} - \mathbf{q}_e\right]\ , \tag{6.42}$$

for the parabolic part, respectively.

We stress that the definitions of the operators given separately for the two regions of phase space join continuously at the binodal curve.

Thermodynamic state of the liquid-vapor mixture Concerning the thermodynamics of the homogeneous vapor-liquid mixture below the binodal, the saturation densities $\rho_V(\theta)$ and $\rho_L(\theta)$, are evaluated as follows. Given the state of the system in terms of density and temperature, the corresponding chemical potential is

$$\mu_c^0 = \frac{8}{3}\theta\left[\frac{\rho}{3-\rho} - \log\left(\frac{K\,(3-\rho)\theta^{1/\delta}}{3\rho}\right)\right] - 6\rho\,. \tag{6.43}$$

Chemical, thermal and mechanical equilibrium require equality of temperature, $\theta_V = \theta_L = \theta$, pressure, $p_V = p_L$, and chemical potential $\mu_V^0 = \mu_L^0$. After some algebra, one ends up with the following non-linear 2x2 system for ρ_L and ρ_V

$$\begin{aligned}
&\frac{8\theta\rho_L}{3-\rho_L} - 3\rho_L^2 = \frac{8\theta\rho_V}{3-\rho_V} - 3\rho_V^2\,,\\
&\theta\left[\frac{3\,(\rho_L-\rho_V)}{(3-\rho_L)\,(3-\rho_V)} + \log\left(\frac{\rho_L\,(3-\rho_V)}{\rho_V\,(3-\rho_L)}\right)\right] =\\
&= \frac{9}{4}\,(\rho_L-\rho_V)\,,
\end{aligned}$$

which is solved by a standard Newton algorithm.

Simulations setup All the simulations have been performed using an axisymmetric code, exploiting cylindrical symmetry, see the sketch in Fig. 6.3. The system is initialized with a vapor bubble of radius R_{eq} centered in z_0, the distance between the wall and the bubble center. The effect of the initial distance is analyzed by performing 5 simulations at different z_0. The vapor

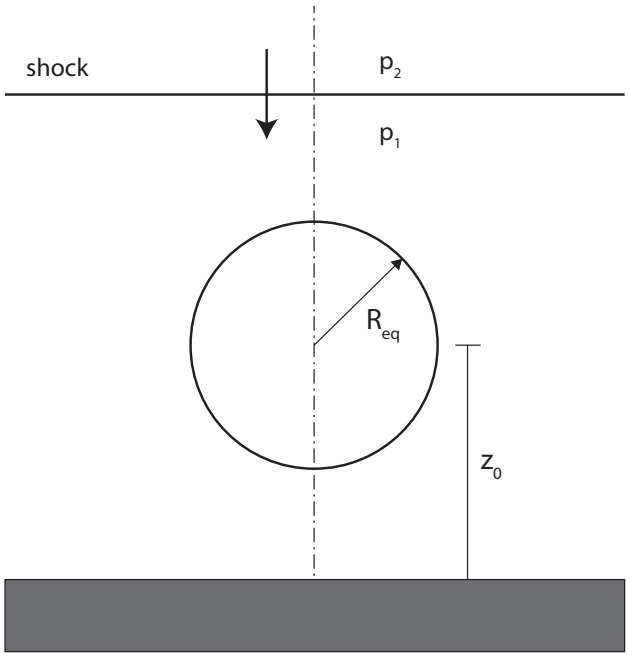

Figura 6.3: Sketch of the simulation setup.

bubble is in equilibrium with the confining liquid at temperature $\theta/\theta_c = 0.6$. A shock wave with intensity $I = (p_2 - p_1)/p_1$, with p_2 and p_1 the pressure in the perturbed and the unperturbed state, respectively, is initialized to hit the bubble and trigger the collapse. In most of the results to be discussed, $I = 75$. A further case at $I = 400$ is also considered, to highlight the destabilizing effect of the impinging shock intensity. The fluid domain has dimension $4R_{eq} \times 4R_{eq}$ and has been discretized with a uniform grid 2048×2048. The mesh influence has been analyzed by comparing the bubble evolution on a coarser mesh, 1024×1024. Since the results are nearly indistinguishable, only those obtained with the finer mesh has been produced here since the accuracy, in particular during the final stage of the collapse, is expected to be slightly better. An adaptive timestep, ranging from 10^{-5} down to 10^{-8},

has been used during the simulations to comply with stability and accuracy requirements. In particular, the smaller ones are used during the collapse stage, when the shockwaves are formed, in order to follow the large and fast changes experienced by the field. Selecting $L_R = R_{eq}$, the dimensionless parameters of the simulations are: $Re = 50$, $Pr = 0.2$ and $\mathcal{C} = 1.6 \times 10^{-4}$. These values correspond, e.g., to a bubble radius order of $100nm$ with typical viscosity, thermal conductivity, surface tension and critical values of water.

Results and discussions

Overall, the dynamics of the bubble is characterized by a sequence of rebounds, as shown by the plots of bubble volume vs time reported in Fig. 6.4 for different wall normal distances of the bubble and for the triggering shock strength $I = 75$. Generically, the first collapse phase (volume decreasing in time), is only slightly affected by the initial wall distance. After the minimum volume is reached, a plateau is observed. It will be shown to be related to the interaction of the bubble with the shock wave which is emitted when the collapse is arrested and is successively reflected back by the wall. After the shock/bubble interaction is completed, the bubble starts expanding up to a maximum volume, which is systematically lower than the initial value. The process ends with the full condensation of the bubble.

Equilibrium vapor bubble Before discussing in detail the actual dynamics observed in the simulations, it may be instrumental to identify the effect of a compression on an equilibrium bubble. Given the temperature, a system formed by a vapor bubble in equilibrium with the liquid should satisfy the

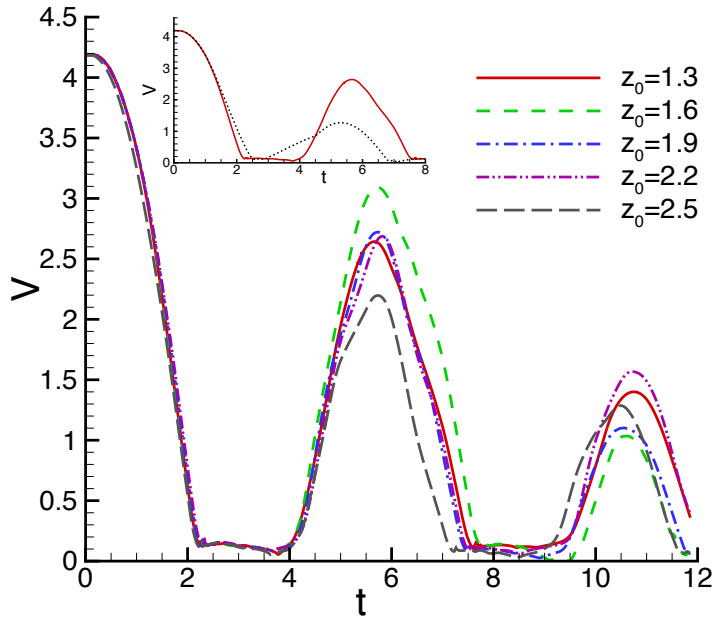

Figura 6.4: Time evolution of the bubble volume for different initial wall–bubble distance z_0. The initial distance does not substantially affect the bubble dynamic during the first collapse, indeed the collapse time remains unaltered in all the numerical experiments. The characteristic frequency of collapse and re-expansion is not a function of the initial position. Conversely, the dynamic of the re-expansion and of the successive collapses is influenced by the initial position in a non trivial way. In the inset it is reported the comparison between the shock-induced collapse near a wall (the solid red curve, $z_0 = 1.3$) and in free space (dotted black curve) where the bubble does not experience a volume plateau after the collapse.

conditions of constant chemical potential, Eq. (8.16),

$$\mu_c^0(\rho_L, \theta) = \mu_{eq}$$
$$\mu_c^0(\rho_V, \theta) = \mu_{eq}\,,$$

where the equilibrium state is parametrized by θ and μ_{eq}, and the chemical potential for a van der Waals fluid is explicitly provided in Eq. (6.43).

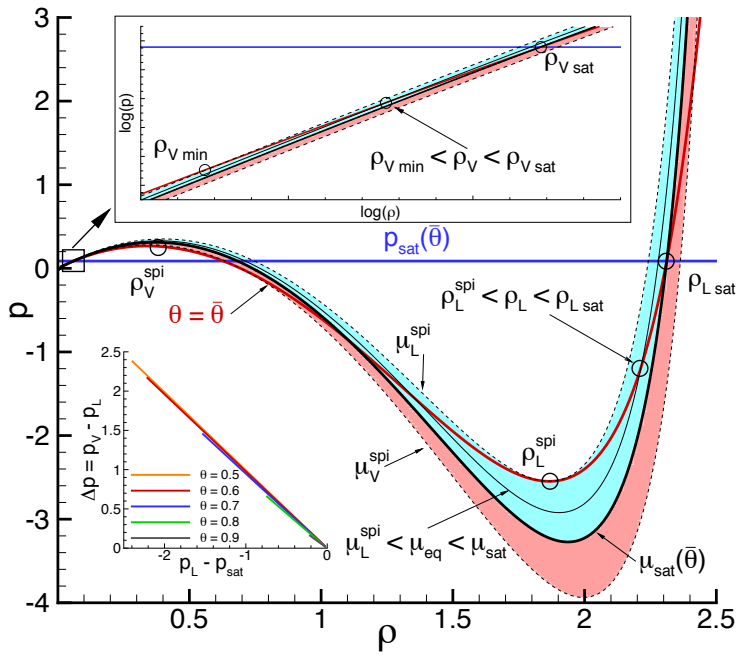

Figura 6.5: Illustration of the iso-chemical potential (black curves), isotherm (red curve, $\bar{\theta} = 0.6$) and isobar (blue curve) for a van der Waals equation of state in the ρ–p plane. The range of very low densities is enlarged in the top inset. The equilibrium properties (same chemical potential, temperature and pressure) identify the saturation densities (ρ_{Vsat} and ρ_{Lsat}) as the intersection of the iso-chemical potential μ_{sat} (thicker black curve) and the isotherm and isobar. The two colored regions span the chemical potential values where a vapor bubble (light blue) or a liquid drop (light red) can be found as a metastable equilibrium condition for the fluid system. In the bottom inset the effect of reducing the liquid pressure, p_L, under the saturation value on the equilibrium pressure difference, Δp, between the vapor bubble and the external liquid, is plotted for different fixed temperatures. The corresponding bubble radius can be obtained by the classical Young-Laplace equation.

The equilibrium conditions are described in Fig. 6.5, where a constant chemical potential line, thin solid line, is plotted in the $\rho - p$ plane. An isotherm is also reported as a red solid line. The intersection of the two curves

determines three points in the plane. The low density one corresponds to the vapor, ρ_V, p_V, and is hardly visible on the scale of the plot, see the enlargement on the upper part of the figure. The intersection at largest density corresponds to the liquid, ρ_L, p_L. The third intersection, at intermediate density $\rho_V^{spi}(\theta) < \rho_{un} < \rho_L^{spi}(\theta)$, always belongs to the unstable region of the phase space, below the spinodal, see Fig. 6.2. The region of the phase space where the above three intersections exist is shown by the colored band in the figure. More specifically, denoted by $\mu_L^{spi}(\theta)$ and $\mu_V^{spi}(\theta)$ the chemical potential at the liquid and vapor spinodal, the condition $\mu_L^{spi}(\theta) < \mu_{eq} < \mu_V^{spi}(\theta)$ defines the relevant range of chemical potential. Outside the colored band, only one intersection is found, corresponding to vapor or liquid, according to the condition $\mu_{eq} < \mu_L^{spi}$ or $\mu_{eq} > \mu_V^{spi}$, respectively.

The pressure, of the vapor, say, is recovered from the pressure equation of state (6.24), in combination with the expression for the chemical potential Eq. (6.43), to yield $p_V = p_V(\mu_{eq}, \theta)$. The chemical potential at saturation, black thick line in Fig. 6.5, is such that $p_V(\mu_{sat}, \theta) = p_L(\mu_{sat}, \theta) = p_{sat}(\theta)$. As a property of the solution, $p_L \lesseqgtr p_V$ when $\mu_{eq} \lesseqgtr \mu_{sat}$. It follows that, in order to have a bubble ($p_V > p_L$), the chemical potential must be smaller than the saturation value, $\mu_L^{spi} < \mu_{eq} < \mu_{sat}$, light blue band in Fig. 6.5. In this case the vapor is stable (i.e. the vapor point is above the binodal) and the liquid is metastable (liquid between binodal and spinodal). The other case, $\mu_V^{spi} > \mu_{eq} > \mu_{sat}$, corresponds to a drop of stable liquid in metastable vapor (light red band in the figure).

By inverting the relationship $p_L = p_L(\mu_{eq}, \theta)$ and inserting it in the expression for vapor pressure, $p_V = p_V(\mu_{eq}, \theta)$, allows to express the pressure

difference between vapor and liquid as a function of the liquid pressure,

$$\Delta p = p_V - p_L = f(p_L, \theta)\,,$$

where $\Delta p > 0$ (vapor bubble) when $p_L < p_{sat}$. This relation, illustrated in the lower inset of Fig. 6.5 for several temperatures, is hardly distinguishable from a straight line on the adopted scale. Since $\mu_L^{spi} < \mu_{eq} < \mu_{sat}$, the corresponding range of liquid pressure is $p_L^{spi} < p_L < p_{sat}(\theta)$, where p_L^{spi} is the pressure at the liquid spinodal. When the liquid pressure belongs to the allotted interval, the equilibrium radius of the bubble can then be estimated by using the Young-Laplace equation, $R_{eq} = 2\sigma/\Delta p$ (the exact solution requires solving the corresponding problem in the phase field context [45]).

Let us consider the bubble-liquid system in equilibrium with a given pressure p_L in the liquid. Assume the liquid is now compressed to a new state, $p'_L = p_L + \delta p_L$. If the compression is such that $p'_L < p_{sat}$, the bubble will find a new equilibrium condition, with a new pressure p'_V and a new radius R'_{eq}. A counterintuitive effect is that, under compression of the liquid, the radius of the new equilibrium bubble increases. This is opposite to the behavior expected from a gas bubble, and is explained by the inset of Fig. 6.5 where the pressure jump across the interface is shown to be a decreasing function of the liquid pressure. A little more though immediately provides the clue for understanding this behavior. In fact, increasing the pressure, the liquid gets closer to saturation conditions, implying that also the vapor inside the bubble approaches saturation, see the inset of Fig. 6.5. The consequence is that the pressure difference Δp between vapor and liquid decreases, leading to a larger equilibrium radius as a consequence of the Young-Laplace equation.

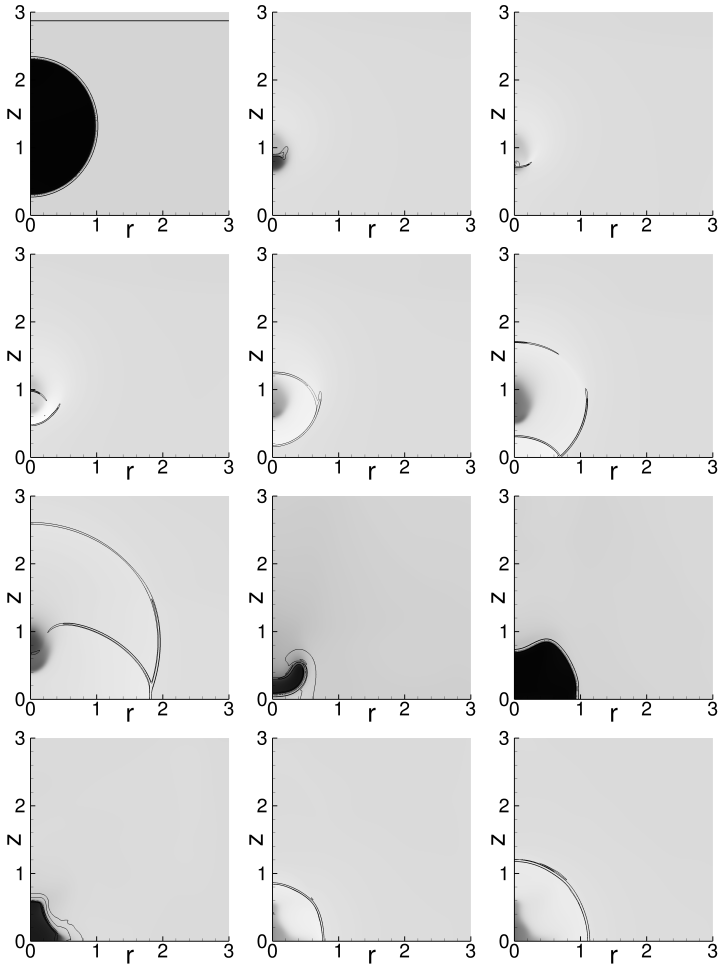

Figura 6.6: Snapshots during the evolution of a collapsing bubble with $z_0 = 1.3$. The sequence runs from left to right and from top to bottom and is not uniformly spaced in time ($t = 0, 2.237, 2.261, 2.28, 2.316, 2.376, 2.527, 4.152, 6.407, 7.474, 7.683, 7.736$). The grey tones from darker to lighter represent the density field from smaller (vapor phase) to higher (liquid phase). The black lines are Schlieren-like iso-lines obtained as $S = \exp(-|\boldsymbol{\nabla} p_0|/|\boldsymbol{\nabla} p_0|_{max})$. The drawn iso-levels are $S = 0.9$ and $S = 1$ in order to highlight the regions with the highest pressure gradients, i.e. the vapor-liquid interface and the shockwaves.

If the compression exceeds the saturation pressure, no vapor bubble can exist in equilibrium with the compressed liquid: in this case the vapor condenses altogether, and the new equilibrium state corresponds to a single phase, pure liquid. Our interest here is focused on the non equilibrium process that leads to such eventual condensation, when the compression is associated to a shock wave in the liquid impinging the vapor bubble. In order to achieve full condensation the shock wave amplitude $p_2 - p_1$ should be larger than $p_{sat} - p_1$, i.e. $I > p_{sat}/p_1 - 1$, where p_1 is the liquid pressure in equilibrium with the initial vapor bubble.

Non-equilibrium process Experiments on laser induced bubbles in water [109] show that energy deposition by a focused laser beam leads to a fast local vaporization and the compression of the liquid. By measuring the speed of the shock wave, the authors could find the intensity of the shock wave as a function of the energy of the laser pulse. It is found that pressures in excess of 10 GPa are easily excited in water at standard conditions. Clearly the strength of the shock wave decreases with the distance from the focusing point, confirming that almost planar waves can easily be generated in the liquid with the intensity we are using here to trigger the collapse of the bubble ($I \in [75, 400]$).

The evolution of the vapor bubble is represented in Figs. 6.6-6.7 for two different initial wall distances, $z_0 = 1.3$ and $z_0 = 1.9$, respectively. The weak impinging shockwave and the proximity of the wall is not sufficient to immediately break the spherical symmetry and to produce the classical liquid jet that porates the bubble, clearly observed in millimeter-bubble experiments [14, 86, 112]. At sub-micron scale the surface tension is, in fact, predominant

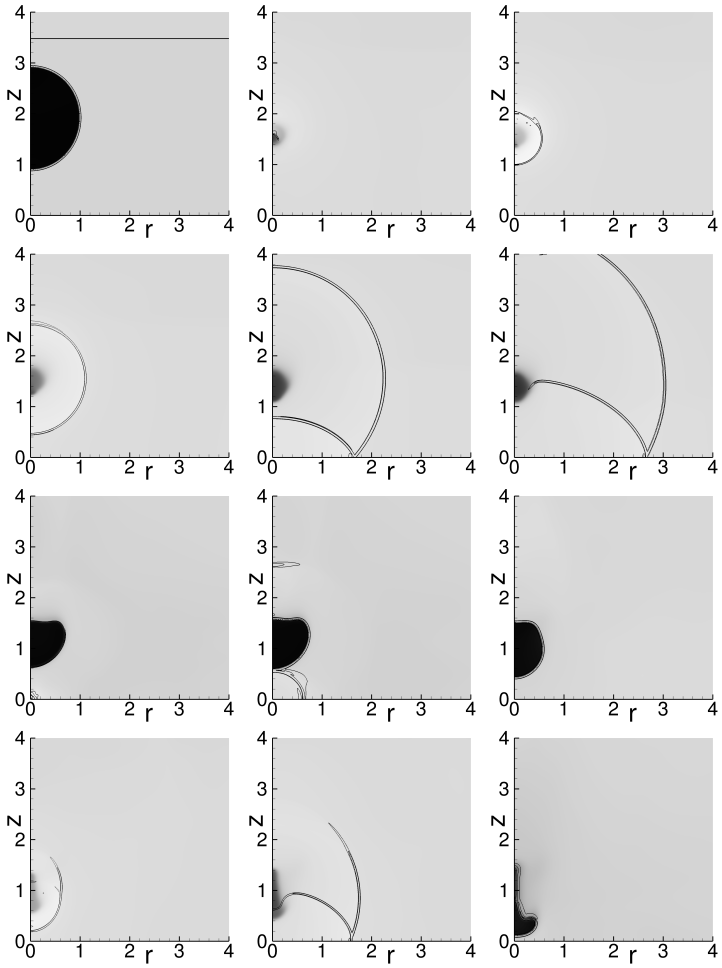

Figura 6.7: Snapshots during the evolution of a collapsing bubble with $z_0 = 1.9$ taken at times $t = 0, 2.266, 2.319, 2.395, 2.399, 2.771, 4.545, 4.627, 7.04, 7.533, 7.736, 9.482$. The grey tones and the iso-lines are the same of Fig. 6.6.

and preserves the nearly spherical shape during the first part of the evolution. Symmetry breaking eventually occurs when the bubble shrinks to its minimum volume and a non-spherical shockwave is emitted. By comparing Figs. 6.6 and 6.7, the asymmetry is stronger for the bubble closer to the wall,

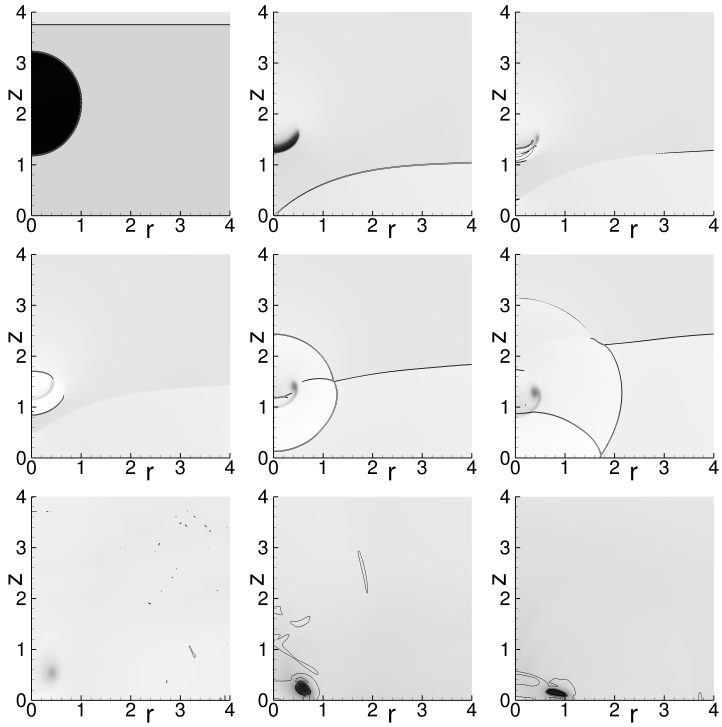

Figura 6.8: Snapshots during the evolution of a collapsing bubble with $z_0 = 2.2$ and a trigger shockwave with intensity $I = 400$. The time instants correspond to $t = 0, 0.948, 0.985, 1.007, 1.068, 1.156, 1.766, 2.36, 2.822$. The grey tones and the iso-lines are the same of Fig. 6.6. The stronger impinging shock initiates the liquid jet formation and leads to the bubble poration.

where, instead of being more or less spherical, the shockwave produced at collapse consists of two curved shock fronts that propagate toward and away from the wall. The former is eventually reflected by the solid wall and strikes again the re-expanding bubble. During this stage the bubble becomes flatter (elongated in the radial direction) and moves toward the wall. The expansion stage is strongly affected by the bubble–wall distance, with the closest bubble (Fig. 6.6) touching the wall and the farthest one (e.g. in Fig. 6.7) remaining detached. During the bubble expansion, the liquid in the thin layer between

vapor and wall is compressed and a new shockwave is observed, third row of Fig. 6.7. This sequence of events completely breaks the spherical symmetry, thereby reducing the strength of the successive collapse. Eventually, the field becomes more and more complex, until dissipation prevails. It is worth noting that, at a qualitative level, the configuration of the shock waves compares very well with results found in experiments in similar conditions, [139]. It should be stressed however that in the experiments the bubble is usually much larger, typically millimeter size. However femtosecond lasers allow to generate nano-sized bubbles, see [145].

Increasing the strength of the impinging shockwave, liquid-jet formation is observed. In Fig. 6.8 the evolution of the vapor bubble triggered by a shockwave of intensity $I = 400$ is represented up to the first re-expansion stage. The shape of the collapsing bubble becomes much flatter than observed at weaker shock strengths and the strong vorticity generated at the periphery of the bubble gives rise to the bubble poration by inducing a liquid jet focused toward the wall. In the third row of Fig. 6.8, during the re-expansion stage, the bubble acquires an annular shape and the liquid jet impinges the wall and produces a radial flow.

A direct comparison of the flow induced by the bubble collapse at different strengths of the triggering shockwave is reported in Fig. 6.9. The liquid jet directed toward the wall is more pronounced for $I = 400$ and the flow is strong enough to pierce the bubble leading to an annular shape. In fact, although a wall-directed flow is observed also in the case of the weaker initial shockwave, at $I = 75$ the bubble is not flat enough to be pierced by the liquid jet and the overall effect reduces to a displacement of the bubble toward the wall.

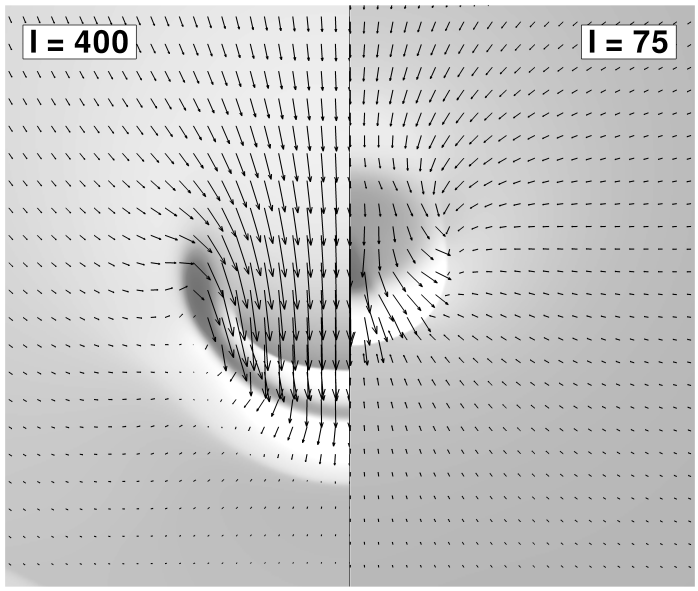

Figura 6.9: Comparison of the flow fields for two different shock intensities. On the left the case $I = 400$ where it is apparent the liquid jet formation. On the right the case $I = 75$. The plotted vectors are not at the maximum grid resolution to increase the clearness of the figure.

A crucial aspects of the phenomenology is the transition to supercritical conditions during the last stage of the collapse [96]. The formation of an incondensable phase prevents the complete collapse of the bubble, reverting the motion to an outward expansion. Overall, a sequence of oscillations sets in, as shown in Fig. 6.4, where the quantity reported on the ordinate is the volume of the non-liquid phase in the system (vapor and supercritical phases). During each successive collapse, the vapor is compressed and its temperature raises locally bringing the system in supercritical conditions. As already anticipated, Fig. 6.4, the volume during the first collapse stage is almost independent of the bubble-wall distance. On the contrary, the re-

expansion stage is affected by the initial position. The following dynamics is affected by the complex interactions between the reflected shockwaves and the bubble motion. The time of the successive collapses are slightly different for the different cases (differences up to 10%) and the maximum volume achieved after the second re-expansion is not monotonous with z_0. In the inset of Fig. 6.4 we compare the volume evolution of a shock-induced collapse in free space (black dotted curve) with the one near the wall (red solid curve, $z_0 = 1.3$). The overall dynamics is again a series of collapses and rebounds but, after each collapse, the bubble in free space does not experience the volume plateau which is an effect of the interaction between the re-expanding bubble and the shockwave reflected back by the wall. The reflected shock counteracts the re-expansion and keeps the bubble small for a longer time.

The eccentricity of the bubble, $e = a/b$, where a is the semi-axis in the z-direction and b is the other semi-axis of the ellipsoid with the same volume of the bubble, $V = 4\pi ab^2/3$, can be used to quantify the change in bubble shape, with $e < 1$ for a flat bubble (elongated in the radial direction). The time evolution of the eccentricity is reported in Fig. 6.10, for several initial distances z_0.

Let us focus on the first collapse stage. As anticipated, during the initial phase of the first collapse, all the bubbles remain almost spherical. The initial distance affects, instead, the shape in the final part of the collapse in such a way that the farther bubbles take a flatter shape ($e < 1$) while the closer ones get slightly elongated toward the wall ($e > 1$) . This trend is the consequence of two counteracting effects of the triggering shockwave. On one hand the impinging shock flattens the bubble during the collapse. On the other hand the bubble-shock interaction weakens the pressure wave and

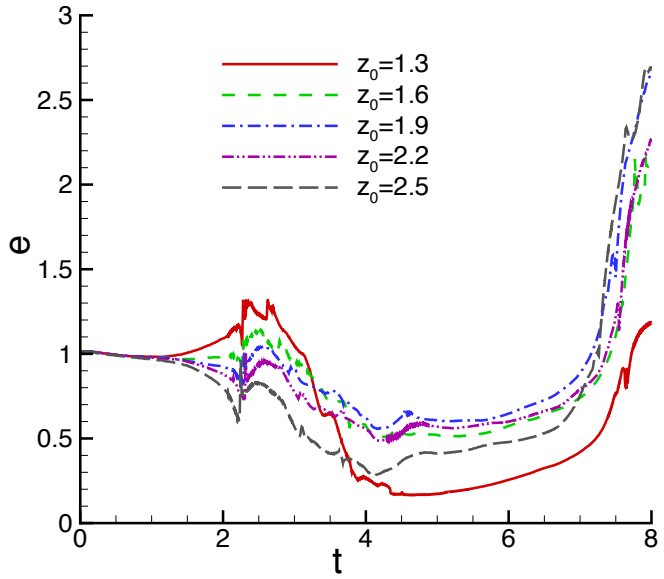

Figura 6.10: Time evolution of eccentricity for different initial distance. The first stage of the collapse is substantially spherical for all the initial distances. The break of symmetry occurs during the final stage of the collapse with the nearest bubble (red curve in the online version) that slightly extends toward the wall while the others in the radial direction. During the shock-interaction stage all the bubbles assumes a pronounced flat shape and remains elongated in the radial direction through all the re-expansion phase. The more drastic change of topology occurs during the second collapse when all the bubbles rapidly invert the elongation toward the wall.

slows it down locally in the region occupied by the bubble (see the second and third snapshots in the first row of Fig. 6.8). Its reflection at the wall produces a non-uniform shockwave impinging again the bubble. The reflected shock is now more intense on the sides than on the center of the bubble thereby enhancing the elongation in the z-direction. The effect is clearly more intense for bubbles closer to the wall.

After the first collapse, up to the re-expansion stage, all the bubbles

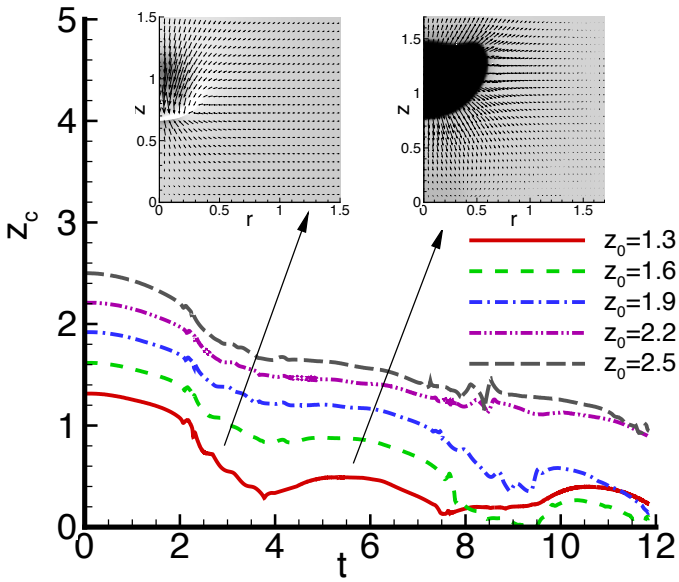

Figura 6.11: Evolution of the position of the bubble center. The faster migration toward the wall occurs between the collapse and the re-expansion stages when the flow produced during the bubble collapse is stronger and convects the bubble. The two snapshots in the insets show the velocity vectors in two different stages: on the left it is highlighted the axial flow during the bubble migration, while on the right it is shown the characteristic quasi-radial flow during the re-expansion phase that stops the axial motion of the bubble.

flatten as a consequence of the radial flow occurring near the wall. The second collapse is characterized by a rapid reduction of the radial semi-axis b (see the third and the forth rows of Fig. 6.7) and therefore by a quick increase of the eccentricity as a consequence of the local high curvature at the equator of the bubble in association with surface tension.

The flow produced during the bubble collapse and the consequent bubble motion is investigated in Fig. 6.11 showing the position of bubble center of mass, z_c. A strong axial flow, clearly visible in the inset on the left, is produ-

ced near the bubble axis during the collapse stage. This flow is responsible for the bubble migration toward the wall after the collapse ($t > 2$). Overall, despite the difference in lengthscale, the observed phenomenology is entirely consistent with the experimental observations on millimeter bubbles reported in [116]. During the re-expansion stage the flow is directed radially outward (inset on the right), stopping the bubble motion toward the wall. The subsequent collapse regenerates the axial flow and the bubble approaches the wall again.

Shockwaves and jets formed during bubble collapse are associated with intense pressure and temperature peaks. At each time instant maximum pressure and temperature are recorded and reported in the plots of Fig. 6.12 and 6.13, respectively. The first peak, both in pressure and temperature, occurs at the end of the first collapse stage, when the bubble stops shrinking. This peak is the strongest one for a bubble collapsing in free space [96]. Figure 6.12 shows that the end of the first collapse is the instant of maximum pressure also for most cases of bubbles collapsing near the wall. However there are conditions where a successive peak exceeds by far the first one. When it occurs, such extremely intense pressure peak is due to the bubble experiencing the second collapse after it translated to get in touch with the wall, see the snapshots in the last row of Fig. 6.6. It may even happen that an intermediate pressure peak occurs between the first and the second collapse. When present, this is due to the expansion of the bubble at a suitable distance to the wall that generates a compression of the fluid between bubble and wall (third row of Fig. 6.7). As already commented, the increase in the triggering shock intensity leads to bubble poration and jet development. Interestingly, at the moment of jet formation, a peak in the pressure field is observed, inset

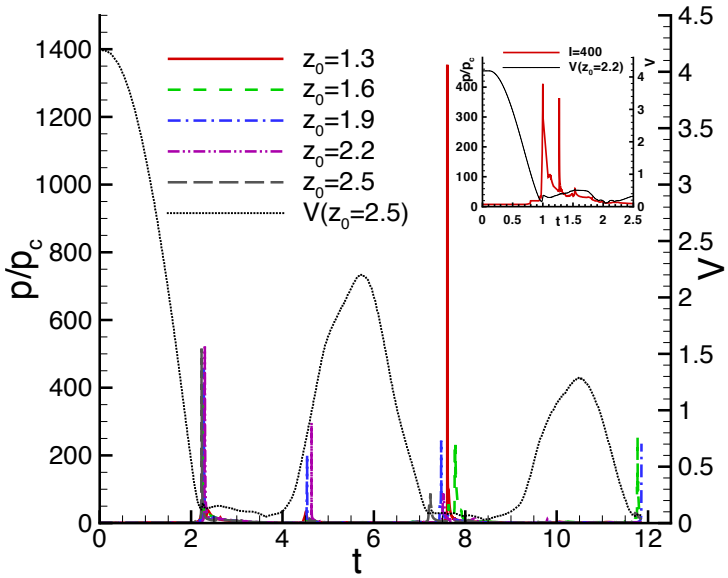

Figura 6.12: Time evolution of the maximum pressure recorded in the whole fluid domain for the five different initial wall-bubble distances. As a reference the dotted curve reports the bubble volume evolution. The most intense pressure peaks are observed when the bubble reaches its minimum volume. In the case of $z_0 = 1.3$, the maximum value is reached at the second collapse because the bubble is pinned on the solid boundary and its collapse is more intense. Of particular interest are the pressure peaks observed during the re-expansion stage for the cases $z_0 = 1.6$ and $z_0 = 2.2$ which are related to the compression of the liquid film between the bubble and the wall, as explained in the text. In the inset we report the time evolution of the maximum pressure in the case with the higher triggering shock intensity.

of figure 6.12. The origin of the pressure peak is purely hydrodynamical, since no corresponding temperature peak occurs, see inset of figure 6.13. Since the jet-induced pressure peak is comparable with that of the shock, the present results seems to confirm the high damaging potential of the jetting phase.

The collapsing bubble induces a strong stress on the solid wall. Figu-

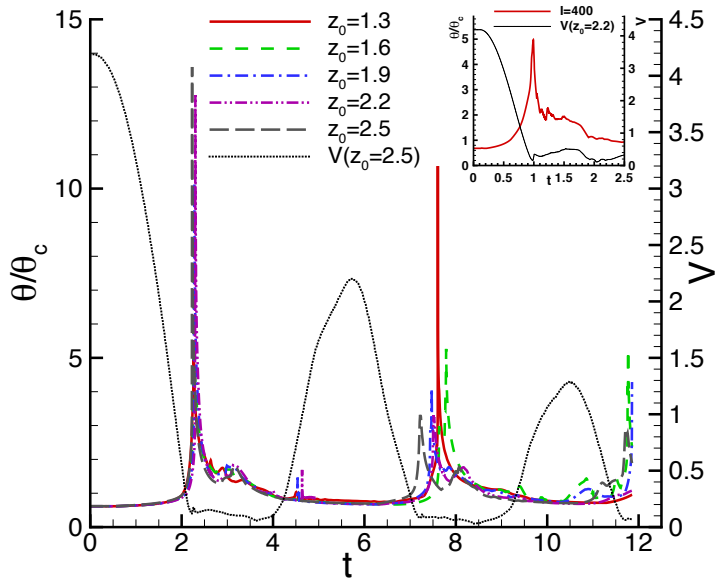

Figura 6.13: Time evolution of maximum temperature recorded in the whole fluid domain. As well as the pressure peaks, the temperature reaches the local maxima when the collapse is completed. Again, it is possible to observe a temperature peak during the re-expansion stage, but it is less apparent than its pressure equivalent. In the inset we report the time evolution of the maximum pressure in the case $I = 400$.

re 6.14 reports the envelope of the pressure maxima at the wall for different initial bubble positions. The inset illustrates the way the envelope is constructed from instantaneous pressure distributions at the wall at successive time instants. By comparing with the pressure maxima in the field, Fig. 6.12, it is clear that the pressure at the wall is much weaker than the maximum inside the field. Nevertheless the typical pressure at the wall is very large, order ten times the critical pressure of the fluid. For water, this would correspond to a pressure in the order of 200 MPa, a figure which compares well with experimental measurements on collapsing bubbles near solid walls [139].

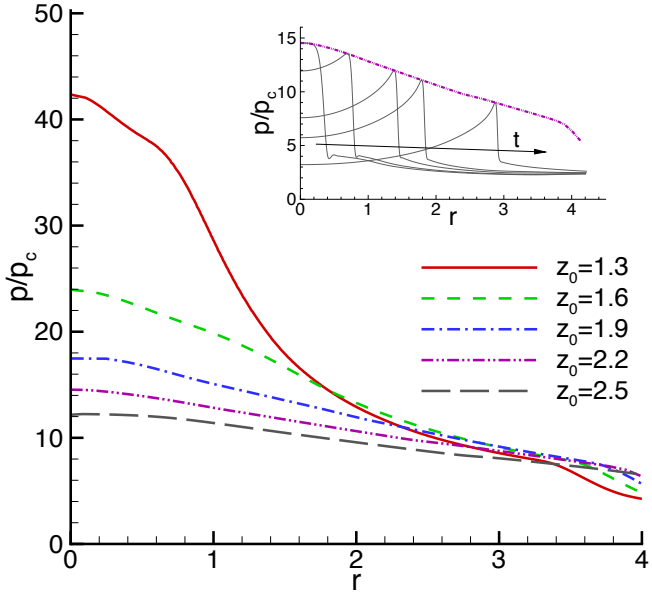

Figura 6.14: Spatial evolution of the maximum pressure values recorded on the wall during propagation of the shock wave for each initial condition. The pressure values are decreasing with increasing of initial bubble distance from the wall. It's possible to observe that for the bubbles placed at distances closer to the wall the shape of the envelope varies strongly due to interaction with the shockwave reflection. Inset: Radial evolution of the pressure range recorded on the wall for initial condition $z_0 = 2.2$. The different dotted lines correspond to different time instants and the purple line corresponds to the envelope of the maximum pressure values.

Concerning the temperature at the wall, in the present conditions extreme values were never experienced, except in cases where the collapsing bubble came in direct contact with the wall.

	p_{max}/p_c	θ_{max}/θ_c
spherical	3×10^5	708
shock induced - no wall	175.16	3.29
shock induced - near wall	384	8.22

Tabella 6.1: Comparison of the maximum pressure and temperature reached during the first collapse in three different geometrical configurations. In all the cases the overpressure that triggers the collapse is of intensity $I = 75$. The data shown as representative of the shock induced collapse in proximity of the wall is referred to the case with $z_0 = 1.6$.

Conclusions

We have numerically studied the collapse of a pure vapor nanobubble near a solid boundary by applying a diffuse interface approach. The model is specially suitable to describe in a consistent and unified way the complex phenomena occurring during cavitation, namely: phase change, latent heat release, shock wave formation and propagation, transition to supercritical conditions. Like in the case of spherically symmetric collapse, a pure vapor bubble is found to collapse with a sequence of volume oscillations, associated to a sequence of successive collapses which are arrested and inverted by the formation of the incondensable, supercritical phase due to compression and latent heat release. In comparison with symmetric collapse, the peak pressures and temperature are significantly lower in the case of aspherical bubble collapse, see Table 6.1. Interestingly, the peak pressure for shock wave induced collapse in free space leads to even lower pressure and temperatures in comparison with those reached when the collapse is triggered near the wall. This indicates that the wall, by confining the radial expansion of the bubble and reflecting the triggering shock enhances the peak pressure level. Despite the pressure peak realized at the wall is significantly lower than the maxima

found inside the field, still large level of stress is transferred to the wall, as potential source of damage. A strong jet is found when the triggering shock strength is sufficiently large. In fact, jet impingement on the wall is often quoted as a concurrent cause of material damage [139].

It is worthwhile noting that the peak pressure and temperature levels obtained in the present simulations are expected to overestimate the experimental values. The reason is the simple equation of state used to make the computations more easily affordable. In particular, a pressure equation equation of state better suited to model a real fluid could help to reduce the peak temperature and pressure values. Moreover, unless extremely weak forcing is used to initiate the bubble collapse, the large temperatures reached inside the bubble are expected to lead to dissociation and ionization phenomena, which concur in substantially limiting the peak temperature.

A further aspect to be considered for future works is the presence of dissolved gas in the liquid to reproduce the condition of partially gas-filled cavitation bubbles that are more commonly found in applications.

Aknowledgement

The research leading to these results has received funding from the European Research Council under the European Union's Seventh Framework Programme (FP7/ 2007-2013)/ERC Grant Agreement No. [339446].
We acknowledge the CINECA award under the Iscra project (project id: IscrC_VBC), for the availability of high performance computing resources and support.

Capitolo 7

Thermally activated vapor bubble nucleation: the Landau–Lifshitz/Van der Waals approach

In this work a the stochastic approach described in Chapter 3 is exploited to study the homogeneous nucleation process. In particular, the liquid-vapor spontaneous phase transition is addressed in a closed system (NVE ensemble) for a Lennard-Jones fluid, initialized in a metastable state (metastable liquid). Starting from a homogeneous liquid phase, thermal fluctuations lead the system to spontaneously decompose in two different phases, and overall the nucleation dynamics can be framed in three different phases. The initial phase (*nucleating phase*) is characterized by a linear growth of the bubble number in time (i.e. at a constant nucleation rate). The second phase (*collapsing phase*) depicting the first part of the expansion stage, and is characterized by a rapidly decreasing number of bubbles mainly due to collapse. Finally, the last phase (*slowly expanding phase*), preceding the new equilibrium state for the system, is governed by the long-time dynamics of

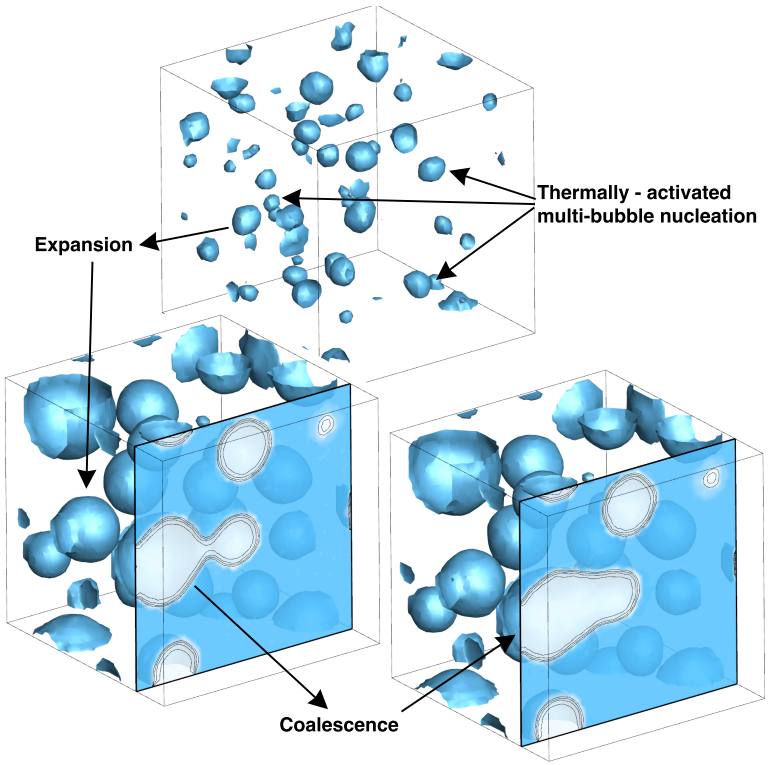

Figura 7.1: Simulation snapshots illustrating the different phases of the nucleation dynamics.

the multi-bubble system. These aspects are clearly summarized in Fig.7.1, representing the different phases we discussed above. The evaluation of the bubble nucleation rates, showed good agreement has been found with MD simulations and with more conventional techniques. Furthermore, in comparison with more classical approaches, this methodology allows to deal with much larger systems observed for a much longer times, otherwise not possible with even the most advanced atomistic models, providing the possibility of observing the long term dynamics of the metastable system, up to the bubble coalescence and expansion stages.

The complete results have been published on PRF (PHYSICAL REVIEW FLUIDS 3, 053604 (2018)), and are reported here with the permission of the authors.

Note: for the sake of brevity the appendices of the paper are not reported, however all the details required are reported in Chapter 3.

abstract

Vapor bubbles are formed in liquids by two mechanisms: evaporation (temperature above the boiling threshold) and cavitation (pressure below the vapor pressure). The liquid resists in these metastable (overheating and tensile, respectively) states for a long time since bubble nucleation is an activated process that needs to surmount the free energy barrier separating the liquid and the vapor states. The bubble nucleation rate is difficult to assess and, typically, only for extremely small systems treated at atomistic level of detail. In this work a powerful approach, based on a continuum diffuse interface modeling of the two-phase fluid embedded with thermal fluctuations (Fluctuating Hydrodynamics) is exploited to study the nucleation process in homogeneous conditions, evaluating the bubble nucleation rates and following the long term dynamics of the metastable system, up to the bubble coalescence and expansion stages. In comparison with more classical approaches, this methodology allows on the one hand to deal with much larger systems observed for a much longer times than possible with even the most advanced atomistic models. On the other it extends continuum formulations to thermally activated processes, impossible to deal with in a purely determinist setting.

Introduction

Thermal fluctuations play a dominant role in the dynamics of fluid systems below the micrometer scale. Their effects are significant in, e.g., the smallest micro-fluidic devices [47, 20] or in biological systems such as lipid membranes [107], for Brownian engines and in artificial molecular motors [115]. They are crucial for thermally activated processes such as nucleation, the precursor of the phase change in metastable systems. Nucleation is directly connected to the phenomenon of bubble cavitation [28] and of freezing rain [32], to cite a few. There, thermal fluctuations allow to overcome the energy barriers for phase transitions [76, 79, 90]. Depending on the thermodynamic conditions, the nucleation time may be exceedingly long, the so-called "rare-event" issue. Classical nucleation theory (CNT) [18] provides the basic understanding of the phenomenon which is nowadays addressed through more sophisticated models like density functional theory (DFT) [113, 92] or by means of molecular dynamics (MD) simulations [49]. These approaches need to be coupled to specialized techniques for rare events, like the string method [148], the forward flux sampling [4] and the transition path sampling [23], to reliably evaluate the nucleation barrier and determine the transition path [67]. For many real systems they are often computationally too expensive and therefore limited to very small domains.

Here we adopt a mesoscopic continuum approach, embedding stochastic fluctuations, for the numerical simulation of thermally activated bubble nucleation. Since the pioneering work of Landau and Lifshitz (1958, 1959) [84] several works contributed to the growing field of "Fluctuating Hydrodynamics" (FH) [61]. More recently the theoretical effort has been followed by a

flourishing of highly specialized numerical methods for the treatment of the stochastic contributions [54, 46, 11, 53]. The present model is based on a diffuse interface [141] description of the two–phase vapor–liquid system [96] similar to the one recently exploited by Chaudhri *et al.* [33] to address the spinodal decomposition. The thermodynamic range of applicability of this approach is subjected to some restrictions: i) at the very first stage of nucleation the vapor nucleii, smaller than the critical size, need to be numerically resolved; analogously, ii) the thin liquid-vapor interface needs to be captured for the correct evaluation of the capillary stresses; iii) fluctuating hydrodynamics predicts that the fluctuation intensity grows with the inverse cell volume, ΔV, leading to intense fluctuations, contrary to the assumption of weak noise needed to derive the model ($\sqrt{\langle \delta f^2 \rangle}/\langle f \rangle \ll 1$). Notwithstanding these restrictions, where it can be applied, this mesoscale approach offers a good level of accuracy (as will be shown when discussing the results) at a very cheap computational cost compared to other techniques. The typical size of the system we simulate on a small computational cluster ($200 \times 200 \times 200\,\mathrm{nm}^3$, corresponding to a system of order 10^8 atomistic particles) is comparable with one of the largest MD simulations [6] on a tier-0 machine. Moreover the simulated time is here $T_{\max} \sim \mu$s to be compared with the MD $T_{max} \sim$ ns. The enormous difference between the two time extensions allows us to address the simultaneous nucleation of several vapor bubbles, their expansion, coalescence and, at variance with most of the available methods dealing with quasi-static conditions, the resulting excitation of the macroscopic velocity field.

The approach we follow basically amounts to directly solving the equa-

tion of motion for the capillary system endowed with thermal fluctuations. In order to interpret the results, a reference nucleation theory is needed. In literature classical nucleation theory (CNT) is the standard choice [18]. In CNT, the two phase system comprising an isolated bubble immersed in the metastable liquid is described by the so-called sharp-interface model where, at fixed temperature, the density field is piecewise continuous, with the density of the liquid outside and that of vapor inside the bubble. CNT determines the size of the critical bubble, corresponding to the transition state. It may happen that the size of the critical bubble is so small to be comparable with the physical thickness of the interface. In such conditions the predictions of CNT can be inaccurate. In order to consider a nucleation theory consistent with our diffuse interface approach, which takes into account the actual thickness of the interface, a more sophisticated theory is needed. Hence, beside CNT, we will use the so-called string method applied to the diffuse interface model to identify the critical state and the transition path leading from the metastable liquid to the cavitated vapor. The two reference nucleation theories will be used to interpret the results of the direct simulation of the nucleation process. In such comparison, one should take in mind that the actual process we simulate is typically significantly more complex than assumed in the reference theories. In particular, at least three effects which are neglected in the ordinary approaches are taken into consideration by our simulations: i) several bubbles are simultaneously present in the system; ii) there is a dynamical interaction between the bubbles; iii) temperature is a field, which may fluctuate in time and space due to several reasons, namely the stochastic forcing itself, and, more significantly, the intrinsic dynamics of the bubbles, including expansion, compression and latent heat release, all of

which are comprised in our description.

The paper is structured as follows: in Section II we discuss the mathematical aspects of the two-phase modeling. First, in Section II.1 we address the Diffuse Interface approach exploited to describe vapor–liquid systems embedded with capillarity effects. A purely thermodynamic analysis allow us to obtain important informations about the properties of critical nucleii, in particular the critical bubble radius and the energy barrier required for the transition from the metastable liquid to the nucleated vapor bubble. The issue is addressed through the application of the string method [149] illustrated in Section II.2. In Section II.3 we introduce Fluctuating Hydrodynamics in the context of the Diffuse Interface approach. The model consists in a set of stochastic partial differential equations (SPDE). The specialist aspects are derived in full details in Appendix A and B, respectively devoted to a discussion of the equilibrium statistical properties of the fluctuating field and to the specific form the Fluctuation-Dissipation balance takes in the present context. Section III deals with the numerical simulations. More specifically, Subsection III.1 illustrates the properties of the numerical scheme and Subsection III.2 addresses bubble nucleation results, with particular attention to nucleation rate, bubble volume distribution and bubble–bubble interaction effects during the process. Finally Section IV is devoted to the conclusions and to the open problems in the field.

Mathematical Model

Diffuse Interface approach for vapor–liquid systems

The diffuse interface modeling adopted here has a strict relationship with more fundamental atomistic approaches, since it is based on a suitable approximation of the free energy functional derived in DFT [92]. It dates back to the famous Van der Waals square gradient approximation of the Helmholtz free energy functional

$$F\left[\rho,\theta\right]=\int_V f\,dV=\int_V\left(f_b\left(\rho,\theta\right)+\frac{1}{2}\lambda\boldsymbol{\nabla}\rho\cdot\boldsymbol{\nabla}\rho\right)\,dV\ , \tag{7.1}$$

where f_b is the classical bulk free energy density, expressed as a function of density ρ and temperature θ. λ is the capillarity coefficient that controls the (equilibrium) surface tension γ and interface thickness. In particular the temperature dependent surface tension can be obtained as [98, 92]

$$\gamma(\theta)=\int_{\rho_v^{sat}(\theta)}^{\rho_l^{sat}(\theta)}\sqrt{2\lambda\left[f_b(\rho,\theta)-f_b(\rho_v^{sat}(\theta),\theta)-\mu_b(\rho,\theta)\rho+\mu^{sat}(\theta)\rho_v^{sat}(\theta)\right]}d\rho\,, \tag{7.2}$$

with $\mu_b=\partial f_b/\partial\rho|_\theta$ the bulk chemical potential and the superscript *sat* denoting saturation conditions. In this work we will compare our numerical simulations with results obtained with Molecular Dynamics of Lennard-Jones fluids, hence for a fairy comparison we adopted as bulk free energy $f_b(\rho,\theta)$ the modified Benedict-Webb-Rubin equation of states (MBWR EoS) that well reproduces the thermodynamic properties of an LJ fluid [75]. All quantities are made dimensionless according to $\rho^*=\rho/\rho_r$, $\theta^*=\theta/\theta_r$, by introducing as reference quantities the parameters of the LJ potential, $\sigma=3.4\times10^{-10}\,\mathrm{m}$ as length, $\epsilon=1.65\times10^{-21}\,\mathrm{J}$ as energy, $m=6.63\times10^{-26}\,\mathrm{kg}$ as mass and $\theta_r=\epsilon/k_B$ as temperature. In the left panel of Fig. 7.2 we compared the tem-

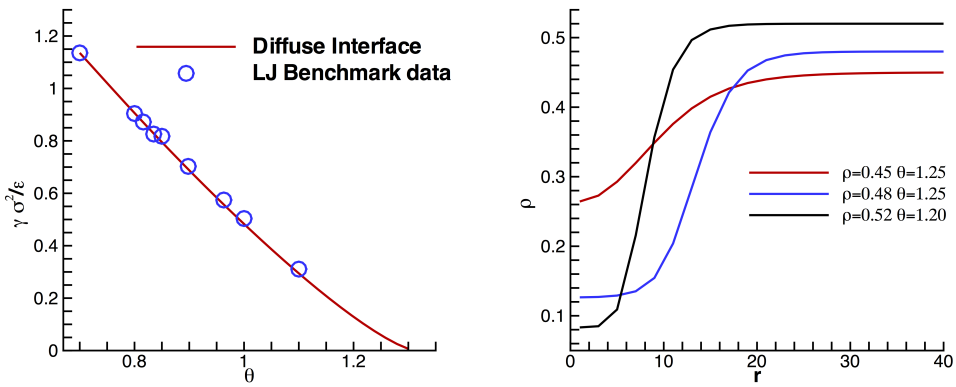

Figura 7.2: Left panel: Comparison between the temperature dependence of the surface tension obtained through Eq. (7.2), when using the Lennard-Jones EoS [75], and the benchmark data provided at the url *https://www.nist.gov/mml/csd/chemical-informatics-research-group/lennard-jones-fluid-properties*. The value of the capillary coefficient is fixed to $\lambda m^2/(\sigma^5\epsilon) = 5.224$. Right panel: Density profiles of the critical nucleii, evaluated with the string method, at different thermodynamic conditions of the metastable liquid.

perature dependence of the surface tension obtained through application of Eq. (7.2) coupled with the MBWR EoS, and some benchmark values obtained through Monte Carlo simulations. In order to reproduce the benchmark results we fixed the value of the capillary coefficient to $\lambda^* = \lambda m^2/(\sigma^5\epsilon) = 5.224$. It is worthwhile stressing that a constant coefficient is sufficient to reproduce the correct temperature dependence of the surface tension. Hereafter the symbol * will be omitted to simplify notation.

Transition path and the critical bubble

The minimization of the free energy functional (7.1), stating that the generalized chemical potential $\mu_c = \mu_c^b(\rho) - \lambda\nabla^2\rho$ must be constant and equal

to the external chemical potential μ_{ext}, allows the evaluation of the equilibrium density profiles at the different thermodynamic conditions. Clearly, in thermodynamic conditions where either the liquid or the vapor are stable, constant chemical potential corresponds to a homogeneous phase. When the liquid or the vapor are metastable instead three solutions at constant chemical potential are found: i) the homogeneous vapor; ii) the homogeneous liquid; iii) a two-phase solution with a spherical (critical) nucleus of a given radius (vapor/liquid in the case of bubble/droplet, respectively), the critical nucleus being surrounded by the metastable phase.

Dealing with nucleation, the non-trivial solution of case (iii), $\rho(r) = \rho_{crit}(r)$ where the critical bubble is surrounded by the metastable liquid at $\rho = \rho_L^{met}, \theta = \bar{\theta}$ and $\mu_c(\rho_L^{met}, \bar{\theta}) = \mu^{met}$ is particularly significant. The solution $\rho(r) = \rho_{crit}(r)$ is found by solving the non linear Euler-Lagrange equation of the functional 7.1 which, in spherical coordinates and at fixed temperature, reads

$$\mu_c^b(\rho, \bar{\theta}) - \frac{\lambda}{r^2}\frac{\partial}{\partial r}\left(r^2 \frac{\partial \rho}{\partial r}\right) = \mu^{met} \,. \tag{7.3}$$

The critical bubble, $\rho_c(r)$, is an unstable solution of Eq. (7.3) which requires specialized numerical techniques. In this work we applied the powerful string method [149] which, as a by-product, identifies the transition path joining the metastable liquid to the cavitated (stable) vapor. The transition path can be visualized as the continuous sequence of density configurations, $\rho(r, \alpha)$, the system assumes when transitioning from the metastable to the stable state, where α is a suitably defined parameter along the path. The distance between two configurations is expressed as

$$\Delta\ell = \sqrt{\frac{1}{V}\int \Delta\rho^2(r) dV} \tag{7.4}$$

and defines the arclength along the path. The discrete form of the path, consisting of a finite number of configurations, is called the *string*. The string method numerically approximates the transition path starting from an initial set of N_s configurations $\{\rho^k(r)\}$, which form the initial guess for the discretized transition path. The head of the string ($k = 1$) is initialized as a uniform density field corresponding to the uniform metastable liquid $\rho(r) = \rho_L^{met}$; the tail ($k = N_s$) is initialized as a guessed tanh-density profile adjoining the liquid and the vapor density to approximate a vapor bubble. All the intermediate images on the string are obtained by interpolation of these two density fields with respect to the above defined arclength. The algorithm used to relax the string to its final configuration corresponding to the actual transition path follows two steps. 1) All the images $\rho^k(r)$ are evolved over one pseudo-timestep $\Delta\tau$ following the steepest-descent algorithm

$$\frac{\partial \rho}{\partial \tau} = \mu^{met} - \left[\mu_c^b(\rho) - \frac{\lambda}{r^2}\frac{\partial}{\partial r}\left(r^2 \frac{\partial \rho}{\partial r}\right)\right] . \tag{7.5}$$

2) The images are redistributed along the string following a reparametrization procedure by equal arclength. The algorithm is arrested when the string converges within a prescribed error.

The density profile of the critical nucleus, plotted in the right panel of Fig. (7.2) at different metastable conditions, allows the evaluation of the critical radius, by following the relation [43]

$$R_c = \frac{\displaystyle\int_0^\infty r(\partial\rho_c/\partial r)^2 r^2 \,\mathrm{d}r}{\displaystyle\int_0^\infty (\partial\rho_c/\partial r) r^2 \,\mathrm{d}r} , \tag{7.6}$$

and the evaluation of the energy barrier

$$\widetilde{\Delta\Omega} = \int_0^\infty \left\{ f(\rho_c(r)) - f(\rho_L^{met}) - \mu^{met}\left[\rho_c(r) - \rho_L^{met}\right]\right\} 4\pi r^2 \mathrm{d}r , \tag{7.7}$$

defined as the difference in grand potential Ω between the critical nucleus and the metastable liquid.

The results of the string method are compared in Tab. 7.1 with those obtained by classical nucleation theory (CNT) which yields the estimate $\widetilde{\Delta\Omega}^{CNT} = 4/3\pi\gamma R_c^2$. The data show that CNT underestimates the energy barrier at high temperature while overestimates it near the spinodal [31].

θ_0	ρ_L^{met}	R_c	R_c^{CNT}	$\widetilde{\Delta\Omega}/\theta_0$	$\widetilde{\Delta\Omega}^{CNT}/\theta_0$
1.25	0.45	12.04	8.07	2.99	12.89
1.25	0.46	11.16	8.42	11.21	14.05
1.25	0.47	11.85	9.17	22.81	16.67
1.25	0.48	14.18	10.64	43.5	22.41
1.20	0.51	8.28	6.35	19.20	18.13
1.20	0.52	8.79	6.93	33.58	21.60

Tabella 7.1: Comparison between CNT and the string method applied to the Diffuse Interface model. Critical radii and (Landau) free energy barriers $\widetilde{\Delta\Omega}$ for bubble nucleation from the liquid. The discrepancy close to the spinodal and at higher temperature are well known from the literature.

Fluctuating Hydrodynamics: the Landau–Lifshitz/Navier–Stokes model embedded with capillarity

The deterministic time evolution of the two–phase, vapor–liquid, system obeys mass, momentum and energy conservation. The thermodynamic considerations of Section II.1 embed capillary effects in the equilibrium model. Following the procedure of non-equilibrium thermodynamics, [37], which can be nowadays considered a standard approach, the description is straightforwardly extended to dynamic conditions. New stress and energy flux contributions arise from the capillary term in the free energy (Eq. 7.1). In particular

(see [98, 72] for the detailed derivation) the stress tensor reads

$$\boldsymbol{\Sigma} = \left[-p + \frac{\lambda}{2}|\boldsymbol{\nabla}\rho|^2 + \lambda\rho\boldsymbol{\nabla}\cdot(\lambda\boldsymbol{\nabla}\rho)\right]\boldsymbol{I} - \lambda\boldsymbol{\nabla}\rho\otimes\boldsymbol{\nabla}\rho + \mu\left[(\boldsymbol{\nabla}\mathbf{u} + \boldsymbol{\nabla}\mathbf{u}^T) - \frac{2}{3}\boldsymbol{\nabla}\cdot\mathbf{u}\,\boldsymbol{I}\right], \tag{7.8}$$

with $p = -\rho^2\partial(f_b/\rho)/\partial\rho = f_b - \mu_c^b\rho$ the pressure and μ the dynamic viscosity. The energy flux entering the energy equation is augmented with a capillarity term which adds to the standard Fourier contribution,

$$\boldsymbol{q} = \lambda\rho\boldsymbol{\nabla}\rho\boldsymbol{\nabla}\cdot\mathbf{u} - k\boldsymbol{\nabla}\theta\,, \tag{7.9}$$

with k the thermal conductivity.

Thermal fluctuations needs to be included in the classical hydrodynamic equations in order to describe fluid motion at mesoscopic scale. Based on phenomenological arguments, the theory of fluctuating hydrodynamics has been originally developed by Landau and Lifshitz (1958, 1959)[84] to be later framed in the general contest of stochastic processes [61]. Landau and Lifshitz's original idea was to treat the thermodynamic fluxes, namely stress tensor and energy flux, as stochastic processes. As prescribed by the thermodynamics of irreversible processes at macroscopic level, thermodynamic fluxes are the expression of microscopic molecular degrees of freedom of the thermodynamic system. Under this respect dissipation in fluids can be seen as the macroscopic manifestation of the energy transfer arising from random molecular interactions. Thus at mesoscopic scale, thermodynamic fluxes have to be modeled as stochastic tensor fields, whose statistical properties can be inferred by enforcing the *fluctuation-dissipation balance* (FDB) .
The detailed derivation of the stochastic contributions is postponed to appendices A-B. Here we summarise the main aspects of the model. The stochastic evolution of the system is described by the conservation laws of mass,

momentum and energy,

$$\begin{aligned}
\frac{\partial \rho}{\partial t} + \boldsymbol{\nabla} \cdot (\rho \mathbf{u}) &= 0\,, \\
\frac{\partial \rho \mathbf{u}}{\partial t} + \boldsymbol{\nabla} \cdot (\rho \mathbf{u} \otimes \mathbf{u}) &= \boldsymbol{\nabla} \cdot \boldsymbol{\Sigma} + \boldsymbol{\nabla} \cdot \boldsymbol{\delta\Sigma}\,, \\
\frac{\partial E}{\partial t} + \boldsymbol{\nabla} \cdot (\mathbf{u} E) &= \boldsymbol{\nabla} \cdot (\boldsymbol{\Sigma} \cdot \mathbf{u} - \mathbf{q}) + \boldsymbol{\nabla} \cdot (\boldsymbol{\delta\Sigma} \cdot \mathbf{u} - \boldsymbol{\delta q})\,,
\end{aligned} \tag{7.10}$$

where $\mathbf{u}$ is the fluid velocity, E is the total energy density, $E = \mathcal{U} + 1/2\rho|\mathbf{u}|^2 + 1/2\lambda|\boldsymbol{\nabla}\rho|^2$, with $\mathcal{U}$ the internal energy density. In the momentum and energy equations, $\boldsymbol{\Sigma}$ and $\mathbf{q}$ are the classical deterministic stress tensor and energy flux, respectively, defined in Eqs. (7.8, 7.9) while the terms with the prefix δ are the stochastic parts, required to satisfy the FDB. Enforcing the fluctuation-dissipation balance, the covariance of the stochastic fluxes follows as

$$\langle \boldsymbol{\delta\Sigma}(\hat{x}, \hat{t}) \otimes \boldsymbol{\delta\Sigma}^{\dagger}(\tilde{x}, \tilde{t}) \rangle = \mathbf{Q}^{\boldsymbol{\Sigma}} \delta(\hat{x} - \tilde{x}) \delta(\hat{t} - \tilde{t})\,, \tag{7.11}$$

and

$$\langle \boldsymbol{\delta q}(\hat{x}, \hat{t}) \otimes \boldsymbol{\delta q}^{\dagger}(\tilde{x}, \tilde{t}) \rangle = \mathbf{Q}^{\mathbf{q}} \delta(\hat{x} - \tilde{x}) \delta(\hat{t} - \tilde{t})\,, \tag{7.12}$$

where ${\mathbf{Q}^{\boldsymbol{\Sigma}}}_{\alpha\beta\nu\eta} = 2\mathrm{k}_B \theta \mu \left(\delta_{\alpha\nu}\delta_{\beta\eta} + \delta_{\alpha\eta}\delta_{\beta\nu} - 2/3\delta_{\alpha\beta}\delta_{\nu\eta}\right)$ and ${\mathbf{Q}^{\mathbf{q}}}_{\alpha\beta} = 2\mathrm{k}_B \theta^2 k \delta_{\alpha\beta}$, with k_B the Boltzmann constant. Thanks to the Curie-Prigogine principle [37], the cross-correlation between different tensor rank fluxes vanishes, *i.e.* ($\left\langle \delta\mathbf{q}^{\dagger}(\tilde{x}, \tilde{t}) \otimes \delta\boldsymbol{\Sigma}(\hat{x}, \hat{t}) \right\rangle = 0$).

Even in equilibrium conditions, thermal noise forces the different fields to fluctuate. The complete (equilibrium) correlation tensor $\mathbf{C}_{\boldsymbol{\Delta}}(\hat{\mathbf{r}}, \tilde{\mathbf{r}}) = \langle \boldsymbol{\Delta}(\hat{\mathbf{r}}) \otimes \boldsymbol{\Delta}^{\dagger}(\tilde{\mathbf{r}}) \rangle$, with the field fluctuations organised in a 5-component vector $\boldsymbol{\Delta}(\mathbf{r}) = \{\delta\rho(\mathbf{r}), \delta\mathbf{u}(\mathbf{r}), \delta\theta(\mathbf{r})\}$, is found to be, Appendix A,

$$\mathbf{C}_{\boldsymbol{\Delta}}(\hat{\mathbf{r}}, \tilde{\mathbf{r}}) = \begin{pmatrix} C_{\delta\rho\delta\rho} & 0 & 0 \\ 0 & \mathbf{C}_{\delta\mathbf{u}\delta\mathbf{u}} & 0 \\ 0 & 0 & C_{\delta\theta\delta\theta} \end{pmatrix}\,, \tag{7.13}$$

with

$$C_{\delta\rho\delta\rho}(\hat{\mathbf{r}},\tilde{\mathbf{r}}) = \frac{\mathrm{k}_B\theta_0}{4\pi\lambda\,|\hat{\mathbf{r}}-\tilde{\mathbf{r}}|}\exp\left(-|\hat{\mathbf{r}}-\tilde{\mathbf{r}}|\sqrt{\frac{c_T^2}{\rho_0\lambda}}\right)\ , \tag{7.14}$$

$$\mathbf{C}_{\delta\mathbf{u}\delta\mathbf{u}}(\hat{\mathbf{r}},\tilde{\mathbf{r}}) = \frac{k_B\theta_0}{\rho_0}\mathbf{I}\delta\left(\hat{\mathbf{r}}-\tilde{\mathbf{r}}\right)\ , \tag{7.15}$$

$$C_{\delta\theta\delta\theta}(\hat{\mathbf{r}},\tilde{\mathbf{r}}) = \frac{k_B\theta_0^2}{\rho_0 c_v}\delta\left(\hat{\mathbf{r}}-\tilde{\mathbf{r}}\right)\ . \tag{7.16}$$

In these equations ρ_0 and θ_0 are the equilibrium density and temperature, respectively, $c_T^2 = \partial p/\partial\rho|_T$ the isothermal speed of sound, and c_v the specific heat at constant volume. It is worth noting that the spatial correlation of density fluctuations arise from the long range capillary interactions and is not spatially δ-correlated as usual in simple fluids [40].

Results and Discussion

Stochastic pde's and numerical integration

System (7.10) has been discretised in the spirit of the method of lines, which consists of two stages: spatial discretisation and temporal integration, respectively. Concerning spatial discretisation, the different physical phenomena described by the LLNS system ask for specialised numerical techniques. A crucial point is the correct reproduction of the statistical properties at the discrete level [8], consistency with fluctuation-dissipation balance in particular. Eqs. (7.10) have been discretised on a uniformly spaced staggered grid, following [54]. Due to staggering, scalar fields, like e.g. density, are located at the cell center while components of vector fields in a given direction are located at the center of the perpendicular face.

The numerical scheme has been validated by comparing the numerical equilibrium static correlations with the theoretical ones in the discretized

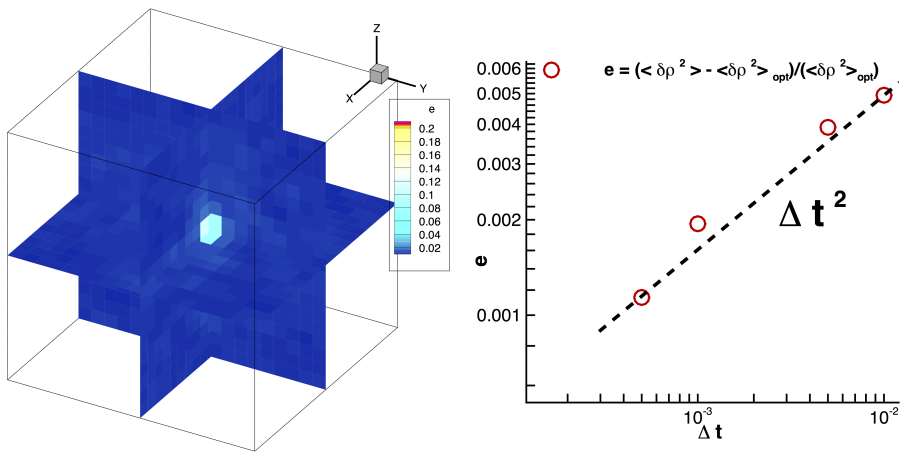

Figura 7.3: Left panel: Static structure factor comparison for a capillary fluid in a 3D system. We report the relative error $e = |S_f - S_t|/S_t$ between the theoretical prediction and numerical calculation for each wavenumbers k_x, k_y, k_z in the Fourier space. Right panel: Error of the density variance at different simulation time steps. As expected, the error follows a square power law $e \propto \Delta t^2$.

equations. Here we report the comparison of the density static structure factor, which is the Fourier transform of the static correlation function $C_{\delta\rho\delta\rho}$ in Eq. (7.14). In the discrete limit, the theoretical static structure factor reads

$$S_t(\mathbf{k_d}) = \frac{\rho_0 k_B \theta_0}{c_T^2 + \rho_0 \lambda \mathbf{k_d} \cdot \mathbf{k_d}} \ , \tag{7.17}$$

where

$$\mathbf{k_d} \cdot \mathbf{k_d} = \left(\frac{\sin\left(k_x \Delta x/2\right)}{\Delta x/2}\right)^2 + \left(\frac{\sin\left(k_y \Delta y/2\right)}{\Delta y/2}\right)^2 + \left(\frac{\sin\left(k_z \Delta z/2\right)}{\Delta z/2}\right)^2 \tag{7.18}$$

is the discrete version of the square norm of $\mathbf{k}$, arising from the discrete Laplacian operator in Fourier space [33]. The numerical estimate of the density structure factor is calculated, following its definition, as

$$S_f(\mathbf{k_d}) = \langle \delta\rho(\mathbf{k_d}) \delta\rho^*(\mathbf{k_d}) \rangle \ , \tag{7.19}$$

where dependency on the wavenumber implicitly denotes Fourier components. As shown in the left panel of Fig. 7.3, numerical results are in very good agreement with the theoretical prediction. In particular the relative error e is almost everywhere less than $2-3\%$ in the field, except for the small wavenumbers, due to the slow convergence of low wavelength modes [33]. Nevertheless, even in the latter case, the relative error is less then 10%.
As a second test, we compared the variance of velocity and temperature fluctuations. In particular, the velocity fluctuations must reproduce the celebrated equipartition theorem, here reported in the discretes version:

$$\langle \delta \mathbf{u} \cdot \delta \mathbf{u} \rangle = 3 \frac{k_B \theta_0}{\rho_0 \Delta V} \,, \tag{7.20}$$

$$\left\langle \delta \theta^2 \right\rangle = \frac{k_B \theta_0^2}{\rho_0 c_v \Delta V} \,. \tag{7.21}$$

The values reported in Tab. 7.2 clearly show a perfect matching between numerical results and theoretical expectation.

Variances	Theoretical prediction	Numerical value	Error %
$\langle \delta u_x^2 \rangle$	$1.3333 \cdot 10^{-4}$	$1.3332 \cdot 10^{-4}$	0.01
$\langle \delta u_y^2 \rangle$	$1.3333 \cdot 10^{-4}$	$1.3331 \cdot 10^{-4}$	0.02
$\langle \delta u_z^2 \rangle$	$1.3333 \cdot 10^{-4}$	$1.3335 \cdot 10^{-4}$	0.02
$\langle \delta \theta^2 \rangle$	$5.8361 \cdot 10^{-5}$	$5.8443 \cdot 10^{-5}$	0.15

Tabella 7.2: Numerical temperature and velocity variances in comparison with theoretical values.

As a last test, we validated the accuracy of our time integration method. We performed the time evolution by means of a second order Runge Kutta scheme [46]. We compared the numerical error, e, on the variance of density fluctuations $\langle \delta \rho(\mathbf{x})^2 \rangle$ at different time steps Δt with respect to $\langle \delta \rho(\mathbf{x})^2 \rangle_{opt}$

obtained with our finest integration step $\Delta t = 10^{-4}$

$$e = \frac{|\langle \delta\rho(\mathbf{x})^2 \rangle - \langle \delta\rho(\mathbf{x})^2 \rangle_{opt}|}{\langle \delta\rho(\mathbf{x})^2 \rangle_{opt}}\,, \tag{7.22}$$

where the average is evaluated as $1/(T\,V)\int_0^T \int_V \delta\rho(\mathbf{x})^2\, dV dt$ with the time window T fixed as $T = 100$ LJ units. The right panel of Fig. 7.3 clearly shows the expected power law, $e \propto \Delta t^2$.

All these tests ensure that the numerical scheme correctly reproduces the statistical properties of the system, i.e. the fluctuation-dissipation balance is preserved in the discretised equations.

The dynamics of vapor bubble nucleation

Bubble nucleation is investigated in a metastable liquid enclosed in a cubic box with periodic boundary conditions, with fixed volume, total mass and energy (NVE). The equation of state (EoS) we use, which can be chosen freely among available models, e.g. van der Waals or IAPWS [82] EoS for water, corresponds to a Lennard-Jones (LJ) fluid [75] to allow direct comparison with MD simulations. The system volume $V = 600^3$ has been discretised on a uniform grid with 50 cells per direction. After a convergence analysis we found that the chosen grid size, $\Delta x = 12$, is sufficient for a reliable simulation in these thermodynamic conditions. Moreover, thanks to the extension of the simulated domain ten runs for each condition, with different values of the seed employed to generate random numbers, provide a well converged statistics.

Among the different conditions we have investigated, we mainly focus here on the initial temperature $\theta_0 = 1.25$ at changing bulk density to explore the corresponding metastable range $\rho_L \in [\rho_{spin}, \rho_{sat}] = [0.44, 0.51]$, where ρ_{sat} and ρ_{spin} are the saturation and spinodal densities, respectively. A few

snapshots of the evolution for two different initial conditions are shown in the left panels of Fig.s 7.4 and 7.5. Starting from a homogeneous metastable liquid phase, the fluctuations lead the system to spontaneously nucleate vapor bubbles. The nucleii start out with a complex, far from spherical, shape, see, e.g., [49]. Roughly, when they happen to reach a size larger than critical they typically expand. Eventually, after a long and complex dynamics where bubbles expand and coalesce, stable equilibrium conditions are reached. The existence of such equilibrium is due to the constraint on volume and mass of the system. Note that, most often, nucleation is addressed in the grand-canonical ensemble, where volume and chemical potential are specified. The eventual configuration is characterized by several vapor bubbles in equilibrium with the surrounding liquid. The case at $\rho_L = 0.46$, the closest one to the spinodal we considered here, is the most populated, Fig. 7.4 in comparison with Fig. 7.5. This system has a barrier lower than those further from the spinodal (see Tab. 7.1), hence it nucleates faster. The initial (metastable) thermodynamic condition also influences the number and typical

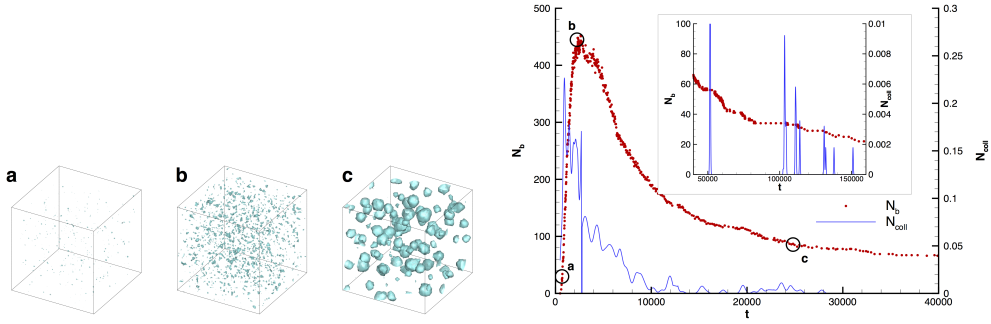

Figura 7.4: Left panel: bubble configurations along nucleation ($\rho = 0.46$, $\theta_0 = 1.25$), from left to right $t = 400$, $t = 2000$, $t = 25000$. Animation available in Supplemental Material [128]. Right panel: bubble number evolution (red symbols) and number of coalescence events (blue line).

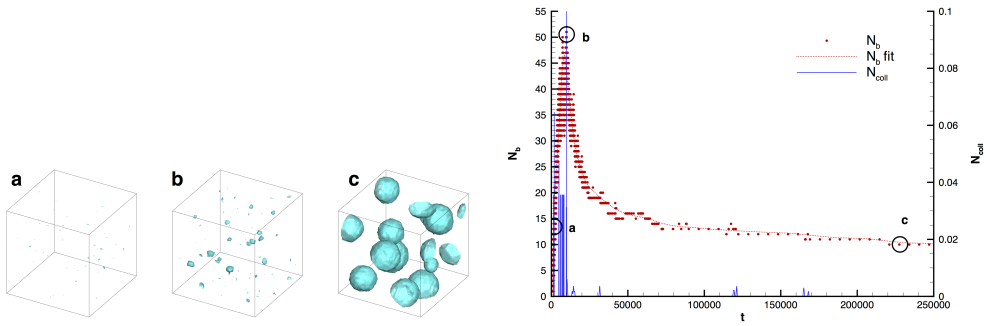

Figura 7.5: Same as Figure 7.4 at $\rho = 0.48$, $\theta_0 = 1.25$. Snapshots taken at $t = 2000$, $t = 11000$, $t = 230000$. The bubble number vs time in the right panel is fitted by the dotted red line for better readability.

dimension of the bubbles in the final stage, right panels of Fig.s 7.4 and 7.5 providing the bubble number N_b as a function of time. A tracking procedure has been put forward to follow the evolution of the distinct bubbles. By monitoring bubble volume, mass, center of mass and its velocity, the tracking algorithm allows for detecting coalescence events. The actual number of collisions between bubbles $\tilde{N}_{coll}$ evaluated at each time step is characterized by a highly discontinuous fingerprint. We smoothed the curve with a Gaussian kernel with standard deviation of order 50 time units to extract more robust indications. The time evolution of the bubble number N_b, Fig.s 7.4 and 7.5, presents three main phases: i) the initial *nucleating* phase – when N_b grows linearly with time (i.e. at a constant nucleation rate); ii) the *collapsing* phase during the first part of the expansion stage – characterized by a rapidly decreasing number of bubbles mainly due to collapse; and iii) a *slowly expanding* phase characterizing the long-time dynamics of the multi-bubble system. The smoothed number of collisions N_{coll}, plotted with the blue line in the figures, shows a strong correlation with the number of bub-

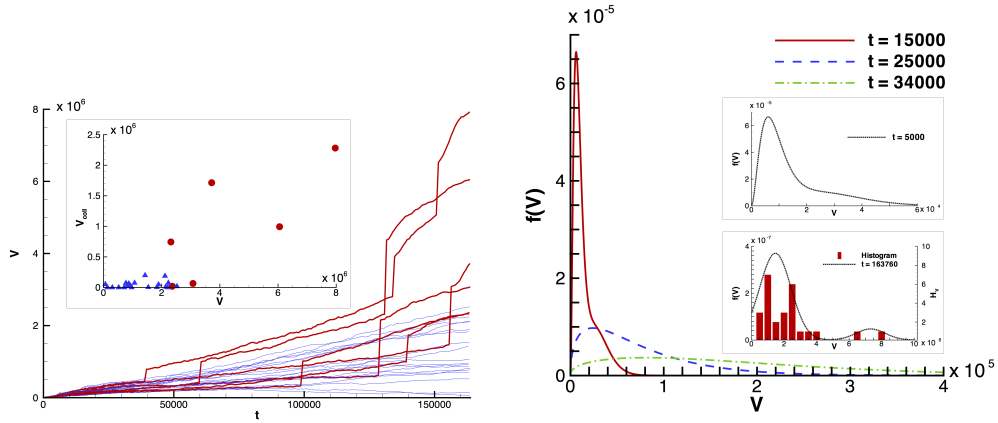

Figura 7.6: Left panel: Volume history of the bubbles surviving the entire simulation ($\rho = 0.46$ and $\theta_0 = 1.25$). Intense coalescence events, characterized by a sudden volume jump, are identified in the red curves. The corresponding volumes are shown by the red dots in the inset providing the $V - V_{coll}$ scatter plot, where V_{coll} is the volume acquired by coalescence. The largest bubbles experienced intense coalescence events. Right panel: Probability distribution function $f(V)$ of the bubble volumes during the nucleation, at different times ($\theta_0 = 1.25$, $\rho = 0.46$, critical volume $V_c = 4445$).

bles throughout the nucleating phase and the collapsing phase. Nucleating and collapsing phases are characterized by a competing-growth mechanism [**?**] due to the constraints of constant mass and volume, explaining the high number of supercritical bubble collapses. The coalescence events start being less and less probable during the slowly-expanding phase. The inset of the Fig. 7.4 zooms into this phase showing that isolated collision events still occurr, contributing to important acceleration toward the final equilibrium condition.

The volume history of the distinct bubbles (in particular those survived up to the last time investigated) have been plotted in the left panel of Fig. 7.6. Among the different bubble evolutions, we highlighted in red the

volume histories of those bubbles that experienced intense coalescence events, characterized by a sudden increase in volume. It is apparent that the larger bubbles gained substantial part of their volume by coalescence. To substantiate this impression, for each bubble in the last configuration, the sum of the volumes acquired by coalescence throughout the whole evolution, V_{coll}, was calculated, inset of left Fig. 7.6. The present mesoscale approach allows to access the statistics of bubble dimensions. The probability distribution function of bubble volumes $f(V)$ is plotted in the right panel of Fig. 7.6. During both the *nucleating* and *collapsing* phases the pdf is sharply peaked at small volumes, of the order of 2–4 V_c. The successive bubble expansion phase is substantially slower and calls for a much longer observation time to detect a significant growth (green dash-dotted curve at $t = 34000$). The intense coalescence events explain the presence of the second peak in the pdf at very large volume (black curve in the inset on the right panel of Fig. 7.6 at $t = 163760$).

The initial *nucleating* stage, where the bubble number increases linearly, gives access to the nucleation rate J in terms of bubbles formed per unit time and volume. It is here calculated as the slope of the linear fit to the curves of Fig.s 7.4 and 7.5 near the origin. The results are plotted in Fig. 8.6 which also provides a direct comparison with some MD simulations [49, 110]. The values agree comfortably well with molecular dynamic simulations in the NVE ensemble. As common in literature, the present results are compared also with CNT prediction for the nucleation rate, $J_{CNT} = n_L\sqrt{2\gamma/m\pi}\exp(-\widetilde{\Delta\Omega}^{CNT}/k_B\theta)$, where n_L is the liquid number density. The expression of the energy barrier was already explicitly given in Section II.2 while the pre-exponential factor is taken in the classical form

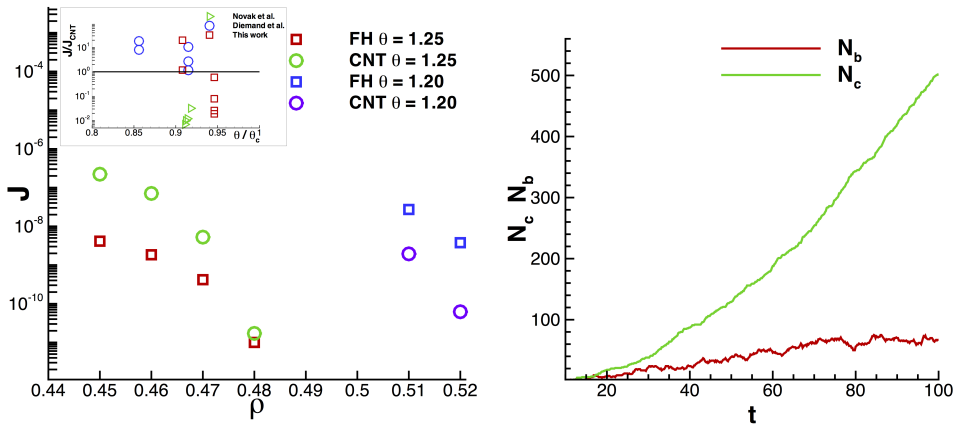

Figura 7.7: Left panel: Comparison of the nucleation rate obtained via FH simulations (red squares at $\theta_0 = 1.25$ and blue squares at $\theta_0 = 1.20$) with respect to CNT predictions (green circles at $\theta_0 = 1.25$ and purple circles at $\theta_0 = 1.20$). The inset shows the comparison with other authors. Right panel: Time evolution of the number of supercritical bubbles N_b and the total collapsed supercritical bubble N_c up to time instant t. The number of bubbles is rescaled with the maximum number of bubble observed during the simulation, N_{max}, which correspond to $N_{max} = 458$ in the thermodynamic condition with $\rho_L = 0.46$ and $N_{max} = 52$ in the case with $\rho_L = 0.48$. The time is shifted and rescaled in such a way that all the curves start when the first bubble appears, at $t = t_s$, and finish when N_{max} is reached, at $t = t_{max}$.

proposed by Blander and Katz [18], and already used in [49] as a reference for a large number of MD simulations. It is worth noting that the energy barriers estimated from CNT and from the string method (Table 7.1) are strongly based on the assumption that only a single bubble can nucleate. As already discussed when commenting on the coalescence events, in the thermodynamic conditions we studied the effects of bubble-bubble interaction are instead crucial to understand the full dynamics of the bubble evolution. In particular, the conditions assumed in our present simulations and in the MD

simulations used for comparison correspond instead to given system volume, energy and mass – NVE ensemble – and the system is free to simultaneously nucleate several bubbles. The consequence of fixing the mass of the system is that the larger is the overall volume of the different bubbles that are simultaneously nucleated the more the liquid is compressed. As a result the nucleation process is discouraged. To further substantiate the importance of this point we evaluated the number of collapsed bubble after crossing the critical size. The total number, up to the current time, is plotted in the right panel of Fig. 7.7 labeled as N_c. If no collapse occurred, the total number of bubbles in the system would have been $N_{tot} = N_b + N_c$ and the rate would have been larger by roughly a factor 15.

Conclusions

In conclusion, the FH approach together with a diffuse interface modeling of the multiphase system have been exploited to study homogeneous nucleation of vapor bubbles in metastable liquids. We evaluated the nucleation rate and compared it favorably with state of the art simulations. Concerning the comparison with classical approaches, CNT and the string method for the diffused interface model, we found that the simultaneous nucleation of several bubbles has a strong effect on the nucleation rate, that is found to be altered with respect to the above single-bubble models. The present technique has revealed extremely cheaper with respect to MD simulations, allowing the analysis of the very long bubble expansion stage where bubble-bubble interaction/coalescence events turn out to determine the eventual bubble size distribution. The accurate results and the efficiency of the modeling encou-

rage the exploitation for more complex conditions, like e.g. heterogeneous nucleation and multi-species systems, and could pave the way for the development of innovative continuum formulation to address thermally activated processes.

acknowledgments

The research leading to these results has received funding from the European Research Council under the European Union's Seventh Framework Programme (FP7/ 2007-2013)/ERC Grant agreement no. [339446].

Capitolo 8

A Mesoscale Model for Heterogeneous Nucleation

In this work, the mesoscale fluctuating diffuse interface model described in the previous chapters was extended to wall bounded systems, and subsequently exploited to address heterogeneous nucleation. We numerically evaluate the nucleation rates for different thermodynamic conditions and different wall wetting properties. Dealing with wall wettability, calls for a thermodynamic consistent model of the solid-wall free energy, to this end its mathematical form was found, univocally relating the contact angle with the bulk properties of the fluid. Furthermore, the model foresees depletion or absorption layering of the liquid in proximity of the solid surfaces, as commonly detected in MD simulations. These aspects play a crucial role in heterogeneous nucleation, showing unusual effects. In particular for moderately hydrophilic walls, homogeneous nucleation seems to be the most probable event, due to the liquid accumulation to the wall.

As a simple comparison, we compare our numerical results, with classical nucleation theory, both with Blander and Katz approach and with Kramers theory. For weakly hydrophilic/hydrophobic surfaces, a good agreement with

classical theory, is found. In particular with Kramers theory, here formulated for heterogeneous nucleation.

What follows is the paper in preparation.

Introduction

The effects of thermal fluctuations are relevant in the dynamics of fluid systems below the micrometer scale. Hence a fluid dynamic model addressed to capture the phenomena at mesoscopic scales must embed this crucial aspect, hence calling for a suitable description of stochastic fluctuations. Starting from the eminent work of Landau and Lifshitz (1958, 1959) [84] several models have been developed to embed thermal fluctuations in continuum mechanics equations [61] contributing to the growing field of "Fluctuating Hydrodynamics". In the last decades the mathematical modeling has been followed by an exponential increase of numerical methods for the correct evaluation of the stochastic contributions [54, 46, 11, 53]. The comprehension of the effects of thermal fluctuations in a mesoscale system not only play an important role in physics of fluids, but a deep understanding of these phenomena is necessary for the progress of some of the latest nanotechnology. For instance a suitable modeling of stochastic fluctuations is crucial in the design of flow-driven micro-devices, or in the study of biological systems, such as lipid membranes [107], or even in the theory of Brownian engines and in the development of artificial molecular motors prototypes [115, 47]. Another problem with a huge theoretical and technological impact is the phenomenon of nucleation, the precursor of the phase change in metastable systems. This problem is strongly connected to the phenomenon of bubble cavitation [28] and of freezing rain [32], to cite a few. In fact thermal fluctuations allow

to overcome the energy barriers for phase transitions [76, 79, 90]. Before discussing the mathematical model, it is worth to remember the main features of nucleation in liquid system. A liquid held at atmospheric pressure can be heated up to a temperature far beyond its boiling point. In this condition the liquid is called superheated, or more generally metastable. Metastability can be obtained analogously by decreasing isothermally the pressure under its saturation value. At low enough temperature – at ambient temperature in the case of water, e.g. – the liquid can be stretched down to negative pressure, the so called tensile condition. When the liquid is in metastable conditions a vapor bubble can nucleate with a probability related to the level or superheating or stretching and we refer to the nucleation event as boiling or cavitation, respectively [28]. Bubble nucleation is an activated process, since an amount of energy is needed to overcome the activation barrier. The presence of impurity or dissolved gas nuclei strongly lowers the energy barrier and simplifies the bubble formation, as well as the presence of solid boundaries. In fact the energy needed to form a vapor bubble on a solid surface depends on the contact angle, and as explained in the next section it can be significant lower than its counterpart in a bulk phase. This is the reason why it is extremely easy to experience a cavitation event in water at non-extremely negative pressures even if it has been proven [10] that ultra-pure water can sustain $1\,kbar$ tensions. Moreover recent experimental works have highlighted how the wettability of ultra-smooth surface can strongly influence the onset temperature of pool boiling in superheated liquids [26, 25, 100].

Several theoretical models have been proposed in order to estimate the energy barrier and the nucleation rate, both in homogeneous and heterogeneous (near boundaries) conditions. The classical nucleation theory (CNT)

[18], poses the basis for the understanding of the phenomena, and it may be easily extended to the non-homogeneous case [147], as recalled in Sec.II. More sophisticated theories like density functional theory (DFT) [113] or molecular dynamics (MD) simulations can give more precise estimates of the barriers and can correct some mis–prediction of the CNT. Both the methods are extremely powerful in stationary conditions and need to be coupled to specialized techniques, like the string method [148], to study the nucleation events and the transition path [67]. Another promising approach is to use a phase field model where the order parameter is the mass density itself. In stationary conditions it recovers the DFT description with a squared-gradient approximation of the excess energy [92]. The phase field model has the advantage of being easily extended to unsteady situations, enabling the full description of both the thermodynamic and the fluid dynamics fields [96]. The model, in its original form, is deterministic and cannot capture spontaneous nucleation originated by thermal fluctuations, in absence of external forcing. To this purpose, the theory of fluctuating hydrodynamic [40, 33] represents the natural framework to embed thermal fluctuations inside the phase field description. Recently a novel approach in the context of continuum mechanics, based on a diffuse interface description of the two-phase vapor-liquid system embedded with thermal fluctuations through a fluctuating hydrodynamics modeling, has been used to address bubble nucleation process [63, 64] in the homegeneous case. Aim of this work is to extend our previous works to the study of heterogeneous nucleation, in particular, here we studied the spontaneous vapor bubble nucleation in a metastable liquid in presence of solid boundaries. The heterogeneous nucleation has been addressed by the means of diffuse interface fluctuating model, and we numerically

evaluate the nucleation rates for different wall wetting properties. An analytic form of the solid-wall free energy is derived, relating its expression with the thermodynamics of the bulk phase and the contact angle with the spatial derivative of the density.

As a simple comparison, we compare our numerical results, with classical nucleation theory, both with Blander and Katz approach and with Kramers theory. For weakly hydrophilic/hydrophobic surfaces, we found a good agreement with classical theory, in particular with Kramers theory, here formulated for heterogeneous nucleation.

Classical Nucleation Theory

Classical nucleation theory (CNT) [80, 28, 147] provides the fundamental understanding of bubble nucleation in a metastable liquid, both for homogenous (bubble forming in the bulk liquid)) and heterogenous conditions (bubble forming in contact with an extraneous phase, typically a solid with given geometry and chemical properties). The simplest example of heterogenous nucleation is a vapor bubble nucleating on a flat solid surface at fixed contact angle ϕ.

The free energy of a spherical cup laying on a flat solid wall,

$$\begin{aligned} \Omega\left(R,\phi\right) &= -\Delta p V_V\left(R,\phi\right) + \gamma_{LV} A_{LV}\left(R,\phi\right) + \\ &+ \gamma_{SV} A_{SV}\left(R,\phi\right) + \gamma_{LS} A_{LS}\left(R,\phi\right) \ , \end{aligned} \tag{8.1}$$

depends on the vapor-liquid pressure jump $\Delta p = p_V - p_L$ (the Laplace pressure), the bubble volume V_V, the area of liquid-vapor A_{LV}, solid-vapor A_{SV} and liquid-solid A_{LS} interfaces and the respective surface energies $\gamma_{LV}, \gamma_{SV}, \gamma_{LS}$. Introducing the equilibrium (or Young) contact angle $\phi = \cos^{-1}(\gamma_{LS} -$

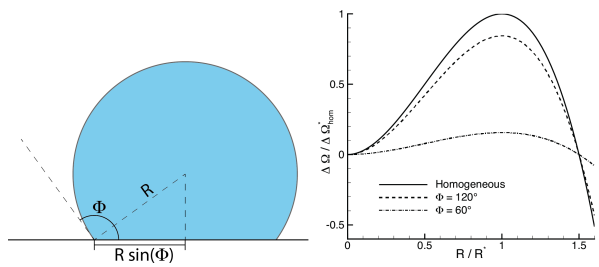

Figura 8.1: Left panel: bubble sketch illustrating the equilibrium contact angle ϕ and the bubble radius R. Right panel: CNT prediction of free-energy profiles for different contact angle ϕ, the continuous line corresponds to the homogeneous case ($\phi = \pi$), the dotted lines represent the heterogeneous case.

$\gamma_{SV})/\gamma_{LV})$ (see the sketch in fig. 8.1, where, at variance with the standard convention, the angle is measured from the vapor-solid interface, i.e. $\phi > \pi/2$ means hydrophilic) allows for re-expressing the relevant geometric quantities as $A_{SV} = \pi R^2 \sin^2\phi$, $A_{LV} = 2\pi R^2(1-\cos\phi)$, $A_{LS} = A_w - A_{SV}$, $V_V(R,\phi) = V_V(R,\pi)\Psi(\phi)$, where is A_w the total surface of the solid wall and $\Psi(\phi) = 1/4(1-\cos\phi)^2(2+\cos\phi)$. As $\phi \to \pi$ the free energy reduces to the homogeneous case. Thus, starting from a homogeneous metastable liquid and denoting by $\Delta\Omega_{hom} = -\Delta p V_V(R,\pi) + \gamma_{LV} A_{LV}(R,\pi)$ spent for a spherical bubble of radius R in the bulk liquid, the energy required to form a spherical cup at the wall reads

$$\Delta\Omega\left(R,\phi\right) = \Delta\Omega_{hom}\left(R\right)\Psi\left(\phi\right) \ . \tag{8.2}$$

The free energy consists of two contribution, one associated with volume terms and decreasing like R^3 with increasing bubble radius and the other depending on the surface area which increases with like the square of the bubble radius. The free-energy attains a maximum, the critical state, at the

critical radius R^*.

$$R^* = \frac{2\gamma_{LV}}{\Delta p} \ , \tag{8.3}$$

The corresponding free energy barrier is

$$\Delta\Omega^* = \Delta\Omega\left(R^*, \phi\right) = \Delta\Omega^*_{hom}\Psi\left(\phi\right) = \frac{16}{3}\pi\frac{\gamma_{LV}^3}{\Delta p^2}\Psi\left(\phi\right) \ . \tag{8.4}$$

The critical radius is the same both for heterogeneous and homogenous nucleation. On the opposite, the barrier $\Delta\Omega^*$ for heterogenous nucleation is lower than $\Delta\Omega_{hom}$ ($\Psi(\phi) \leq 1$). Clearly, for trivial geometrical reasons, also the critical volume $V^* = 4/3\pi {R^*}^3\Psi(\phi)$ is smaller for the heterogeneous case.

The crucial observable in the nucleation process is the nucleation rate, i.e. the normalized number of super-critical bubbles formed per unit time. In the heterogeneous context the normalization is per unit surface (as opposed to unit volume used in homogeneous conditions). The expression for the nucleation rate[18, 41] is

$$J_{BK} = n_L^{2/3}\frac{(1-\cos\phi)}{2}\sqrt{\frac{2\gamma_{LV}}{\pi m}}\exp\left(-\frac{\Delta\Omega^*}{k_B\theta}\right) \ , \tag{8.5}$$

where n_L is the liquid number density and m the mass of the liquid molecule. Kramers theory [83] provides the mean time τ for the diffusion across a barrier (mean first passage time) of a random walker trapped in the metastable basin of a given potential. In the present context the random walker is the nucleating bubble which is assumed to obey a Langevin equation [101] with free energy given by eq. (8.4). The resulting expression is

$$\tau\left(\phi\right) = \frac{1}{D^*}\frac{k_B\theta}{4\Psi(\phi)\gamma_{LV}}\exp\left(\frac{\Delta\Omega^*}{k_B\theta}\right) \ . \tag{8.6}$$

The diffusion coefficient in correspondence with the critical state[101] is $D^* = k_B\theta/16\mu\pi R^*$, where μ is the fluid viscosity, providing the estimate

$$J_{het} = \frac{{n_L}^{2/3}}{\tau} = {n_L}^{2/3}\frac{\Psi(\phi)\gamma_{LV}}{4\mu\pi R^*}\exp\left(-\frac{\Delta\Omega^*}{k_B\theta}\right) \tag{8.7}$$

for the nucleation rate[12, 55].

Thermodynamics of non-homogeneous systems in contact with a solid surface

In order to describe a non-homogeneous liquid-vapor system interacting with a solid surface, we adopted the Van der Waals square gradient approximation of the (Helmoholtz) free energy functional,

$$F[\rho,\theta] = \int_V dV \left(f_b(\rho,\theta) + \frac{1}{2}\lambda \nabla\rho \cdot \nabla\rho \right) + \int_{\partial V} dS f_w(\rho,\theta) \ , \tag{8.8}$$

where f_b is the classical bulk free energy density and λ is the capillary coefficient, controlling both the surface tension and the interface thickness. The free energy contribution f_w arises from the fluid-wall interactions and accounts for the wetting properties of the surface.

The entropy functional S is obtained as the functional derivative of the free energy with respect to temperature

$$\begin{aligned} S[\rho,\theta] &= \int_V -\frac{\delta F}{\delta\theta}\, dV = \\ &= -\int_V \frac{\partial f_b}{\partial\theta}\, dV - \int_{\partial V} \frac{\partial f_w}{\partial\theta}\, dS \\ &= \int_V s_b(\rho,\theta)\ dV + \int_{\partial V} s_w(\rho,\theta)\, dS \ , \end{aligned} \tag{8.9}$$

where the third equality holds for a temperature-independent λ. The last identity follows from the definition of the bulk entropy density s_b after introducing the surface entropy density s_w. For a closed and isolated thermodynamic system of given energy E_0 and mass M_0, the constrained entropy functional (S_c) reads

$$S_c = S + l_1 \left(M_0 - \int_V \rho\, dV \right) + l_2 (E_0 - U) \ , \tag{8.10}$$

where l_1 and l_2 are two Lagrange multipliers and the internal energy U is

$$\begin{aligned} U &= F + \theta S = \int_V u\left(\rho, \nabla\rho, \theta\right) dV + U_w\left[\rho, \theta\right] \\ &= \int_V dV \left(u_b\left(\rho, \theta\right) + \frac{1}{2}\lambda \nabla\rho \cdot \nabla\rho \right) dV + \int_{\partial V} f_w + \theta s_w \, dS \,, \end{aligned} \tag{8.11}$$

with $u_b = f_b - \theta \partial f_b / \partial\theta$. By maximizing the entropy,

$$\begin{aligned} \delta S_c\left[\rho, \theta\right] &= \delta \int_V \left(s_b - l_2 u\left(\rho, \nabla\rho, \theta\right) - l_1 \rho\right) dV + \\ &+ \delta \int_{\partial V} \left[s_w - l_2\left(f_w + \theta s_w\right)\right] dS = 0 \,, \end{aligned} \tag{8.12}$$

the Lagrange multipliers are identified as $l_1 = -(\mu_c^b - \lambda\nabla^2\rho)/\theta$ and $l_2 = 1/\theta$, where μ_c^b is the bulk chemical potential. It follows that, in equilibrium, temperature and (generalized) chemical potential μ_c must be constant, as well known,

$$\theta = const = \theta_{eq} \tag{8.13}$$

$$\mu_c = \mu_c^b - \lambda\nabla^2\rho = const = \mu_c^{eq} \ . \tag{8.14}$$

Furthermore the boundary term gives rise to the additional requirement

$$\left(\lambda \nabla\rho \cdot \hat{\mathbf{n}} + \frac{\partial f_w}{\partial \rho} \right) \bigg|_{\partial V} = 0 \,, \tag{8.15}$$

where $\hat{\mathbf{n}}$ is the outward normal, to be read as a (non-linear) boundary condition for the density.

The above equilibrium conditions provide a relationship between the spatial density distribution and the thermodynamic properties of the system. Such relationship is here illustrated for an interface whose direction of inhomogeneity is $\hat{\mathbf{s}}$, under the assumption of constant λ. In order to evaluate the equilibrium density profile, the equilibrium condition Eq. 8.14 is enforced

along the direction $\hat{\mathbf{s}}$

$$\mu_c = \mu_c^b(\rho,\theta) - \lambda \frac{d^2\rho}{ds^2} = \mu_{eq}\,, \tag{8.16}$$

by multiplying Eq. 8.16 by $d\rho/ds$ and integrating between $\rho_\infty = \rho_V$ and ρ, one has

$$w_b(\rho,\theta) - w_b(\rho_V(\theta)) = \frac{\lambda}{2}\left(\frac{d\rho}{ds}\right)^2\,, \tag{8.17}$$

with $w_b = f_b - \mu_{eq}\rho$ is the bulk Landau free energy density (Grand Potential).

The grand potential is defined as the Legendre transform of the free energy,

$$\Omega = F - \int_V \rho \frac{\delta F}{\delta \rho} dV = \int_V w dV\,, \tag{8.18}$$

where $w = f_b + \lambda \nabla\rho\cdot\nabla\rho + \mu_c\rho$ is the actual grand potential density.

The surface tension can be defined as the excess (*actual*) grand potential density,

$$\begin{aligned} \gamma_{LS} &= \int_{-\infty}^{S_i} (w[\rho,\theta] - w[\rho_V])\, ds + \\ &+ \int_{S_i}^{\infty} (w[\rho,\theta] - w[\rho_L])\, ds = \int_{-\infty}^{\infty} (w[\rho,\theta] - w[\rho_V])\, ds, \end{aligned} \tag{8.19}$$

where S_i denotes the position of the Gibbs dividing surface. The definition of $w[\rho]$, Eq. 8.18, and the equilibrium condition Eq. 8.16, provide

$$\begin{aligned} \gamma_{LS} &= \int_{-\infty}^{\infty} \left[f_b + \frac{1}{2}\lambda\left(\frac{d\rho}{ds}\right)^2 - \mu_{eq}\rho - w_b(\rho_V) \right] ds = \\ &= \int_{-\infty}^{\infty} \left[w_b + \frac{1}{2}\lambda\left(\frac{d\rho}{ds}\right)^2 - w_b(\rho_V) \right] ds\ . \end{aligned} \tag{8.20}$$

Using Eq. (8.17) one finds

$$\gamma_{LS} = \int_{-\infty}^{+\infty} \lambda \left(\frac{d\rho}{ds}\right)^2 ds = \int_{\rho_V}^{\rho_L} \sqrt{2\lambda\left(w_b(\rho,\theta) - w_b(\rho_V)\right)}\, d\rho\,, \tag{8.21}$$

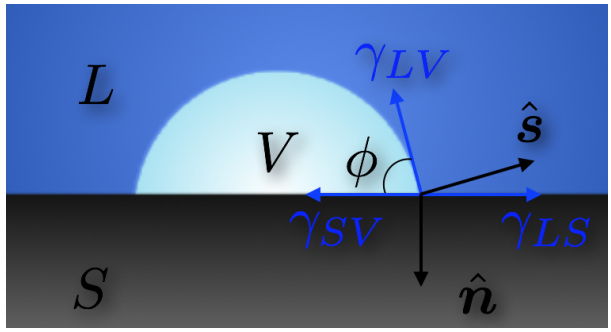

Figura 8.2: Bubble sketch illustrating both geometrical and wetting properties.

It is worth stressing that, the surface tension only depends on bulk grand potential density $w_b(\rho, \theta)$, and on the value of the capillary coefficient λ.

For f_w we deduced an analytic form that generalizes the well known approach used to describe two immiscible fluids, see e.g [126, 71].

The analytic form of f_w is constructed by observing that the equilibrium contact angle ϕ is related to the inhomogeneity direction $\hat{\mathbf{s}}$ as $\hat{\mathbf{s}} \cdot \hat{\mathbf{n}} = -\cos\phi$, (see Fig. 8.2), and the density gradient is $\boldsymbol{\nabla}\rho = d\rho/ds\,\hat{\mathbf{s}}$, so that Eq. 8.15 reads

$$\frac{df_w}{d\rho} - \lambda \frac{d\rho}{ds} \cos\phi = 0\,, \tag{8.22}$$

the above equation can be integrated by using Eq. 8.17 providing

$$f_w(\rho, \theta) = \cos\phi \int_{\rho_V}^{\rho} \sqrt{2\lambda \left(w_b\left(\tilde{\rho}, \theta\right) - w_b\left(\rho_V\right)\right)}\, d\tilde{\rho} + f_w\left(\rho_V\right)\,. \tag{8.23}$$

The analytic form of f_w recovers the physical evidence that for a pure vapor of density ρ_V in contact with the wall, the free-energy should be given by the solid-vapor surface tension, $f_w(\rho_V) = \gamma_{SV}$, Similarly, for a pure liquid of density ρ_L, $f_w(\rho_L) = \gamma_{LS}$. These aspects become even more evident by

enforcing Eq. 8.21, leading to

$$f_w(\rho_L) = \gamma_{LS} = \gamma_{LV} \cos\phi + \gamma_{SV} \,, \tag{8.24}$$

that is well known in CNT context.

Using the model expression (8.23), $\partial f_w/\partial\rho \equiv 0$ outside the coexistence and metastable regions. In this case eq. (8.15) is tantamount to enforcing zero normal derivative for the density outside these regions and assigning the contact angle ϕ in the otherwise, i.e. in the small but finite thickness region of the wall separating the liquid from the vapor. In addition, when a pure liquid in metastable state is in contact with the wall, the model provides a wall normal stratified density profile, in which the density is higher toward the solid surface, for a hydrophilic wall, and is lower for a hydrophobic one. Depletion or absorption layering of the liquid in proximity of the solid surfaces, as commonly detected [34, 74] in MD simulations. The density profiles do not show monotonic trend upon the wall normal direction, foretelling for hydrophilic walls, a wide area (near the solid surface) in which the local density is lower than its mean value ($\phi > \pi/2$). Clearly hydrophobic surfaces show the opposite behavior. These aspects play an important role in heterogeneous nucleation, inasmuch they stimulate the bubble formation on the hydrophobic walls as well as discourage it on hydrophilic surface. Such qualitative statement is corroborated both by energetic considerations and by fluctuating hydrodynamics simulations of spontaneous heterogeneous bubble nucleation. As discussed in Sec.VIII.

Landau-Lifshitz-Navier-Stokes equations with capillarity

The dynamics of the mesoscopic system of our interest is governed by a system of equation expressing mass, momentum and energy conservation, with the addition of stochastic contributions (Lifshitz-Landau-Navier-Stokes equations with capillarity LLNS):

$$\begin{aligned}
\frac{\partial \rho}{\partial t} + \boldsymbol{\nabla} \cdot (\rho \mathbf{u}) &= 0\,, \\
\frac{\partial \rho \mathbf{u}}{\partial t} + \boldsymbol{\nabla} \cdot (\rho \mathbf{u} \otimes \mathbf{u}) &= -\boldsymbol{\nabla} p + \boldsymbol{\nabla} \cdot \boldsymbol{\Sigma} + \boldsymbol{\nabla} \cdot \boldsymbol{\delta \Sigma}\,, \\
\frac{\partial E}{\partial t} + \boldsymbol{\nabla} \cdot (\mathbf{u} E) &= \boldsymbol{\nabla} \cdot (-p\mathbf{u} + \mathbf{u} \cdot \boldsymbol{\Sigma} - \mathbf{q}) + \\
&\quad + \boldsymbol{\nabla} \cdot (\mathbf{u} \cdot \boldsymbol{\delta \Sigma} - \boldsymbol{\delta q})\,,
\end{aligned} \tag{8.25}$$

where E is the total energy density, $E = \mathcal{U} + 1/2\rho|\mathbf{u}|^2 + 1/2|\boldsymbol{\nabla}\rho|^2$, with $\mathcal{U}$ the internal energy density. In the momentum and energy equations respectively, $\boldsymbol{\Sigma}$ and $\mathbf{q}$ are the classical deterministic stress tensor and energy flux, respectively, and where the terms with the prefix δ are the stochastic parts, whose statistical properties will be inferred from the fluctuation-dissipation theorem. For a simple one-component Newtonian fluid embedded with capillarity (the free energy functional is expressed as in eq. 8.8) the stress tensor $\boldsymbol{\Sigma}$ and the energy flux $\boldsymbol{q}$ can be easily deduced by standard non-equilibrium thermodynamic methods [98]:

$$\begin{aligned}
\boldsymbol{\Sigma} &= \left(\frac{\lambda}{2}|\boldsymbol{\nabla}\rho|^2 + \rho \boldsymbol{\nabla} \cdot (\lambda \boldsymbol{\nabla}\rho)\right) \boldsymbol{I} - \lambda \boldsymbol{\nabla}\rho \otimes \boldsymbol{\nabla}\rho + \\
&\quad + \mu \left[\left(\boldsymbol{\nabla}\mathbf{u} + \boldsymbol{\nabla}\mathbf{u}^T\right) - \frac{2}{3}\boldsymbol{\nabla} \cdot \mathbf{u} \boldsymbol{I}\right],
\end{aligned} \tag{8.26}$$

$$\boldsymbol{q} = \lambda\rho\boldsymbol{\nabla}\rho\boldsymbol{\nabla}\cdot\mathbf{u} - k\boldsymbol{\nabla}\theta. \tag{8.27}$$

In order to infer the statistical properties of the stochastic fluxes, it must be enforced the *fluctuation-dissipation balance* (FDB). We here report only the major results and we refer to [64] for the complete details. By means of the FDB the covariance of the stochastic process can be written as

$$\left\langle \boldsymbol{\delta\Sigma}(\hat{x},\hat{t}) \otimes \boldsymbol{\delta\Sigma}^{\dagger}(\tilde{x},\tilde{t}) \right\rangle = \mathbf{Q}^{\boldsymbol{\Sigma}}\delta(\hat{x}-\tilde{x})\delta(\hat{t}-\tilde{t}), \tag{8.28}$$

with

$$\mathbf{Q}^{\boldsymbol{\Sigma}}{}_{\alpha\beta\nu\eta} = 2\mathrm{k}_B\theta\mu\left(\delta_{\alpha\nu}\delta_{\beta\eta} + \delta_{\alpha\eta}\delta_{\beta\nu} - \frac{2}{3}\delta_{\alpha\beta}\delta_{\nu\eta}\right), \tag{8.29}$$

concerning the viscous stress tensor, and

$$\left\langle \boldsymbol{\delta q}(\hat{x},\hat{t}) \otimes \boldsymbol{\delta q}^{\dagger}(\tilde{x},\tilde{t}) \right\rangle = \mathbf{Q}^{\mathbf{q}}\delta(\hat{x}-\tilde{x})\delta(\hat{t}-\tilde{t}), \tag{8.30}$$

with

$$\mathbf{Q}^{\mathbf{q}}{}_{\alpha\beta} = 2\mathrm{k}_B\theta^2 k\delta_{\alpha\beta}\,, \tag{8.31}$$

concerning the heat flux. Moreover it is worth noting that the correlation between thermodynamic force of different tensor rank has to be zero due to the Curie-Prigogine principle *i.e.* ($\left\langle \delta\mathbf{q}^{\dagger}(\tilde{x},\tilde{t}) \otimes \delta\boldsymbol{\Sigma}(\hat{x},\hat{t}) \right\rangle = 0$). Thus in the theory of fluctuating hydrodynamics, the effect of thermal fluctuation appears directly in the Navier-Stokes equations as an "external" force arising from the fluctuating part of the thermodynamic fluxes.

From an operative point of view it is more convenient to re-express the stochastic contributions in terms of the standard Wiener process as

$$\boldsymbol{\delta\Sigma} = \sqrt{2\mu\mathrm{k}_B\theta}\tilde{\boldsymbol{W}}^{\boldsymbol{v}} - \frac{1}{3}\sqrt{2\mu\mathrm{k}_B\theta}\,\mathrm{Tr}\left(\tilde{\boldsymbol{W}}^{\boldsymbol{v}}\right)\boldsymbol{I}, \tag{8.32}$$

$$\boldsymbol{\delta q} = \sqrt{2k\mathrm{k}_B\theta^2}\tilde{\boldsymbol{W}}^{\boldsymbol{E}}\,. \tag{8.33}$$

$\tilde{\boldsymbol{W}}^{\boldsymbol{v}} = \left(\boldsymbol{W}^{\boldsymbol{v}} + (\boldsymbol{W}^{\boldsymbol{v}})^T\right)/\sqrt{2}$ is a stochastic symmetric tensor field, and $\tilde{\boldsymbol{W}}^{\boldsymbol{E}}$ is a stochastic vector, with the following statistical properties

$$\left\langle {W^v}_{\alpha\beta}(\hat{x},\hat{t}){W^v}_{\gamma\delta}(\tilde{x},\tilde{t})\right\rangle = \delta_{\alpha\gamma}\delta_{\beta\delta}\delta(\hat{x}-\tilde{x})\delta(\hat{t}-\tilde{t}), \tag{8.34}$$

$$\left\langle {W^E}_{\alpha}(\hat{x},\hat{t}){W^E}_{\beta}(\tilde{x},\tilde{t})\right\rangle = \delta_{\alpha\beta}\delta(\hat{x}-\tilde{x})\delta(\hat{t}-\tilde{t})\,. \tag{8.35}$$

Particular attention must be paid on the boundary conditions for the system of equations (8.25), here we use no-slip condition for the fluid velocity at the solid surface and adiabatic walls, i.e. $\rho\mathbf{u}|_{\partial V} = 0$, $\partial\theta/\partial n = 0$ and $\partial\rho/\partial n|_{\partial V} = g(\theta,\phi)$ concerning the density field. Where the function $g = -\cos\phi\sqrt{2/\lambda\left(w_b\left(\rho,\theta\right) - w_b\left(\rho_V\right)\right)}$ is positive for an hydrophilic wall and is negative for an hydrophobic one, see eq.(8.23). In addition in order to satisfy the FDB in the presence of the solid boundaries we follow the procedure suggested in ([11, 52]), that provide a simple recipe to deal with stochastic fluxes when non-periodic boundary conditions are needed, in particular has been showed that the variance of the stochastic processes W on the wall has to be modified as $\langle WW\rangle|_{\partial V} = \alpha$, where $\alpha = 2$ for Neumann boundary conditions and $\alpha = 0$ for Dirichlet ones, this ensures the preservation of the FDB in the discretized equations.

Equation of State

Two more relations are needed in order to close the system of equations (8.25), i.e. the equations of state that relates the thermodynamic pressure and the internal energy to the density and temperature, $p = p(\rho,\theta)$, $\mathcal{U} = \mathcal{U}(\rho,\theta)$. These two equations both follow by choosing a suitable free energy density $f_b = f_b(\rho,\theta)$ in eq. (8.8). In this work we choose an expression that recover the properties of a Lennard-Jones fluid [75]. The final expressions are too

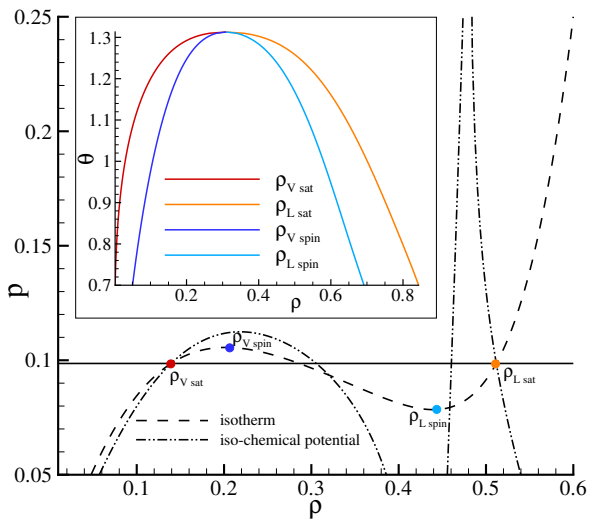

Figura 8.3: Phase diagram for the Lennard-Jones EoS[75]. In the main plot the isotherm $\theta = 1.25$ and the iso-chemical potential $\mu = \mu_{sat}$ with the saturation value are reported with dashed and dash-dotted lines, respectively. The saturation densities are identified as the two points with equal temperature, chemical potential and pressure; the red circle represent the vapor saturation point and the orange circle the liquid one. The other two circles, blue and light blue, represent the spinodal points, vapor and liquid respectively, identified on the isotherm where $\partial p/\partial \rho = 0$. In the inset the loci of all the saturation and spinodal points at different temperatures are reported in the $\rho - \theta$ plane.

cumbersome to be repeated here, but it is interesting to discuss some of the crucial features that allow the description of a two phase, vapor–liquid, system. The thermodynamic states placed between the saturation and the spinodal lines in the inset of Fig. 8.3 represent the metastable states for vapor and liquid phase respectively. In particular when the thermodynamic state of a fluid is placed in such sets, a nucleus of new phase (vapor bubble in the region of metastable liquid, and liquid droplet in metastable vapor) can nucleate with a probability related to the distance from boundary of the phase diagram, i.e. the probability is high close to the spinodal lines and is low toward the binodal states.

Bubble-Nucleation Simulations

The heterogeneous vapor bubble nucleation is here studied by means of the LLNS system of equations presented in the previous sections. In particular bubble nucleation is investigated in a metastable liquid enclosed in a box with periodic boundary conditions in $x - y$ directions, and two flat solid surface otherwise. The fluid is characterized by an equation of state that recover the properties of a Lennard-Jones fluid [75].

By introducing the following reference quantities $\sigma = 3.4 \times 10^{-10}\ m$ as length, $\epsilon = 1.65 \times 10^{-21}\ J$ as energy, $m = 6.63 \times 10^{-26}\ kg$ as mass, $U_r = (\epsilon/m)^{1/2}$ as velocity, $T_r = \sigma/U_r$ as time, $\theta_r = \epsilon/k_B$ as temperature, $\mu_r = \sqrt{m\epsilon}/\sigma^2$ as shear viscosity, $c_{vr} = mk_B$ as specific heat at constant volume and $k_r = \mu_r c_{vr}$ as thermal conductivity; the dimensionless fields are defined as $\rho^* = \rho/\rho_r$, $\theta^* = \theta/\theta_r$, $\mathbf{u}^* = \mathbf{u}/U_r$.

Hence the dimensionless fluxes (eq. 8.26, 8.27, 8.32, 8.33) read

$$\boldsymbol{\Sigma}^* = \left(\frac{C}{2}|\nabla^*\rho^*|^2 + \rho^*\nabla^*\cdot(C\nabla^*\rho^*)\right)\boldsymbol{I} - C\nabla^*\rho^*\otimes\nabla^*\rho^* + \mu^*\left[\left(\nabla^*\mathbf{u}^* + \nabla\mathbf{u}^{T*}\right) - \frac{2}{3}\nabla^*\cdot\mathbf{u}^*\boldsymbol{I}\right]$$

$$\boldsymbol{q}^* = C\rho^*\nabla^*\rho^*\nabla^*\cdot\mathbf{u}^* - k^*\nabla^*\theta^*\,,$$

$$\boldsymbol{\delta\Sigma}^* = \sqrt{\frac{2\mu^*\theta^*}{\Delta V^*\Delta t^*}}\boldsymbol{W^{v*}} - \frac{1}{3}\sqrt{\frac{2\mu^*\theta^*}{\Delta V^*\Delta t^*}}\,\mathrm{Tr}\left(\boldsymbol{W^{v*}}\right)\boldsymbol{I}\,,$$

$$\boldsymbol{\delta q}^* = \sqrt{\frac{2k^*\theta^{*2}}{\Delta V^*\Delta t^*}}\boldsymbol{W^{E*}}\,,$$

where $C = \lambda\rho_r/\sigma^2U_r^2$ is a capillary number, fixed in our simulations as $C = 5.244$, to reproduce the exact value of surface tension expected for a Lennard-Jones fluid [75], as expleined in the previous section. The system volume $V^* = 750\times750\times500$ has been discretized on a equi-spaced grid, containing 50 cells in z-direction and 75 in $x-y$.

Several metastable conditions have been investigated and here we report in detail the results of four different simulations at initial temperature $\theta^* = \theta^*_{eq} = 1.25$ and different bulk densities $\rho^*_L = 0.47\ ,0.475\ ,0.48\ ,0.485$; for which nucleation is observed almost only near solid boundaries. In fact, this mesoscale approach allows for exploring very large system (in comparison with molecular dynamics simulations) and for a very long time, for this reason it possible to observe also homogeneous nucleation even though the higher barrier of the homogenous case. The metastable range of densities is $\rho^*_L \in \left[\rho^*_{sat}, \rho^*_{spin}\right] = [0.44, 0.51]$, where ρ^*_{sat} and ρ^*_{spin} are the dimensionless saturation and spinodal densities, respectively. Only ten runs for each simulation have been carried out in order to perform statistical averages of the results since the macroscopical observables, like the nucleation rates, have demonstrated to be statistically robust.

For a detailed explanation of bubble identification procedure, we refer to [64].

A few snapshots of the system evolution in the different metastable conditions are shown in the top pannels of Fig.s 8.4,8.5. Starting from a homogeneous liquid phase, the hydrodynamic fluctuations lead the system to spontaneously decompose in two different phases. The vapor nucleii starts forming with a complex shape, far from a spherical one, as observed in other works [49]. After reaching the critical size, they start expanding up to a stable equilibrium state. This new thermodynamic state is characterized by the presence of several stable vapor bubbles in equilibrium with the surrounding liquid. The number and the dimension of the bubbles in the latter stage is strictly connected with the initial metastable condition, as evident on the left of panels in Fig.s 8.4,8.5.

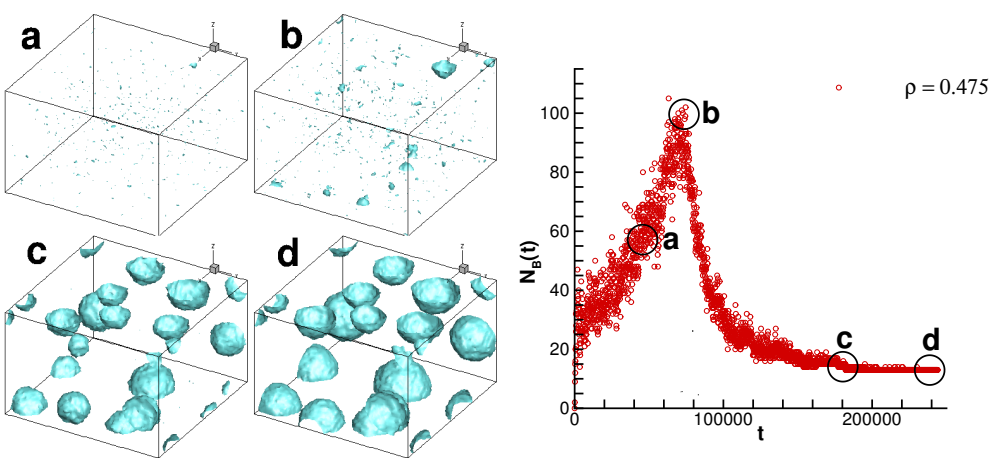

Figura 8.4: Left panel: snapshots during the nucleation process in the thermodynamic condition $\rho^* = 0.475 \quad \theta^* = 1.25$, the snapshots are taken at time $t^* = 60000$, $t^* = 80000$, $t^* = 240000$, $t^* = 264000$. Right panel: number of stable bubble vs time for the aforementioned thermodynamic condition.

In the right of the panels in Fig.s 8.4,8.5 we report a quantitative analysis

of the time evolution of the number of vapor nucleii that exceed the critical size. The same two different metastable conditions of the snapshots reported in Fig.s 8.4,8.5 are here analyzed. The linking between the snapshots and the observable $N_B(t)$ is marked in Fig.s 8.4,8.5 through the letters a, b, c, d.

Similarly to the homogeneous [64], the dynamics of the system can be divided in three main stages: during the first one the number of bubble increases almost linearly with time (with a constant rate); when the system is populated enough, the second stage consists in the expansion-coalescence dynamics when the nucleii increase their size up to the equilibrium radius and some of them coalesce with neighboring bubbles. Furthermore the smallest nucleii start collapsing due to the liquid compression. During the third stage the system reach a more stable thermodynamic condition, in which a small number of stable vapor bubbles are in equilibrium with the surrounding compressed liquid. As shown in Fig. 8.4, the metastable condition at $\rho_L = 0.475$, which, among those we have considered, is one of closest one to the spinodal– hence the one with lower energy barrier to be overcome to nucleate bubbles – leads to a more populated system and clearly shows more frequent coalescence events. At $\rho_L = 0.485$, instead, only the expansion of the bubbles is observed after reaching an almost stable number of bubbles.

The analysis of the first stage of the dynamics, when the number of bubble increases, gives access to another crucial observable, the nucleation rate J^*, representing the number of bubbles formed per unit time and per unit area. From an operative point of view, the nucleation rate is here calculated as the slope of the linear fit of the initial part of the curves in fig. 8.5, as suggested in [49]. The calculated nucleation rates at different metastable conditions are compared in fig. 8.6 with the theoretical predictions given by

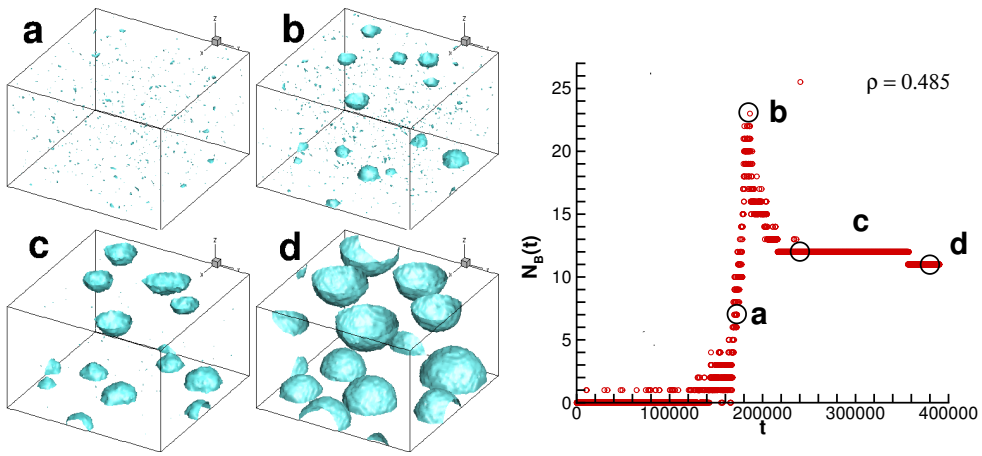

Figura 8.5: Left panel: snapshots during the nucleation process in the thermodynamic condition $\rho^* = 0.485 \quad \theta^* = 1.25$, the snapshots are taken at time $t^* = 180000$, $t^* = 1900$, $t^* = 280000$, $t^* = 360000$. Right panel: number of stable bubble vs time for the aforementioned thermodynamic condition.

the Kramers theory applied to classical nucleation theory (CNTK), and the Blander and Katz CNT formulation, formulated here in heterogeneous case, see Sec. I for details. Despite the strong assumptions in CNT, the rates calculated with our numerical simulations are slightly smaller than predicted by classical theory, in particular when compared with the Krames approach, as exposed for the homogeneous case in [64, 49] and also in the heterogeneous case in [110], particularly for higher temperatures. This discrepancy is mostly related to the overcrowding of bubbles in the system [62], in fact as evident in fig. 8.6 the theoretical predicted rates are more precise as the system is less populated. Furthermore as already mentioned before, since the system dimensions are relevant, several nucleation event are detected also in the bulk liquid, in the latter case the imposed mass constrain leads the liquid to compress, inhibiting the nucleation process. These aspects has been quantitative evaluated in the homogeneous case, by evaluating the number

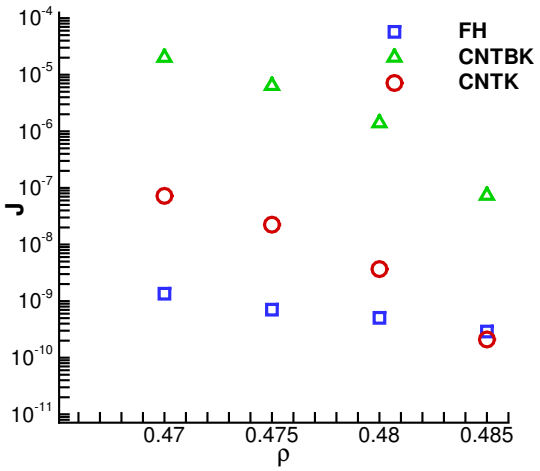

Figura 8.6: Nucleation rate comparison between fluctuating hydrodynamics numerical results (blue squares FH), Blander and Katz rate predictions (green delta CNTBK) and Kramers theory (red circles CNTK) at different metastable conditions.

of coalescence and collapse events, showing how the hydrodynamic effects are crucial in the dynamics of the system and strongly affect the nucleation rate [64]. For the specific thermodynamic condition $\theta^* = 1.25\,, \rho^* = 0.48$, for which the majority of nucleation events are detected on the solid surface, we analyze the wetting influence on the nucleation rate. We perform several numerical simulation, by changing the chemistry of the surface, spanning from hydrophobic conditions ($\cos(\phi) > 0$) to hydrophilic ones ($\cos(\phi) < 0$). As expected according to energy barrier considerations, the nucleation rate increase when the contact angle decrease, as it is evident in Fig. 8.7, and the numerical results agree with the classical theoretical predictions, especially with Kramers theory. However the qualitative accordance with the classical theory is detected only when considering weakly hydrophilic walls, in fact

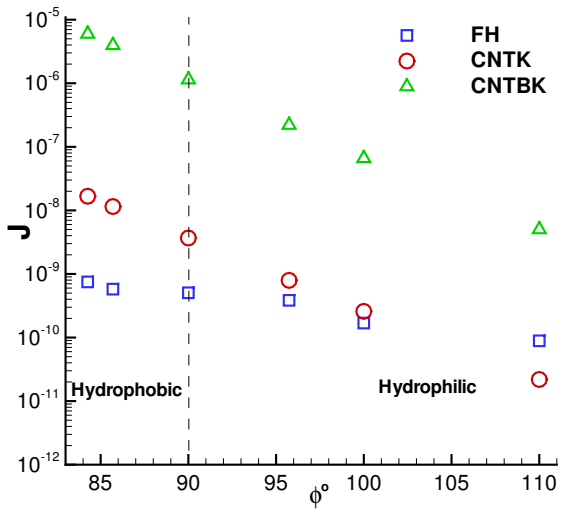

Figura 8.7: Nucleation rate comparison between fluctuating hydrodynamics numerical results (blue squares FH), Blander and Katz rate predictions (green delta CNTBK) and Kramers theory (red circles CNTK) for different wall wettabilities.

as ϕ increases the nucleation events are detected mostly in the bulk phase, despite the presence of solid surfaces, as evident in Fig. 8.9.

In Fig. 8.8 is reported the number of stable bubbles detected on the walls as a function of time. The left panel shows the number of bubbles nucleated on the walls, the right one the totality of the bubbles nucleated in the domain. It is evident how, by increasing the contact angle, the heterogeneous nucleation events decrease drastically, but several bubbles are formed in the bulk liquid. In particular, for $\phi > \phi_{crit}$ with $\phi_{crit} \approx 120°$ almost all nucleation events are homogeneous. This unexpected behavior can be justified according to two different considerations: 1) for a thermodynamic point of view, the hydrophilic nature of the surfaces involves accumulation of liquid to the wall, providing strongly disincentivizing of vapor nuclei in these zo-

nes, 2) In addition, for hydrophilic surfaces, heterogeneous and homogeneous nucleation barriers are comparable, but the number of nucleation size in the bulk phase is greater than the one on the walls, making the homogeneous nucleation probability higher with respect to the heterogeneous one.

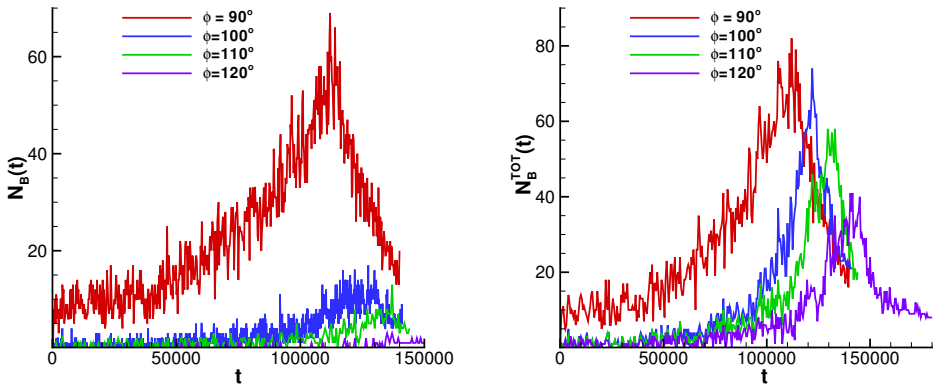

Figura 8.8: Number of supercritical bubbles vs time. The different curves refer to different contact angles ϕ. In the left panel is reported the number of bubbles detected on the walls, on the right the total number of bubble detected in the domain.

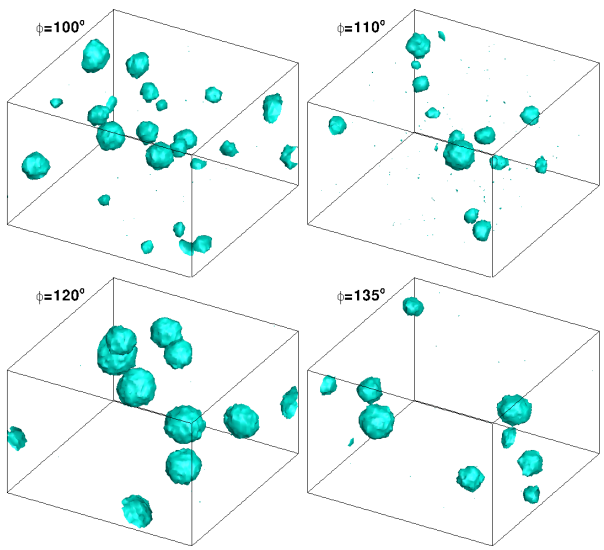

Figura 8.9: Snapshots during the nucleation process in the thermodynamic condition $\rho^* = 0.48 \quad \theta^* = 1.25$ for different contact angles.

Appendice A

Gaussian Path Integrals

Let us consider a characteristic functional

$$\Phi[\lambda] = \int Dx \, \exp\left[-\frac{1}{2}\int\int d\hat{\mathbf{r}}d\tilde{\mathbf{r}}\, x\left(\hat{\mathbf{r}}\right)\, A\left(\hat{\mathbf{r}},\tilde{\mathbf{r}}\right)\, x\left(\tilde{\mathbf{r}}\right) + \int \lambda\left(\hat{\mathbf{r}}\right) x\left(\hat{\mathbf{r}}\right) d\hat{\mathbf{r}}\right], \tag{A.1}$$

we aim to evaluate it by using an appropriate coordinate transformation. Let $\hat{\mathbf{A}}$ be an Hermitian bounded operator on a Hilbert space $\mathcal{H}$ defined as

$$\hat{\mathbf{A}} v\left(\hat{\mathbf{r}}\right) = \int A\left(\hat{\mathbf{r}},\tilde{\mathbf{r}}\right)\, v\left(\tilde{\mathbf{r}}\right) d\tilde{\mathbf{r}}\,, \tag{A.2}$$

Since $\hat{\mathbf{A}}$ is Hermitian, an orthonormal basis exists $\mathcal{B}$ of $\mathcal{H}$ consisting of eigenfunctions of $\hat{\mathbf{A}}$, such that

$$\hat{\mathbf{A}} v^{\mu}\left(\hat{\mathbf{r}}\right) = \int A\left(\hat{\mathbf{r}},\tilde{\mathbf{r}}\right)\, v^{\mu}\left(\tilde{\mathbf{r}}\right) d\tilde{\mathbf{r}} = \omega_{\mu} v^{\mu}\left(\hat{\mathbf{r}}\right)\,, \tag{A.3}$$

$$\int v^{\mu}\left(\tilde{\mathbf{r}}\right) v^{\nu}\left(\tilde{\mathbf{r}}\right) d\tilde{\mathbf{r}} = \delta^{\mu\nu}\,, \tag{A.4}$$

where ω_{μ} are real eigenvalues and the eigenfunction v^{μ} are orthonormal. Hence the representation of the functions $x(\hat{\mathbf{r}}), \lambda(\hat{\mathbf{r}})$ are

$$x\left(\hat{\mathbf{r}}\right) = \sum_{\mu} a_{\mu} v^{\mu}\left(\hat{\mathbf{r}}\right)\,, \qquad \lambda\left(\hat{\mathbf{r}}\right) = \sum_{\mu} b_{\mu} v^{\mu}\left(\hat{\mathbf{r}}\right)\,, \tag{A.5}$$

furthermore, the integration measure is

$$Dx = \det\left(\frac{\delta x\left(\hat{\mathbf{r}}\right)}{\delta a_\beta}\right)\prod_\beta da_\beta = \prod_\beta da_\beta\,, \tag{A.6}$$

where $\det\left(\frac{\delta x\left(\hat{\mathbf{r}}\right)}{\delta a_\beta}\right) = 1$ due to orthonormal transformation (isometry). Thus the representation of $\Phi\left[\lambda\right]$ onto the functional basis $\mathcal{B}$ reads

$$\Phi\left[b\right] = \int\prod_\beta da_\beta \exp\left[-\frac{1}{2}\int\int\sum_{\mu,\nu} a_\mu v^\mu\left(\hat{\mathbf{r}}\right) A\left(\hat{\mathbf{r}},\tilde{\mathbf{r}}\right)\ a_\nu v^\nu\left(\tilde{\mathbf{r}}\right) d\hat{\mathbf{r}}d\tilde{\mathbf{r}} + \int\sum_{\mu,\nu} b_\mu v^\mu\left(\hat{\mathbf{r}}\right) a_\nu v^\nu\left(\hat{\mathbf{r}}\right) d\hat{\mathbf{r}}\right]$$

$$\Phi\left[b\right] = \int\prod_\beta da_\beta \exp\left[-\frac{1}{2}\int\sum_{\mu,\nu} a_\mu v^\mu\left(\hat{\mathbf{r}}\right)\hat{\mathbf{A}} v^\nu\left(\tilde{\mathbf{r}}\right) d\hat{\mathbf{r}} + \sum_\mu b_\mu a_\mu\right]\,, \tag{A.7}$$

$$\Phi\left[b\right] = \int\prod_\beta da_\beta \exp\left[-\frac{1}{2}\sum_\mu\left(a_\mu^2\omega_\mu - b_\mu a_\mu\right)\right]\,,$$

$$\Phi\left[b\right] = \prod_\mu\int_{-\infty}^{+\infty} da_\mu \exp\left[-\frac{1}{2}\omega_\mu a_\mu^2 + b_\mu a_\mu\right]\,, \tag{A.8}$$

The last integral can be evaluated by completing the square in the integrand exponent, this procedure leads to

$$\Phi\left[b\right] = \Phi\left[0\right]\prod_\mu \exp\left[\frac{1}{2}\omega_\mu^{-1} b_\mu^2\right] = \Phi[0]\ \exp\left[\frac{1}{2}\int\int d\hat{\mathbf{r}}d\tilde{\mathbf{r}}\,\lambda\left(\hat{\mathbf{r}}\right)\ G\left(\hat{\mathbf{r}},\tilde{\mathbf{r}}\right)\ \lambda\left(\tilde{\mathbf{r}}\right)\right]\,, \tag{A.9}$$

where $\Phi\left[0\right] = \prod_\mu \omega_\mu$, and $\hat{\mathbf{G}} = \hat{\mathbf{A}}^{-\mathbf{1}}$. Indeed, let $\hat{\mathbf{G}}$ be the inverse of the operator $\hat{\mathbf{A}}$, by multiplying both sides of Eq. (A.3) by the operator $\hat{\mathbf{G}}$ one has

$$\hat{\mathbf{G}} v^\mu\left(\hat{\mathbf{r}}\right) = \int G\left(\hat{\mathbf{r}},\tilde{\mathbf{r}}\right) v^\mu\left(\tilde{\mathbf{r}}\right) d\tilde{\mathbf{r}} = \frac{1}{\omega_\mu} v^\mu\left(\hat{\mathbf{r}}\right)\,, \tag{A.10}$$

hence the eigenvalues of $\hat{\mathbf{G}}$ are $\frac{1}{\omega_\mu}$. So that, the integral

$$\int\int d\tilde{\mathbf{r}}d\hat{\mathbf{r}}\lambda\left(\hat{\mathbf{r}}\right) G\left(\hat{\mathbf{r}},\tilde{\mathbf{r}}\right)\lambda\left(\tilde{\mathbf{r}}\right)\,, \tag{A.11}$$

can be written as

$$\int\int d\tilde{\mathbf{r}}d\hat{\mathbf{r}}\lambda\left(\hat{\mathbf{r}}\right)G\left(\hat{\mathbf{r}},\tilde{\mathbf{r}}\right)\lambda\left(\tilde{\mathbf{r}}\right)\ , \tag{A.12}$$

$$\int\int d\tilde{\mathbf{r}}d\hat{\mathbf{r}}\sum_{\mu,\nu}b_{\mu}v^{\mu}\left(\hat{\mathbf{r}}\right)G\left(\hat{\mathbf{r}},\tilde{\mathbf{r}}\right)b_{\nu}v^{\nu}\left(\tilde{\mathbf{r}}\right)\ , \tag{A.13}$$

$$\int d\hat{\mathbf{r}}\sum_{\mu,\nu}b_{\mu}v^{\mu}\left(\hat{\mathbf{r}}\right)\frac{1}{\omega_{\nu}}b_{\nu}v^{\nu}\left(\hat{\mathbf{r}}\right)=\sum_{\mu}b_{\mu}^{2}\frac{1}{\omega_{\mu}}\,, \tag{A.14}$$

and so

$$\sum_{\mu}b_{\mu}^{2}\frac{1}{\omega_{\mu}}=\int\int d\hat{\mathbf{r}}d\tilde{\mathbf{r}}\,\lambda\left(\hat{\mathbf{r}}\right)\ G\left(\hat{\mathbf{r}},\tilde{\mathbf{r}}\right)\ \lambda\left(\tilde{\mathbf{r}}\right)\ . \tag{A.15}$$

The latter equation is known as Parseval's identity.

Appendice B

Ito Stochastic Integration

In this appendix the main features of the stochastic calculus are retraced for the reader's convenience, focusing on the Ito interpretation. For the reader interested in further deepening the search of stochastic calculus see [66].

Let us consider a continuous function $g(t)$ on the bounded interval $S = [a, b]$, and a partition of S into n small subintervals $s_j = [t_j, t_{j-1}]$, such that $\delta_j = t_j - t_{j-1}$, the Riemann-Stieltjes integral is defined as

$$\int_a^b g(t)dF(t) = \lim_{n\to\infty} \sum_{j=1}^{n} g\left(t_{j-1}\right) \left(F\left(t_j\right) - F\left(t_{j-1}\right)\right) , \tag{B.1}$$

if the function F is a function of bounded variation, i.e.

$$\lim_{n\to\infty} \sum_{j=1}^{n} \left| \left(F\left(t_j\right) - F\left(t_{j-1}\right)\right) \right| < \infty . \tag{B.2}$$

Any differentiable function has a finite variation, so that, it is a function of bounded variation. Roughly when considering single variable functions, and a point moving on its graphic, the functions of bounded variation are those having a finite trajectory onto a generic subset of the graphic. Hence, although represented by a continuous function, it should be intuitive that a

Brownian path can not be of bounded variation, since it shows rapid variations on infinitesimal subintervals. More rigorously, the probability that the first derivative with respect to the generic time instant t does not exist is equal to 1, or

$$P\left[\lim_{n\to\infty}\sum_{j=1}^{n}\left|\left(B\left(t_j\right)-B\left(t_{j-1}\right)\right)\right|=\infty\right]=1\,, \tag{B.3}$$

where $B(t)$ is a Wiener process, having the following properties

- $B(0)=0$ almost surely,
- $\langle B(t)\,B(t+\tau)\rangle=0$ (independent increment),
- $B(t)-B(t+\tau)\sim\mathcal{N}(0,\tau)$,
- $B(t)$ is almost surely continuous.

As a consequence, it is not possible to directly define the integral

$$\int_0^t H(s)dB(s) \tag{B.4}$$

in a Riemann-Stieltjes sense.

However, after defining the *mean square limit* of the following partial sums, as

$$\mathrm{ms}-\lim_{n\to\infty}\mathcal{S}_n\stackrel{\mathrm{def}}{=}\left\langle\lim_{n\to\infty}\left[\sum_{j=1}^{n}\Delta S(t_j)-\langle\Delta S\rangle\right]^2\right\rangle \tag{B.5}$$

it is possible to define the *Ito stochastic integral* of a function $H(t)$ as

$$\int_0^t H(s)dB(s)=\mathrm{ms}-\lim_{n\to\infty}\sum_{j=1}^{n}H\left(t_{j-1}\right)\left[B\left(t_j\right)-B\left(t_{j-1}\right)\right]\,. \tag{B.6}$$

Before providing an example of stochastic integration according to the Ito rules, it is useful to remember an important notable special sum, often used

when performing stochastic integration. The sum consists in a sequence of Brownian increment as

$$\sum_{j=1}^{n} \left\langle \left[B\left(t_j\right) - B\left(t_{j-1}\right)\right]^2 \right\rangle - t = 0\,, \tag{B.7}$$

because the sequence $B\left(t_j\right) - B\left(t_{j-1}\right)$ is normally distributed with zero mean and variance t/n, i.e. $\left\langle \left(B\left(t_j\right) - B\left(t_{j-1}\right)\right)^2 \right\rangle = t/n$.

Let us evaluate the following stochastic integral by simply applying the definition Eq. B.6

$$\begin{aligned} \int_0^t B(s)dB(s) &= \mathrm{ms} - \lim_{n\to\infty} \sum_{j=1}^{n} B\left(t_{j-1}\right)\left[B\left(t_j\right) - B\left(t_{j-1}\right)\right] = \\ &= \frac{1}{2}B(t)^2 - \frac{1}{2}\lim_{n\to\infty} \left\langle \left\{ \sum_{j=1}^{n} \left[B\left(t_j\right) - B\left(t_{j-1}\right)\right]^2 - t \right\}^2 \right\rangle\,, \end{aligned} \tag{B.8}$$

where the relationship Eq. B.7 has been used, and the last term of the RHS of Eq. B.8 can be written as

$$\begin{aligned} \left\langle \left\{ \sum_{j=1}^{n} \left[B\left(t_j\right) - B\left(t_{j-1}\right)\right]^2 - t \right\}^2 \right\rangle &= \left\langle \sum_{j=1}^{n} \left[B\left(t_j\right) - B\left(t_{j-1}\right)\right]^4 \right\rangle + \\ &+ \left\langle 2\sum_{j=1}^{n}\sum_{k<j}^{n} \left[B\left(t_j\right) - B\left(t_{j-1}\right)\right]^2 \left[B\left(t_k\right) - B\left(t_{k-1}\right)\right]^2 \right\rangle + \\ &- 2t \left\langle \sum_{j=1}^{n} \left[B\left(t_j\right) - B\left(t_{j-1}\right)\right]^2 \right\rangle + t^2\,, \end{aligned} \tag{B.9}$$

by enforcing the statistical properties of the Gaussian increments one has

$$\begin{aligned} \lim_{n\to\infty} \left\langle \left\{ \sum_{j=1}^{n} \left[B\left(t_j\right) - B\left(t_{j-1}\right)\right]^2 - t \right\}^2 \right\rangle &= \\ &= \lim_{n\to\infty} \left[\frac{3t^2}{n} + \frac{n(n-1)}{n}t^2 - t^2 \right] = 0\,, \end{aligned} \tag{B.10}$$

thus

$$\text{ms} - \lim_{n\to\infty} \sum_{j=1}^{n} \left[B\left(t_j\right) - B\left(t_{j-1}\right)\right]^2 = t\,, \tag{B.11}$$

providing

$$\int_0^t B(s)dB(s) = \frac{1}{2}B(t)^2 - \frac{1}{2}t^2\,. \tag{B.12}$$

The result obtained in Eq. B.12 is evidently in contrast with the usual Riemann-Stieltjes rule, in which the term $1/2t^2$ does not appear. In the Ito integrals this term arises from the fact that $|B\left(t_j\right) - B\left(t_{j-1}\right)|$ is always of order $t^{1/2}$, so that, the second order terms do not vanish when performing the limit. It is also evident from Eq. B.10 as the Ito integral definition provides the following equality

$$\int_0^t \left(dB(s)\right)^2 = t \implies dB^2 = dt\,. \tag{B.13}$$

After introducing the stochastic integral, we can define an Ito process as $H = \{H(t), t \geq 0\}$ solving

$$H(t) = H(0) + \int_0^t \mu\left(H(s), s\right) ds + \int_0^t \sigma\left(H(s), s\right) dB(s)\,, \tag{B.14}$$

or equivalently

$$dH(t) = \mu\left(H(s), s\right) dt + \sigma\left(H(s), s\right) dB(s)\,, \tag{B.15}$$

where μ and σ are the drift and the diffusion terms, respectively.

The general differentiation rules in Ito calculus are described by the *Ito's lemma*, that is retraced here for a generic single variable function, and it will be recalled in the next section for a multidimensional case. Let us consider a twice-differentiable scalar function $f\left(H, t\right)$, the second order Taylor

expansion reads

$$df(H,t) = \frac{\partial f}{\partial t}dt + \frac{\partial f}{\partial H}dH + \frac{\partial^2 f}{\partial H \partial t}dH dt + \frac{1}{2}\frac{\partial^2 f}{\partial t^2}dt^2 + \frac{1}{2}\frac{\partial^2 f}{\partial H^2}dH^2 + o\left(t^{3/2}\right) , \tag{B.16}$$

by substituting as dH the Eq. B.15 and by performing the limit for $dt \to 0$, since $dB^2 \sim dt$ one has

$$df(H,t) = \left[\frac{\partial f}{\partial t} + \mu\frac{\partial f}{\partial H} + \frac{\sigma^2}{2}\frac{\partial^2 f}{\partial H^2}\right] dt + \sigma\frac{\partial f}{\partial H} , \tag{B.17}$$

that represents an Ito process for the function $f(H,t)$.

Appendice C

Backward-Forward Kolmogorov Equations

Let us consider a multi-dimensional Ito process driven by the standard Wiener process $\mathbf{B}$

$$d\mathbf{X} = \mu\left(\mathbf{X}, t\right) dt + \sigma\left(\mathbf{X}, t\right) d\mathbf{B}\,. \tag{C.1}$$

where $\mathbf{X} = \left(X_1, X_2, ..., X_N\right)^T$ is a collection of Ito processes, $\mu = \left(\mu_1, \mu_2, ..., \mu_N\right)^T$ a drift vector, and $\sigma\sigma^T = 2\mathbf{D}$ a $N \times N$ diffusion matrix. For any twice-differentiable function $\Phi\left(\mathbf{X}, t\right)$ Ito's lemma yields (see Eq. B.17)

$$d\Phi = \left[\frac{\partial \Phi}{\partial t} + \frac{\partial \Phi}{\partial X_\alpha}\mu_\alpha + D_{\alpha\beta}\frac{\partial^2 \Phi}{\partial X_\alpha \partial X_\beta}\right] dt + \frac{\partial \Phi}{\partial X_\alpha}\sigma_{\alpha\beta} dB_\beta\,, \tag{C.2}$$

Let Ψ be a compactly supported function on a set $\mathcal{I}$, $\Psi\left(\mathbf{X}, t\right) \in C_0^1\left(\mathcal{I}\right)$, $\mathcal{I} = (t_0, T)$, Ito's lemma provides

$$\Psi\left(\mathbf{Y}, t_0\right) - \Psi\left(\mathbf{X}_T, T\right) = \int_{t_0}^{T}\left[\frac{\partial \Psi}{\partial t} + \frac{\partial \Psi}{\partial X_\alpha}\mu_\alpha + D_{\alpha\beta}\frac{\partial^2 \Psi}{\partial X_\alpha \partial X_\beta}\right] dt + \int_{t_0}^{T}\frac{\partial \Psi}{\partial X_\alpha}\sigma_{\alpha\beta} dB_\beta\,, \tag{C.3}$$

since $\langle dB_\beta(\mathbf{X}, t)|\mathbf{Y}, t_0\rangle = 0$ and $\Psi\left(\mathbf{X}, t\right)$ has compact support in $\mathcal{I}$, by multiplying Eq. (C.3) by the transition probability $P(\mathbf{X}, t|\mathbf{Y}, t_0)$ and integrating

on its support one has

$$\int_{t_0}^{T}\int_{\mathbb{R}^N} d\mathbf{X}\,dt\left[\frac{\partial\Psi}{\partial t}+\frac{\partial\Psi}{\partial x_\alpha}\mu_\alpha+D_{\alpha\beta}\frac{\partial^2\Psi}{\partial x_\alpha\partial x_\beta}\right]P(\mathbf{x},t|\mathbf{x}_0,0)=0\,. \tag{C.4}$$

After changing the order of integration Eq. (C.4), can be integrated by parts twice to get

$$\int_{\mathbb{R}^N}\int_{t_0}^{T} d\mathbf{X}\,dt\left[\frac{\partial P}{\partial t}+\frac{\partial}{\partial X_\alpha}\left(\mu_\alpha P\right)-\frac{\partial^2}{\partial X_\alpha\partial X_\beta}\left(D_{\alpha\beta}P\right)\right]\Psi(\mathbf{X},t)=0\,. \tag{C.5}$$

Since Eq. (C.5) holds $\forall\,\Psi\left(\mathbf{x},t\right)\in C_0^1\left(\mathcal{I}\right)$, we get the following evolution equation for the transition probability $P\left(\mathbf{X},t|\mathbf{Y},t_0\right)$

$$\frac{\partial P\left(\mathbf{X},t|\mathbf{Y},t_0\right)}{\partial t}=-\frac{\partial}{\partial X_\alpha}\left(\mu_\alpha P\left(\mathbf{X},t|\mathbf{Y},t_0\right)\right)+\frac{\partial^2}{\partial X_\alpha\partial X_\beta}\left(D_{\alpha\beta}P\left(\mathbf{X},t|\mathbf{Y},t_0\right)\right)\,. \tag{C.6}$$

The above equation represent the temporal evolution of the transition probability $P\left(\mathbf{X},t|\mathbf{Y},t_0\right)$ starting from the state $\mathbf{Y}$ at the time $t_0<t$ forward in time, and it is called Forward Kolmogorov Equation (also known as Fokker-Planck equation in the physics community). After defining the operator $\mathcal{F}$

$$\mathcal{F}=\frac{\partial}{\partial\mathbf{X}}\cdot\mu\left(\mathbf{X}\right)-\frac{\partial}{\partial\mathbf{X}}\otimes\frac{\partial}{\partial\mathbf{X}}:\mathbf{D}\,, \tag{C.7}$$

Eq. (C.6) can be rewritten in operator form as

$$\frac{\partial P\left(\mathbf{X},t|\mathbf{Y},t_0\right)}{\partial t}=-\mathcal{F}P\left(\mathbf{X},t|\mathbf{Y},t_0\right)\,. \tag{C.8}$$

Its formal solution is found to be

$$P\left(\mathbf{X},t|\mathbf{Y},t_0\right)=\exp\left[-\mathcal{F}\left(t-t_0\right)\right]P\left(\mathbf{X},t_0|\mathbf{Y},t_0\right)\,. \tag{C.9}$$

We now wish to derive an evolution equation for the transition probability starting from the time $t>t_0$ backward in time. Let us considering the state $\mathbf{Z}$ at the time q such that $t\in(t_0,q)$. The Chapman-Kolmogorov equation

$$P\left(\mathbf{Z},q|\mathbf{Y},t_0\right)=\int P\left(\mathbf{Z},q|\mathbf{X},t\right)P\left(\mathbf{X},t|\mathbf{Y},t_0\right)\,d\mathbf{X}\,, \tag{C.10}$$

can be differentiated with respect to the time t leading to

$$\int \frac{\partial P\left(\mathbf{Z}, q|\mathbf{X}, t\right)}{\partial t} P\left(\mathbf{X}, t|\mathbf{Y}, t_0\right) - P\left(\mathbf{Z}, q|\mathbf{X}, t\right) \frac{\partial P\left(\mathbf{X}, t|\mathbf{Y}, t_0\right)}{\partial t} d\mathbf{X}\,, \quad \text{(C.11)}$$

since $P\left(\mathbf{Z}, q|\mathbf{Y}, t_0\right)$ does not depend on time t.

Using relationship (C.8) on the second term and integrating by parts make the adjoint operator $\mathcal{F}^\dagger$ appear, leading to the new form of Eq. (C.10)

$$\int \left[\frac{\partial P\left(\mathbf{Z}, q|\mathbf{X}, t\right)}{\partial t} - \mathcal{F}^\dagger P\left(\mathbf{Z}, q|\mathbf{X}, t\right)\right] P\left(\mathbf{X}, t|\mathbf{Y}, t_0\right)\, d\mathbf{X} = 0\,, \quad \text{(C.12)}$$

where we stress that $q > t$. Since the transition (or conditional probability) is positive, Eq. (C.12) leads to the so-called Backward Kolmogorov Equation

$$\frac{\partial P\left(\mathbf{Z}, q|\mathbf{X}, t\right)}{\partial t} - \mathcal{F}^\dagger P\left(\mathbf{Z}, q|\mathbf{X}, t\right) = 0\,. \quad \text{(C.13)}$$

The backward equation, and has the following informal interpretation: given state of the system $\mathbf{Z}$ at a future time q, the transition probability distribution evolves with respect to the current time t according to the Eq. (C.13), by imposing the terminal condition and by integrating backward in time.

Appendice D

Bubble Kinematics

In this section a procedure to extract some geometric and kinematic properties of the bubbles and to track their motion into the macroscopic fluid dynamic fields is developed, using a diffuse interface approach. Let us consider the evolution of a density iso-surface $\rho\left[\left(\mathbf{x}\left(\eta,t\right),t\right)\right]=\rho_0$, representing a bubble interface, in the reference configuration $\mathbf{x}=\mathbf{x}\left(\eta,t\right)$. The time derivative reads

$$\frac{d}{dt}\rho\left[\left(\mathbf{x}\left(\eta,t\right),t\right)\right]=\frac{\partial\rho}{\partial t}+\dot{\mathbf{x}}\cdot\nabla\rho=0, \tag{D.1}$$

and iso-surface velocity

$$\mathbf{w}\left(\mathbf{x},t\right):=\dot{\mathbf{x}}=-\frac{\partial\rho}{\partial t}\frac{\nabla\rho}{\nabla\rho\cdot\nabla\rho}. \tag{D.2}$$

Let $\phi\left(\mathbf{x},t\right)$ be a generic physical quantity related to the bubble B_i, its evolution reads

$$\begin{aligned}\dot{\Phi} &= \frac{d}{dt}\int_{\mathbf{B}_i(t)}\phi\left(\mathbf{x},t\right)\,dV=\frac{d}{dt}\int_{\mathbf{B}_i^{\eta}}\phi\left(\mathbf{x}\left(\eta,t\right),t\right)\mathbf{J}^{\eta}\,dV^{\eta}\\ &= \int_{\mathbf{B}_i(t)}\frac{D^{(w)}}{Dt}\phi+\phi\,\nabla\cdot\mathbf{w}\,dV\,,\end{aligned} \tag{D.3}$$

where $D^{(w)}/Dt = \partial/\partial t + \mathbf{w}\cdot\nabla$ is the material derivative, having $\mathbf{w}$ as velocity field, and $\mathbf{J}^{\eta}$ is the Jacobian determinant of the map $\mathbf{x} = \mathbf{x}(\eta, t)$, whose time derivative is $\dot{\mathbf{J}}^{\eta} = \mathbf{J}^{\eta}\,\nabla\cdot\mathbf{w}$.

For each bubble, let us define the peculiar velocity $\mathbf{w}_i^{'}(\mathbf{x}, t) := \mathbf{w}_i(\mathbf{x}, t) - \mathbf{u}(\mathbf{x}, t)$, where $\mathbf{u}(\mathbf{x}, t)$ is the macroscopic velocity field, and let M_{B_i} be the mass of the i-th bubble in the liquid. The evolution equation of the bubble masses can be obtained from eq. (D.3) by replacing $\phi(\mathbf{x}, t) = \rho(\mathbf{x}, t)$, and by enforcing the total mass conservation of the fluid, i.e. $\partial\rho/\partial t + \nabla\cdot(\rho\mathbf{u}) = 0$. The bubble mass variations are

$$\dot{M}_{B_i} = \frac{d}{dt}\int_{\mathbf{B}_i(t)} \rho(\mathbf{x}, t)\; dV = \oint_{\partial\mathbf{B}_i(t)} \rho(\mathbf{x}, t)\; \mathbf{w}_i^{'}(\mathbf{x}, t)\cdot\mathbf{n}\, dS\,, \tag{D.4}$$

where $\mathbf{B_i(t)}$ are the regions of the space occupied by the bubbles B_i. For each bubble, the velocity of the center of mass is evaluated as

$$\dot{\mathbf{X}}_{g_i} = \frac{1}{M_{B_i}}\frac{d}{dt}\int_{\mathbf{B}_i(t)} \mathbf{x}\rho(\mathbf{x}, t)\; dV\; - \frac{\dot{M}_{B_i}}{M_{B_i}}\mathbf{X}_{g_i}\,. \tag{D.5}$$

By evaluating the first term of the RHS of eq. (D.5) as above in eq. (D.3) one has

$$\dot{\mathbf{X}}_{g_i} = \frac{1}{M_{B_i}}\int_{\mathbf{B}_i(t)} \rho(\mathbf{x}, t)\,\mathbf{u}(\mathbf{x}, t) - \nabla\cdot\mathbf{G}_i(\mathbf{x}, t, \mathbf{X}_{g_i})\; dV\,, \tag{D.6}$$

where the second order tensor $\mathbf{G}_i(\mathbf{x}, t, \mathbf{X}_{g_i})$, arising from the density gradient in the field, turns out to be

$$\mathbf{G}_i(\mathbf{x}, t, \mathbf{X}_{g_i}) = \rho(\mathbf{x}, t)\,(\mathbf{x} - \mathbf{X}_{g_i}) \otimes \left(\frac{\partial\rho}{\partial t}\frac{\nabla\rho}{\nabla\rho\cdot\nabla\rho} - \mathbf{u}(\mathbf{x}, t)\right). \tag{D.7}$$

Similarly the time derivative of the bubble volumes reads

$$\dot{V}_{B_i} = \oint_{\partial\mathbf{B}_i(t)} \mathbf{w}_i^{'}(\mathbf{x}, t)\cdot\mathbf{n}\, dS\,. \tag{D.8}$$

The above procedure is implemented in an algorithm to identify the distinct bubbles, and to evaluate their physical properties, and has been used in [64], to follow the nucleated bubble (see Chapter 6 for details).

Bibliografia

[1] Yusuf G Adewuyi. Sonochemistry in environmental remediation. 1. combinative and hybrid sonophotochemical oxidation processes for the treatment of pollutants in water. *Environmental science & technology*, 39(10):3409–3420, 2005.

[2] I Akhatov, O Lindau, A Topolnikov, R Mettin, N Vakhitova, and W Lauterborn. Collapse and rebound of a laser-induced cavitation bubble. *Physics of Fluids*, 13(10):2805–2819, 2001.

[3] Rosalind J Allen, Daan Frenkel, and Pieter Rein ten Wolde. Simulating rare events in equilibrium or nonequilibrium stochastic systems. *The Journal of chemical physics*, 124(2):024102, 2006.

[4] Rosalind J Allen, Chantal Valeriani, and Pieter Rein ten Wolde. Forward flux sampling for rare event simulations. *Journal of physics: Condensed matter*, 21(46):463102, 2009.

[5] DM Anderson, GB McFadden, and AA Wheeler. Diffuse-interface methods in fluid mechanics. *Annual Review of Fluid Mechanics*, 30(1):139–165, 1998.

[6] Raymond Angélil, Jürg Diemand, Kyoko K Tanaka, and Hidekazu Tanaka. Bubble evolution and properties in homogeneous nucleation simulations. *Physical review E*, 90(6):063301, 2014.

[7] John C Angus and Cliff C Hayman. Low-pressure, metastable growth of diamond and" diamondlike" phases. *Science*, 241(4868):913–921, 1988.

[8] Paul J Atzberger. Spatially adaptive stochastic numerical methods for intrinsic fluctuations in reaction–diffusion systems. *Journal of Computational Physics*, 229(9):3474–3501, 2010.

[9] Nicolas Auffray, Francesco dell?Isola, Victor A Eremeyev, Angela Madeo, and Giuseppe Rosi. Analytical continuum mechanics à la hamilton–piola least action principle for second gradient continua and capillary fluids. *Mathematics and Mechanics of Solids*, 20(4):375–417, 2015.

[10] Mouna El Mekki Azouzi, Claire Ramboz, Jean-François Lenain, and Frédéric Caupin. A coherent picture of water at extreme negative pressure. *Nature Physics*, 9(1):38–41, 2013.

[11] Florencio Balboa, John B Bell, Rafael Delgado-Buscalioni, Aleksandar Donev, Thomas G Fai, Boyce E Griffith, and Charles S Peskin. Staggered schemes for fluctuating hydrodynamics. *Multiscale Modeling & Simulation*, 10(4):1369–1408, 2012.

[12] Jean-Louis Barrat and Jean-Pierre Hansen. *Basic concepts for simple and complex liquids*. Cambridge University Press, 2003.

[13] John B Bell, Alejandro L Garcia, and Sarah A Williams. Computational fluctuating fluid dynamics. *ESAIM: Mathematical Modelling and Numerical Analysis*, 44(5):1085–1105, 2010.

[14] T. B. Benjamin and A. T. Ellis. The collapse of cavitation bubbles and the pressures thereby produced against solid boundaries. *Philosophical transactions of the Royal Society of London. Series A, Mathematical and physical sciences*, 260(1110):221–240, 1966.

[15] Bruce J Berne and Robert Pecora. *Dynamic light scattering: with applications to chemistry, biology, and physics*. Courier Corporation, 1976.

[16] John R Blake and DC Gibson. Growth and collapse of a vapour cavity near a free surface. *Journal of Fluid Mechanics*, 111:123–140, 1981.

[17] John R Blake and DC Gibson. Cavitation bubbles near boundaries. *Annual review of fluid mechanics*, 19(1):99–123, 1987.

[18] Milton Blander and Joseph L Katz. Bubble nucleation in liquids. *AIChE Journal*, 21(5):833–848, 1975.

[19] Martin JK Blomley, Jennifer C Cooke, Evan C Unger, Mark J Monaghan, and David O Cosgrove. Science, medicine, and the future: Microbubble contrast agents: a new era in ultrasound. *BMJ: British Medical Journal*, 322(7296):1222, 2001.

[20] Lydéric Bocquet and Elisabeth Charlaix. Nanofluidics, from bulk to interfaces. *Chemical Society Reviews*, 39(3):1073–1095, 2010.

[21] NN Bogoliubov. Nn bogoliubov, j. phys.(moscow) 10, 256 (1946). *J. Phys.(Moscow)*, 10:256, 1946.

[22] Peter G Bolhuis, David Chandler, Christoph Dellago, and Phillip L Geissler. Transition path sampling: Throwing ropes over rough mountain passes, in the dark. *Annual review of physical chemistry*, 53(1):291–318, 2002.

[23] Peter G Bolhuis, David Chandler, Christoph Dellago, and Phillip L Geissler. Transition path sampling: Throwing ropes over rough mountain passes, in the dark. *Annual review of physical chemistry*, 53(1):291–318, 2002.

[24] J-P Bouchaud, ME Cates, J Ravi Prakash, and SF Edwards. Hysteresis and metastability in a continuum sandpile model. *Physical review letters*, 74(11):1982, 1995.

[25] Benoit Bourdon, Emilie Bertrand, Paolo Di Marco, Marco Marengo, Romain Rioboo, and Joël De Coninck. Wettability influence on the onset temperature of pool boiling: Experimental evidence onto ultra-smooth surfaces. *Advances in colloid and interface science*, 221:34–40, 2015.

[26] Benoit Bourdon, Romain Rioboo, Marco Marengo, Emmanuel Gosselin, and Joël De Coninck. Influence of the wettability on the boiling onset. *Langmuir*, 28(2):1618–1624, 2012.

[27] Christopher E Brennen. Cavitation in biological and bioengineering contexts. 2003.

[28] Christopher E Brennen. *Cavitation and bubble dynamics*. Cambridge University Press, 2013.

[29] Christopher Earls Brennen. Cavitation in medicine. *Interface Focus*, 5(5):20150022, 2015.

[30] Michael P Brenner, Sascha Hilgenfeldt, and Detlef Lohse. Single-bubble sonoluminescence. *Reviews of Modern Physics*, 74(2):425, 2002.

[31] John W Cahn and John E Hilliard. Free energy of a nonuniform system. iii. nucleation in a two-component incompressible fluid. *The Journal of chemical physics*, 31(3):688–699, 1959.

[32] Liangliang Cao, Andrew K Jones, Vinod K Sikka, Jianzhong Wu, and Di Gao. Anti-icing superhydrophobic coatings. *Langmuir*, 25(21):12444–12448, 2009.

[33] Anuj Chaudhri, John B Bell, Alejandro L Garcia, and Aleksandar Donev. Modeling multiphase flow using fluctuating hydrodynamics. *Physical Review E*, 90(3):033014, 2014.

[34] Niharendu Choudhury and B Montgomery Pettitt. On the mechanism of hydrophobic association of nanoscopic solutes. *Journal of the American Chemical Society*, 127(10):3556–3567, 2005.

[35] Constantin C Coussios and Ronald A Roy. Applications of acoustics and cavitation to noninvasive therapy and drug delivery. *Annual Review of Fluid Mechanics*, 40:395–420, 2008.

[36] Giuseppe Da Prato. *Kolmogorov equations for stochastic PDEs*. Birkhäuser, 2012.

[37] Sybren Ruurds De Groot and Peter Mazur. *Non-equilibrium thermodynamics*. Courier Dover Publications, 2013.

[38] R De Luca, G Silvani, C Scognamiglio, G Sinibaldi, G Peruzzi, M Chinappi, MF Kiani, and CM Casciola. Towards cavitation-enhanced permeability in blood vessel on a chip. In *AIP Conference Proceedings*, volume 1873, page 020010. AIP Publishing, 2017.

[39] JM Ortiz de Zárate, F Peluso, and JV Sengers. Nonequilibrium fluctuations in the rayleigh-bénard problem for binary fluid mixtures. *The European Physical Journal E*, 15(3):319–333, 2004.

[40] Jose M Ortiz De Zarate and Jan V Sengers. *Hydrodynamic fluctuations in fluids and fluid mixtures*. Elsevier, 2006.

[41] Pablo G Debenedetti. *Metastable liquids: concepts and principles*. Princeton University Press, 1996.

[42] Christoph Dellago and Peter G Bolhuis. Transition path sampling and other advanced simulation techniques for rare events. In *Advanced Computer Simulation Approaches for Soft Matter Sciences III*, pages 167–233. Springer, 2009.

[43] F Dell'Isola, H Gouin, and G Rotoli. Nucleation of spherical shell-like interfaces by second gradient theory: Numerical simulations. *European Journal of Mechanics, B/Fluids*, 15(4):545–568, 1996.

[44] Francesco Dell'Isola, Henri Gouin, and Giacomo Rotoli. Nucleation of spherical shell-like interfaces by second gradient theory: numerical simulations. *arXiv preprint arXiv:0906.1897*, 2009.

[45] Francesco Dell'Isola, Henri Gouin, Pierre Seppecher, et al. Radius and surface tension of microscopic bubbles by second gradient theory. *Comptes Rendus de l Académie des Sciences-Series IIB-Mechanics*, 320, 1995.

[46] Steven Delong, Boyce E Griffith, Eric Vanden-Eijnden, and Aleksandar Donev. Temporal integrators for fluctuating hydrodynamics. *Physical Review E*, 87(3):033302, 2013.

[47] François Detcheverry and Lydéric Bocquet. Thermal fluctuations in nanofluidic transport. *Physical review letters*, 109(2):024501, 2012.

[48] Sylvain Deville, Eric Maire, Guillaume Bernard-Granger, Audrey Lasalle, Agnès Bogner, Catherine Gauthier, Jérôme Leloup, and Christian Guizard. Metastable and unstable cellular solidification of colloidal suspensions. *Nature materials*, 8(12):966, 2009.

[49] Jürg Diemand, Raymond Angélil, Kyoko K Tanaka, and Hidekazu Tanaka. Direct simulations of homogeneous bubble nucleation: Agreement with classical nucleation theory and no local hot spots. *Physical review E*, 90(5):052407, 2014.

[50] Rory Dijkink and Claus-Dieter Ohl. Laser-induced cavitation based micropump. *Lab on a Chip*, 8(10):1676–1681, 2008.

[51] Zhong Ding and SM Gracewski. The behaviour of a gas cavity impacted by a weak or strong shock wave. *Journal of Fluid Mechanics*, 309:183–209, 1996.

[52] Aleksandar Donev, John B Bell, Alejandro L Garcia, and Berni J Alder. A hybrid particle-continuum method for hydrodynamics of complex fluids. *Multiscale Modeling & Simulation*, 8(3):871–911, 2010.

[53] Aleksandar Donev, Andy Nonaka, Yifei Sun, Thomas Fai, Alejandro Garcia, and John Bell. Low mach number fluctuating hydrodynamics of diffusively mixing fluids. *Communications in Applied Mathematics and Computational Science*, 9(1):47–105, 2014.

[54] Aleksandar Donev, Eric Vanden-Eijnden, Alejandro Garcia, and John Bell. On the accuracy of finite-volume schemes for fluctuating hydrodynamics. *Communications in Applied Mathematics and Computational Science*, 5(2):149–197, 2010.

[55] Miguel A Durán-Olivencia and James F Lutsko. Unification of classical nucleation theories via a unified itô-stratonovich stochastic equation. *Physical Review E*, 92(3):032407, 2015.

[56] Jens Eggers. Dynamics of liquid nanojets. *Physical review letters*, 89(8):084502, 2002.

[57] Albert Einstein. Theorie der opaleszenz von homogenen flüssigkeiten und flüssigkeitsgemischen in der nähe des kritischen zustandes. *Annalen der Physik*, 338(16):1275–1298, 1910.

[58] Albert Einstein. *Investigations on the Theory of the Brownian Movement*. Courier Corporation, 1956.

[59] Pep Español. Stochastic differential equations for non-linear hydrodynamics. *arXiv preprint cond-mat/9705183*, 1997.

[60] David J Flannigan and Kenneth S Suslick. Plasma formation and temperature measurement during single-bubble cavitation. *Nature*, 434(7029):52–55, 2005.

[61] Ronald Forrest Fox and George E Uhlenbeck. Contributions to non-equilibrium thermodynamics. i. theory of hydrodynamical fluctuations. *Physics of Fluids (1958-1988)*, 13(8):1893–1902, 1970.

[62] Mirko Gallo, Francesco Magaletti, and Carlo M Casciola. Phase field/fluctuating hydrodynamics approach for bubble nucleation. In *ICHMT DIGITAL LIBRARY ONLINE*. Begel House Inc., 2018.

[63] Mirko Gallo, Francesco Magaletti, and Carlo Massimo Casciola. Fluctuating hydrodynamics as a tool to investigate nucleation of cavitation bubbles. *International Journal of Computational Methods and Experimental Measurements*, 6(2):345–357, 2017.

[64] Mirko Gallo, Francesco Magaletti, and Carlo Massimo Casciola. Thermally activated vapor bubble nucleation: The landau-lifshitz–van der waals approach. *Phys. Rev. Fluids*, 3:053604, May 2018.

[65] Alejandro L Garcia, M Malek Mansour, George C Lie, and Enrico Cementi. Numerical integration of the fluctuating hydrodynamic equations. *Journal of statistical physics*, 47(1-2):209–228, 1987.

[66] Crispin Gardiner. *Stochastic methods*, volume 4. springer Berlin, 2009.

[67] Alberto Giacomello, Simone Meloni, Mauro Chinappi, and Carlo Massimo Casciola. Cassie–baxter and wenzel states on a nanostructured surface: phase diagram, metastabilities, and transition mechanism

by atomistic free energy calculations. *Langmuir*, 28(29):10764–10772, 2012.

[68] Joachim Heierli. Solitary fracture waves in metastable snow stratifications. *Journal of Geophysical Research: Earth Surface*, 110(F2), 2005.

[69] Robert Hickling and Milton S Plesset. Collapse and rebound of a spherical bubble in water. *Physics of Fluids (1958-1988)*, 7(1):7–14, 1964.

[70] Stuart Ibsen, Carolyn E Schutt, and Sadik Esener. Microbubble-mediated ultrasound therapy: a review of its potential in cancer treatment. *Drug design, development and therapy*, 7:375, 2013.

[71] David Jacqmin. Contact-line dynamics of a diffuse fluid interface. *Journal of Fluid Mechanics*, 402:57–88, 2000.

[72] D Jamet, O Lebaigue, N Coutris, and JM Delhaye. The second gradient method for the direct numerical simulation of liquid–vapor flows with phase change. *Journal of Computational Physics*, 169(2):624–651, 2001.

[73] Didier Jamet. *Etude des potentialités de la théorie du second gradient pour la simulation numérique directe des écoulements liquide-vapeur avec changement de phase*. PhD thesis, 1998.

[74] Jiří Jane?ek and Roland R Netz. Interfacial water at hydrophobic and hydrophilic surfaces: Depletion versus adsorption. *Langmuir*, 23(16):8417–8429, 2007.

[75] J Karl Johnson, John A Zollweg, and Keith E Gubbins. The lennard-jones equation of state revisited. *Molecular Physics*, 78(3):591–618, 1993.

[76] SF Jones, GM Evans, and KP Galvin. Bubble nucleation from gas cavities?a review. *Advances in colloid and interface science*, 80(1):27–50, 1999.

[77] Wei Kang and Uzi Landman. Universality crossover of the pinch-off shape profiles of collapsing liquid nanobridges in vacuum and gaseous environments. *Physical Review Letters*, 98(6):064504, 2007.

[78] Mehran Kardar, Giorgio Parisi, and Yi-Cheng Zhang. Dynamic scaling of growing interfaces. *Physical Review Letters*, 56(9):889, 1986.

[79] D Kashchiev and GM Van Rosmalen. Review: nucleation in solutions revisited. *Crystal Research and Technology*, 38(7-8):555–574, 2003.

[80] Dimo Kashchiev. *Nucleation*. Elsevier, 2000.

[81] Joseph B Keller and Ignace I Kolodner. Damping of underwater explosion bubble oscillations. *Journal of Applied physics*, 27(10):1152–1161, 1956.

[82] J Kestin, JV Sengers, B Kamgar-Parsi, and JMH Levelt Sengers. Thermophysical properties of fluid h2o. *Journal of Physical and Chemical Reference Data*, 13(1):175–183, 1984.

[83] Hendrik Anthony Kramers. Brownian motion in a field of force and the diffusion model of chemical reactions. *Physica*, 7(4):284–304, 1940.

[84] LD Landau and EM Lifshitz. Statistical physics, vol. 5. *Course of theoretical physics*, 30, 1980.

[85] Amy E Larsen and David G Grier. Like-charge attractions in metastable colloidal crystallites. *Nature*, 385(6613):230, 1997.

[86] W Lauterborn and H Bolle. Experimental investigations of cavitation-bubble collapse in the neighbourhood of a solid boundary. *Journal of Fluid Mechanics*, 72(02):391–399, 1975.

[87] Werner Lauterborn and Alfred Vogel. Shock wave emission by laser generated bubbles. In *Bubble Dynamics and Shock Waves*, pages 67–103. Springer, 2013.

[88] T Leighton. *The acoustic bubble*. Academic press, 2012.

[89] Robin Hui Liu, Ralf Lenigk, Roberta L Druyor-Sanchez, Jianing Yang, and Piotr Grodzinski. Hybridization enhancement using cavitation microstreaming. *Analytical Chemistry*, 75(8):1911–1917, 2003.

[90] Detlef Lohse and Andrea Prosperetti. Homogeneous nucleation: Patching the way from the macroscopic to the nanoscopic description. *Proceedings of the National Academy of Sciences*, 113(48):13549–13550, 2016.

[91] James F Lutsko. Density functional theory of inhomogeneous liquids. ii. a fundamental measure approach. *The Journal of chemical physics*, 128(18):184711, 2008.

[92] James F Lutsko. Density functional theory of inhomogeneous liquids. iv. squared-gradient approximation and classical nucleation theory. *The Journal of chemical physics*, 134(16):164501, 2011.

[93] James F Lutsko. A dynamical theory of nucleation for colloids and macromolecules. *The Journal of chemical physics*, 136(3):034509, 2012.

[94] James F Lutsko. Systematically extending classical nucleation theory. *New Journal of Physics*, 2018.

[95] James F Lutsko and Miguel A Durán-Olivencia. A two-parameter extension of classical nucleation theory. *Journal of Physics: Condensed Matter*, 27(23):235101, 2015.

[96] F Magaletti, L Marino, and CM Casciola. Shock wave formation in the collapse of a vapor nanobubble. *Physical Review Letters*, 114(6):064501, 2015.

[97] Francesco Magaletti, Mirko Gallo, Luca Marino, and Carlo Massimo Casciola. Dynamics of a vapor nanobubble collapsing near a solid boundary. In *Journal of Physics: Conference Series*, volume 656, page 012012. IOP Publishing, 2015.

[98] Francesco Magaletti, Mirko Gallo, Luca Marino, and Carlo Massimo Casciola. Shock-induced collapse of a vapor nanobubble near solid boundaries. *International Journal of Multiphase Flow*, 84:34–45, 2016.

[99] Francesco Magaletti, Luca Marino, and Carlo Massimo Casciola. Diffuse interface modeling of a radial vapor bubble collapse. In *Journal of*

Physics: Conference Series, volume 656, page 012028. IOP Publishing, 2015.

[100] Ileana Malavasi, Bernard Bourdon, Paolo Di Marco, Joël De Coninck, and Marco Marengo. Appearance of a low superheat ?quasi-leidenfrost? regime for boiling on superhydrophobic surfaces. *International Communications in Heat and Mass Transfer*, 63:1–7, 2015.

[101] Georg Menzl, Miguel A Gonzalez, Philipp Geiger, Frédéric Caupin, José LF Abascal, Chantal Valeriani, and Christoph Dellago. Molecular mechanism for cavitation in water under tension. *Proceedings of the National Academy of Sciences*, 113(48):13582–13587, 2016.

[102] EE Michaelides and KL Zissis. Velocity of sound in two-phase mixtures. *International Journal of Heat and Fluid Flow*, 4(2):79–84, 1983.

[103] Emily B Moore and Valeria Molinero. Structural transformation in supercooled water controls the crystallization rate of ice. *Nature*, 479(7374):506, 2011.

[104] VG Morozov. On the langevin formalism for nonlinear and nonequilibrium hydrodynamic fluctuations. *Physica A: Statistical Mechanics and its Applications*, 126(3):443–460, 1984.

[105] Michael Moseler and Uzi Landman. Formation, stability, and breakup of nanojets. *Science*, 289(5482):1165–1169, 2000.

[106] Daniel M Murphy and Thomas Koop. Review of the vapour pressures of ice and supercooled water for atmospheric applications. *Quar-*

terly Journal of the Royal Meteorological Society: A journal of the atmospheric sciences, applied meteorology and physical oceanography, 131(608):1539–1565, 2005.

[107] Ali Naji, Paul J Atzberger, and Frank LH Brown. Hybrid elastic and discrete-particle approach to biomembrane dynamics with application to the mobility of curved integral membrane proteins. *Physical review letters*, 102(13):138102, 2009.

[108] Charl F Naudé and Albert T Ellis. On the mechanism of cavitation damage by nonhemispherical cavities collapsing in contact with a solid boundary. *Journal of Fluids Engineering*, 83(4):648–656, 1961.

[109] Joachim Noack and Alfred Vogel. Single-shot spatially resolved characterization of laser-induced shock waves in water. *Applied Optics*, 37(19):4092–4099, 1998.

[110] Brian R. Novak, Edward J. Maginn, and Mark J. McCready. Comparison of heterogeneous and homogeneous bubble nucleation using molecular simulations. *Phys. Rev. B*, 75:085413, Feb 2007.

[111] C-D Ohl, A Philipp, and W Lauterborn. Cavitation bubble collapse studied at 20 million frames per second. *Annalen der Physik*, 507(1):26–34, 1995.

[112] Claus-Dieter Ohl, Manish Arora, Rory Dijkink, Vaibhav Janve, and Detlef Lohse. Surface cleaning from laser-induced cavitation bubbles. *Applied Physics Letters*, 89(7):074102, 2006.

[113] David W Oxtoby and R Evans. Nonclassical nucleation theory for the gas–liquid transition. *The Journal of chemical physics*, 89(12):7521–7530, 1988.

[114] Giovanna Peruzzi, Giorgia Sinibaldi, Giulia Silvani, Giancarlo Ruocco, and Carlo Massimo Casciola. Perspectives on cavitation enhanced endothelial layer permeability. *Colloids and Surfaces B: Biointerfaces*, 168:83–93, 2018.

[115] Charles S Peskin, Garrett M Odell, and George F Oster. Cellular motions and thermal fluctuations: the brownian ratchet. *Biophysical journal*, 65(1):316, 1993.

[116] A Philipp and W Lauterborn. Cavitation erosion by single laser-produced bubbles. *Journal of Fluid Mechanics*, 361:75–116, 1998.

[117] Milton S Plesset and Richard B Chapman. Collapse of an initially spherical vapour cavity in the neighbourhood of a solid boundary. *Journal of Fluid Mechanics*, 47(02):283–290, 1971.

[118] Milton S Plesset and Andrea Prosperetti. Bubble dynamics and cavitation. *Annual review of fluid mechanics*, 9(1):145–185, 1977.

[119] Milton S Plesset and Andrea Prosperetti. Bubble dynamics and cavitation. *Annual Review of Fluid Mechanics*, 9(1):145–185, 1977.

[120] MS Plesset and AT Ellis. On the mechanism of cavitation damage. *Transactions of the ASME*, 77:1055–1064, 1955.

[121] Lord Rayleigh. Viii. on the pressure developed in a liquid during the collapse of a spherical cavity. *The London, Edinburgh, and Dublin Philosophical Magazine and Journal of Science*, 34(200):94–98, 1917.

[122] Weiqing Ren. Wetting transition on patterned surfaces: transition states and energy barriers. *Langmuir*, 30(10):2879–2885, 2014.

[123] JM Rubí. Fluctuations around equilibrium. In *Recent Developments in Nonequilibrium Thermodynamics*, pages 233–266. Springer, 1984.

[124] JM Rubı and P Mazur. Nonequilibrium thermodynamics and hydrodynamic fluctuations. *Physica A: Statistical Mechanics and its Applications*, 276(3):477–488, 2000.

[125] GN Sankin, F Yuan, and P Zhong. Pulsating tandem microbubble for localized and directional single-cell membrane poration. *Physical Review Letters*, 105(7):078101, 2010.

[126] Paolo Sartori, Damiano Quagliati, Silvia Varagnolo, Matteo Pierno, Giampaolo Mistura, Francesco Magaletti, and Carlo Massimo Casciola. Drop motion induced by vertical vibrations. *New Journal of Physics*, 17(11):113017, 2015.

[127] Chiara Scognamiglio, Francesco Magaletti, Yaroslava Izmaylov, Mirko Gallo, Carlo Massimo Casciola, and Xavier Noblin. The detailed acoustic signature of a micro-confined cavitation bubble. *Soft matter*, 2018.

[128] see Supplemental Material at http://correct.site.url for details. see.

[129] A Shima and Y Sato. The collapse of a spheroidal bubble near a solid wall. *Journal de Mecanique*, 20(2):253–271, 1981.

[130] Chi-Wang Shu. *Essentially non-oscillatory and weighted essentially non-oscillatory schemes for hyperbolic conservation laws*. Springer, 1998.

[131] D Silberrad. Propeller erosion. *Engineering*, pages 33–35, 1912.

[132] Herbert Spohn. Nonlinear fluctuating hydrodynamics for anharmonic chains. *Journal of Statistical Physics*, 154(5):1191–1227, 2014.

[133] Herbert Spohn and Gabriel Stoltz. Nonlinear fluctuating hydrodynamics in one dimension: the case of two conserved fields. *Journal of Statistical Physics*, 160(4):861–884, 2015.

[134] Brian D Storey and Andrew J Szeri. Water vapour, sonoluminescence and sonochemistry. In *Proceedings of the Royal Society of London A: Mathematical, Physical and Engineering Sciences*, volume 456, pages 1685–1709. The Royal Society, 2000.

[135] Gilbert Strang. On the construction and comparison of difference schemes. *SIAM Journal on Numerical Analysis*, 5(3):506–517, 1968.

[136] Rouslan L Stratonovich. *Nonlinear nonequilibrium thermodynamics I: linear and nonlinear fluctuation-dissipation theorems*, volume 57. Springer Science & Business Media, 2012.

[137] H_M Strong and RE Hanneman. Crystallization of diamond and graphite. *The Journal of Chemical Physics*, 46(9):3668–3676, 1967.

[138] Robert E Tipton, Daniel J Steinberg, and Yukio Tomita. Bubble expension and collapse near a rigid wall. *JSME international journal. Ser. 2, Fluids engineering, heat transfer, power, combustion, thermophysical properties*, 35(1):67–75, 1992.

[139] Y Tomita and A Shima. Mechanisms of impulsive pressure generation and damage pit formation by bubble collapse. *Journal of Fluid Mechanics*, 169:535–564, 1986.

[140] A Unsworth, D Dowson, and V Wright. 'cracking joints'. a bioengineering study of cavitation in the metacarpophalangeal joint. *Annals of the rheumatic diseases*, 30(4):348, 1971.

[141] JD Van der Waals. The thermodynamic theory of capillarity under the hypothesis of a continuous variation of density. *Journal of Statistical Physics*, 20(2):200–244, 1979.

[142] W Van Saarloos, D Bedeaux, and P Mazur. Non-linear hydrodynamic fluctuations around equilibrium. *Physica A: Statistical Mechanics and its Applications*, 110(1-2):147–170, 1982.

[143] A Vogel, W Lauterborn, and R Timm. Optical and acoustic investigations of the dynamics of laser-produced cavitation bubbles near a solid boundary. *Journal of Fluid Mechanics*, 206:299–338, 1989.

[144] A Vogel, J Noack, G Hüttman, and G Paltauf. Mechanisms of femtosecond laser nanosurgery of cells and tissues. *Applied Physics B*, 81(8):1015–1047, 2005.

[145] Alfred Vogel, Norbert Linz, Sebastian Freidank, and Günther Paltauf. Femtosecond-laser-induced nanocavitation in water: implications for optical breakdown threshold and cell surgery. *Physical Review Letters*, 100(3):038102, 2008.

[146] Zun-Jing Wang, Chantal Valeriani, and Daan Frenkel. Homogeneous bubble nucleation driven by local hot spots: A molecular dynamics study. *The Journal of Physical Chemistry B*, 113(12):3776–3784, 2008.

[147] CA Ward, WR Johnson, RD Venter, S Ho, TW Forest, and WD Fraser. Heterogeneous bubble nucleation and conditions for growth in a liquid–gas system of constant mass and volume. *Journal of Applied Physics*, 54(4):1833–1843, 1983.

[148] E Weinan, Weiqing Ren, and Eric Vanden-Eijnden. String method for the study of rare events. *Physical Review B*, 66(5):052301, 2002.

[149] E Weinan, Weiqing Ren, and Eric Vanden-Eijnden. Simplified and improved string method for computing the minimum energy paths in barrier-crossing events. *Journal of Chemical Physics*, 126(16):164103, 2007.

[150] Nanrong Zhao, Andrea Mentrelli, Tommaso Ruggeri, and Masaru Sugiyama. Admissible shock waves and shock-induced phase transitions in a van der waals fluid. *Physics of Fluids*, 23:086101, 2011.

[151] Songlin Zhu, Franklin H Cocks, Glenn M Preminger, and Pei Zhong. The role of stress waves and cavitation in stone comminution in shock wave lithotripsy. *Ultrasound in Medicine & Biology*, 28(5):661–671, 2002.

[152] DN Zubarev and VG Morozov. Statistical mechanics of nonlinear hydrodynamic fluctuations. *Physica A: Statistical Mechanics and its Applications*, 120(3):411–467, 1983.